Kerr Solitons and Brillouin Lasers in Optical Microresonators

Thesis by
Heming Wang

In Partial Fulfillment of the Requirements for the
Degree of
Doctor of Philosophy

CALIFORNIA INSTITUTE OF TECHNOLOGY
Pasadena, California

2021
Defended May 18th 2021

Heming Wang
ORCID: 0000-0003-3861-0624

ACKNOWLEDGEMENTS

First of all, I would like to thank Prof. Kerry Vahala for his supervision. He has both intuition and rigor when it comes to problem solving, and the free research environment in his group has made everyone productive.

None of this research would have been fruitful without discussions with coauthors, group members and collaborators. They include: Jiang Li, Seung Hoon Lee, Dongyoon Oh, Xinbai Li, Kiyoul Yang, Xu Yi, Myoung-Gyun Suh, Yu-Hung Lai, Qifan Yang, and Chengying Bao, former group members and now alumni of the Vahala group; Boqiang Shen, Lue Wu, Zhiquan Yuan, Maodong Gao, Qingxin Ji, and Bohan Li, current group members at Vahala group; Chang Lin, Minh Tran, and Prof. John Bowers at University of California, Santa Barbara (UCSB); Junqiu Liu and Prof. Tobias Kippenberg at Swiss Federal Institute of Technology Lausanne (EPFL); Prof. Andrey Matsko and Prof. Vladimir Ilchenko at Jet Propulsion Laboratory (JPL); Prof. Scott Diddams and Prof. Scott Papp at National Institute of Standards and Technology (NIST); and Prof. Hansuek Lee at KAIST. They have all provided valuable input to the work included here.

I am grateful for the support from the various funding agencies that power our research and prevent my stomach from going empty.

Special credits go to my undergraduate advisors and close friends, Prof. Liangzhu Mu and Prof. Yunfeng Xiao at Peking University, who have been influential to my understanding of physics as a whole.

Finally, I acknowledge my family, my classmates, and the countless friends that could not be enumerated here, who have lent me support and courage during my long and adventurous academic journey.

ABSTRACT

Optical resonators are capable of storing electromagnetic energies in the visible and infrared band. The light intensity is greatly enhanced within the resonator, which makes them suitable as a platform for nonlinear optics studies. Here, using silica microresonators as platforms, we explore the fundamental nonlinear dynamics of light induced by Kerr nonlinearity and Brillouin scattering. The first half of the thesis analyzes optical solitons as a result of Kerr nonlinearity, including its universal scaling, its dynamics in the presence of laser feedback, the analytical properties of its relativistic counterpart, as well as its applications as a wavelength reference. The second half of the thesis focuses on stimulated Brillouin lasers and their linewidth performance, demonstrating new performance levels of the Brillouin laser and two correction factors to its linewidth that have been established for semiconductor lasers.

PUBLISHED CONTENT AND CONTRIBUTIONS

Wu, L. *et al.* Greater than one billion Q factor for on-chip microresonators. *Optics Letters* **45**, 5129–5131 (2020), DOI: 10.1364/OL.394940.
H.W. participated in the conception of the project, fabricated the devices, assisted the experiments, analyzed the data, and contributed to writing the manuscript.

Li, X. *et al.* Universal isocontours for dissipative Kerr solitons. *Optics Letters* **43**, 2567–2570 (2018), DOI: 10.1364/OL.43.002567.
H.W. participated in the conception of the project, performed the theoretical calculations, assisted the experiment, analyzed the data, and contributed to writing the manuscript.

Shen, B. *et al.* Integrated turnkey soliton microcombs. *Nature* **582**, 365–369 (2020), DOI: 10.1038/s41586-020-2358-x.
H.W. participated in the conception of the project, performed the theoretical calculations, assisted the experiments, analyzed the data, and contributed to writing the manuscript.

Lee, S. H. *et al.* Towards visible soliton microcomb generation. *Nature Communications* **8**, 1295 (2017), DOI: 10.1038/s41467-017-01473-9.
H.W. participated in the conception of the project, assisted the fabrication of devices, modeled the device designs, performed the experiment for 1064 nm solitons, analyzed the data, and contributed to writing the manuscript.

Wang, H. *et al.* Dirac solitons in optical microresonators. *Light: Science & Applications* **9**, 205 (2020), DOI: 10.1038/s41377-020-00438-w.
H.W. participated in the conception of the project, performed the theoretical calculations, modeled the device designs, assisted the experiments, analyzed the data, and contributed to writing the manuscript.

Yang, Q.-F. *et al.* Vernier spectrometer using counterpropagating soliton microcombs. *Science* **363**, 965–968 (2019), DOI: 10.1126/science.aaw2317.
H.W. participated in the conception of the project, devised the data processing algorithm, assisted the experiment, analyzed the data, and contributed to writing the manuscript.

Wang, H., Wu, L., Yuan, Z. & Vahala, K. Towards milli-hertz laser frequency noise on a chip. Preprint at https://arxiv.org/abs/2010.09248 (2020).
H.W. participated in the conception of the project, performed the experiments, analyzed the data, and contributed to writing the manuscript.

Yuan, Z., Wang, H., Wu, L., Gao, M. & Vahala, K. Linewidth enhancement factor in a microcavity Brillouin laser. *Optica* **7**, 1150–1153 (2020), DOI:

10.1364/OPTICA.394311.
H.W. participated in the conception of the project, performed the theoretical calculations, assisted the experiments, analyzed the data, and contributed to writing the manuscript.

Wang, H., Lai, Y.-H., Yuan, Z., Suh, M.-G. & Vahala, K. Petermann-factor sensitivity limit near an exceptional point in a Brillouin ring laser gyroscope. *Nature Communications* **11**, 1610 (2020), DOI: 10.1038/s41467-020-15341-6.
H.W. participated in the conception of the project, performed the theoretical calculations, assisted the experiments, analyzed the data, and contributed to writing the manuscript.

TABLE OF CONTENTS

LIST OF ILLUSTRATIONS

Chapter 1

INTRODUCTION

Nonlinear physical systems and their associated nonlinear problems have attracted great interest in the past century. In particular, nonlinear optics studies have benefited from the invention of lasers and low-loss fibers, and have resulted in many fundamental breakthroughs such as the frequency comb technology (awarded the 2005 Nobel physics prize). Optical microresonators [1] have emerged as a particularly promising platform for nonlinear optics due to their ability to store light energy and enhance the intensity inside the resonator, triggering nonlinear effects with moderate levels of input power. Such effects not only are intriguing on their own, but also help us have a better understanding of the fundamental nonlinear processes. Here we explore two of the optical nonlinearities commonly found in materials: Kerr nonlinearity and Brillouin scattering. The Kerr nonlinearity can create optical solitons in the resonator, and we study their characteristics as well as how to deterministically generate them. On the other hand, Brillouin scattering can lead to stimulated Brillouin lasers, and we focus on their linewidth and demonstrating new performance levels.

1.1 Optical microresonators and their characterization

Optical microresonators, in their broadest sense, can refer to any device that can store external electromagnetic energies within a predetermined frequency band (usually the visible and infrared band). The "micro" traditionally refers to the overall small size of the resonator (usually tens of μm), but now millimeter- and centimeter-sized resonators are also classified as microresonators as long as their mode area is on the μm^2 level. Microresonators can be realized by different configurations [1], such as Fabry-Perot (two reflectors trapping the light within), waveguide ring (a waveguide with its head connected to tail, in which light can circulate), whispering-gallery (similar to waveguide ring but replaces the waveguiding mechanism by total internal reflection), and photonic crystal (periodic arrangement of structure that leads to band gaps and embedded energy levels).

For simplicity we will focus on the waveguide ring and whispering-gallery resonators. The waveguide itself supports *transverse modes*, where light distributes itself across the waveguide cross section while satisfying the Maxwell equations.

If the waveguide dimension is large enough, the waveguide may support multiple transverse modes with different field profiles. Because of the periodic condition present in these resonators, light can sustain itself only when it constructively interferes with itself after one round trip. Such states are known as *longitudinal modes*, or *resonances* of the resonator, where the ring circumsference is an integer multiple (known as the *mode number*) of the wavelength. The frequencies of such modes (*resonance frequencies*, or *mode frequencies*) are discrete and are the only frequencies where light can be effectively stored in the resonator. The distance between adjacent mode frequencies equals the *free spectral range* (FSR) of the resonator.

To allow light from outside the resonator to be transferred into the resonator, there is *external coupling* from the environment to the resonator. For example, a mirror with reflectivity less than 1 will allow the light to pass through the mirror in a Fabry-Perot resonator, and another waveguide can be brought to close proximity to the ring resonator so its evanescent field overlap and light can tunnel from the external waveguide to the resonator. The external coupling is described by the *coupling rate*, denoted as κ_{ex} and has dimension T^{-1}. Note that, while the coupling itself is conservative, it appears as a loss source of the resonator, consistent with the Fermi's golden rule (see next section). There may also be *intrinsic losses* of the resonator as a result of material absorption or surface scattering. This is described by the *energy loss rate* κ_0, the rate that energy is lost from the resonator through intrinsic loss channels, and it also has dimension T^{-1}. The total loss κ of a specific mode can then be written as a sum of its intrinsic and external losses:

$$\kappa = \kappa_0 + \kappa_{\text{ex}}. \tag{1.1}$$

The loss is usually compared to the resonance frequency of the mode, and the dimensionless *quality factor* (*Q factor*) of the mode can be defined:

$$Q = \frac{\omega_0}{\kappa}, \tag{1.2}$$

where ω_0 is the angular resonance frequency in rad/s units. The Q factor describes how many oscillation cycles the light can complete before its energy decays to $1/e$ of its initial value. Higher Q factor leads to more long-lived photons inside the resonator and is more beneficial for nonlinear applications. Similar to the overall Q factor, intrinsic and external quality factors, Q_0 and Q_{ex}, can be defined for their respective loss channel by replacing κ with κ_0 and κ_{ex}. They satisfy

$$Q^{-1} = Q_0^{-1} + Q_{\text{ex}}^{-1}. \tag{1.3}$$

A similar concept is the *finesse*, comparing the loss to the resonator FSR:

$$F = \frac{\mathrm{FSR}}{\kappa}. \tag{1.4}$$

The finesse describes how many round trips the light can complete before its energy decays to $1/e$ of its initial value. The *intrinsic finesse* and *external finesse* can be similarly defined. State-of-the-art microresonators can attain a finesse of 10^2 to 10^5, and Q factors of 10^7 to 10^9.

A special coupling condition is the *critical coupling*, where $\kappa_{\mathrm{ex}} = \kappa_0 = \kappa/2$. At this condition all incoming light is transferred to the resonator, and there is no light bypassing the resonator (a quantitative description is given in the next section). This is similar to the impedance matching concept in electronics, where impedance mismatch at the two sides of a port will create reflections of the electrical signal.

For nonlinear applications, it is preferable to focus the light onto a smaller spot, which increases the energy flux for a fixed power and enhances nonlinear effects. The *effective mode area* of a transverse mode describes its spatial extent within the waveguide:

$$A_{\mathrm{eff}} = \frac{\left(\int |\mathbf{E}|^2 dA\right)^2}{\int |\mathbf{E}|^4 dA}, \tag{1.5}$$

where $\mathbf{E}$ is the modal field distribution, and the integral goes over the entire cross-section. There are many other definitions for mode area, but this one involving the fourth power of $\mathbf{E}$ is closely related to the Kerr nonlinearity process with four photon ladder operators in its Hamiltonian. We note that the above definitions can be directly applied only to resonators made with a single material; the integral needs to be weighted by material nonlinearities if multiple materials are present in the resonator. A related concept is the *effective mode volume*, describing the spatial extent of the mode in the entire resonator:

$$V_{\mathrm{eff}} = \frac{\left(\int |\mathbf{E}|^2 dV\right)^2}{\int |\mathbf{E}|^4 dV}. \tag{1.6}$$

Smaller mode volumes increase confinement of the field, and, combined with a high Q factor, increase the overall nonlinear effect inside the resonator and decrease power requirements. For example, the parametric oscillation threshold, the external power required to make the resonator generate optical sidebands, scales as V_{eff}/Q^2.

1.2 The mode equation

The mode equations give a complete description of the dynamics of resonator modes. There are many ways to determine the mode dynamics. The projection method starts from the Maxwell equations and projects them onto a specific mode family [2, 3]. This method is rigorous and capable of linking the coupling coefficients to fundamental material properties (i.e. from the modal nonlinear coefficient to material third-order nonlinear susceptibility $\chi^{(3)}$ or nonlinear refractive index n_2). However, for simplicity considerations, here we will directly start from Hamiltonians and write down the dynamics using Heisenberg equations. This is simpler when the expression for coupling is not important and can be obtained from experiments.

The simplest Hamiltonian consists of a single number operator:

$$H = \hbar\omega\bar{a}^\dagger\bar{a}, \tag{1.7}$$

where $\hbar$ is the reduced Planck constant, ω is the resonance frequency of the mode, and $\bar{a}$ is the lowering operator of the mode. From here the equation of dynamics can be obtained as

$$\frac{d\bar{a}}{dt} = -i\omega\bar{a}. \tag{1.8}$$

It would be convenient to "reference" all equations to a specific frequency (usually the external pumping frequency ω_P or the true oscillating frequency of the mode in question) to eliminate time dependencies from the equations. To this end, we define a slow-varying version of $\bar{a}$, $a = \bar{a}e^{i\omega_\mathrm{P}t}$. The equation for the slow-varying a reads

$$\frac{da}{dt} = -i(\omega - \omega_\mathrm{P})a = -i\delta\omega a, \tag{1.9}$$

where we have defined the *detuning* of the mode $\delta\omega \equiv \omega - \omega_\mathrm{P}$. $\delta\omega < 0$ indicates that pump frequency is higher than the mode frequency, and is known as *blue detuned*; conversely $\delta\omega > 0$ indicates that pump frequency is lower than the mode frequency, and is known as *red detuned*. The effective Hamiltonian using the slow-varying variables reads

$$H = \hbar\delta\omega a^\dagger a. \tag{1.10}$$

To incorporate the effects of intrinsic loss, a phenomenological term is directly added to the equation of motion:

$$\frac{da}{dt} = -i\delta\omega a - \frac{\kappa_0}{2}a. \tag{1.11}$$

This non-Hermitian term can not be directly incorporated into the Hamiltonian and is usually added by hand into the Heisenberg equation.

The external coupling is realized through coupling to a continuum of modes supported by the external waveguide. To correctly normalize the external modes, we will first assume a length L_{ex} for the waveguide and impose periodic boundary conditions, then let $L_{\mathrm{ex}} \to \infty$ at the end. The slow-varying lowering operator for the continuum is denoted as $A(\delta\omega_{\mathrm{ex}})$ labeled by its detuning $\delta\omega_{\mathrm{ex}}$. It is normalized to photon number per unit length to facilitate normalization. The Hamiltonian in this case reads

$$\begin{aligned} H &= \hbar\delta\omega a^\dagger a \\ &+ \sum_{\delta\omega_{\mathrm{ex}}} \hbar\delta\omega_{\mathrm{ex}} L_{\mathrm{ex}} A^\dagger(\delta\omega_{\mathrm{ex}}) A(\delta\omega_{\mathrm{ex}}) - \hbar[g_{\mathrm{ex}} a^\dagger A(\delta\omega_{\mathrm{ex}}) + g_{\mathrm{ex}}^* A^\dagger(\delta\omega_{\mathrm{ex}}) a], \end{aligned} \tag{1.12}$$

where g_{ex} is the matrix element for external coupling, assumed to be real and constant over the frequency range of A being considered. The coupling term does not explicitly depend on L_{ex}, as increasing the external waveguide length should not affect the local coupling between the waveguide and resonator.

The equation for a can be derived in an analogous manner of deriving Fermi's golden rule. We solve the amplitudes of A from the Hamiltomian:

$$\frac{dA}{dt} = -i\delta\omega_{\mathrm{ex}} A + i\frac{g_{\mathrm{ex}}^*}{L_{\mathrm{ex}}} a, \quad A = \frac{1 - e^{-i\delta\omega_{\mathrm{ex}} t}}{\delta\omega_{\mathrm{ex}}} \frac{g_{\mathrm{ex}}^*}{L_{\mathrm{ex}}} a, \tag{1.13}$$

and the dynamics of a can be written as

$$\frac{da}{dt} = -i\delta\omega a + i g_{\mathrm{ex}} \sum_{\delta\omega_{\mathrm{ex}}} A = -i\delta\omega a - \frac{|g_{\mathrm{ex}}|^2}{L_{\mathrm{ex}}} a \sum_{\delta\omega_{\mathrm{ex}}} \frac{1 - e^{-i\delta\omega_{\mathrm{ex}} t}}{i\delta\omega_{\mathrm{ex}}}. \tag{1.14}$$

By taking the limit of $L_{\mathrm{ex}} \to \infty$, we can replace the sum with an integral, multiplied by the density of states of the waveguide. The integral reads

$$\int \frac{1 - e^{-i\delta\omega_{\mathrm{ex}} t}}{i\delta\omega_{\mathrm{ex}}} d\delta\omega_{\mathrm{ex}} \approx \int_{-\infty}^{\infty} \frac{\sin(\delta\omega_{\mathrm{ex}} t)}{\delta\omega_{\mathrm{ex}}} d\delta\omega_{\mathrm{ex}} = \pi. \tag{1.15}$$

The density of states reads $L_{\mathrm{ex}}/(2\pi v)$, where v is the speed of light in the waveguide. Combining all the results above and adding the intrinsic loss, we get

$$\frac{da}{dt} = -i\delta\omega a - \frac{\kappa_0}{2} a - \frac{|g_{\mathrm{ex}}|^2}{2v} a, \tag{1.16}$$

and we can associate $\kappa_{\mathrm{ex}} \equiv |g_{\mathrm{ex}}|^2/v$ with the external coupling-induced loss of the resonator. The appearance of a loss-like term in a conservative system is not surprising: it captures the central result of Fermi's golden rule, where transition

rate to a continuum of modes is a constant (similar to loss), rather than linear in time (similar to single-mode conservative coupling). Effectively, the external coupling creates another loss channel for the resonator, adding to the intrinsic loss and determining the overall loss of the mode.

For external pumping, the term $-\hbar|g_{\mathrm{ex}}|(a^\dagger A_{\mathrm{in}} + A_{\mathrm{in}}^* a)$ can be added to the Hamiltonian, where A_{in} is a classical pumping amplitude, and the extra phase from g_{ex} can be absorbed into A_{in}. There is no detuning term as the equation has already been referenced to the pumping frequency. The equation of a thus reads

$$\frac{da}{dt} = -i\delta\omega a - \frac{\kappa_0 + \kappa_{\mathrm{ex}}}{2} a + i\sqrt{\kappa_{\mathrm{ex}}}\sqrt{v} A_{\mathrm{in}}. \tag{1.17}$$

Note that $|A|^2$ represents the photon number per unit length, and $v|A_{\mathrm{in}}|^2$ would represent the input photon number per unit time, or the optical power P_{in} divided by $\hbar\omega_0$. It would thus be convenient to define an input term as $a_{\mathrm{in}} = \sqrt{v}|A_{\mathrm{in}}| = \sqrt{P_{\mathrm{in}}/(\hbar\omega)}$, which would be normalized to photon flux. We therefore have

$$\frac{da}{dt} = -i\delta\omega a - \frac{\kappa}{2} a + i\sqrt{\kappa_{\mathrm{ex}}} a_{\mathrm{in}}, \tag{1.18}$$

with $\kappa = \kappa_0 + \kappa_{\mathrm{ex}}$, which is the starting point for resonator mode dynamics.

As an example of applying the mode equation, we derive the critical coupling condition as mentioned above. We would like to know the field amplitude that bypasses the resonator after some portion of the light is coupled into the resonator. Using the above Hamiltonian formalism, we found that the output field a_{out}, again normalized to photon flux, reads

$$a_{\mathrm{out}} = a_{\mathrm{in}} + i\sqrt{\kappa_{\mathrm{ex}}} a, \tag{1.19}$$

The steady-state solution for a reads

$$a = \frac{i\sqrt{\kappa_{\mathrm{ex}}} a_{\mathrm{in}}}{\kappa/2 + i\delta\omega}. \tag{1.20}$$

Thus the output photon flux reads

$$|a_{\mathrm{out}}|^2 = \left|1 - \frac{\kappa_{\mathrm{ex}}}{\kappa/2 + i\delta\omega}\right|^2 |a_{\mathrm{in}}|^2 = \left(1 - \frac{\kappa_0\kappa_{\mathrm{ex}}}{\kappa^2/4 + \delta\omega^2}\right)|a_{\mathrm{in}}|^2. \tag{1.21}$$

This result is consistent with energy conservation, i.e. those photons coupled to the resonator are dissipated through their intrinsic loss channel:

$$|a_{\mathrm{in}}|^2 - |a_{\mathrm{out}}|^2 = \kappa_0 |a|^2. \tag{1.22}$$

Note again that, although the κ_{ex} appears like a loss to the resonator, it is not a loss for the entire resonator-waveguide system, and does not appear in the energy conservation calculation.

We return to the expression for the output photon flux and define a transmission coefficient as the ratio of photon bypassing the resonator:

$$T = \frac{|a_{out}|^2}{|a_{in}|^2} = 1 - \frac{\kappa_0 \kappa_{ex}}{\kappa^2/4 + \delta\omega^2}. \tag{1.23}$$

The transmission has a Lorentzian lineshape in the frequency domain (with respect to $\delta\omega$), and its full width at half maximum is given by κ. T reaches minimum at $\delta\omega = 0$ (i.e. the pump is exactly on resonance), where

$$T_{min} = 1 - \frac{\kappa_0 \kappa_{ex}}{\kappa^2/4} = \left(\frac{\kappa_0 - \kappa_{ex}}{\kappa_0 + \kappa_{ex}}\right)^2. \tag{1.24}$$

At the critical coupling condition ($\kappa_0 = \kappa_{ex}$), we got $T_{min} = 0$, and the transfer of photons to the resonator is the most efficient. Deviations from the critical coupling result in nonzero transmission. In the case of $\kappa_0 < \kappa_{ex}$, the system is said to be *undercoupled*, and in the case of $\kappa_0 > \kappa_{ex}$, the system is said to be *overcoupled*.

1.3 Kerr nonlinearities, frequency combs, and optical solitons

Kerr nonlinearities refer to the change of refractive index in material proportional to light intensity. They are named by analogy of the Kerr electrooptical effect, where the change of refractive index scales with the square of the external electric field [4]. The mechanism responsible for the change is the third-order nonlinear susceptibility $\chi^{(3)}$. Light propagating in the material will induce polarization changes, which determine the refractive index of the material. The nonlinear susceptibility induces extra polarization changes, changing the effective refractive index the light experiences. Higher orders of nonlinear susceptibility induce refractive index changes proportional to higher powers of the electric field, which makes $\chi^{(3)}$ the dominant contribution to nonlinearity. Note that the second-order nonlinear susceptibility $\chi^{(2)}$ are present only when inversion symmetry of atom arrangement is broken (lithium niobate being the prominent example) or when electric quadruple and magnetic dipole transitions are considered.

To simplify the discussions, we will assume the resonator is perfecly circular so we can define an angular coordinate θ. In this case the mode number m also represents the angular momentum number and the mode profile is proportional to $\exp(im\theta)$. We also assume that the transverse mode profile is constant within the

band being considered. The Kerr nonlienar part of the Hamiltonian for this circular microresonator can be written as

$$H_{\mathrm{K}} = -\frac{\hbar g_{\mathrm{K}}}{2} \int_0^{2\pi} a^\dagger(\theta) a^\dagger(\theta) a(\theta) a(\theta) \frac{d\theta}{2\pi}, \tag{1.25}$$

where $a(\theta) = \int_0^{2\pi} a_m \exp(im\theta) d\theta$ is the Fourier-transformed slow-varying lowering operator that operates on the field at angular position θ, and a_m is the slow-varying lowering operator for the mode with mode number m. The Kerr coupling g_{K} can be derived as

$$g_{\mathrm{K}} = \hbar\omega_0 \frac{n_2 \omega_0 c}{n^2 V_{\mathrm{eff}}}, \tag{1.26}$$

where n_2 is the nonlinear refractive index (the ratio of refractive index change to light intensity) and n is the linear refractive index of the material. As n_2 is positive in most materials, the negative sign in the Hamiltonian indicates that the nonlinear interaction lowers the energy of the system and red-shifts the resonance frequency.

Since the H_{K} term creates and annihilates two photons, it is possible to convert the photons on the pump mode to other modes with different frequencies. This process is known as *four-wave mixing*. For example, H_{K} may take two photons on the mode m_0 being pumped, and send them to modes $m_0 - \delta m$ and $m_0 + \delta m$ respectively. Note that energy and momentum must be conserved, and the sums of two mode numbers before and after conversion are equal. The special case where the pump with a single frequency is converted to two sidebands is known as *optical parametric oscillation*. For a quantitative description, we project the H_{K} onto the space spanned by three modes, $a_{\mathrm{P}} \equiv a_{m_0}$, $a_+ \equiv a_{m_0+\delta m}$ and $a_- \equiv a_{m_0-\delta m}$. The full Hamiltonian reads

$$\begin{aligned} H = {} & \hbar\delta\omega_0 a_{\mathrm{P}}^\dagger a_{\mathrm{P}} + \hbar\delta\omega_- a_-^\dagger a_- + \hbar\delta\omega_+ a_+^\dagger a_+ \\ & - \frac{\hbar g_{\mathrm{K}}}{2} a_{\mathrm{P}}^\dagger a_{\mathrm{P}}^\dagger a_{\mathrm{P}} a_{\mathrm{P}} \\ & - \frac{\hbar g_{\mathrm{K}}}{2} \left[4 a_{\mathrm{P}}^\dagger a_{\mathrm{P}} \left(a_-^\dagger a_- + a_+^\dagger a_+ \right) + 2 a_{\mathrm{P}}^\dagger a_{\mathrm{P}}^\dagger a_- a_+ + 2 a_{\mathrm{P}} a_{\mathrm{P}} a_-^\dagger a_+^\dagger \right] \\ & - \frac{\hbar g_{\mathrm{K}}}{2} \left[a_-^\dagger a_-^\dagger a_- a_- + a_+^\dagger a_+^\dagger a_+ a_+ + 4 a_-^\dagger a_- a_+^\dagger a_+ \right]. \end{aligned} \tag{1.27}$$

The nonlinear part of H is separated into terms quartic in a_{P} (self-phase modulation), quadratic in a_{P} (cross-phase modulation and four-wave mixing), and quartic in $a_\pm$. We will ignore the last section of H by assuming the amplitudes on $a_\pm$ are small, and demote a_{P} to a classical variable to simplify calculations. The equations for $a_\pm$ read

$$\frac{da_-}{dt} = -\frac{\kappa}{2} a_- - i\delta\omega_- a_- + i g_{\mathrm{K}} \left(2|a_{\mathrm{P}}|^2 a_- + a_{\mathrm{P}}^2 a_+^\dagger \right), \tag{1.28}$$

$$\frac{da_+}{dt} = -\frac{\kappa}{2}a_+ - i\delta\omega_+ a_+ + ig_{\mathrm{K}}\left(2|a_{\mathrm{P}}|^2 a_+ + a_{\mathrm{P}}^2 a_-^\dagger\right). \tag{1.29}$$

This is a set of linear equations in a_- and $a_+^\dagger$. If light can be sustained on the modes, at least one eigenvalue should be zero. This gives the following conditions:

$$\delta\omega_- = \delta\omega_+, \tag{1.30}$$

$$g_{\mathrm{K}}^2|a_{\mathrm{P}}|^4 = \frac{\kappa^2}{4} + \left(\delta\omega_- - 2g_{\mathrm{K}}|a_{\mathrm{P}}|^2\right)^2. \tag{1.31}$$

Using energy conservation, we can express the detuning using the pump frequency and the mode resonance frequencies, which results in

$$g_{\mathrm{K}}^2|a_{\mathrm{P}}|^4 = \frac{\kappa^2}{4} + \left(\frac{\omega_- + \omega_+ - 2\omega_{\mathrm{P}}}{2} - 2g_{\mathrm{K}}|a_{\mathrm{P}}|^2\right)^2. \tag{1.32}$$

If the resonance frequencies are perfectly equidistant (i.e. equal FSR everywhere), and the pump frequency coincides with the pump mode resonance frequency, the $\omega_- + \omega_+ - 2\omega_{\mathrm{P}}$ term will vanish, and the above condition to sustain light on the sidebands can never be satisfied due to nonlinear shifting of the frequency breaking the energy conservation condition. Therefore we have to consider the *dispersion* effect of the resonator, where the FSR (or equivalently the group velocity) changes with wavelength. The dispersion is usually quantified by expressing the resonance frequency as a Taylor series in mode number:

$$\omega_m = \omega_{m_0} + \mathrm{FSR}\cdot(m - m_0) + \frac{D_2}{2!}(m - m_0)^2 + ..., \tag{1.33}$$

where D_2 is the *second-order dispersion parameter*, and higher-order terms have been neglected. The system has *normal* dispersion when $D_2 < 0$, and *anomalous* dispersion when $D_2 > 0$, which derive their names from the corresponding behavior in bulk materials. With anomalous dispersion, the nonlinear frequency shifting can be correctly compensated by selecting a suitable δm, and it is possible for sidebands to appear within the resonator. The threshold of $|a_{\mathrm{P}}|$ for this to occur reads

$$|a_{\mathrm{P}}|^2 = \frac{\kappa}{2g_{\mathrm{K}}}, \tag{1.34}$$

or in terms of input power,

$$P_{\mathrm{in}} = \hbar\omega_0\frac{\kappa^3}{8\kappa_{\mathrm{ex}}g_{\mathrm{K}}}. \tag{1.35}$$

known as the *parametric oscillation threshold*.

When light is sustained on the sidebands, it may initiate additional four-wave mixing processes, generating light on more and more sidebands. Light on all modes is

coherent as a whole, and looks like a comb when represented on the frequency spectrum, with a sharp line near the resonance frequency of each mode. This is the basic concept of *frequency combs*, now widely applied to ranging, timing, and spectroscopy applications. Note that nonlinearity in resonators is not the only way of generating frequency combs; other methods, such as electro-optic modulation, are outside the scope of this thesis.

The frequency comb and its formation can also be described in the time domain. To this end we write down the Hamiltonian density for the resonator:

$$H = \int_0^{2\pi} \eta(\theta) \frac{d\theta}{2\pi}, \tag{1.36}$$

$$\begin{aligned}\eta = {} & \hbar\omega_{m_0} \bar{a}^\dagger(\theta)\bar{a}(\theta) \\ & + \hbar \mathrm{FSR} \bar{a}^\dagger(\theta)(-i\partial_\theta - m_0)\bar{a}(\theta) \\ & + \hbar \frac{D_2}{2} \bar{a}^\dagger(\theta)(-i\partial_\theta - m_0)^2 \bar{a}(\theta) \\ & - \frac{\hbar g_\mathrm{K}}{2} \bar{a}^\dagger(\theta)\bar{a}^\dagger(\theta)\bar{a}(\theta)\bar{a}(\theta),\end{aligned} \tag{1.37}$$

where $\bar{a}$ is the physical lowering operators (not the slow-varying ones). Ignoring the loss and pump terms, the equation of dynamics of the field $\bar{a}$ can be found as

$$\frac{\partial \bar{a}}{\partial t} = -i\omega_{m_0}\bar{a} - i\mathrm{FSR}(-i\partial_\theta - m_0)\bar{a} - i\frac{D_2}{2}\bar{a}^\dagger(-i\partial_\theta - m_0)^2\bar{a} + ig_\mathrm{K}\bar{a}^\dagger\bar{a}\bar{a}. \tag{1.38}$$

The fast time dependence is removed by $\bar{a} \to a\exp(-i\omega_\mathrm{P} t)$, the fast spatial dependence is removed by $a \to \bar{\psi}\exp(im_0\theta)$, and we choose a comoving frame by setting $\psi(\theta', t) = \bar{\psi}(\theta' + \mathrm{FSR}\cdot t, t)$ to remove the linear term. Demoting ψ to a classical field, we find that

$$\frac{\partial \psi}{\partial t} = -i\delta\omega\psi + i\frac{D_2}{2}\frac{\partial^2\psi}{\partial\theta'^2} + ig_\mathrm{K}|\psi|^2\psi. \tag{1.39}$$

This is known as the nonlinear Schrödinger equation, which admits many complex solutions and has been studied both analytically and experimentally. In this equation, D_2 plays the role of kinetic energy, $\delta\omega$ is the energy level, and g_K is the nonlinearity of the field. For non-periodic coordinates (i.e. θ extends to $\pm\infty$), there are *soliton* solutions, which resemble a stationary wavepacket that tends to zero when $\theta' \to \pm\infty$. The fundamental solution can be expressed as

$$\psi = \sqrt{\frac{2\delta\omega}{g_\mathrm{K}}}\mathrm{sech}\left(\sqrt{\frac{2\delta\omega}{D_2}}\theta'\right), \tag{1.40}$$

which traps itself in the potential well created by its nonlinearity.

The soliton solution above can be shown to be robust in the presence of loss and external pump. Most solitons in resonators have a much shorter pulse width compared to the resonator circumsference, and therefore their shape can be approximated by a sech function even when periodic boundary conditions are imposed. Coupling the soliton out of the resonator leads to a train of soliton pulses, each separated by the round trip time (1/FSR) of the soliton within the resonator. When viewed on the frequency domain, these solitons function the same as other frequency combs, and sometimes these solitons are also called *soliton frequency combs*, or in the context of microresonators, *soliton microcombs*.

1.4 Brillouin scattering and stimulated Brillouin laser

Brillouin scattering refers to the nonlinear interaction between light and acoustic waves in the material. The mechanism responsible for the interaction is electrostriction [4]. From a classical viewpoint, the acoustic waves induce periodic density changes within the material, forming a moving grating, and the pump light may scatter off the moving grating with its frequency shifted due to the Doppler effect. From a quantum mechanical viewpoint, a pump photon may either emit a phonon and becomes a photon with lower frequency (the *Stokes* process), or absorb a phonon and becomes a photon with higher frequency (the *anti-Stokes* process). For the resonators with ring-type geometry, light and acoustic waves can only propagate forward and backward, and the scattered light can only travel to the opposite direction of pump to satisfy the energy and momentum conservation laws. Due to the ways the quasi-particles are created or annihilated, the Stokes process is dominant over the anti-stokes process when only the pump mode has a significant number of particles.

The Stokes angular frequency shift of the pump photon, which equals the generated acoustic wave angular frequency, can be solved from energy and momentum conservation as

$$\Omega = \frac{2v_A}{v_P + v_A}\omega_P, \tag{1.41}$$

where v_P (v_A) is the speed of light (sound) in the material and ω_P is the angular frequency of the pump light. Since $v_A \ll v_P$, the above relation is often approximated as

$$\Omega = \frac{2v_A}{v_P}\omega_P. \tag{1.42}$$

In order to facilitate the Brillouin scattering process, there should be an optical mode with a resonance frequency close to the Stokes wave frequency, and a mechanical mode located with a resonance frequency close to the Stokes frequency shift. While the latter requirement is usually not a problem in microresonators, as the mechanical modes are much denser compared to optical resonances, the requirement on optical modes requires special attention. Methods to align the mode frequencies include matching the FSR to the Brillouin shift, sweeping the mode spectrum to find a suitable pair of modes, or tuning the temperature to change v_A and therefore the frequency shifts.

The Hamiltonian of the system, assuming perfectly aligned frequencies to the respective modes, reads

$$H = \hbar g_\mathrm{B}(b^\dagger a_\mathrm{S}^\dagger a_\mathrm{P} + b a_\mathrm{S} a_\mathrm{P}^\dagger), \tag{1.43}$$

where a_P, a_S, and b are the slow-varying lower operators for the pump, Stokes and acoustic mode, respectively. The g_B is the photon-phonon coupling and is proportional to the electrostriction coefficient and the overlap between photon and phonon modes. The equations of motions for individual modes are:

$$\frac{da_\mathrm{P}}{dt} = -\frac{\kappa}{2}a_\mathrm{P} - ig_\mathrm{B} b a_\mathrm{S} + i\sqrt{\kappa_\mathrm{ex}}a_\mathrm{in}, \tag{1.44}$$

$$\frac{da_\mathrm{S}}{dt} = -\frac{\kappa}{2}a_\mathrm{S} - ig_\mathrm{B} b^\dagger a_\mathrm{P}, \tag{1.45}$$

$$\frac{db}{dt} = -\frac{\gamma}{2}b - ig_\mathrm{B} a_\mathrm{S}^\dagger a_\mathrm{P}, \tag{1.46}$$

where γ is the acoustic loss rate, and we used the same loss rate for the two optical modes.

We now make the assumption that the acoustic loss γ is much larger than the optical loss κ, which is true for the silica wedge resonators used for generating Brillouin lasers here. This allows us to adiabatically eliminate b from the system:

$$b = \frac{-ig_\mathrm{B} a_\mathrm{S}^\dagger a_\mathrm{P}}{\gamma/2}, \tag{1.47}$$

$$\frac{da_\mathrm{S}}{dt} = -\frac{\kappa}{2}a_\mathrm{S} + \frac{2g_\mathrm{B}^2}{\gamma}|a_\mathrm{P}|^2 a_\mathrm{S}. \tag{1.48}$$

Therefore the Brillouin process acts as a gain on the a_S mode, and the gain is proportional to the pump photons. At the point where Brillouin gain equals Stokes

mode loss, photons will start to accumulate in the Stokes mode and form the stimulated Brillouin laser. The threshold for pump photons reads

$$|a_{\mathrm{P}}|^2 = \frac{\kappa\gamma}{4g_{\mathrm{B}}^2}. \tag{1.49}$$

The corresponding input power reads

$$P_{\mathrm{in}} = \hbar\omega_0|a_{\mathrm{in}}|^2 = \hbar\omega_0\frac{\kappa^3}{8\kappa_{\mathrm{ex}}}\frac{\gamma}{2g_{\mathrm{B}}^2}. \tag{1.50}$$

The pump photon number remains constant even when the input power exceeds the above threshold (the *clamping* of pump photons), because extra pump photons increase the Stokes gain and will be converted to Stokes photons.

The full-width-half-maximum fundamental linewidth of the stimulated Brilluoin laser has been derived as [5]

$$2\pi\Delta\nu = \frac{\kappa}{2|a_{\mathrm{S}}|^2}(n_{\mathrm{th}} + N_{\mathrm{th}} + 1) = \frac{\hbar\omega_0^3}{2Q_{\mathrm{ex}}QP_{\mathrm{out}}}(n_{\mathrm{th}} + N_{\mathrm{th}} + 1), \tag{1.51}$$

where P_{out} is the output laser power and n_{th} and N_{th} are the number of thermal quanta in the acoustic and optical mode respectively. This is similar to the well-known Schawlow-Townes formula for semiconductor lasers, with the inversion factor set to 1 and the half photon characterizing spontaneous emission replaced by the total number of thermal quanta plus one half from both modes.

1.5 Overview of chapters

High optical Q factor in optical microresonators is critically important, as many figures of merit vary inverse quadratically with Q, such as parametric oscillation threshold, Raman and Brillouin laser threshold, and Schawlow-Townes linewidth of a laser. In **Chapter 2** a record Q-factor over 1.1 billion for on-chip silica resonators is demonstrated. Sub-milliwatt parametric oscillation threshold is also measured in 9 GHz free-spectral-range devices.

Chapters 3 to 7 deal with the properties and applications of optical Kerr solitons in microresonators. In **Chapter 3**, we derive dimensionless, closed-form expressions for soliton power and pulse width to leading order (including Raman contributions). The contours of constant soliton power and constant pulse width in this region are studied through measurement and simulation. Such isocontours impart structure to the existence region, improve understanding of soliton locking and stabilization methods, and, as universal expressions, can simplify the estimation of soliton properties across a wide range of systems.

In **Chapter 4**, we study a new approach of generating solitons automatically in integrated laser-resonator systems. The removal of isolators on the laser chip and backscattering from the resonator allows light be fed back to the laser and its frequency locked to the resonance. We show theoretically that this leads to a new continuous-wave operating point of the system which allows direct comb formation, and validates the results with experiments.

In **Chapter 5**, optical solitons working outside the telecommunications band have been generated. These include solitons with a central wavelength of 1064 nm and 780 nm. This is enabled by devices with high Q factors, low parametric oscillation thresholds, and in the case of 780 nm, controlling the mode dispersion via degeneracy and mode crossing. The results pave the way for creating solitons with even shorter wavelengths and potentially in the visible band.

Chapter 6 closely follows Chapter 5 and studies the solitons that result from mode crossings theoretically. The dynamics of the solitons are shown to be governed by a version of nonlinear Dirac equations, and an approximate closed-form solution to the soliton is derived. Properties of the mode crossing of the resonator are also investigated in detail. The theoretical result is compared against simulations and experiments and shows good agreement.

In **Chapter 7** we present an application of the optical solitons by using them to determine the frequency of an optical signal precisely over a wide range. Two optical solitons form a vernier in the frequency domain, and the signal frequency can be reconstructed by extracting the beating frequency between the signal and two solitons. The method is applied to measure static and scanning lasers, multiple signals, and spectral positions of gas absorption peaks.

Chapters 8 to 10 study the various characteristics of Brillouin lasers in microresonators, with an emphasis on their linewidth performance. In **Chapter 8** we push the white frequency noise of a Brillouin laser below 10 mHz·Hz/Hz. This is accomplished by blocking the Brillouin cascading process and increasing the laser power. Such low noises require special measurement protocols, and we document the use of cross-correlation techniques in conjunction with a standard phase discrimination measurement.

Chapter 9 studies the linewidth enhancement factor (also known as Henry factor) of the Brillouin laser. The factor is shown to be equal to the normalized phase mismatch of the Brillouin process, and may significantly increase the laser linewidth

by 50 times. Measurements of the laser linewidth are performed for different phase mismatch and validate the model. The results emphasize the necessity to maintain the phase matching condition to improve linewidth performance.

Finally, **Chapter 10** studies the Petermann factor that affects the laser linewidth when two or more lasing modes are present. The larger effective noises on each mode can be attributed to the non-orthogonality of lasing modes. These results are linked to exceptional point sensors, where the signal enhancement factor is exactly canceled by increasing noise when working near an exceptional point, providing no fundamental signal-to-noise ratio improvement.

References

[1] Vahala, K. J. Optical microcavities. *Nature* **424**, 839–846 (2003).

[2] Agrawal, G. P. *Nonlinear fiber optics* (Springer, 2013).

[3] Snyder, A. W. & Love, J. *Optical waveguide theory* (Springer Science & Business Media, 2012).

[4] Boyd, R. W. *Nonlinear optics* (San Diego: Academic Press, 2008).

[5] Li, J., Lee, H., Chen, T. & Vahala, K. J. Characterization of a high coherence, Brillouin microcavity laser on silicon. *Optics Express* **20**, 20170–20180 (2012).

Chapter 2

GREATER THAN ONE BILLION Q FACTOR FOR ON-CHIP MICRORESONATORS

Wu, L. *et al.* Greater than one billion Q factor for on-chip microresonators. *Optics Letters* **45**, 5129–5131 (2020).

The many applications of high optical quality (Q)-factor microresonators [1] have stimulated remarkable progress in boosting the Q value across a range of material systems and device platforms (see results and table in Ref. [2]). Q factor frequently enters quadratically into device performance. For example, in Raman [3], parametric [4, 5], and Brillouin [6–8] nonlinear optical oscillators, the threshold varies inverse quadratically with Q. Moreover, this same Q dependence enters the fundamental linewidth of laser oscillators [9] such as microcavity Brillouin lasers [10]. Ultimately, these considerations are key performance drivers in soliton microcomb systems [11], microresonator gyroscopes [12–15], and microwave sources [14, 16, 17]. For chip-based systems, silica microresonators using thermally grown oxide offer the highest Q factors [8]. Here, by optimizing fabrication methods for silica whispering gallery resonators, the Q factor of this system has been boosted to over 1.1 billion. The results are confirmed through linewidth, ring-down, and parametric oscillation measurements.

In the investigation, wedge whispering-gallery resonator devices are fabricated using a combination of thermal oxidation (8 μm thickness on 4 in. (100 mm) high-purity float-zone silicon wafers), optical lithography, buffered HF silica wet etch and XeF_2 silicon dry etch as detailed in reference [8]. The wedge angle was 27-30°. To boost overall Q performance, several process and mask layout improvements were implemented. The resist pattern and subsequent buffered HF silica wet-etch-defined trenches are narrowed as illustrated in Figs. 2.1(a) and 2.1(b). This lowers dry-etch time for silicon removal and thereby reduces unintended microscopic silica dry etching. The temperature of each fabrication step is also strictly controlled within a ±0.5°C range. This includes both the dry etcher temperature and the XeF_2 source temperature, both of which are servo controlled to ensure reproducible results. The importance of this latter temperature control is that it permits a more precise

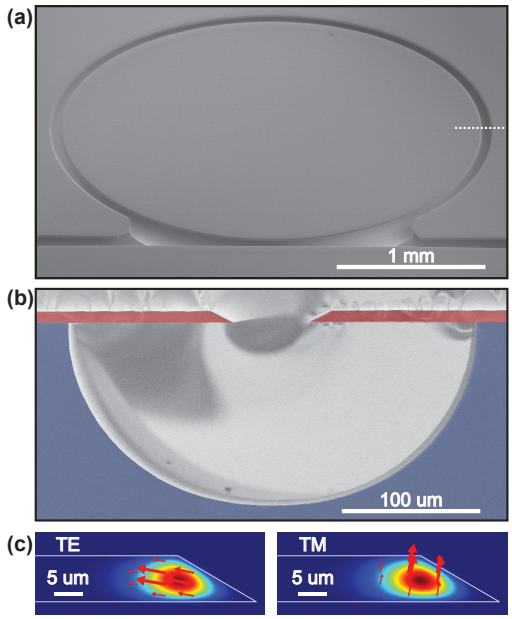

Figure 2.1: Microresonator images and mode profiles. (a) Scanning electron microscope (SEM) image of microresonator (~22 GHz FSR; 3 mm diameter). Dotted white line indicates cross section in panel b. (b) False-color SEM cross section with narrow trench structure and 120 µm undercut. (c) Left (right) panel, fundamental TE (TM) mode electrical field distribution from numerical simulation. Arrows indicate electric field vectors.

determination (and maximization) of silicon undercut to reduce optical loss. The ultimate limit of undercut is determined by silica buckling [18]. Finally, the silica microresonators are annealed 2–3 times for 20 h in an ultra-pure nitrogen ambient at 1000°C to remove water and to release bulk stress in the suspended silica structure.

Intrinsic Q factors (Q_0) are measured by characterization of resonance linewidths (accounting for waveguide loading effects) and through cavity ring-down measurements. Coupling to the resonators using a tapered fiber coupler [19] and a polarization controller was used to excite modes that are primarily TE- or TM-like (see Fig. 2.1(c)). As an aside on the optical coupling, mechanical vibrations are present on the tapered fiber coupler. To suppress these vibrations, it is possible to place the tapered fiber on the top of the wedge edge in contact with the silica surface. As a result, the coupling condition becomes stable without inducing much scattering loss to the resonator. At the same time, the amount of coupling can be readily controlled by simply moving the contact location of the taper on the resonator. This has the effect of adjusting the distance between the taper waveguide and the location of the optical mode (see Fig. 2.1(c)) to thereby adjust the resonator loading by the

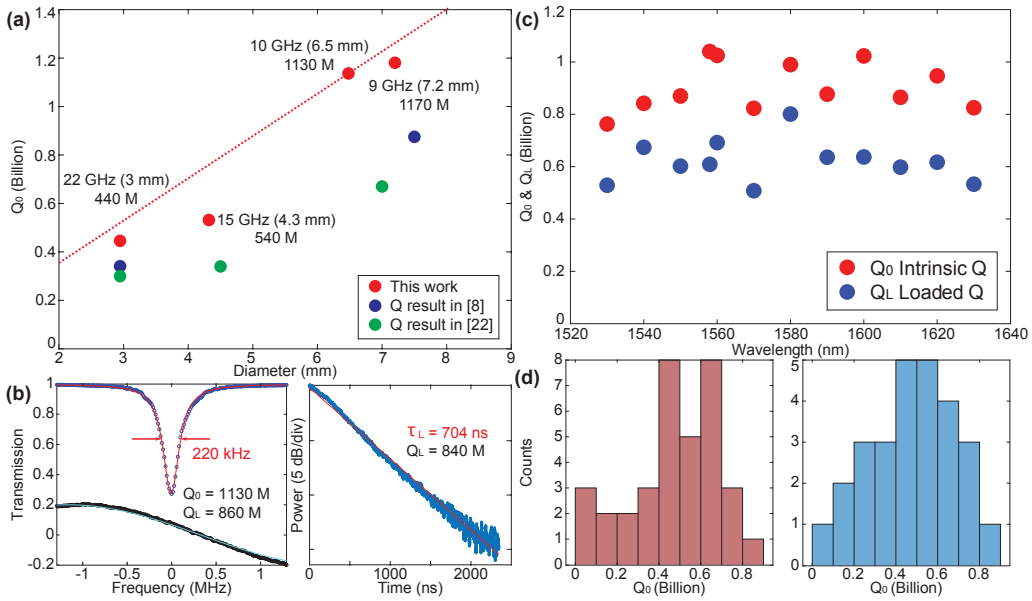

Figure 2.2: Q measurements. (a) Measured intrinsic Q_0 versus resonator diameter. FSR, resonator diameters, and Q_0 values are indicated. Red dotted line corresponds to a finesse of 60,000. (b) Left panel: resonance linewidth measurement of a 10 GHz FSR device at 1585 nm. Upper trace is resonance transmission (blue dots) with Lorentzian lineshape fitting (red curve). The linewidth is 220 kHz, corresponding to an intrinsic Q_0 = 1130 M and loaded Q_L = 860 M. Lower trace is a frequency calibration (black dots) from a Mach-Zehnder interferometer (FSR is 5.979 MHz) with sinusoidal fitting (cyan curve). Right panel: ring-down measurement (blue) of the device measured in the left panel. An exponential decay fitting is shown in red. Photon lifetime is 704 ns, corresponding to loaded $Q_L \approx$ 840 M. (c) Intrinsic Q_0 and loaded Q_L data measured from 1530 nm to 1630 nm. (d) Distribution of Q_0 values measured from different mode families for TE (left panel) and TM (right panel) mode polarization measured in a single FSR.

waveguide.

Fig. 2.2(a) plots the highest intrinsic Q-factors obtained for several device diameters. Two device sizes have Q factors over 1.1 billion. A typical spectral measurement is illustrated in the left panel of Fig. 2.2(b), which shows a transmission spectrum for a device having a free-spectral-range (FSR) of approximately 10 GHz (diameter 6.5 mm). The full-width-at-half-maximum linewidth is measured (at 1585 nm) to be 220 kHz, corresponding to a loaded Q factor Q_L = 860 million. By measuring the transmission depth, a coupling Q factor of Q_c = 3.6 billion is determined from which an intrinsic Q_0 = 1.1 billion is inferred (note: $1/Q_L = 1/Q_0 + 1/Q_c$). The rising dependence of intrinsic Q factor with increasing resonator diameter has been previously observed in the wedge resonator structure and results from round trip loss

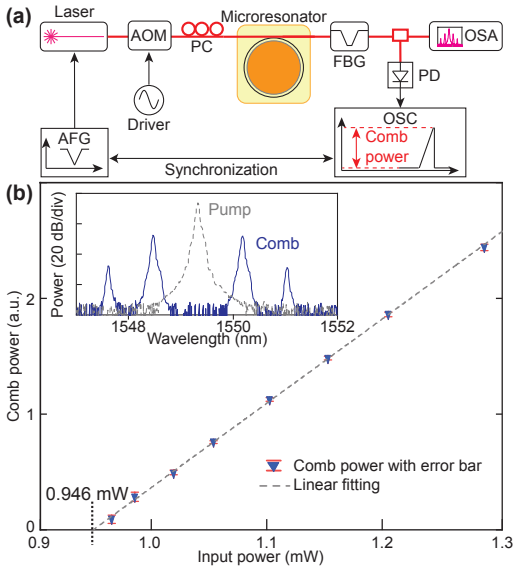

Figure 2.3: Sub-milli-Watt parametric oscillation threshold measured in the device having a 9 GHz FSR. (a) Experimental setup. AOM, acousto-optic modulator; PC, polarization controller; FBG, fiber Bragg grating filter; PD, photo detector; OSA, optical spectrum analyzer; OSC, oscilloscope; AFG, arbitrary function generator. (b) Plot of parametric oscillation power versus input power (1550 nm) showing oscillation threshold of 0.946 mW. Inset: parametric oscillation spectrum (solid blue) and filtered pump (dashed gray) at 1.12 mW input power.

that is limited by surface scattering [8]. To further confirm the Q results, the ring-down of cavity power was also performed. Ring-down data from the same device measured in the left panel of Fig. 2.2(b) is shown in the right panel of Fig. 2.2(b). The ring-down decay gives a photon lifetime of about 704 ns, which corresponds to Q_{L} = 840 M in close agreement with the linewidth-inferred loaded Q. To the authors' knowledge, these are the highest optical Q factors reported for on-chip devices. In particular, previous high-performance results for silica resonators are also plotted as blue and green points in Fig. 2.2(a). It is also worth noting that the $Q_0 > 1$ billion performance has been maintained for more than half a year to date by enclosing the resonators in a purged plexiglass box. The devices possess ultra-high-Q over a broad spectral band, as shown in Fig. 2.2(c), where measured intrinsic and loaded Q factors in a 9 GHz FSR resonator (diameter 7.3 mm) are plotted versus wavelength.

In a typical resonator, there are dozens of modes from different mode families and polarizations that have ultra-high-Q factors. Histograms of measured Q_0 values for TE (left panel) and TM (right panel) mode families in a 9 GHz FSR resonator (near

1550 nm) are plotted in Fig. 2.2(d). Q-factors in the histograms are measured by linewidth fitting on spectra taken by fast frequency scanning of an external-cavity diode laser. The scan was intentionally performed from blue to red wavelengths so that resonator thermal hysteresis effects [20] would tend to degrade the apparent Q factor. As a result, the measured Q values are likely somewhat lower than the actual Q values. To further confirm the Q measurements, the parametric oscillation threshold was also measured using the experimental setup in Fig. 2.3(a). As shown in Fig. 2.3(b), a sub-milliwatt threshold (0.946 mW) was measured using a 9 GHz FSR device at 1550 nm. This is a record low threshold for this low FSR [21]. To perform this measurement, the pump line was filtered using a fiber Bragg grating, as shown in the setup. The pure frequency comb power was then measured and plotted. The inset to Fig. 2.3(b) shows both the filtered and unfiltered spectrum at 1.12 mW input power.

In summary, by optimizing fabrication methods and recipe parameters, we have demonstrated a record on-chip Q-factor over 1.1 billion for silica microresonators. Future efforts will be directed towards implementing these improvements in fully-waveguide-integrated ultra-high-Q resonators [22]. Moreover, besides pure silica structures [8, 22], there is significant progress in ultra-high-Q structures where silica provides the cladding for low confinement silicon nitride waveguides [14, 23]. In these structures, it is important to understand loss limits imposed by silica on the overall design. More generally, the results presented here establish an upper bound for optical loss in structures using thermally grown silica.

References

[1] Vahala, K. J. Optical microcavities. *Nature* **424**, 839–846 (2003).

[2] Chang, L. *et al.* Ultra-efficient frequency comb generation in AlGaAs-on-insulator microresonators. *Nature Communications* **11**, 1–8 (2020).

[3] Spillane, S., Kippenberg, T. & Vahala, K. Ultralow-threshold Raman laser using a spherical dielectric microcavity. *Nature* **415**, 621–623 (2002).

[4] Kippenberg, T., Spillane, S. & Vahala, K. Kerr-nonlinearity optical parametric oscillation in an ultrahigh-Q toroid microcavity. *Physical Review Letters* **93**, 083904 (2004).

[5] Savchenkov, A. A. *et al.* Low threshold optical oscillations in a whispering gallery mode CaF_2 resonator. *Physical Review Letters* **93**, 243905 (2004).

[6] Tomes, M. & Carmon, T. Photonic micro-electromechanical systems vibrating at X-band (11-GHz) rates. *Physical Review Letters* **102**, 113601 (2009).

[7] Grudinin, I. S., Matsko, A. B. & Maleki, L. Brillouin lasing with a CaF_2 whispering gallery mode resonator. *Physical Review Letters* **102**, 043902 (2009).

[8] Lee, H. *et al.* Chemically etched ultrahigh-Q wedge-resonator on a silicon chip. *Nature Photonics* **6**, 369–373 (2012).

[9] Schawlow, A. L. & Townes, C. H. Infrared and optical masers. *Physical Review* **112**, 1940 (1958).

[10] Li, J., Lee, H., Chen, T. & Vahala, K. J. Characterization of a high coherence, Brillouin microcavity laser on silicon. *Optics Express* **20**, 20170–20180 (2012).

[11] Kippenberg, T. J., Gaeta, A. L., Lipson, M. & Gorodetsky, M. L. Dissipative Kerr solitons in optical microresonators. *Science* **361**, eaan8083 (2018).

[12] Li, J., Suh, M. G. & Vahala, K. J. Microresonator Brillouin gyroscope. *Optica* **4**, 346–348 (2017).

[13] Liang, W. *et al.* Resonant microphotonic gyroscope. *Optica* **4**, 114–117 (2017).

[14] Gundavarapu, S. *et al.* Sub-Hertz fundamental linewidth photonic integrated Brillouin laser. *Nature Photonics* **13**, 60–67 (2019).

[15] Lai, Y.-H. *et al.* Earth rotation measured by a chip-scale ring laser gyroscope. *Nature Photonics* **14**, 345–349 (2020).

[16] Li, J., Lee, H. & Vahala, K. J. Microwave synthesizer using an on-chip Brillouin oscillator. *Nature Communications* **4**, 2097 (2013).

[17] Liang, W. *et al.* High spectral purity Kerr frequency comb radio frequency photonic oscillator. *Nature Communications* **6**, 7957.

[18] Chen, T., Lee, H. & Vahala, K. J. Thermal stress in silica-on-silicon disk resonators. *Applied Physics Letters* **102**, 031113 (2013).

[19] Cai, M., Painter, O. & Vahala, K. J. Observation of critical coupling in a fiber taper to a silica-microsphere whispering-gallery mode system. *Physical Review Letters* **85**, 74–77 (2000).

[20] Carmon, T., Yang, L. & Vahala, K. J. Dynamical thermal behavior and thermal self-stability of microcavities. *Optics Express* **12**, 4742–4750 (2004).

[21] Suh, M.-G. & Vahala, K. Gigahertz-repetition-rate soliton microcombs. *Optica* **5**, 65–66 (2018).

[22] Yang, K. Y. *et al.* Bridging ultrahigh-Q devices and photonic circuits. *Nature Photonics* **12**, 297–302 (2018).

[23] Spencer, D. T., Bauters, J. F., Heck, M. J. R. & Bowers, J. E. Integrated waveguide coupled Si3N4 resonators in the ultrahigh-Q regime. *Optica* **1**, 153–157 (2014).

Chapter 3

UNIVERSAL ISOCONTOURS FOR DISSIPATIVE KERR SOLITONS

Li, X. *et al.* Universal isocontours for dissipative Kerr solitons. *Optics Letters* **43**, 2567–2570 (2018).

Temporal optical solitons resulting from the balance of dispersion with the Kerr nonlinearity have long been studied in optical fiber systems [1, 2]. In addition to their many remarkable properties, these nonlinear waves are important in mode locking [3], continuum generation [4], and were once considered as a means to send information over great distances [5, 6]. Recently, a new type of dissipative temporal soliton [7] was observed in optical fiber resonators [8]. These coherently driven cavity solitons (CSs) were previously considered a theoretical possibility [9], and related soliton phenomena, including breather solitons and Raman interactions, have also been reported in this system [10–12]. While leveraging the Kerr effect to balance dispersion, this soliton also regenerates using Kerr-induced parametric amplification [13]. Their recent demonstration in microcavity systems [14–20] has made possible highly stable frequency microcombs [21, 22]. Referred to as dissipative Kerr solitons (DKs) in the microcavity system, soliton phenomena including the Raman self-shift [23–25], optical Cherenkov radiation [16, 25–28], multi-soliton systems [29–31], and the co-generation of new types of solitons [32] have been reported. Moreoever, the compact soliton microcomb devices are being studied for systems-on-a-chip applications such as dual-comb spectroscopy [33, 34], precision distance measurement [35, 36], optical communications [37], and optical frequency synthesis [38].

Regions of stability and existence are well known in driven soliton systems [39]. These properties of DKs and CSs have been studied using the Lugiato-Lefever (LL) equation [9, 40] in a space of normalized pumping power and cavity-pump frequency detuning [14, 41–43]. In analogy with thermodynamic phase diagrams, this soliton existence diagram also contains other regions of existence including those for breather solitons as well as more complex dynamical phenomena [44–46]. Fig. 3.1 is a typical diagram showing only the stable soliton region. In thermodynamic

phase diagrams, another useful construct is the iso-contour for processes performed with a state variable held constant (e.g., isochors and isotherms) [47]. These contours not only provide a way to understand processes within the framework of the phase diagram, but impart structure to the phase diagram that improves intuition of thermodynamical processes. In this work, contours of constant soliton power and constant pulse width are measured and compared with theory. Closed-form expressions for normalized power and pulsewidth are also developed, including the Raman process.

The normalized LL equation is shown below as Eq. 3.1 [14]. The slowly-varying field envelope ψ is defined such that $|\psi|^2 = (2g/\kappa)N$, where N is photon number, κ is the cavity mode power damping rate, and $g = \hbar\omega_c^2 c n_2/(n^2 V_0)$ is the Kerr coefficient with material refractive index n, Kerr nonlinear index n_2, optical mode volume V_0, cavity resonant frequency ω_c, Planck's constant $\hbar$, and speed of light c. $\tau = \kappa t/2$ and $\theta \equiv \phi\sqrt{\kappa/2D_2}$ are the normalized time and cavity polar coordinate (ϕ) where D_2 is the second-order dispersion parameter [14, 15]. $f^2 \equiv P/P_{\text{th}}$ is the ratio of the input pump power and parametric threshold power [13, 15] and $\zeta \equiv (\omega_c - \omega_p)(2/\kappa)$ is the normalized frequency detuning between cavity resonant frequency ω_c, and pump frequency ω_p. $\gamma \equiv D_1\tau_R\sqrt{\kappa/2D_2}$ is the normalized Raman coefficient where τ_R is the material Raman constant [24] and $D_1/2\pi$ is the cavity free-spectral-range [14, 15].

$$\frac{\partial\psi}{\partial\tau} = i\frac{1}{2}\frac{\partial^2\psi}{\partial\theta^2} + i|\psi|^2\psi - (1+i\zeta)\psi + i\gamma\frac{\partial|\psi|^2}{\partial\theta}\psi + f. \tag{3.1}$$

Iso-power contours found by solving Eq. 3.1 are shown in Fig. 3.1 as red contours. The analysis is performed for a high-Q silica resonator and parameters used in the calculation are provided below and in the Fig. 3.1 caption. Numerical simulation is based on propagating the LL equation from an initial soliton seed until steady-state is achieved [24].

The following simplified analytical solution is also used to study soliton behavior [14]: $\psi = A + B\,\text{sech}(\theta/\tau_\theta)e^{i\phi_0}$, where A is the soliton background field, B is the amplitude, ϕ_0 is the soliton phase, and $\tau_\theta \equiv \tau_s/\tau_0$ is the normalized soliton pulse width (τ_s is the physical pulse width and $\tau_0 \equiv \sqrt{2D_2/(\kappa D_1^2)}$). By Fourier transform, the soliton spectrum in optical frequency ν varies as $\text{sech}(\nu/\nu_s)$, where $\nu_s\tau_s = \pi^{-2}$. Approximate expressions giving the Raman-free dependence of amplitude and pulse width on detuning and pump power have been developed [14, 48]. By including high-order corrections and Raman corrections, the following improved expressions

result as well an expression for soliton average power,

$$B(\zeta, f, \gamma) \approx \sqrt{2\zeta}\left(1 + \frac{5}{8}\sqrt{\frac{\pi^2 f^2 - 8\zeta}{2\zeta^3}}\right)\left(1 - \frac{64}{225}\gamma^2\zeta^3\right), \tag{3.2}$$

$$\tau_\theta(\zeta, f, \gamma) \approx \frac{1}{\sqrt{2\zeta}}\left(1 - \frac{1}{4}\sqrt{\frac{\pi^2 f^2 - 8\zeta}{2\zeta^3}}\right)\left(1 + \frac{64}{225}\gamma^2\zeta^3\right), \tag{3.3}$$

$$p(\zeta, f, \gamma) \approx \sqrt{2\zeta}\left(1 + \sqrt{\frac{\pi^2 f^2 - 8\zeta}{2\zeta^3}}\right)\left(1 - \frac{64}{225}\gamma^2\zeta^3\right), \tag{3.4}$$

where $p \equiv P_{\mathrm{sol}}/P_0$ is the normalized time-averaged soliton power P_{sol} and $P_0 \equiv (\kappa_E \hbar\omega_c/\pi g)\sqrt{\kappa D_2/2}$ with κ_E the optical loss rate from waveguide-resonator coupling [15]. As an aside, the requirement of the square root to be real in these expressions ($\zeta < \pi^2 f^2/8$) gives the approximate upper bound of detuning for soliton existence in the phase diagram [14, 39, 49]. Dotted lines in Fig. 3.1 are the iso-power contours using Eq. 3.4 (equivalently $p(\zeta, f, \gamma) =$ constant for $\gamma = 2.1 \times 10^{-3}$), and they are in excellent agreement with the simulation contours. Raman contributions become especially important at larger detuning values where the soliton spectrum increases in width [23, 24]. To illustrate this point, the dashed curves in Fig. 3.1 result by using Eq. 3.4 except with $\gamma = 0$.

The experimental setup is shown in Fig. 3.2a. The resonator was an ultra-high-Q silica wedge resonator having a diameter of approximately 3 mm (free spectral range $D_1/2\pi = 21.9$ GHz). Further details on its fabrication are presented elsewhere [50]. The measurement used the TE_1 mode family pumped at 1550 nm, and the second-order dispersion was measured to be $D_2/2\pi = 12.1$ kHz at 1550 nm by a method reported elsewhere [15]. The mode area was calculated to be $A_{\mathrm{eff}} = 40$ $\mu\mathrm{m}^2$, and the silica Raman constant $\tau_{\mathrm{R}} = 2.4$ fs was also used [24], which is valid when the soliton spectral width is below 13 THz [51]. Finally, the resonator used in this measurement featured minimal avoided mode crossings and dispersive waves. Their presence would interfere with the ideal power dependence predicted by the LL equation. To measure pump detuning, weak phase-modulation of the pump light and detection of converted amplitude modulation sidebands was performed [43, 52]. In this method, pump light reflected by the fiber Bragg grating (FBG) contains the modulation information and is analyzed by an electrical spectrum analyzer (ESA) to retrieve the detuning frequency. The soliton spectrum transmitted past the FBG

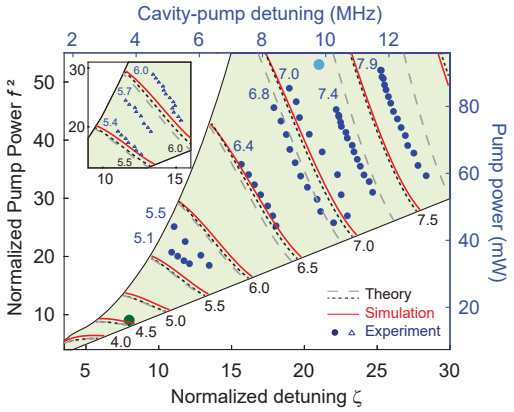

Figure 3.1: Dissipative Kerr soliton phase diagram and iso-power contours. The phase diagram features normalized pump power f^2 along the vertical axis and normalized detuning ζ along the horizontal axis. The green region contains stable soliton states. Black dotted lines (gray dashed lines) are iso-power contours using Eq. 3.4 with Raman term (w/o Raman). p is incremented from 4.0 to 8.0 in steps of 0.5. Red lines are simulated iso-power contours using Eq. 3.1. Blue dots give the measured soliton iso-power contours at the following soliton powers: 93, 99.5, 117.5, 125, 129, 136, 145 μW (left to right), which correspond to p values of 5.1, 5.5, 6.4, 6.8, 7.0, 7.4, and 7.9. For these measurements, Q = 197 million ($\kappa/2\pi$ = 0.98 MHz), κ_E/κ = 0.26, and $\gamma = 2.1 \times 10^{-3}$. Inset shows the measured iso-power contours using another similar device, with soliton powers of 299, 320, and 335 μW (left to right), which correspond to p values of 5.4, 5.7, and 6.0. For these measurements, Q = 115 million ($\kappa/2\pi$ = 1.69 MHz), κ_E/κ = 0.39, and $\gamma = 2.8 \times 10^{-3}$. Large green and blue data points correspond to spectra in Fig. 2b.

is sent to a detector and optical spectrum analyzer (OSA) for analysis. To determine soliton power, the FBG filtered line was manually reinserted.

Triggering and locking of single-soliton states used the soliton average power to servo control the pump laser frequency [53]. Because this soliton locking method maintains a constant soliton power, it provides a convenient way to map out the iso-power contours. Specifically, as opposed to varying (ζ, f^2) in the phase diagram and monitoring soliton power, the iso-power measurement proceeded by varying only the pumping power with the soliton locked at constant output power. The servo control then compensates for these variations by adjusting the pumping frequency. The corresponding detuning was then recorded as described above. Pump power was varied using a combination of an acousto-optical modulator (AOM) and Erbium-doped fiber amplifier (EDFA). Upon completion of an iso-power contour, the soliton power setpoint was adjusted and the measurement repeated. The measured iso-power data points are shown in the main panel of Fig. 3.1. Each measurement proceeded

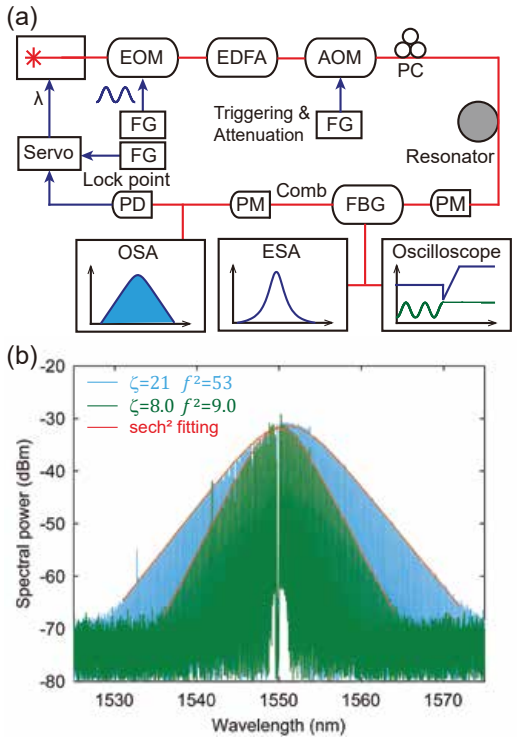

Figure 3.2: Measurement system and low-power operation. (a) Measurement setup. EOM: electro-optical phase modulator. PC: polarization controller. PM: In-line power meter. PD: Photodetector. FG: function generator. (b) Soliton spectra at normalized detuning and pumping power ($\zeta = 21$, $f^2 = 53$) (blue) and ($\zeta = 8.0$, $f^2 = 9.0$) (green). The corresponding phase diagram locations are marked in Fig. 3.1. Red curve: squared hyperbolic-secant fitting.

until it was no longer possible to reliably lock the soliton state. There is overall good agreement between measurement and theory. Errors are largest at lowest detuning values, however, even here they are relatively small (~10%). The ability to measure the contours over such large ranges and their good agreement with theory and simulations showcases the system's robustness and quality. As an additional test, a second loading condition was also measured. The inset to Fig. 3.1 shows this data, which is in reasonable agreement with simulation and Eq. 3.4. Measured soliton powers have experienced an ~1.2 dB insertion loss between the resonator and the detector. It is also noted that breather solitons could be stably locked near the upper boundary in Fig. 3.1. However, the region was small, making measurement of iso-power contours difficult. As a result, breathers were not studied in this work.

Stable generation of solitons at small detuning is of practical importance for low pumping power operation of the soliton system. To this end, the green data point

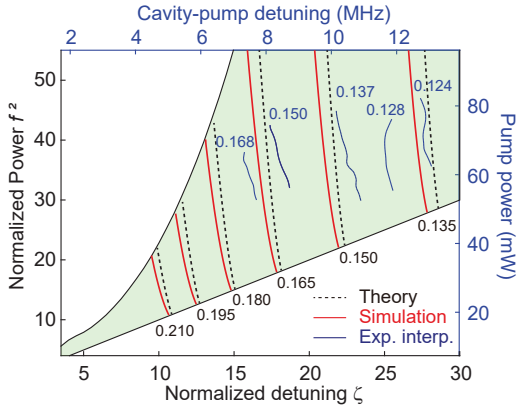

Figure 3.3: Iso-contours of soliton pulse width. The device is unchanged from Fig. 3.1 main panel. Red solid lines (black dotted lines) are simulated (Eq. 3.3 theory) iso-contours of normalized pulse width τ_θ ranging from 0.21 to 0.135 (equidistant steps of 0.015). Blue solid lines are the linear interpolation from measurement of iso-contours at 190, 170, 155, 145, 140 fs, which correspond to τ_θ: 0.168, 0.150, 0.137, 0.128, 0.124.

(ζ=8.0, f^2=9.0) in Fig. 3.1 shows both the lowest detuning and the lowest power soliton state observed in this study. The corresponding unnormalized quantities are 4.2 MHz and 10.8 mW. This is, to the authors' knowledge, the lowest operating power reported for any soliton microcomb platform. Making this result equally important is that the repetition rate is detectable (21.9 GHz), requiring large mode volume and hence higher pumping power levels as compared to, for example, THz-rate microcombs. Corresponding soliton spectra are presented in Fig. 3.2b. The result was achieved by both the use of a high-quality-factor resonator sample as well as the improved understanding gained through these measurements of the stability regional boundaries [53]. For comparison, a soliton spectrum produced at (ζ=21, f^2=53) is also shown in Fig. 3.2b. These values are plotted as the light blue data point in Fig. 3.1 and correspond to unnormalized quantities 11.3 MHz and 63.5 mW. The cavity loading condition for these two spectra is: loaded Q = 182 million and $\kappa_E/\kappa = 0.44$.

In parallel with the iso-power data point collection, the soliton pulse width was also measured by fitting of the optical spectral envelope [15]. Then the data set $(\zeta, f^2, \tau_\theta)$ was linearly interpolated to determine iso-contours of pulse width (blue contours in Fig. 3.3). It was not possible to interpolate iso-pulse-width contours at lower detuning values where there are fewer iso-power data points. For comparison, simulated pulse width (red) and the analytical expression, Eq. 3.3 (dotted black) are

plotted. The interpolated pulse width iso-contours are less accurate than the directly measured power contours but nonetheless show reasonable agreement between the data and theory. Overall, the pulse width contours are more weakly dependent upon normalized pumping power (i.e. more vertical) as compared to the soliton power contours.

In summary, contours of constant power and constant pulse width have been measured for dissipative Kerr solitons. Measurements were found to be in good agreement with the LL equation numerical model augmented by Raman interactions. There was also good agreement with the predictions of closed-form expressions that include the Raman interaction. Compared with the the large-detuning approximation which predicts that soliton power depends only upon resonator-pump detuning (i.e. vertical iso-power contours), it is found that soliton power depends both upon pumping power and detuning. The resulting tilt of iso-power contours at low detuning suggests that soliton locking by servo control of pumping power could potentially be an option for low-detuning ranges, just as servo control of pump frequency is used at larger detuning ranges. Stable soliton operation for pump powers as low as 10.8 mW was also demonstrated in the course of this work. These measurements provide structure to the phase diagram picture of soliton existence. The universal nature of the closed-form expressions should make them suitable for use in other CS and DK soliton platforms. Future work could consider incorporating higher-order dispersion into the analysis to include, for example, the impact of phenomena such as dispersive waves.

References

[1] Kivshar, Y. S. & Agrawal, G. *Optical solitons: from fibers to photonic crystals* (Academic press, 2003).

[2] Agrawal, G. P. *Nonlinear fiber optics* (Academic press, 2007).

[3] Cundiff, S. Soliton dynamics in mode-locked lasers. In *Dissipative Solitons*, 183–206 (Springer, 2005).

[4] Dudley, J. M., Genty, G. & Coen, S. Supercontinuum generation in photonic crystal fiber. *Reviews of Modern Physics* **78**, 1135 (2006).

[5] Hasegawa, A. & Kodama, Y. Signal transmission by optical solitons in monomode fiber. *Proceedings of the IEEE* **69**, 1145–1150 (1981).

[6] Haus, H. A. & Wong, W. S. Solitons in optical communications. *Reviews of Modern Physics* **68**, 423 (1996).

[7] Akhmediev, N. & Ankiewicz, A. *Dissipative Solitons: From Optics to Biology and Medicine* (Berlin: Springer, 2008).

[8] Leo, F. *et al.* Temporal cavity solitons in one-dimensional Kerr media as bits in an all-optical buffer. *Nature Photonics* **4**, 471–476 (2010).

[9] Wabnitz, S. Suppression of interactions in a phase-locked soliton optical memory. *Optics Letters* **18**, 601–603 (1993).

[10] Jang, J. K., Erkintalo, M., Murdoch, S. G. & Coen, S. Observation of dispersive wave emission by temporal cavity solitons. *Optics Letters* **39**, 5503–5506 (2014).

[11] Anderson, M., Leo, F., Coen, S., Erkintalo, M. & Murdoch, S. G. Observations of spatiotemporal instabilities of temporal cavity solitons. *Optica* **3**, 1071–1074 (2016).

[12] Wang, Y., Anderson, M., Coen, S., Murdoch, S. G. & Erkintalo, M. Stimulated Raman scattering imposes fundamental limits to the duration and bandwidth of temporal cavity solitons. *Physical Review Letters* **120**, 053902 (2018).

[13] Kippenberg, T., Spillane, S. & Vahala, K. Kerr-nonlinearity optical parametric oscillation in an ultrahigh-Q toroid microcavity. *Physical Review Letters* **93**, 083904 (2004).

[14] Herr, T. *et al.* Temporal solitons in optical microresonators. *Nature Photonics* **8**, 145–152 (2014).

[15] Yi, X., Yang, Q.-F., Yang, K. Y., Suh, M.-G. & Vahala, K. Soliton frequency comb at microwave rates in a high-Q silica microresonator. *Optica* **2**, 1078–1085 (2015).

[16] Brasch, V. *et al.* Photonic chip-based optical frequency comb using soliton Cherenkov radiation. *Science* **351**, 357–360 (2016).

[17] Joshi, C. *et al.* Thermally controlled comb generation and soliton modelocking in microresonators. *Optics Letters* **41**, 2565–2568 (2016).

[18] Wang, P.-H. *et al.* Intracavity characterization of micro-comb generation in the single-soliton regime. *Optics Express* **24**, 10890–10897 (2016).

[19] Yu, M., Okawachi, Y., Griffith, A. G., Lipson, M. & Gaeta, A. L. Mode-locked mid-infrared frequency combs in a silicon microresonator. *Optica* **3**, 854–860 (2016).

[20] Li, Q. *et al.* Stably accessing octave-spanning microresonator frequency combs in the soliton regime. *Optica* **4**, 193–203 (2017).

[21] Del'Haye, P. *et al.* Optical frequency comb generation from a monolithic microresonator. *Nature* **450**, 1214–1217 (2007).

[22] Kippenberg, T. J., Holzwarth, R. & Diddams, S. Microresonator-based optical frequency combs. *Science* **332**, 555–559 (2011).

[23] Karpov, M. *et al.* Raman self-frequency shift of dissipative Kerr solitons in an optical microresonator. *Physical Review Letters* **116**, 103902 (2016).

[24] Yi, X., Yang, Q.-F., Yang, K. Y. & Vahala, K. Theory and measurement of the soliton self-frequency shift and efficiency in optical microcavities. *Optics Letters* **41**, 3419–3422 (2016).

[25] Yi, X. *et al.* Single-mode dispersive waves and soliton microcomb dynamics. *Nature Communications* **8**, 14869 (2016).

[26] Akhmediev, N. & Karlsson, M. Cherenkov radiation emitted by solitons in optical fibers. *Physical Review A* **51**, 2602 (1995).

[27] Bao, C. *et al.* Spatial mode-interaction induced single soliton generation in microresonators. *Optica* **4**, 1011–1015 (2017).

[28] Cherenkov, A., Lobanov, V. & Gorodetsky, M. Dissipative Kerr solitons and Cherenkov radiation in optical microresonators with third-order dispersion. *Physical Review A* **95**, 033810 (2017).

[29] Yang, Q.-F., Yi, X., Yang, K. & Vahala, K. Counter-propagating solitons in microresonators. *Nature Photonics* **11**, 560–564 (2017).

[30] Cole, D. C., Lamb, E. S., Del'Haye, P., Diddams, S. A. & Papp, S. B. Soliton crystals in kerr resonators. *Nature Photonics* **11**, 671–676 (2017).

[31] Joshi, C. *et al.* Counter-rotating cavity solitons in a silicon nitride microresonator. *Optics Letters* **43**, 547–550 (2018).

[32] Yang, Q.-F., Yi, X., Yang, K. Y. & Vahala, K. Stokes solitons in optical microcavities. *Nature Physics* **13**, 53–57 (2017).

[33] Suh, M.-G., Yang, Q.-F., Yang, K. Y., Yi, X. & Vahala, K. Microresonator soliton dual-comb spectroscopy. *Science* **354**, 600–603 (2016).

[34] Dutt, A. *et al.* Dual-comb spectroscopy using on-chip mode-locked frequency combs. In *CLEO: Science and Innovations*, STh3L–2 (Optical Society of America, 2017).

[35] Suh, M.-G. & Vahala, K. J. Soliton microcomb range measurement. *Science* **359**, 884–887 (2018).

[36] Trocha, P. *et al.* Ultrafast optical ranging using microresonator soliton frequency combs. *Science* **359**, 887–891 (2018).

[37] Marin-Palomo, P. *et al.* Microresonator-based solitons for massively parallel coherent optical communications. *Nature* **546**, 274–279 (2017).

[38] Spencer, D. T. *et al.* An optical-frequency synthesizer using integrated photonics. *Nature* **557**, 81–85 (2018).

[39] Barashenkov, I. & Smirnov, Y. S. Existence and stability chart for the AC-driven, damped nonlinear schrödinger solitons. *Physical Review E* **54**, 5707 (1996).

[40] Lugiato, L. A. & Lefever, R. Spatial dissipative structures in passive optical systems. *Physical Review Letters* **58**, 2209 (1987).

[41] Leo, F., Gelens, L., Emplit, P., Haelterman, M. & Coen, S. Dynamics of one-dimensional Kerr cavity solitons. *Optics Express* **21**, 9180–9191 (2013).

[42] Godey, C., Balakireva, I. V., Coillet, A. & Chembo, Y. K. Stability analysis of the spatiotemporal Lugiato-Lefever model for Kerr optical frequency combs in the anomalous and normal dispersion regimes. *Physical Review A* **89**, 063814 (2014).

[43] Guo, H. *et al.* Universal dynamics and deterministic switching of dissipative Kerr solitons in optical microresonators. *Nature Physics* **13**, 94–102 (2017).

[44] Bao, C. *et al.* Observation of Fermi-Pasta-Ulam recurrence induced by breather solitons in an optical microresonator. *Physical Review Letters* **117**, 163901 (2016).

[45] Lucas, E., Karpov, M., Guo, H., Gorodetsky, M. & Kippenberg, T. Breathing dissipative solitons in optical microresonators. *Nature Communications* **8**, 736 (2017).

[46] Yu, M. *et al.* Breather soliton dynamics in microresonators. *Nature Communications* **8**, 14569 (2017).

[47] Sonntag, R. E., Borgnakke, C., Van Wylen, G. J. & Van Wyk, S. *Fundamentals of thermodynamics* (Wiley New York, 2003).

[48] Guo, H. *et al.* Universal dynamics and deterministic switching of dissipative kerr solitons in optical microresonators. *Nature Physics* **13**, 94–102 (2016).

[49] Coen, S. & Erkintalo, M. Universal scaling laws of kerr frequency combs. *Optics Letters* **38**, 1790–1792 (2013).

[50] Lee, H. *et al.* Chemically etched ultrahigh-Q wedge-resonator on a silicon chip. *Nature Photonics* **6**, 369–373 (2012).

[51] Erkintalo, M., Genty, G., Wetzel, B. & Dudley, J. M. Limitations of the linear Raman gain approximation in modeling broadband nonlinear propagation in optical fibers. *Optics Express* **18**, 25449–25460 (2010).

[52] Lucas, E., Guo, H., Jost, J. D., Karpov, M. & Kippenberg, T. J. Detuning-dependent properties and dispersion-induced instabilities of temporal dissipative Kerr solitons in optical microresonators. *Physical Review A* **95**, 043822 (2017).

[53] Yi, X., Yang, Q.-F., Yang, K. Y. & Vahala, K. Active capture and stabilization of temporal solitons in microresonators. *Optics Letters* **41**, 2037–2040 (2016).

Chapter 4

INTEGRATED TURNKEY SOLITON MICROCOMBS

Shen, B. *et al.* Integrated turnkey soliton microcombs. *Nature* **582**, 365–369 (2020).

Optical frequency combs have found a remarkably wide range of applications in science and technology [1]. And a recent development that portends a revolution in miniature and integrated comb systems is dissipative Kerr soliton formation in coherently pumped high-quality-factor (high-Q) optical microresonators [2–9]. To date, these soliton microcombs [10] have been applied to spectroscopy [11–13], the search for exoplanets [14, 15], optical frequency synthesis [16], time keeping [17], and other areas [10]. Also, the recent integration of microresonators with lasers has revealed the viability of fully chip-based soliton microcombs [18, 19]. However, despite the enormous promise of microcombs, their operation requires complex startup and feedback protocols that necessitate difficult-to-integrate optical and electrical components. Moreover, electronics-rate microcombs, required in nearly all comb systems, have resisted integration because of their power requirements. Here, a regime for turnkey operation of soliton microcombs co-integrated with a pump laser is demonstrated and theoretically explained. Significantly, a new operating point is shown to appear from which solitons are generated through binary turn-on and turn-off of the pump laser, thereby eliminating all photonic/electronic control circuitry. These features are combined with high-Q Si_3N_4 resonators to fully integrate into a butterfly package microcombs with repetition frequencies as low as 15 GHz, thereby offering compelling advantages for high-volume production.

4.1 Main results

The integration of microcomb systems faces two considerable obstacles. First, complex tuning schemes and feedback loops are required for generation and stabilization of solitons [2, 20, 21]. These not only introduce redundant and power-hungry electronic components [18, 19], but also require optical isolation, a function that has so far been challenging to integrate at acceptable performance levels. Second, repetition frequencies that are both detectable and readily processed by integrated electronic circuits, such as complementary metal–oxide–semiconductor (CMOS) circuits, are essential for comb self-referencing, the key process that underlies many

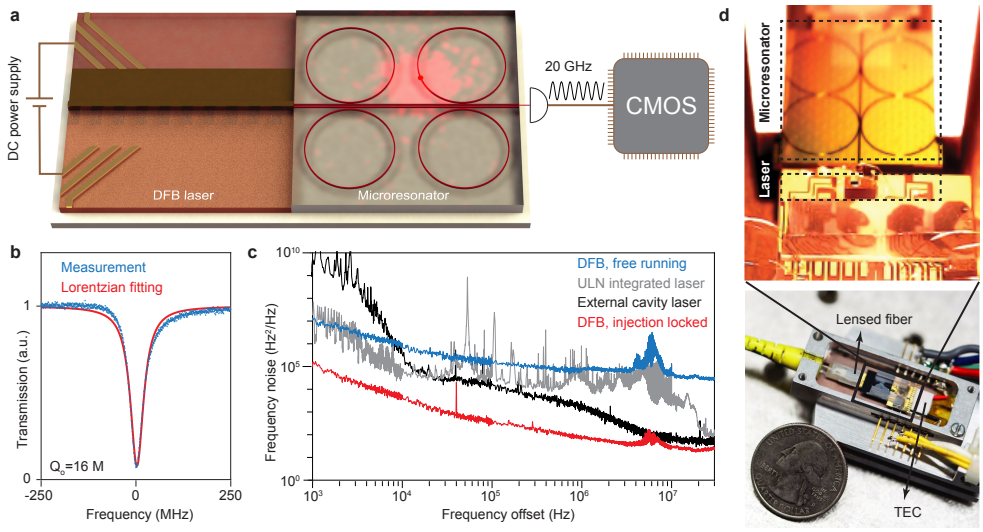

Figure 4.1: Integrated soliton microcomb chip. (a) Rendering of the soliton microcomb chip that is driven by a DC power source and produces soliton pulse signals at electronic-circuit rates. Four microcombs are integrated on one chip, but only one is used in these measurements. (b) Transmission signal when scanning the laser across a cavity resonance (blue). Lorentzian fitting (red) reveals 16 million intrinsic Q factor. (c) Frequency noise spectral densities (SDs) of the DFB laser when it is free running (blue) and feedback-locked to a high-Q Si_3N_4 microresonator (red). For comparison, the frequency noise SDs of an ultra-low-noise integrated laser on silicon (grey) and a table-top external cavity diode laser (black) are also plotted. (d) Images of a pump/microcomb in a compact butterfly package.

comb applications [1]. And while ultra-high-Q silica resonators [5, 22] and Damascene Si_3N_4 resonators [23] can attain these rates, their integration with pumps has not been possible. Here, we show that the nonlinear dynamics of an unisolated laser-microcomb system creates a new operating point from which the pump laser is simply turned-on to initiate the soliton mode-locking process. Theory and experimental demonstration of the existence and substantial benefits of this new turnkey operating point are demonstrated. Moreover, the resulting microcomb system features Q factor performance that enables electronic-circuit rate operation using an integrated pump.

In the experiment, integrated soliton microcombs whose fabrication and repetition rate (40 GHz down to 15 GHz) are compatible with CMOS circuits [24] are butt-coupled to a commercial distributed-feedback (DFB) laser via inverse tapers (Fig. 4.1a). The microresonators are fabricated using the photonic Damascene reflow process [23, 25] and feature Q factors exceeding 16 million (Fig. 4.1b), resulting

in a low milliwatt-level parametric oscillation threshold, despite the larger required mode volumes of the GHz-rate microcombs. This enables chip-to-chip pumping of microcombs for the first time at these challenging repetition rates. Up to 30 mW of optical power is launched into the microresonator. Feedback from the resonator suppresses frequency noise by around 30 dB compared with that of a free-running DFB laser (Fig. 4.1c), so that the laser noise performance surpasses state-of-the-art monolithically integrated lasers [26] and table-top external-cavity-diode-lasers (ECDL). Given its compact footprint and the absence of control electronics, the pump-laser/microcomb chipset was mounted into a butterfly package (Fig. 4.1d) to facilitate measurements and also enable portability. This level of integration and packaging combined with turnkey operation makes this a completely functional device suitable for use in any system-level demonstration.

In conventional pumping of microcombs, the laser is optically-isolated from the downstream optical path so as to prevent feedback-induced interference (Fig. 4.2a). And on account of strong high-Q-induced resonant build-up and the Kerr nonlinearity, the intracavity power as a function of pump-cavity detuning features bistability. The resulting dynamics can be described using a phase diagram comprising continuous-wave (c.w.), modulation instability (MI) combs, and soliton regimes that are accessed as the pump frequency is tuned across a cavity resonance. A typical plot (Fig. 4.2b) is made versus $\delta\omega$, the difference of cavity resonance and pump laser frequency (i.e., $\delta\omega > 0$ indicates red detuning of the pump frequency relative to the cavity frequency) [2]. The tuning through the MI regime functions to seed the formation of soliton pulses. On account of the thermal hysteresis [27] and the abrupt intracavity power discontinuity upon transition to the soliton regime (Fig. 4.2c), delicate tuning waveforms [2, 21] or active capturing techniques [20] are essential to compensate thermal transients, except in cases of materials featuring effectively negative thermo-optic response [8].

Now consider removing the optical isolation as shown in Fig. 4.2d so that backscatter feedback occurs from pumping a resonator mode. In prior work, semiconductor laser locking to the resonator mode as well as laser line narrowing have been shown to result from backscattering of the intracavity optical field [28]. These attributes as well as mode selection when using a broadband pump have also been profitably applied to operate microcomb systems without isolation [18, 19, 29, 30]. However, these prior studies of feedback effects have considered the resonator to be linear so that the detuning between the feedback-locked laser and the cavity resonance

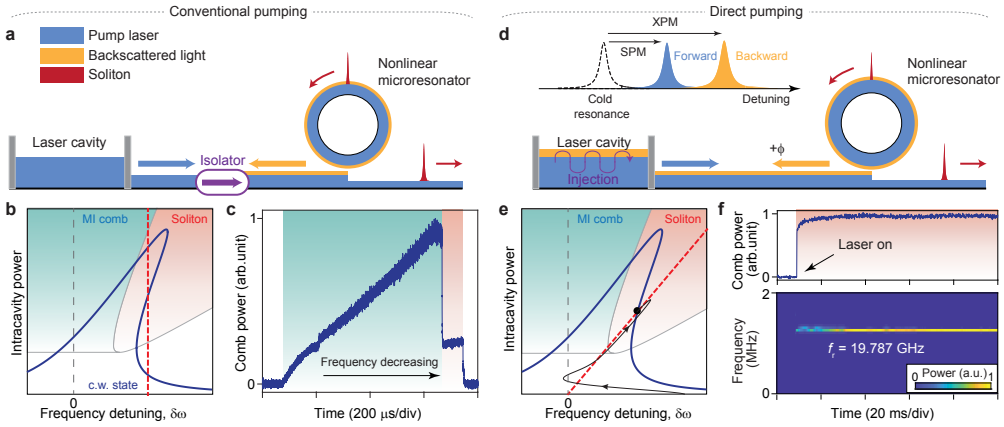

Figure 4.2: The turnkey operating point. (a) Conventional soliton microcomb operation using a tunable c.w. laser. An optical isolator blocks the back-scattered light from the microresonator. (b) Phase diagram, hysteresis curve and dynamics of the microresonator pumped as shown in (a). The blue curve is the intracavity power as a function of cavity-pump frequency detuning. Laser tuning (dashed red line) accesses multiple equilibria. (c) Measured evolution of comb power pumped by an isolated, frequency-scanned ECDL. The step in the trace is a characteristic feature of soliton formation. (d) Turnkey soliton microcomb generation. Non-isolated operation allows back-scattered light to be injected into the pump laser cavity. Resonances are red-shifted due to self-phase modulation (SPM) and cross-phase modulation (XPM). (e) Phase diagram, hysteresis curve and dynamics of pump/microresonator system. A modified laser tuning curve (dashed red line) intersects the intracavity power curve (blue) to establish a new operating point from which solitons form. The feedback phase ϕ is set to 0 in the plot. Simulated evolution upon turning-on of the laser at a red detuning outside the soliton regime but within the locking bandwidth is plotted (solid black curve). (f) Measured comb power (upper panel) and detected soliton repetition rate signal (lower panel) with laser turn-on indicated at 10 ms.

is determined solely by the phase ϕ accumulated in the feedback path [31]. In contrast, here the nonlinear behavior of the microresonator is included and is shown to have a dramatic effect on the system operating point. And the nonlinear behavior causes the resonances to be red-shifted by intensity-dependent self- and cross-phase modulation. As a result, the relationship between frequency detuning and intracavity power of the pump mode P_0 can be shown (see Supplementary information) to be approximately given by

$$\frac{\delta\omega}{\kappa/2} = \tan\frac{\phi}{2} + \frac{3}{2}\frac{P_0}{P_{\text{th}}}, \tag{4.1}$$

where κ is the power decay rate of the resonance and P_{th} is the parametric oscillation threshold for intracavity power. This dependence of detuning on intracavity power

gives rise to a single operating point at the intersection of Eq. (1) and the hysteresis as shown in Fig. 4.2e. Control of the feedback phase shifts the x-intercept of Eq. (1) and thereby adjusts the operating point.

In the Supplementary information, it is shown that the system converges to this operating point once the laser frequency is within a locking bandwidth (estimated to be 5 GHz in the present case). As verified both numerically (Fig. 4.2e) and experimentally (Fig. 4.2f), this behavior enables soliton mode-locking by simple power-on of the pump laser (i.e., no triggering or complex tuning schemes). A simulated trajectory is shown in Fig. 4.2e wherein a laser is initially started to the red of the high-Q cavity resonant frequency and well outside its linewidth. The system is attracted towards the resonance through a process that at first resembles injection locking of the III-V laser. However, as the laser frequency moves towards the resonant frequency, the resonator power rises and the Kerr nonlinearity induces evolution towards the operating point. The system transiently exceeds the threshold for parametric oscillation and, as shown in the Supplementary information, Turing rolls form that ultimately evolve into the solitons as the system achieves steady state. An experimental trace of the comb power shows that a steady soliton power plateau is reached immediately after turn-on of the laser. And the stable soliton emission is further confirmed by monitoring the real-time evolution of the soliton repetition rate signal (Fig. 4.2f). Numerical simulation of this startup process is provided in the Supplementary information. The turnkey operation demonstrated here is automatic, such that the entire soliton initiation and stabilization is described and realized by the physical dynamics of laser self-injection locking in combination with the nonlinear resonator response. Consistent with this point, the system is observed to be highly robust with respect to temperature and environmental disturbances. Indeed, soliton generation without any external feedback control was possible for several hours in the laboratory.

Figure 4.3 shows the optical spectra of a single-soliton state with 40 GHz repetition rate and multi-soliton states with 20 GHz and 15 GHz repetition rates. The deviation from the theoretical sech^2 spectral envelope is believed to result from a combination of mode crossing induced dispersion and the dispersion of the waveguide-resonator coupling strength. The pump laser at 1556 nm is attenuated at the output by a fiber-Bragg-grating notch filter in these spectra. The coherent nature of these soliton microcombs is confirmed by photodetection of the soliton pulse streams, and reveals high-contrast, single-tone electrical signals at the indicated repetition

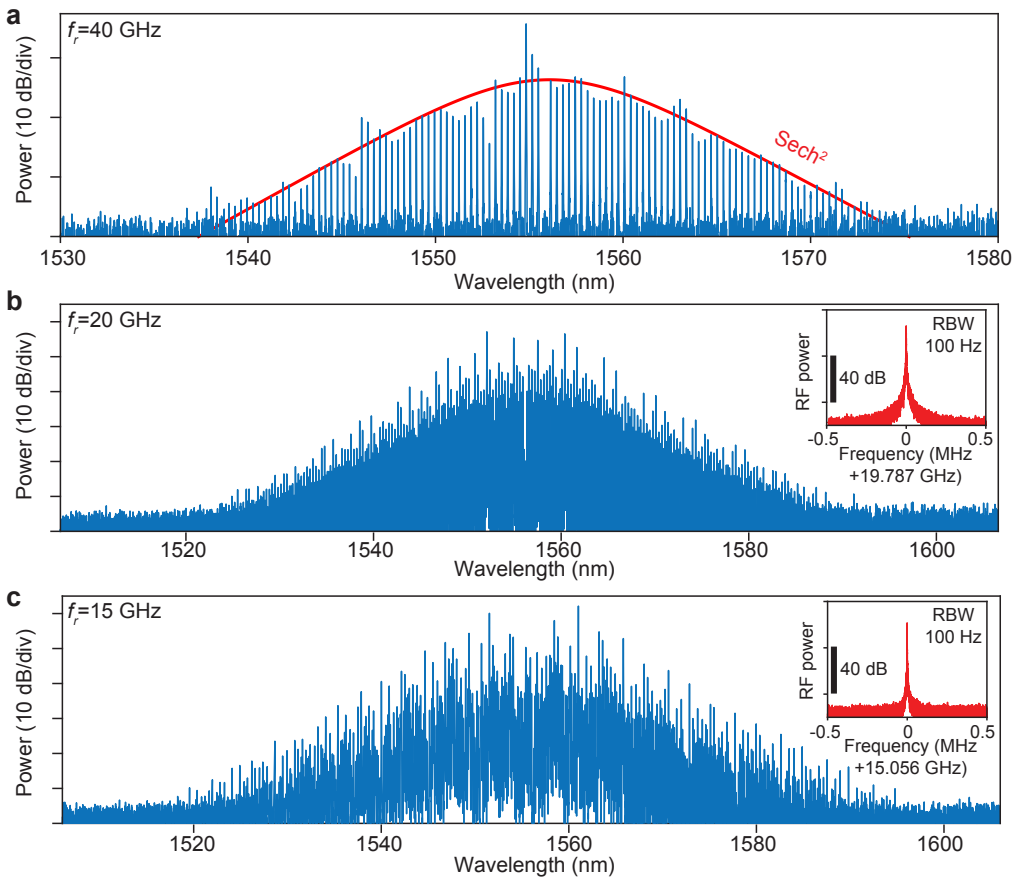

Figure 4.3: Optical and electrical spectra of solitons. (a) The optical spectrum of a single-soliton state with repetition rate f_r = 40 GHz. The red curve shows a sech^2 fitting to the soliton spectral envelope. (b-c) Optical spectra of multi-soliton states at 20 GHz and 15 GHz repetition rates. Insets: Electrical beatnotes showing the repetition rates.

rates. Numerical simulations have confirmed the tendency of turnkey soliton states consisting of multiple solitons, which is a direct consequence of the high intracavity power and its associated MI gain dynamics (see Supplementary information for details). However, single-soliton operation is accessible for a certain combination of pump power and feedback phase.

To demonstrate repeatable turnkey operation, the laser current is modulated to a preset current by a square wave to simulate the turn-on process. Soliton microcomb operation is reliably achieved as confirmed by monitoring soliton power and the single-tone beating signal (Fig. 4.4a). More insight into the nature of the turnkey operation is provided by the phase diagram near the equilibrium point for different feedback phase and pump power (Fig. 4.4b). The turnkey regime occurs above a

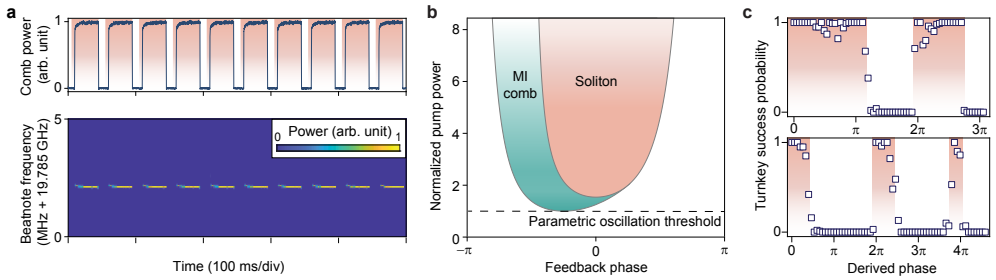

Figure 4.4: Demonstration of turnkey soliton generation. (a) 10 consecutive switching-on tests are shown. The upper panel gives the measured comb power versus time. The laser is switched on periodically as indicated by the shaded regions. The lower panel is a spectrogram of the soliton repetition rate signal measured during the switching process. (b) Phase diagram of the integrated soliton system with respect to feedback phase and pump power. The pump power is normalized to the parametric oscillation threshold. (c), Turnkey success probability versus relative feedback phase of 20 GHz (upper panel) and 15 GHz (lower panel) devices. Each data point is acquired from 100 switch-on attempts. See Methods for additional discussion.

threshold power within a specific range of feedback phases. Moreover, the regime recurs at 2π increments of feedback phase, which is verified experimentally (Fig. 4.4c). Consistent with the phase diagram, a binary-like behavior of turn-on success is observed as the feedback phase is varied. In the measurement, the feedback phase was adjusted by control of the gap between the facets of the laser and the microcomb bus waveguide. A narrowing of the turn-on success window with an increased feedback phase is believed to result from the reduction of the pump power in the bus waveguide with increasing tuning gap (consistent with Fig. 4.4b).

Besides the physical significance and practical impact of the new operating point, our demonstration of a turnkey operating regime is an important simplification of soliton microcomb systems. Moreover, the application of this method in an integrated CMOS-compatible system represents a milestone towards mass production of optical frequency combs. The butterfly packaged devices will benefit several comb applications including miniaturized frequency synthesizers [16] and optical clocks [17]. In these applications, their CMOS rates, besides enabling integration of electrical control and processing functions, provide for simple detection and processing of the comb pulses (i.e. without the need for millimeter-wave-rate frequency mixers). Moreover, the recent demonstration of low-power comb formation in III-V microresonators [32] suggests that monolithic integration of pumps and soliton microcombs is feasible using the methods developed here. A phase section could be

included therein or in advanced versions of the current approach to electronically control the feedback phase. The ability to create a complete system including pump laser without optical isolation is also significant. Even in cases where solitons are pumped using amplification such as with laser cavity solitons [9], full integration would require difficult-to-integrate optical isolators. It is also important to note that the current turnkey approach is a soliton forming comb while other recent work reports on non-soliton Kerr combs [33]. Finally, due to its simplicity, this approach could be applied in other integrated high-Q microresonator platforms [7, 8, 22] to attain soliton microcombs across a wide range of wavelengths.

4.2 Methods

Silicon nitride chip fabrication

The Si_3N_4 [34] chip devices were fabricated using the photonic Damascene reflow process [35]. Deep-UV stepper lithography is used to pattern the waveguides as well as the stress-release patterns [35] to prevent Si_3N_4 film cracks from the low-pressure chemical vapor deposition (LPCVD) process. The waveguide patterns are dry-etched into the SiO_2 substrate from the photoresist mask. The substrate is then annealed at 1250°C at atmospheric pressure, such that SiO_2 reflow happens which reduces the waveguide sidewall roughness [36]. Afterwards, LPCVD Si_3N_4 is deposited on the substrate, followed by chemical-mechanical polishing to planarize the substrate top surface. The substrate is further annealed to remove residual hydrogen contents in Si_3N_4, followed by thick SiO_2 top cladding deposition and SiO_2 annealing.

To separate the wafer into chips of 5×5 mm^2 size, deep reactive ion etching (RIE) is used to define the chip facets for superior surface quality, which is particularly important in order to achieve good contact for the butt coupling between the Si_3N_4 chip and the laser chip. Commonly, dicing of SiO_2 and silicon together is widely used, however this method has challenges to achieve smooth SiO_2 facets due to the very narrow operational window of SiO_2 dicing. In our fabrication process, AZ 9260 photoresist of 8 μm thickness is used as the mask for the deep RIE to create chip facets. The RIE is composed of two steps: dry etch of 7-μm-thick SiO_2 using $He/H_2/C_4F_8$ etchants, and Bosch process to remove 200 μm silicon using SF_6/C_4F_8 etchants. The deep RIE thus can create a smooth chip facet for butt coupling as shown in Extended Data Fig. 4.5b. After the deep RIE, the wafer is diced into chips using only the silicon dicing recipe.

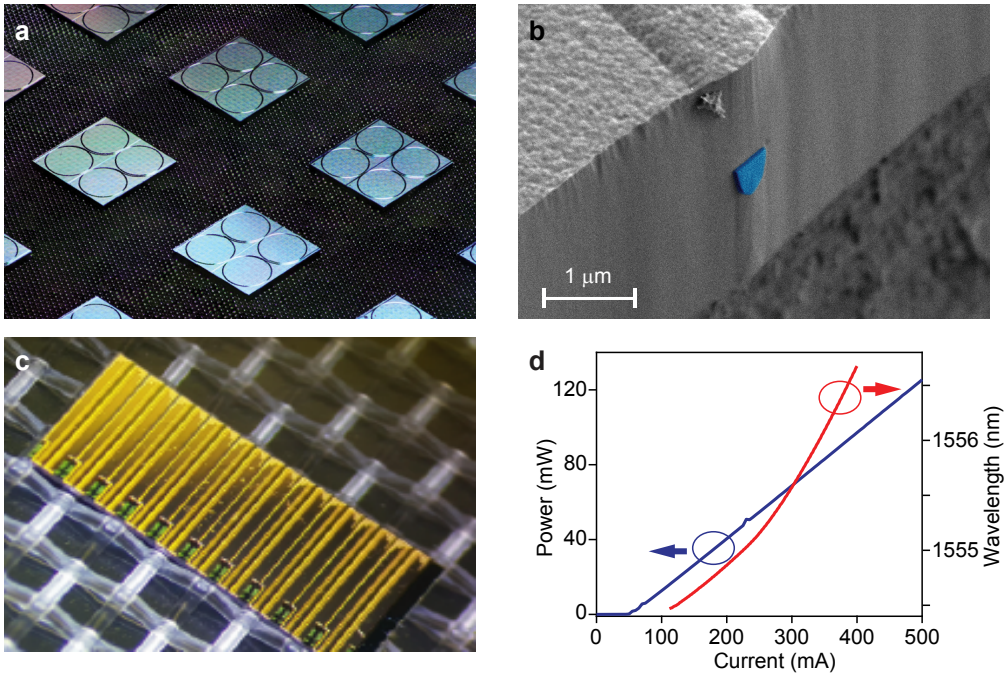

Figure 4.5: (a) Photo of Si_3N_4 microresonator chip devices. (b) Scanning electron microscope (SEM) image of the smooth facet of Si_3N_4 chips. The Si_3N_4 inverse taper for butt coupling is blue-colored. (c) Microscopic image of a chip with 10 DFB lasers. (d) Light-current curve (blue) and the wavelength response (red) of the DFB laser.

DFB laser characterization

The DFB pump laser fabricated by Freedom Photonics [37] has high-reflection coatings at the back-side facet and anti-reflection coatings at the front-side facet. It has a 50 mA threshold current, and the total output power of the laser can reach 125 mW with a slope efficiency around 0.28 mW/mA (see Extended Data Fig. 4.5d). The peak wall-plug efficiency is inferred to be approximately 20%. This power level combined with the substantially reduced loss in the microresonator (high-Q) enables soliton operation using an integrated pump at a low rate that was not attainable in previous work[19]. The lasing is single-mode, and its wavelength also shifts from $\sim$ 1554.5 nm to $\sim$ 1556.5 nm with an increase of bias current ($\sim$ -1.4 GHz/mA). The temperature of the laser diode can be controlled within 1 mK.

Experimental details

The laser frequency noise is obtained using an OEWaves optical frequency noise analyzer. The table-top ECDL used for frequency noise measurement in Fig. 4.1c is the 81608A from Keysight. The soliton beatnote is detected by an external fiber-

coupled fast photodetector and down-mixed with a local oscillator to measure its real-time evolution. The frequency of the local oscillator is set slightly lower than the repetition rate of the solitons. A high-speed oscilloscope is used to record the trace from which the power spectrum is obtained by fast Fourier transform. The time window of the spectrograph is 20 μs, and the resolution bandwidth is 50 kHz.

The relative feedback phases are estimated from the gap between the facets of the laser and the bus waveguide, which can be adjusted by an open-loop piezo micro-stepping motor (PZA12 from Newport). The step size of the actuator was calibrated to be 4.3 ± 0.2 nm by the reference mark on the chip. The derived phase has a relative uncertainty of 4%.

During the experiment, the direct reflection from the smooth resonator chip interface sometimes could cause the laser to operate multi-mode and hamper self-injection to the resonance. To counteract this effect, the laser was tilted vertically 3 to 5 degrees relative to the microcomb chip in order to steer the reflection beam spot away. The facet coupling loss was estimated to be close to 3-5 dB by monitoring the total non-resonant transmission through the waveguide. Discussion of facet reflection and waveguide backscatter is provided in the Supplementary information.

4.3 Supplementary information: Theory of turnkey soliton generation

The injection locking system consists of three parts: the soliton optical field A_S, the backscattering field A_B, and the laser field A_L. The complete equations of motions are [31, 38]:

$$\begin{aligned}
\frac{\partial A_S}{\partial t} &= -\frac{\kappa}{2}A_S - i\delta\omega A_S + i\frac{D_2}{2}\frac{\partial^2 A_S}{\partial\theta^2} + i\frac{\kappa}{2}\frac{|A_S|^2+2|A_B|^2}{E_{th}}A_S + i\beta^*\frac{\kappa}{2}A_B - \sqrt{\kappa_R\kappa_L}e^{i\phi_B}A_L,\\
\frac{dA_B}{dt} &= -\frac{\kappa}{2}A_B - i\delta\omega A_B + i\frac{\kappa}{2}\frac{|A_B|^2+2\int_0^{2\pi}|A_S|^2 d\theta/(2\pi)}{E_{th}}A_B + i\beta\frac{\kappa}{2}\overline{A_S},\\
\frac{dA_L}{dt} &= i(\delta\omega_L-\delta\omega)A_L - \frac{\gamma}{2}A_L + \frac{g(|A_L|^2)}{2}(1+i\alpha_g)A_L - \sqrt{\kappa_R\kappa_L}e^{i\phi_B}A_B,
\end{aligned} \tag{4.2}$$

where the field amplitudes are normalized so that $\int_0^{2\pi}|A_S|^2 d\theta/(2\pi)$, $|A_B|^2$ and $|A_L|^2$ are the optical energies of their respective fields, t is the evolution time, θ is the resonator angular coordinate, κ is the resonator mode loss rate (assumed to be equal for A_S and A_B), $\delta\omega$ is the detuning of the cold-cavity resonance compared to injection-locked laser ($\delta\omega > 0$ indicates red detuning of the pump frequency

relative to the cavity frequency), D_2 is the second-order dispersion parameter, E_{th} is the parametric oscillation threshold for intracavity energy, β is the dimensionless backscattering coefficient (normalized to $\kappa/2$), ϕ_{B} is the propagation phase delay between the resonator and the laser, κ_{R} and κ_{L} are the external coupling rates for the resonator and laser respectively, $\delta\omega_{\text{L}}$ is the detuning of the cold-cavity resonance relative to the cold laser frequency, γ is the laser mode loss rate, $g(|A_{\text{L}}|^2) \equiv g_0/(1+|A_{\text{L}}|^2/|A_{\text{L,sat}}|^2)$ is the intensity-dependent gain, g_0 is the gain coefficient, $|A_{\text{L,sat}}|^2$ is the saturation energy level, and α_g is the amplitude-phase coupling factor. The average soliton field amplitude $\overline{A_{\text{S}}} = \int_0^{2\pi} A_{\text{S}} d\theta/(2\pi)$ is also the amplitude on the pumped mode, and by using $\overline{A_{\text{S}}}$ in the equation for A_{B}, we have assumed that only the mode being pumped contributes significantly in the locking process, which can be justified if a single-frequency laser is used. We note that the equations are effectively referenced to the frequency of the injection-locked laser instead of the free-running laser, which will simplify the following discussions. The frequency difference between the cold laser and the injection-locked laser is given by $\delta\omega - \delta\omega_{\text{L}}$.

We will introduce some other dimensionless quantities to facilitate the discussion. Define: normalized soliton field amplitude as $\psi = A_{\text{S}}/\sqrt{E_{\text{th}}}$, normalized total intracavity power as $P = \int_0^{2\pi} |A_{\text{S}}|^2 d\theta/(2\pi E_{\text{th}})$, normalized amplitude on the pump, backscattering and laser mode as $\rho = \overline{A_{\text{S}}}/\sqrt{E_{\text{th}}}$, $\rho_{\text{B}} = A_{\text{B}}/\sqrt{E_{\text{th}}}$, $\rho_{\text{L}} = A_{\text{L}}/\sqrt{E_{\text{th}}}$ respectively, normalized detuning of cavity as $\alpha = 2\delta\omega/\kappa$, and normalized evolution time as $\tau = \kappa t/2$. The equation for A_{S} and A_{B} can then be put into the dimensionless form

$$\begin{aligned}
\frac{\partial\psi}{\partial\tau} &= -(1+i\alpha)\psi + i\frac{D_2}{\kappa}\frac{\partial^2\psi}{\partial\theta^2} + i(|\psi|^2 + 2|\rho_{\text{B}}|^2)\psi + i\beta^*\rho_{\text{B}} - \frac{2\sqrt{\kappa_{\text{R}}\kappa_{\text{L}}}}{\kappa}e^{i\phi_{\text{B}}}\rho_{\text{L}}, \\
\frac{d\rho_{\text{B}}}{d\tau} &= -(1+i\alpha)\rho_{\text{B}} + i(2P + |\rho_{\text{B}}|^2)\rho_{\text{B}} + i\beta\rho.
\end{aligned} \tag{4.3}$$

The laser dynamics for A_{L} are split into amplitude and phase parts:

$$\begin{aligned}
\frac{1}{|A_{\text{L}}|}\frac{d|A_{\text{L}}|}{dt} &= -\frac{\gamma}{2} + \frac{g(|A_{\text{L}}|^2)}{2} - \text{Re}\left[\sqrt{\kappa_{\text{R}}\kappa_{\text{L}}}e^{i\phi_{\text{B}}}\frac{A_{\text{B}}}{A_{\text{L}}}\right], \\
\frac{d\phi_{\text{L}}}{dt} &= \delta\omega_{\text{L}} - \delta\omega + \frac{g(|A_{\text{L}}|^2)}{2}\alpha_g - \text{Im}\left[\sqrt{\kappa_{\text{R}}\kappa_{\text{L}}}e^{i\phi_{\text{B}}}\frac{A_{\text{B}}}{A_{\text{L}}}\right],
\end{aligned}$$

where $\text{Re}[\cdot]$ and $\text{Im}[\cdot]$ are the real and imaginary part functions, respectively. The laser power without backscatter feedback $|A_{\text{L}}^{(0)}|$ satisfies $g(|A_{\text{L}}^{(0)}|^2) = \gamma$. Expanding

the gain around this point gives

$$\frac{1}{|A_\mathrm{L}|}\frac{d|A_\mathrm{L}|}{dt} = -g'\frac{|A_\mathrm{L}|^2 - |A_\mathrm{L}^{(0)}|^2}{|A_\mathrm{L,sat}|^2} - \mathrm{Re}\left[\sqrt{\kappa_\mathrm{R}\kappa_\mathrm{L}}e^{i\phi_\mathrm{B}}\frac{A_\mathrm{B}}{A_\mathrm{L}}\right],$$

where $g' = g_0/(1 + |A_\mathrm{L}^{(0)}|^2/|A_\mathrm{L,sat}|^2)^2$ is the gain derivative that represents the relaxation rate of the gain dynamics. Typical values for g' are on the order of several GHz for III-V semiconductor lasers, which is much faster compared to the resonator dynamics. Accordingly, the laser amplitude can be adiabatically eliminated (i.e. assume $d|A_\mathrm{L}|/dt = 0$) so that the laser power adiabatically tracks the feedback. The gain can be solved as

$$\frac{g(|A_\mathrm{L}|^2)}{2} = \frac{\gamma}{2} + \mathrm{Re}\left[\sqrt{\kappa_\mathrm{R}\kappa_\mathrm{L}}e^{i\phi_\mathrm{B}}\frac{A_\mathrm{B}}{A_\mathrm{L}}\right],$$

which, under the assumption of fast relaxation rates, becomes independent of the specific details of gain. Substituting this equation into the phase equation and normalizing results in an Adler-like equation:

$$\frac{d\phi_\mathrm{L}}{d\tau} = \alpha_\mathrm{L} - \alpha - \mathrm{Im}\left[\frac{2\sqrt{\kappa_\mathrm{R}\kappa_\mathrm{L}}}{\kappa}(1 - i\alpha_g)e^{i\phi_\mathrm{B}}\frac{\rho_\mathrm{B}}{\rho_\mathrm{L}}\right], \tag{4.4}$$

where $\alpha_\mathrm{L} = (2\delta\omega_\mathrm{L} + \alpha_g\gamma)/\kappa$ is the normalized detuning of the cold-cavity resonance compared to the free-running hot laser.

To simplify the equations further we also consider the following approximation for the propagation phase ϕ_B, which depends on the precise frequency of the locked laser and material dispersion. We assume that the feedback length is short ($L \ll c/(n\kappa)$, where c is the speed of light in vacuum and n is the refractive index of the material) so that ϕ_B can be treated as constant. This approximation is equivalent to assuming that the free spectral range (FSR) of a cavity equal in length to the feedback path is much larger than the linewidth of the high-Q resonator. By defining a pump phase variable $z = -e^{i\phi_\mathrm{B}}e^{i\phi_\mathrm{L}}$, the equations can be written as

$$\begin{aligned}
\frac{\partial\psi}{\partial\tau} &= -(1 + i\alpha)\psi + i\frac{D_2}{\kappa}\frac{\partial^2\psi}{\partial\theta^2} + i(|\psi|^2 + 2|\rho_\mathrm{B}|^2)\psi + i\beta^*\rho_\mathrm{B} + zF, \\
\frac{d\rho_\mathrm{B}}{d\tau} &= -(1 + i\alpha - 2iP - i|\rho_\mathrm{B}|^2)\rho_\mathrm{B} + i\beta\rho, \\
\frac{1}{iz}\frac{dz}{d\tau} &= \alpha_\mathrm{L} - \alpha + K\mathrm{Im}\left[e^{i\phi}\frac{\rho_\mathrm{B}}{i\beta zF}\right], \quad |z| = 1,
\end{aligned} \tag{4.5}$$

where we defined: the normalized pump,

$$F = \frac{2\sqrt{\kappa_R \kappa_L}}{\kappa}|\rho_L|, \tag{4.6}$$

the locking bandwidth,

$$K = \frac{4\kappa_R \kappa_L}{\kappa^2}|\beta|\sqrt{1+\alpha_g^2}, \tag{4.7}$$

and the feedback phase,

$$\phi = 2\phi_B - \arctan(\alpha_g) + \mathrm{Arg}[\beta] + \frac{\pi}{2}, \tag{4.8}$$

where $\mathrm{Arg}[\cdot]$ is the argument function. The feedback phase ϕ contains phase contributions from the propagation length, the amplitude-phase coupling, the backscattering, as well as an extra $\pi/2$ added to the definition of ϕ such that the mode is locked to the center at $\phi = 0$ (as discussed below).

We note that the feedback fields considered in Eq. (4.5) come entirely from inside the resonator. In experiments, defects and facets of the coupling waveguide can also induce reflections. However, these are neglected in the injection locking dynamics by the following arguments. Multiple reflection sources can be incorporated into Eq. (4.5) by adding a feedback term corresponding to each source. However, the cumulative effect of such reflections will be to produce a wavelength dependence that is weak compared to the resonator mode, which is spectrally very narrow on account of its high optical Q. Such a weak wavelength dependence means that these fields do not contribute to the locking (i.e., a constant term is added to the phasor equation in Eq. (4.5), which can then be absorbed into the free-running laser frequency). As a specific illustration of this idea, consider that the facet reflections at the end of the waveguide form a kind of Fabry-Perot resonator. However, the Q of its resonances will be quite low, and accordingly the linewidth will be of order the FSR associated with the waveguide length. Moreover, this FSR is also comparable in scale to the FSR of the high-Q resonator, the resonances of which are many orders narrower than the resonator FSR. As a result, any wavelength dependence introduced by reflections in the waveguide will be spectrally slow in comparison to those introduced by the resonator.

For stationary solutions (e.g., a stable soliton), when backscattering is weak ($\beta \ll 1$) so that nonlinearities caused by $|\rho_B|^2$ in Eq. (4.3) are negligible in comparison to the soliton driven nonlinear terms, ρ_B can be found as

$$\rho_B = \frac{i\beta\rho}{1+i(\alpha-2P)}, \tag{4.9}$$

and the laser phasor equation reduces to an algebraic equation for the detuning α,

$$\alpha = \alpha_{\mathrm{L}} + K\mathrm{Im}\left[e^{i\phi}\frac{1}{1+i(\alpha-2P)}\frac{\rho}{zF}\right]. \tag{4.10}$$

Finally, neglecting the small coupled amplitude from ρ_{B} to ψ, the equation for the soliton field reads

$$-(1+i\alpha)\psi + i\frac{D_2}{\kappa}\frac{\partial^2\psi}{\partial\theta^2} + i|\psi|^2\psi + zF = 0. \tag{4.11}$$

We have therefore recovered a conventional Lugiato-Lefever equation, with an additional equation that describes the detuning determined by injection locking. This shows that the spectral properties of the injection-locked solitons are not much different from a conventional soliton. The main difference is the comb formation dynamics.

It is known that combs and solitons will emerge from a continuous-wave (CW) background when its power exceeds the parametric oscillation threshold ($|\rho| > 1$), and it is desirable to first study the CW excitation of the system by setting $D_2 = 0$. In this case, the Lugiato-Lefever partial differential equation reduces to an ordinary differential equation with $\psi = \rho$ and $P = |\rho|^2$. The steady state solution can be found from

$$zF = [1 + i(\alpha - |\rho|^2)]\rho, \tag{4.12}$$

and the locking equilibrium reduces to

$$\alpha = \alpha_{\mathrm{L}} + K\mathrm{Im}\left[e^{i\phi}\frac{1}{1+i(\alpha-2P)}\frac{1}{1+i(\alpha-P)}\right] = \alpha_{\mathrm{L}} + K\chi(P,\alpha,\phi), \tag{4.13}$$

where we have defined the CW locking response function:

$$\chi(P,\alpha,\phi) = \frac{(3P-2\alpha)\cos\phi + (1-2P^2+3P\alpha-\alpha^2)\sin\phi}{[1+(\alpha-P)^2][1+(\alpha-2P)^2]}. \tag{4.14}$$

To obtain analytical results, we will also make the approximation of infinite locking bandwidth limit (i.e., $K \to \infty$), which makes the detuning independent of the free-running laser frequency. The locking condition is then equivalent to setting the locking response function to zero:

$$(3P-2\alpha)\cos\phi + (1-2P^2+3P\alpha-\alpha^2)\sin\phi = 0. \tag{4.15}$$

Fig. 4.6 shows a plot for Eq. (4.12) with different pumping powers $|F|^2$ and Eq. (4.15) with different feedback phases ϕ. The intersecting point of the two curves

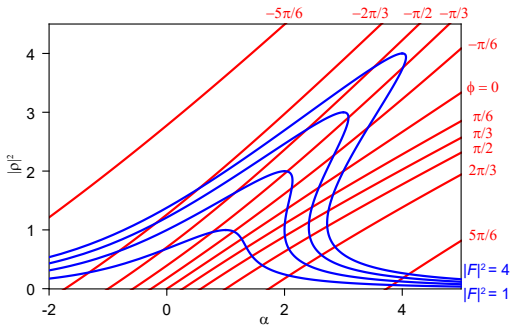

Figure 4.6: Continuous-wave states of the injection-locked nonlinear resonator. Horizontal axis is the normalized detuning α, and vertical axis is the normalized optical energy on the pump mode $|\rho|^2$. Resonator characteristics are shown as the blue curves, with $|F|^2 = 1$ (lower) to 4 (upper). Laser locking characteristics are shown as the red curves, with $\phi = -5\pi/6$ (upper left) to $5\pi/6$ (lower right).

gives the CW steady state of the cavity. Note that there are two solutions to the quadratic equation Eq. (4.15). Only the solution branch that satisfies $\partial\chi/\partial\alpha < 0$ is plotted, which are the stable locking solutions (stable in the sense of CW excitations; the instability arising from modulations are considered below). The opposite case $\partial\chi/\partial\alpha > 0$ drives the frequency away from the equilibrium.

When a resonator is pumped conventionally, the intracavity power P will approach its equilibrium given by Eq. (4.12). In the case of feedback-locked pumping, such power changes will also have an effect on the locking response function χ, pulling the detuning to the new locking equilibrium as well (Fig. 2b,e in main text). A special case is $\phi = 0$, where the locking equilibrium can be simply described as

$$\alpha = \frac{3}{2}P, \tag{4.16}$$

i.e. the detuning is pulled away from the cold cavity resonance, and the effect is exactly $3/2$ times what is expected from the self phase modulation. This is an averaged effect of the self phase modulation on the soliton mode and the cross phase modulation of the backscattered mode from the soliton mode. More generally, the detuning can be solved in terms of P as

$$\alpha = \frac{3}{2}P - \cot\phi + \frac{\sqrt{4 + P^2\sin^2\phi}}{2\sin\phi}, \tag{4.17}$$

where again only the solution satisfying $\partial\chi/\partial\alpha < 0$ is given. Neglecting the higher-order $P^2\sin^2\phi$ term inside the square root results in a lowest-order approximation:

$$\alpha = \tan\frac{\phi}{2} + \frac{3}{2}P, \tag{4.18}$$

which splits into two additive contributions: one from the feedback phase and the other from the averaged nonlinear shift. This is Eq. (1) in the main text when written using dimensional quantities. We note that Eq. (1) in the main text uses power normalized to threshold power, while in the above analysis we used energy normalized to threshold energy. The intracavity power and energy only differ by a factor of round-trip time, and the normalized quantity is essentially the same.

When the dispersion term is considered, the CW solution is no longer stable, which leads to the formation of modulational instability (MI) combs. These combs will evolve into solitons if the CW state is also inside the multistability region of the resonator dynamics. By adjusting the pump power $|F|^2$ and feedback phase ϕ, we can change the operating point of the cavity and map the possible comb states to a phase diagram with $|F|^2$ and ϕ as parameters (Fig. 4b in the main text). It should be noted that as soon as combs start to form inside the resonator, the CW results after Eq. (4.12) become invalid (i.e. due to power appearing in the sidebands, we have $P > |\rho|^2$ when combs are formed instead of $P = |\rho|^2$ in the CW case), and such comb formation will slightly shift the operating point of the system. However, the CW results still indicate whether and how such combs can be started. Contrary to conventional pumping phase diagrams (with $|F|^2$ and α as parameters), where soliton existence regions only imply the possible formation of solitons due to multistability, the soliton existence region here guarantees the generation of solitons as the system bypasses the chaotic comb region before the onset of MI.

We have also performed numerical simulations to verify the above analyses (Fig. 4.7). The simulation numerically integrates Eq. (4.5) with a split-step Fourier method. Noise equivalent to about one-half photon per mode is injected into ψ to provide seeding for comb generation. Parameters common to all simulation cases are $D_2/\kappa = 0.015$ and $|\beta| = 0.5$, while others are varied across different cases and can be found in the caption of Fig. 4.7. As an aside, the magnitude of β was estimated from the resonant backscatter reflectivity. The resonant reflection (measured to be in the range of 4% - 20%) was measured by the detecting the reflected optical power from the resonator while scanning a laser across the resonances. In the first case (Fig. 4.7a), conventional soliton generation by sweeping the laser frequency is presented, showing the dynamics of a random noisy comb waveform collapsing into soliton pulses. This is in contrast to the turnkey soliton generation in the second case (Fig. 4.7b), where solitons directly "grow up" from ripples in the background. Such ripples are generated by MI in those sections of the resonator with local intracavity

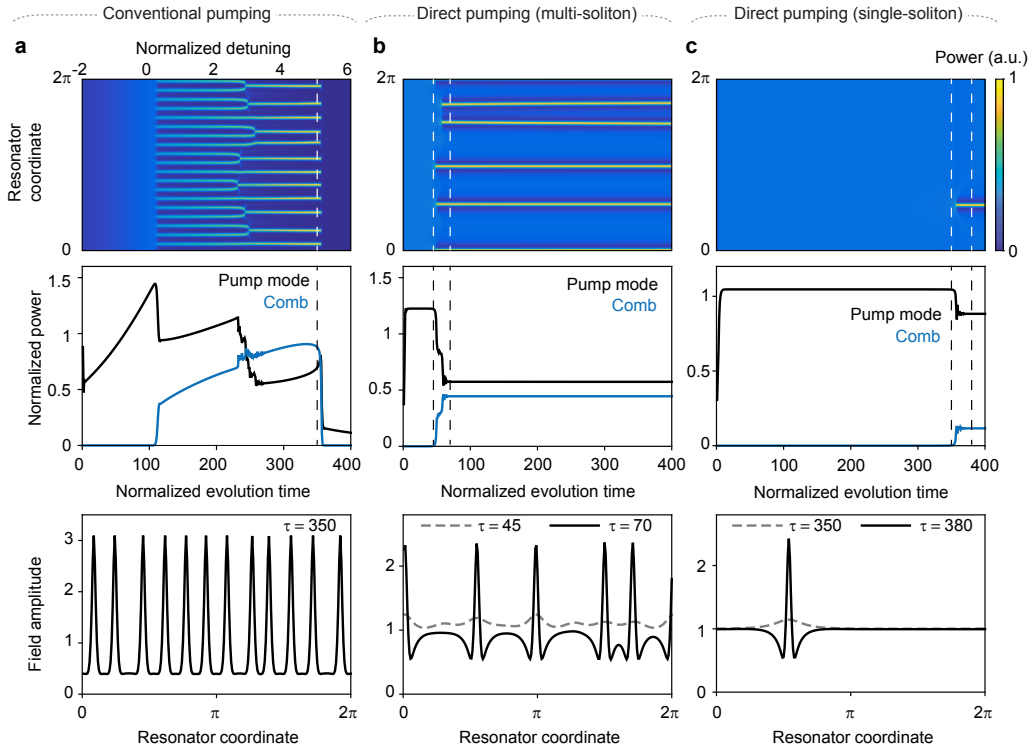

Figure 4.7: Numerical simulations of turnkey soliton generation. (a) Conventional solitons are generated by sweeping the laser frequency. Parameters are $K = 0$ (no feedback) and $|F|^2 = 4$. The normalized laser frequency is swept from $\alpha_L = -2$ to $\alpha_L = 6$ within a normalized time interval of 400. Upper panel: soliton field power distribution as a function of evolution time and coordinates. Middle panel: dynamics of the pump mode power (black) and comb power (blue). Lower panel: a snapshot of the soliton field at evolution time $\tau = 350$ ($\alpha_L = 5$), also marked as a white dashed line in the upper panel and a black dashed line in the middle panel. (b) Multiple solitons are generated under conditions of nonlinear feedback. Parameters are $K = 15$, $\phi = 0.15\pi$, $|F|^2 = 3$ and $\alpha_L = 5$. Upper and middle panels are the same as in (a). Lower panel: snapshots of the soliton field at evolution time $\tau = 45$ (grey dashed line) and $\tau = 70$ (black solid line), also marked as white dashed lines in the upper panel and black dashed lines in the middle panel. (c), A single soliton is generated under conditions of nonlinear feedback. Parameters are $K = 15$, $\phi = 0.3\pi$, $|F|^2 = 3$ and $\alpha_L = 5$. Upper and middle panels are the same as in (a). Lower panel: snapshots of the soliton field at evolution time $\tau = 350$ (grey dashed line) and $\tau = 380$ (black solid line), also marked as white dashed lines in the upper panel and black dashed lines in the middle panel.

power above the threshold. Each peak in the ripples corresponds to one soliton if collisions and other events are not considered. The process of growing solitons out of the background will continue until there is no space for new solitons or when the background falls below the MI threshold, and such dynamics explain the tendency

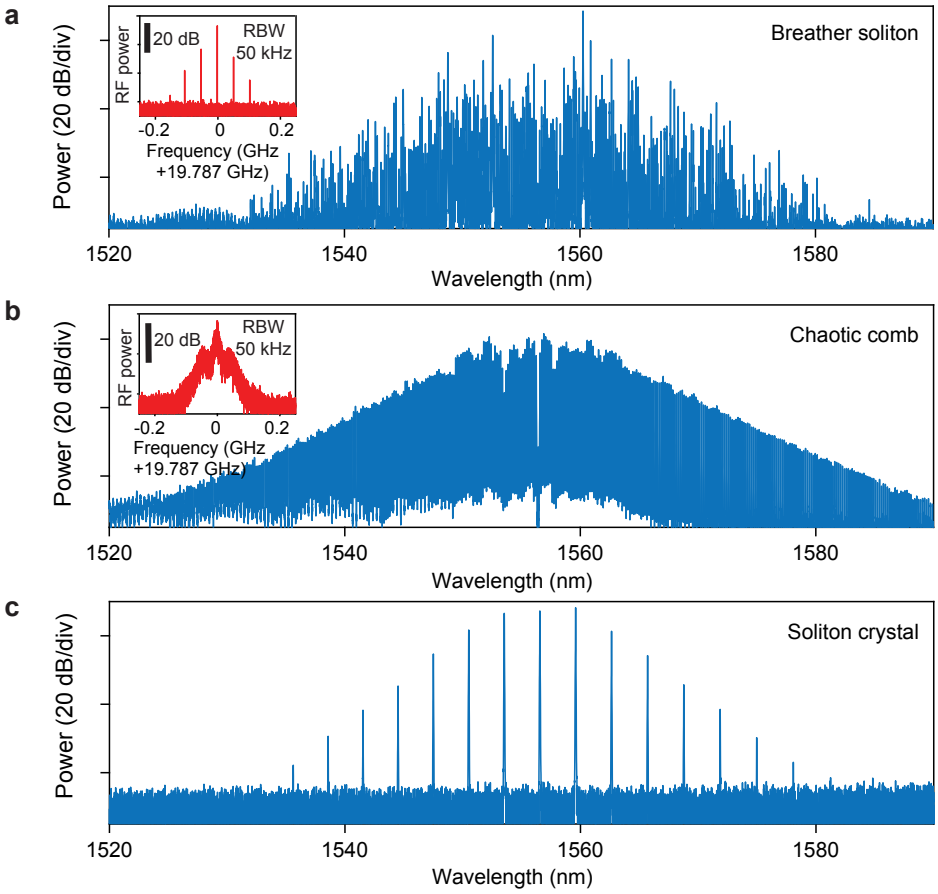

Figure 4.8: Optical and electrical spectra of different microcomb types. (a-b) Optical spectra of breather solitons and a chaotic comb. Inset: Electrical beatnote signals. (c) Optical spectrum of a soliton crystal state.

of the turnkey soliton state to consist of multiple solitons. By carefully tuning the phase and controlling the MI gain, it is still possible to obtain a turnkey single soliton state, as shown in the third case (Fig. 4.7c).

4.4 Supplementary information: Additional measurements

Different types of microcombs in the injection locking system

There are several interesting solutions other than stable solitons that can be derived from the regular Lugiato-Lefever equation [38]. One is the breather soliton, which is the type of soliton whose shape oscillates in time. Another example is the chaotic comb, which corresponds to the unstable Turing patterns or soliton state as the pump power is increased. In addition, solitons can be self-organized and form an equidistant pulse train in the microresonator, which is called a soliton crystal.

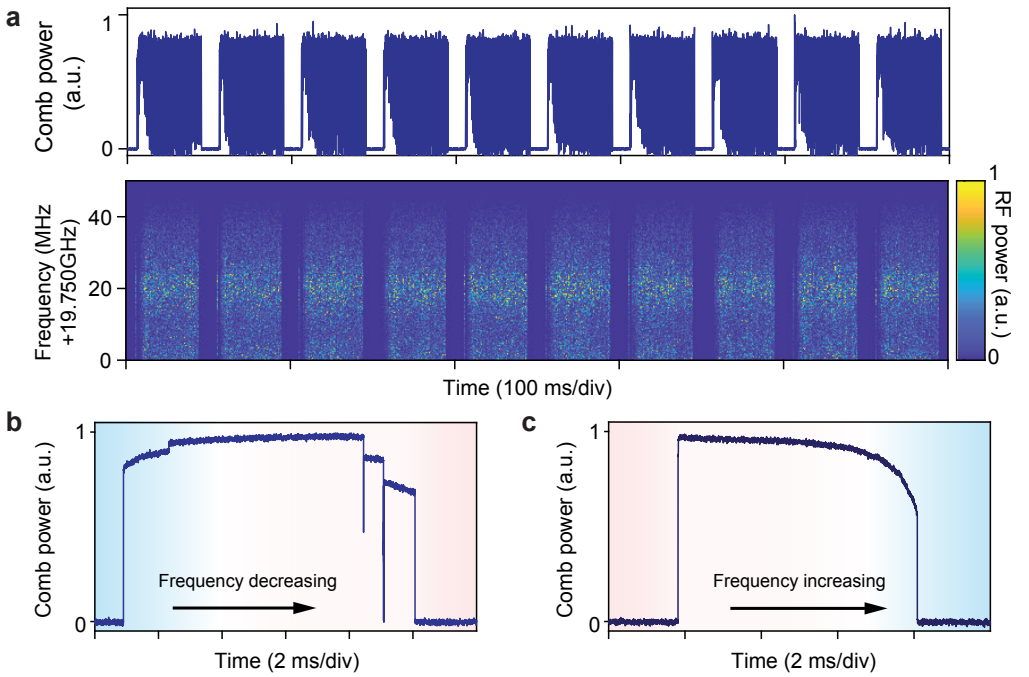

Figure 4.9: (a) Turnkey generation of a chaotic comb. Upper panel: Comb power evolution. Lower panel: Spectrograph of RF beatnote power. (b-c) Comb power evolution when the pump laser frequency is driven from blue to red (b) and red to blue (c).

It is also possible to operate our system in different types of microcomb states under certain feedback phase and laser driving frequency. Fig. 4.8 shows the experimental spectra of breather solitons, a chaotic comb and a soliton crystal state, respectively. The turnkey generation of the chaotic comb is further shown in Fig. 4.9a. The broad and noisy RF spectrum indicates that it is not mode-locked.

Tuning of turnkey soliton microcomb system

To further explore the performance of the turnkey soliton microcomb system, the frequency of the pump laser is driven by a linear current scan (Fig. 4.9b,c). The scan speed of the driving frequency is around 0.36 GHz/ms, estimated from the wavelength-current response when the laser is free running. When the laser is scanned across the resonance, feedback locking occurs and pulls the pump laser frequency towards the resonance until the driving frequency is out of the locking band. As shown in Fig. 4.9b, the power steps indicate that soliton states with different soliton numbers can be accessed as we tune the driving current. It is worth noting that the soliton microcombs can be powered-on when the laser is scanned from red-detuned side (Fig. 4.9c), which seldom happens under conventional pumping,

except in cases of an effectively negative thermo-optic response system [8]. The comb evolution during laser scanning is a useful tool to assess the robustness of the turnkey soliton generation.

References

[1] Diddams, S. A. The evolving optical frequency comb. *Journal of the Optical Society of America B* **27**, B51–B62 (2010).

[2] Herr, T. *et al.* Temporal solitons in optical microresonators. *Nature Photonics* **8**, 145–152 (2014).

[3] Xue, X. *et al.* Mode-locked dark pulse Kerr combs in normal-dispersion microresonators. *Nature Photonics* **9**, 594–600 (2015).

[4] Brasch, V. *et al.* Photonic chip–based optical frequency comb using soliton Cherenkov radiation. *Science* **351**, 357–360 (2016).

[5] Yi, X., Yang, Q.-F., Yang, K. Y., Suh, M.-G. & Vahala, K. Soliton frequency comb at microwave rates in a high-Q silica microresonator. *Optica* **2**, 1078–1085 (2015).

[6] Obrzud, E., Lecomte, S. & Herr, T. Temporal solitons in microresonators driven by optical pulses. *Nature Photonics* **11**, 600–607 (2017).

[7] Gong, Z. *et al.* High-fidelity cavity soliton generation in crystalline AlN micro-ring resonators. *Optics Letters* **43**, 4366–4369 (2018).

[8] He, Y. *et al.* Self-starting bi-chromatic $LiNbO_3$ soliton microcomb. *Optica* **6**, 1138–1144 (2019).

[9] Bao, H. *et al.* Laser cavity-soliton microcombs. *Nature Photonics* **13**, 384–389 (2019).

[10] Kippenberg, T. J., Gaeta, A. L., Lipson, M. & Gorodetsky, M. L. Dissipative Kerr solitons in optical microresonators. *Science* **361**, eaan8083 (2018).

[11] Suh, M.-G., Yang, Q.-F., Yang, K. Y., Yi, X. & Vahala, K. J. Microresonator soliton dual-comb spectroscopy. *Science* **354**, 600–603 (2016).

[12] Dutt, A. *et al.* On-chip dual-comb source for spectroscopy. *Science Advances* **4**, e1701858 (2018).

[13] Yang, Q.-F. *et al.* Vernier spectrometer using counterpropagating soliton microcombs. *Science* **363**, 965–968 (2019).

[14] Suh, M.-G. *et al.* Searching for exoplanets using a microresonator astrocomb. *Nature Photonics* **13**, 25–30 (2019).

[15] Obrzud, E. *et al.* A microphotonic astrocomb. *Nature Photonics* **13**, 31–35 (2019).

[16] Spencer, D. T. *et al.* An optical-frequency synthesizer using integrated photonics. *Nature* **557**, 81–85 (2018).

[17] Newman, Z. L. *et al.* Architecture for the photonic integration of an optical atomic clock. *Optica* **6**, 680–685 (2019).

[18] Stern, B., Ji, X., Okawachi, Y., Gaeta, A. L. & Lipson, M. Battery-operated integrated frequency comb generator. *Nature* **562**, 401–405 (2018).

[19] Raja, A. S. *et al.* Electrically pumped photonic integrated soliton microcomb. *Nature Communications* **10**, 680 (2019).

[20] Yi, X., Yang, Q.-F., Youl, K. & Vahala, K. Active capture and stabilization of temporal solitons in microresonators. *Optics Letters* **41**, 2037–2040 (2016).

[21] Joshi, C. *et al.* Thermally controlled comb generation and soliton modelocking in microresonators. *Optics Letters* **41**, 2565–2568 (2016).

[22] Yang, K. Y. *et al.* Bridging ultrahigh-Q devices and photonic circuits. *Nature Photonics* **12**, 297–302 (2018).

[23] Liu, J. *et al.* Ultralow-power chip-based soliton microcombs for photonic integration. *Optica* **5**, 1347–1353 (2018).

[24] Abidi, A. A. CMOS microwave and millimeter-wave ICs: The historical background. In *2014 IEEE International Symposium on Radio-Frequency Integration Technology*, 1–5 (IEEE, 2014).

[25] Liu, J. *et al.* Photonic microwave generation in the X-and K-band using integrated soliton microcombs. *Nature Photonics* **14**, 486–491 (2020).

[26] Huang, D. *et al.* High-power sub-kHz linewidth lasers fully integrated on silicon. *Optica* **6**, 745–752 (2019).

[27] Carmon, T., Yang, L. & Vahala, K. Dynamical thermal behavior and thermal self-stability of microcavities. *Optics Express* **12**, 4742–4750 (2004).

[28] Liang, W. *et al.* Whispering-gallery-mode-resonator-based ultranarrow linewidth external-cavity semiconductor laser. *Optics Letters* **35**, 2822–2824 (2010).

[29] Liang, W. *et al.* High spectral purity Kerr frequency comb radio frequency photonic oscillator. *Nature Communications* **6**, 7957 (2015).

[30] Pavlov, N. *et al.* Narrow-linewidth lasing and soliton Kerr microcombs with ordinary laser diodes. *Nature Photonics* **12**, 694–698 (2018).

[31] Kondratiev, N. *et al.* Self-injection locking of a laser diode to a high-Q WGM microresonator. *Optics Express* **25**, 28167–28178 (2017).

[32] Chang, L. *et al.* Ultra-efficient frequency comb generation in AlGaAs-on-insulator microresonators. *Nature communications* **11**, 1331 (2020).

[33] Kim, B. Y. *et al.* Turn-key, high-efficiency Kerr comb source. *Optics letters* **44**, 4475–4478 (2019).

[34] Moss, D. J., Morandotti, R., Gaeta, A. L. & Lipson, M. New CMOS-compatible platforms based on silicon nitride and Hydex for nonlinear optics. *Nature Photonics* **7**, 597 (2013).

[35] Pfeiffer, M. H. P. *et al.* Photonic Damascene process for low-loss, high-confinement silicon nitride waveguides. *IEEE J. Sel. Top. Quantum Electron.* **24**, 1–11 (2018).

[36] Pfeiffer, M. H. P. *et al.* Ultra-smooth silicon nitride waveguides based on the Damascene reflow process: fabrication and loss origins. *Optica* **5**, 884–892 (2018).

[37] Mashanovitch, M. *et al.* High-power, efficient DFB laser technology for RF photonics links. In *IEEE Avionics and Vehicle Fiber-Optics and Photonics Conference*, 1–2 (IEEE, 2018).

[38] Godey, C., Balakireva, I. V., Coillet, A. & Chembo, Y. K. Stability analysis of the spatiotemporal Lugiato-Lefever model for Kerr optical frequency combs in the anomalous and normal dispersion regimes. *Physical Review A* **89**, 063814 (2014).

Chapter 5

TOWARDS VISIBLE SOLITON MICROCOMB GENERATION

Lee, S. H. *et al.* Towards visible soliton microcomb generation. *Nature Communications* **8**, 1295 (2017).

Soliton mode locking [1–5] in frequency microcombs [6] provides a pathway to miniaturize many conventional comb applications. It has also opened investigations into new nonlinear physics associated with dissipative Kerr solitons [1] and Stokes solitons [7]. In contrast to early microcombs [6], soliton microcombs eliminate instabilities, provide stable (low-phase-noise) mode locking and feature a highly reproducible spectral envelope. Many applications of these devices are being studied including chip-based optical frequency synthesis [8], secondary time standards [9], and dual-comb spectroscopy [10–12]. Also, a range of operating wavelengths is opening up by use of several low-optical-loss dielectric materials for resonator fabrication. In the near-infrared (IR), microcombs based on magnesium fluoride [1], silica [2, 13] and silicon nitride [3–5, 14, 15] are being studied for frequency metrology and frequency synthesis. In the mid-IR spectral region, silicon nitride [16], crystalline [17], and silicon-based [18] Kerr microcombs as well as quantum-cascade microcombs [19] are being studied for application to molecular fingerprinting.

At shorter wavelengths below 1 μm, microcomb technology would benefit optical atomic clock technology [20], particularly efforts to miniaturize these clocks. For example, microcomb optical clocks based on the D1 transition (795 nm) and the two-photon clock transition [21] (798 nm) in rubidium have been proposed [9, 22]. Also, a microcomb clock using two-point locking to rubidium D1 and D2 lines has been demonstrated [23] by frequency doubling from the near-IR. More generally, microcomb sources in the visible and ultra-violet bands could provide a miniature alternative to larger mode-locked systems such as titanium sapphire lasers in cases where high power is not required. It is also possible that these shorter wavelength systems could be applied in optical coherence tomography systems [24–26]. Efforts directed towards short wavelength microcomb operation include 1 μm microcombs in silicon nitride microresonators [27] as well as harmonically-generated combs. The

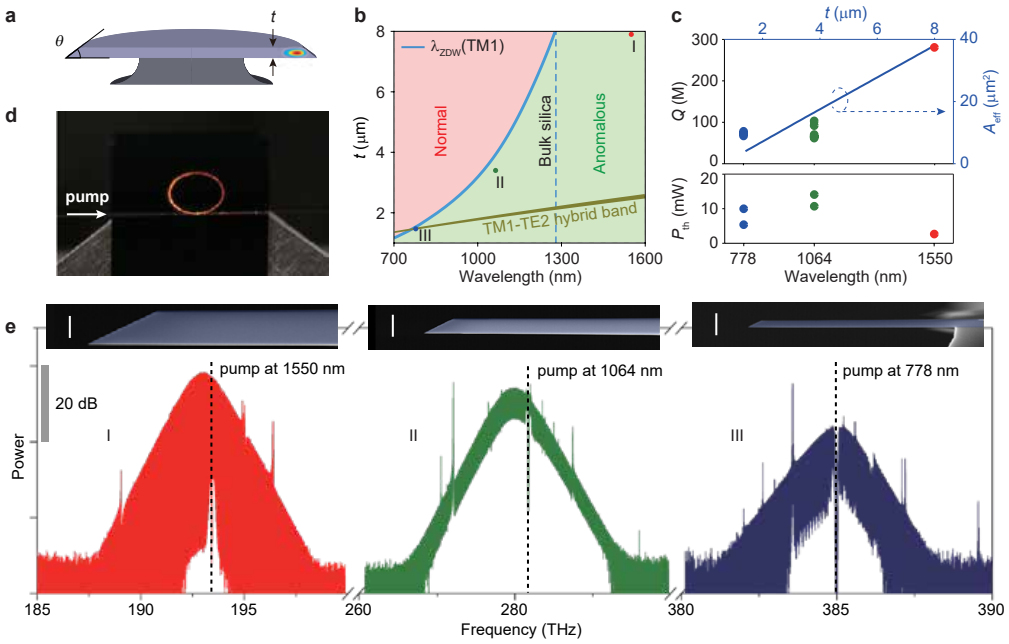

Figure 5.1: Soliton frequency comb generation in dispersion-engineered silica resonators. (a) A rendering of a silica resonator with the calculated TM1 mode profile superimposed. (b) Regions of normal and anomalous dispersion are shown versus silica resonator thickness (t) and pump wavelength. The zero dispersion wavelength (λ_{ZDW}) for the TM1 mode appears as a blue curve. The dark green band shows the 10-dB bandwidth of anomalous dispersion created by TM1-TE2 mode hybridization. The plot is made for a 3.2-mm-diameter silica resonator with a 40° wedge angle. Three different device types I, II, and III (corresponding to t = 7.9 μm, 3.4 μm, and 1.5 μm) are indicated for soliton generation at 1550 nm, 1064 nm, and 778 nm. (c) Measured Q factors and parametric oscillation threshold powers versus thickness and pump wavelength for the three device types. Powers are measured in the tapered fiber coupler under critical coupling. Effective mode area (A_{eff}) of the TM1 mode family is also plotted as a function of wavelength and thickness. (d) A photograph of a silica resonator (Type III device pumped at 778 nm) while generating a soliton stream. (e) Soliton frequency comb spectra measured from the devices. The red, green, and blue soliton spectra correspond to device types I, II, and III designed for pump wavelengths 1550 nm, 1064 nm, and 778 nm, respectively. Pump frequency location is indicated by a dashed vertical line. Differences in signal-to-noise ratio (SNR) of the spectra originate from the resolution of the optical spectrum analyser (OSA). In particular, the 778 nm comb spectrum was measured using the second-order diffracted spectrum of the OSA, while other comb spectra were measured as first-order diffracted spectra. Insets: cross-sectional scanning electron microscope (SEM) images of the fabricated resonators. White scale bar is 5 μm.

latter have successfully converted near-IR comb light to shorter wavelength bands [28] and even into the visible band [29, 30] within the same resonator used to create

the initial comb of near-IR frequencies. Also, crystalline resonators [31] and silica microbubble resonators [32] have been dispersion-engineered for comb generation in the 700 nm band. Finally, diamond-based microcombs afford the possibility of broad wavelength coverage [33]. However, none of the short wavelength microcomb systems have so far been able to generate stable mode-locked microcombs as required in all comb applications.

A key impediment to mode-locked microcomb operation at short wavelengths is material dispersion associated with the various dielectric materials used for microresonator fabrication. At shorter wavelengths, these materials feature large normal dispersion that dramatically increases into the visible and ultra-violet bands. While dark soliton pulses can be generated in a regime of normal dispersion [34], bright solitons require anomalous dispersion. Dispersion engineering by proper design of the resonator geometry [22, 31, 32, 35–41] offers a possible way to offset the normal dispersion. Typically, by compressing the waveguide dimension of a resonator, geometrical dispersion will ultimately compensate a large normal material dispersion component to produce overall anomalous dispersion. For example, in silica, strong confinement in bubble resonators [32] and straight waveguides [42] has been used to push the anomalous dispersion transition wavelength from the near-IR into the visible band. Phase matching to ultra-violet dispersive waves has also been demonstrated using this technique [42]. However, to compensate the rising material dispersion, this compression must increase as the operational wavelength is decreased, and as a side effect, highly-confined waveguides tend to suffer increased optical losses. This happens because mode overlap with the dielectric waveguide interface is greater with reduced waveguide cross section. Consequently, the residual fabrication-induced roughness of that interface degrades the resonator Q factor and increases pumping power (e.g., comb threshold power varies inverse quadratically with Q factor [43]).

Minimizing material dispersion provides one way to ease the impact of these constraints. In this sense, silica offers an excellent material for short wavelength operation, because it has the lowest dispersion among all on-chip integrable materials. For example, at 778 nm, silica has a group velocity dispersion (GVD) equal to 38 $\mathrm{ps}^2\ \mathrm{km}^{-1}$, which is over 5 times smaller than the GVD of silicon nitride at this wavelength ($> 200\ \mathrm{ps}^2\ \mathrm{km}^{-1}$) [44]. Other integrable materials that are also transparent in the visible, such as diamond [33] and aluminium nitride [45], have dispersion that is similar to or higher than silicon nitride. Silica also features a spectrally-broad

low-optical-loss window so that optical Q factors can be high at short wavelengths. Here we demonstrate soliton microcombs with pump wavelengths of 1064 nm and 778 nm. These are the shortest soliton microcomb wavelengths demonstrated to date. By engineering geometrical dispersion and by employing mode hybridization, a net anomalous dispersion is achieved at these wavelengths while also maintaining high optical Q factors (80 million at 778 nm, 90 million at 1064 nm). The devices have large (millimeter-scale) diameters and produce single-soliton pulse streams at rates that are both detectable and processable by low-cost electronic circuits. Besides illustrating the flexibility of silica for soliton microcomb generation across a range of short wavelengths, these results are relevant to potential secondary time standards based on transitions in rubidium [9, 22, 23]. By using dispersive-wave engineering in silica, it might also be possible to extend the emission of these combs into the ultra-violet as recently demonstrated in compact silica waveguides [42].

5.1 Silica resonator design

The silica resonator used in this work is shown schematically in Fig. 5.1a. A fundamental mode profile is overlaid onto the cross-sectional rendering. The resonator design is a variation on the wedge resonator [46], and its geometry can be fully characterized by its resonator diameter, silica thickness (t), and wedge angle (θ) (see Fig. 5.1a). The diameter of all resonators in this work (and the assumed diameter in all simulations) is 3.2 mm, which corresponds to a free spectral range (FSR) of approximately 20 GHz, and the resonator thickness is controlled to obtain net anomalous dispersion at the design wavelengths, as described in detail below. Further details on fabrication are given elsewhere [46]. As an aside, we note that a waveguide-integrated version of this design is also possible [47]. Adaptation of that device using the methods described here would enable full integration with other photonic elements on the silicon chip.

Fig. 5.1b illustrates how the geometrical dispersion induced by varying resonator thickness t offsets the material dispersion. Regions of anomalous and normal dispersion are shown for the TM1 mode family of a resonator having a wedge angle of 40°. The plots show that thinner resonators enable shorter wavelength solitons. Accordingly, three device types (I, II, and III shown as the colored dots in Fig. 5.1b) are selected for soliton frequency comb operation at three different pump wavelengths. At a pump wavelength of 1550 nm, the anomalous dispersion window is wide because bulk silica possesses anomalous dispersion at wavelengths above 1270 nm. For this type I device, a 7.9-μm thickness was used. Devices of type II and

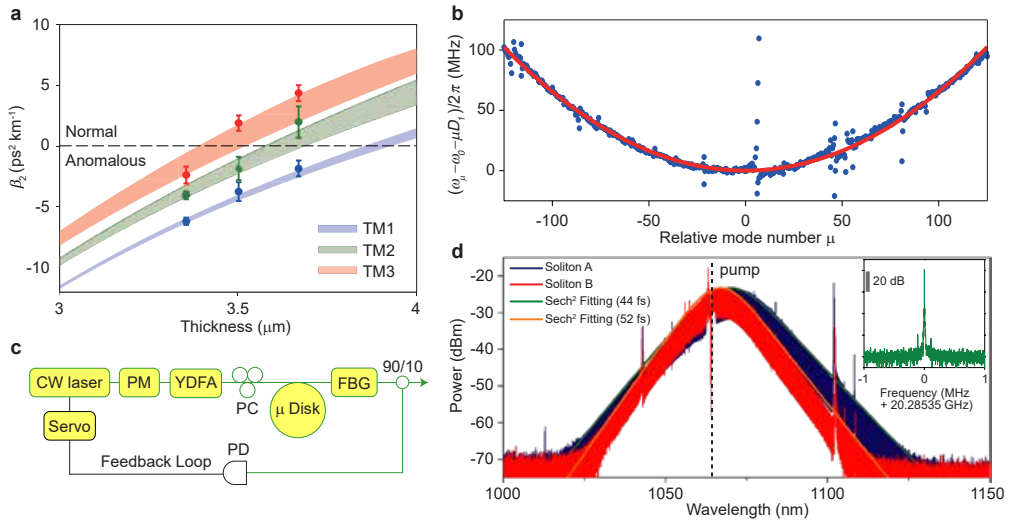

Figure 5.2: Microresonator dispersion engineering and soliton generation at 1064 nm. (a) Simulated group velocity dispersion (GVD) of TM mode families versus resonator thickness. The angle of the wedge ranges from 30° to 40° in the colored regions. Measured data points are indicated and agree well with the simulation. The error bars depict standard deviations obtained from measurement of 8 samples having the same thickness. (b) Measured relative mode frequencies (blue points) plotted versus relative mode number of a soliton-forming TM1 mode family in a 3.4 μm thick resonator. The red curve is a parabolic fit yielding $D_2/2\pi = 3.3$ kHz. (c) Experimental setup for soliton generation. A continuous-wave (CW) fiber laser is modulated by an electro-optic phase modulator (PM) before coupling to a ytterbium-doped fiber amplifier (YDFA). The pump light is then coupled to the resonator using a tapered fiber. Part of the comb power is used to servo-control the pump laser frequency. FBG: fiber Bragg grating. PD: photodetector. PC: polarization controller. (d) Optical spectra of solitons at 1064 nm generated from the mode family shown in (b). The two soliton spectra correspond to different power levels with the blue spectrum being a higher power and wider bandwidth soliton. The dashed vertical line shows the location of the pump frequency. The solid curves are sech^2 fittings. Inset: typical detected electrical beatnote showing soliton repetition rate. The weak sidebands are induced by the feedback loop used to stabilize the soliton. The resolution bandwidth is 1 kHz.

III have thicknesses near 3.4 μm and 1.5 μm for operation with pump wavelengths of 1064 nm and 778 nm, respectively. Beyond geometrical control of dispersion, the type III design also uses mode hybridization to substantially boost the anomalous dispersion. This hybridization occurs within a relatively narrow wavelength band which tunes with t (darker green region in Fig. 5.1b) and is discussed in detail below. Measured Q factors for the three device types are plotted in the upper panel of Fig. 5.1c. Maximum Q factors at thicknesses which also produce anomalous

dispersion were: 280 million (Type I, 1550 nm), 90 million (Type II, 1064 nm), and 80 million (Type III, 778 nm).

Using these three designs, soliton frequency combs were successfully generated with low threshold pump power. Shown in Fig. 5.1d is a photograph of a type III device under conditions where it is generating solitons. Fig. 5.1e shows optical spectra of the soliton microcombs generated for each device type. A slight Raman-induced soliton self-frequency-shift is observable in the type I and type II devices [2, 48–50]. The pulse width of the type III device is longer and has a relatively smaller Raman shift, which is consistent with theory [50]. The presence of a dispersive wave in this spectrum also somewhat offsets the smaller Raman shift [3]. Scanning electron microscope (SEM) images appear as insets in Fig. 5.1e and provide cross-sectional views of the three device types. It is worthwhile to note that microcomb threshold power, expressed as $P_{\mathrm{th}} \sim A_{\mathrm{eff}}/\lambda_{\mathrm{P}} Q^2$ (λ_{P} is pump wavelength and A_{eff} is effective mode area) remains within a close range of powers for all devices (lower panel of Fig. 5.1c). This can be understood to result from a partial compensation of reduced Q factor in the shorter wavelength devices by reduced optical mode area (see plot in Fig. 5.1c). For example, from 1550 nm to 778 nm the mode area is reduced by roughly a factor of 9 and this helps to offset a 3-times decrease in Q factor. The resulting P_{th} increase (5.4 mW at 778 nm versus approximately 2.5 mW at 1550 nm) is therefore caused primarily by the decrease in pump wavelength λ_{P}. In the following sections, additional details on the device design, dispersion, and experimental techniques used to generate these solitons are presented.

5.2 Soliton generation at 1064 nm

Dispersion simulations for TM modes near 1064 nm are presented in Fig. 5.2a and show that TM modes with anomalous dispersion occur in silica resonators having oxide thicknesses less than 3.7 μm. Aside from the thickness control, a secondary method to manipulate dispersion is by changing the wedge angle (see Fig. 5.2a). Both thickness and wedge angle are well controlled in the fabrication process [41]. Precise thickness control is possible because this layer is formed through calibrated oxidation of the silicon wafer. Wedge angles between 30 and 40 degrees were chosen in order to maximize the Q factors [46]. The resonator dispersion is characterized by measuring mode frequencies using a scanning external-cavity diode laser (ECDL) whose frequency is calibrated using a Mach-Zehnder interferometer. As described elsewhere [1, 2], the mode frequencies, ω_μ, are Taylor expanded as $\omega_\mu = \omega_0 + \mu D_1 + \mu^2 D_2/2 + \mu^3 D_3/6$, where ω_0 denotes the pumped mode frequency,

$D_1/2\pi$ is the FSR, and D_2 is proportional to the GVD, β_2 ($D_2 = -cD_1^2\beta_2/n_0$ where c and n_0 are the speed of light and material refractive index). D_3 is a third-order expansion term that is sometimes necessary to adequately fit the spectra (see discussion of 778 nm soliton below). The measured frequency spectrum of the TM1 mode family in a 3.4 μm thick resonator is plotted in Fig. 5.2b. The plot gives the frequency as relative frequency (i.e., $\omega_\mu - \omega_0 - \mu D_1$) to make clear the second-order dispersion contribution. The frequencies are measured using a radio-frequency calibrated Mach-Zehnder interferometer having a FSR of approximately 40 MHz. Also shown is a fitted parabola (red curve) revealing $D_2/2\pi = 3.3$ kHz (positive parabolic curvature indicates anomalous dispersion). Some avoided mode crossings are observed in the spectrum. The dispersion measured in resonators of different thicknesses, marked as solid dots in Fig. 5.2a, is in good agreement with numerical simulations.

The experimental setup for generation of 1064 nm pumped solitons is shown in Fig. 5.2c. The microresonator is pumped by a continuous wave (CW) laser amplified by a ytterbium-doped fiber amplifier (YDFA). The pump light and comb power are coupled to and from the resonator by a tapered fiber [51, 52]. Typical pumping power is around 100 mW. Solitons are generated while scanning the laser from higher frequencies to lower frequencies across the pump mode [1–3]. The pump light is modulated by an electro-optic PM to overcome the thermal transient during soliton generation [2, 3, 53]. A servo control referenced to the soliton power is employed to capture and stabilize the solitons [53]. Shown in Fig. 5.2d are the optical spectra of solitons pumped at 1064 nm. These solitons are generated using the mode family whose dispersion is characterized in Fig. 5.2b. Due to the relatively low dispersion (small D_2), these solitons have a short temporal pulse width. Using the hyperbolic-secant-squared fitting method [2] (see orange and green curves in Fig. 5.2d) a soliton pulse width of 52 fs is estimated for the red spectrum. By increasing the soliton power (blue spectrum), the soliton can be further compressed to 44 fs, which corresponds to a duty cycle of 0.09% at the 20 GHz repetition rate. Finally, the inset in Fig. 5.2d shows the electrical spectrum of the photo-detected soliton pulse stream. Besides confirming the repetition frequency, the spectrum is very stable with excellent signal-to-noise ratio (SNR) greater than 70 dB at 1 kHz resolution bandwidth.

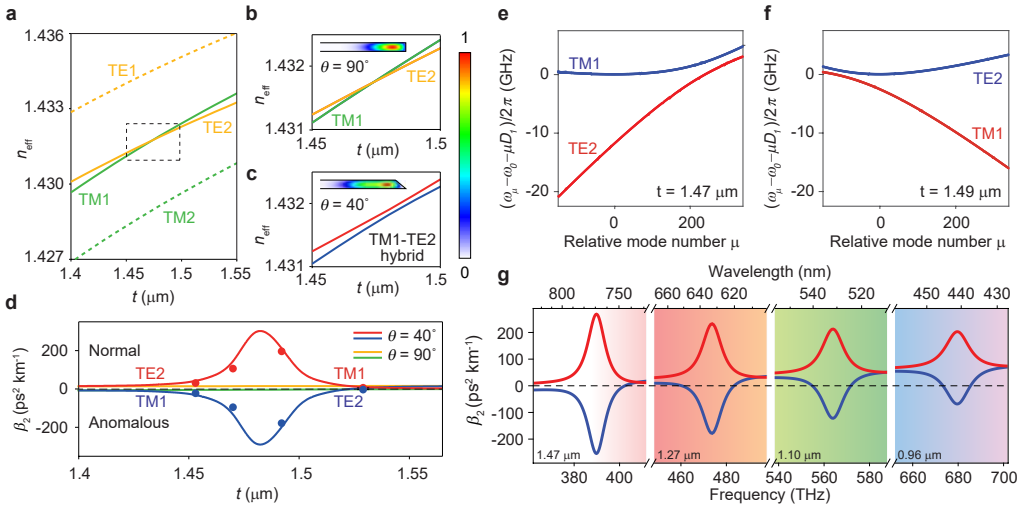

Figure 5.3: Dispersion engineering and solition generation at 778 nm. (a) Calculated effective indices n_{eff} for TE1, TE2, TM1, and TM2 modes at 778 nm plotted versus thickness for a silica resonator with reflection symmetry (i.e. $\theta = 90°$). The TM1 and TE2 modes cross each other without hybridization. (b) Zoom-in of the dashed box in panel (a). (c) As in (b) but for a resonator with $\theta = 40°$. An avoided crossing of TM1 and TE2 occurs due to mode hybridization. Insets of (b) and (c) show simulated mode profiles (normalized electric field) in resonators with $\theta = 90°$ and $\theta = 40°$, respectively. The color bar is shown to the right. (d) Calculated group velocity dispersion (GVD) of the two modes. For the $\theta = 40°$ case, hybridization causes a transition in the dispersion around the thickness 1.48 μm. The points are the measured dispersion values. (e-f) Measured relative mode frequencies of the TM1 and TE2 mode families versus relative mode number μ for devices with $t = 1.47$ μm and $t = 1.49$ μm. (g) Calculated total second-order dispersion versus frequency (below) and wavelength (above) at four different oxide thicknesses (number in lower left of each panel). Red and blue curves correspond to the two hybridized mode families. Anomalous dispersion is negative and shifts progressively to bluer wavelengths as thickness decreases. Background color gives the approximate corresponding color spectrum.

5.3 Soliton generation at 778 nm

As the operational wavelength shifts further towards the visible band, normal material dispersion increases. To generate solitons at 778 nm, an additional dispersion engineering method, TM1-TE2 mode hybridization, is therefore added to supplement the geometrical dispersion control. The green band region in Fig. 5.1b gives the oxide thicknesses and wavelengths where this hybridization is prominent. Polarization mode hybridization is a form of mode coupling induced dispersion control [22, 38, 39, 55]. The coupling of the TM1 and TE2 modes creates two hybrid mode families, one of which features strong anomalous dispersion. This hybridization is

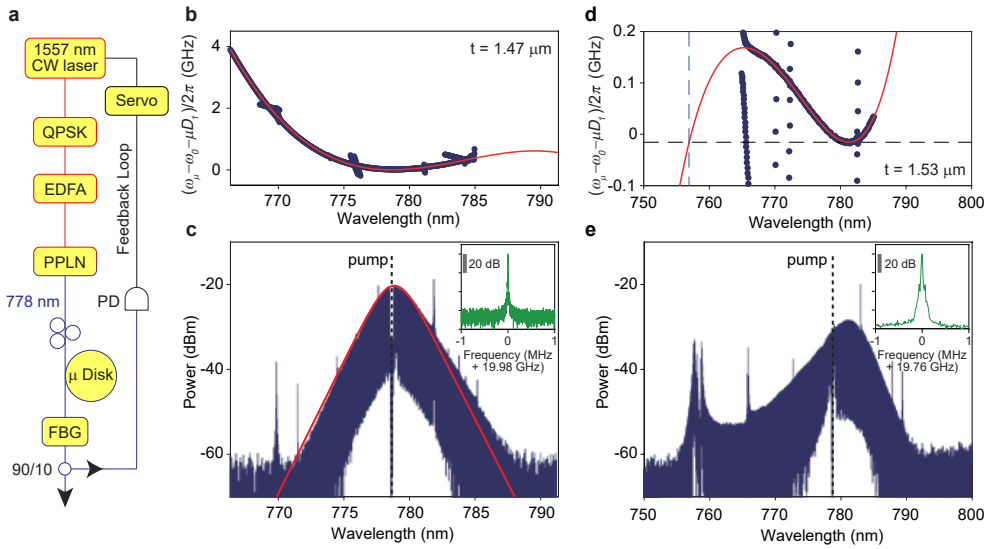

Figure 5.4: Solition generation at 778 nm. (a) Experimental setup for soliton generation. A 1557 nm tunable laser is sent to a quadrature phase-shift keying modulator (QPSK) to utilize frequency-kicking [54] and is then amplified by an erbium-doped fiber amplifier (EDFA). Then, a periodically-poled lithium niobate (PPLN) waveguide frequency-doubles the 1557 nm input into 778 nm output. The 778 nm pump light is coupled to the resonator for soliton generation. A servo loop is used to maintain pump locking [53]. (b) Measured relative mode frequencies of the TM1 mode family versus wavelength for devices with t = 1.47 μm. A number of crossing mode families are visible. The red curve is a numerical fit using $D_2/2\pi$ = 49.8 kHz and $D_3/2\pi$ = 340 Hz. (c) Optical spectrum of a 778 nm soliton generated using the device measured in (b) with pump line indicated by the dashed vertical line. The red curve is a spectral fitting which reveals a pulse width of 145 fs. Most of the spurs in the spectrum correspond to the mode crossings visible in (b). Inset shows the electrical spectrum of the detected soliton pulse stream. The resolution bandwidth is 1 kHz. (d) Measured relative mode frequencies of the TE2 mode family versus wavelength for devices with t = 1.53 μm. The red curve is a fit with $D_2/2\pi$ = 4.70 kHz and $D_3/2\pi$ = −51.6 Hz. (e) Optical spectrum of a soliton generated using the device measured in (d) with pump line indicated as the dashed vertical line. A dispersive wave is visible near 758 nm. Inset shows the electrical spectrum of the detected soliton pulse stream. The resolution bandwidth is 1 kHz.

caused when a degeneracy in the TM1 and TE2 effective indices is lifted by a broken reflection symmetry of the resonator [56]. The wavelength at which the degeneracy occurs is controlled by the oxide thickness and determines the soliton operation wavelength. Finite element method (FEM) simulation in Fig. 5.3a shows that at 778 nm the TM1 and TE2 modes are expected to have the same effective index at the oxide thickness 1.48 μm when the resonator features a reflection symmetry through

a plane that is both parallel to the resonator surface and that lies at the center of the resonator. Such a symmetry exists when the resonator has vertical sidewalls or equivalently a wedge angle $\theta = 90°$ (note: the wet-etch process used to fabricate the wedge resonators does not support a vertical side wall). A zoom-in of the effective index crossing is provided in Fig. 5.3b. In this reflection symmetric case, the two modes cross in the effective-index plot without hybridization. However, in the case of $\theta = 40°$ (Fig. 5.3c), the symmetry is broken and the effective index degeneracy is lifted. The resulting avoided crossing causes a sudden transition in the GVD as shown in Fig. 5.3d, and one of the hybrid modes experiences enhanced anomalous dispersion.

To verify this effect, resonators having four different thicknesses ($\theta = 40°$) were fabricated, and their dispersion was characterized using the same method as for the 1064 nm soliton device. The measured second-order dispersion values are plotted as solid circles in Fig. 5.3d and agree with the calculated values given by the solid curves. Fig. 5.3e and Fig. 5.3f show the measured relative mode frequencies versus mode number of the two modes for devices with $t = 1.47$ μm and $t = 1.49$ μm. As before, upward curvature in the data indicates anomalous dispersion. The dominant polarization component of the hybrid mode is also indicated on both mode-family branches. The polarization mode hybridization produces a strong anomalous dispersion component that can compensate normal material dispersion over the entire band. Moreover, the tuning of this component occurs over a range of larger oxide thicknesses for which it would be impossible to compensate material dispersion using geometrical control alone. To project the application of this hybridization method to yet shorter soliton wavelengths, Fig. 5.3g summarizes calculations of second-order dispersion at a series of oxide thicknesses. At a thickness close to 1 micron, it should be possible to generate solitons at the blue end of the visible spectrum. Moreover, wedge resonators having these oxide film thicknesses have been fabricated during the course of this work. They are mechanically stable with respect to stress-induced buckling [57] at silicon undercut values that are sufficient for high-Q operation.

For soliton generation, the microresonator is pumped at 778 nm by frequency-doubling a continuous wave (CW) ECDL operating at 1557 nm (see Fig. 5.4a). The 1557 nm laser is modulated by a quadrature phase-shift keying (QPSK) modulator for frequency-kicking [54] and then amplified by an erbium-doped fiber amplifier (EDFA). The amplified light is sent into a periodically-poled lithium niobate (PPLN)

device for second-harmonic generation. The frequency-doubled output pump power at 778 nm is coupled to the microresonator using a tapered fiber. The pump power is typically about 135 mW. The soliton capture and locking method was again used to stabilize the solitons [53]. A zoom-in of the TM1 mode spectrum for t = 1.47 μm with a fit that includes third-order dispersion (red curve) is shown in Fig. 5.4b. The impact of higher-order dispersion on dissipative soliton formation has been studied [58, 59]. In the present case, the dispersion curve is well suited for soliton formation. The optical spectrum of a 778 nm pumped soliton formed on this mode family is shown in Fig. 5.4c. It features a temporal pulse width of 145 fs as derived from a sech^2 fit (red curve). The electrical spectrum of the photo-detected soliton stream is provided in the inset in Fig. 5.4c and exhibits high stability.

Fig. 5.4d gives the measured mode spectrum and fitting under conditions of slightly thicker oxide (t = 1.53 μm). In this case, the polarization of the hybrid mode more strongly resembles the TE2 mode family. The overall magnitude of second-order dispersion is also much lower than for the more strongly hybridized soliton in Fig. 5.4b and Fig. 5.4c. The corresponding measured soliton spectrum is shown in Fig. 5.4e and features a dispersive wave near 758 nm. The location of the wave is predicted from the fitting in Fig. 5.4d (see dashed vertical and horizontal lines). The dispersive wave exists in a spectral region of overall normal dispersion, thereby illustrating that dispersion engineering can provide a way to further extend the soliton spectrum towards the visible band. As an aside, the plot in Fig. 5.4d has incorporated a correction to the FSR (D_1) so that the soliton line is given as the horizontal dashed black line. This correction results from the soliton red spectral shift relative to the pump that is apparent in Fig. 5.4e. This shift results from a combination of the Raman self shift [49, 50] and some additional dispersive wave recoil [3]. Finally, the detected beat note of the soliton and dispersive wave is shown as the inset in Fig. 5.4e. It is overall somewhat broader than the beatnote of the other solitons, but is nonetheless quite stable.

5.4 Discussion

We have demonstrated soliton microcombs at 778 nm and 1064 nm using on-chip high-Q silica resonators. Material-limited normal dispersion, which is dominant at these wavelengths, was compensated by using geometrical dispersion through control of the resonator thickness and wedge angle. At the shortest wavelength, 778 nm, mode hybridization was also utilized to achieve anomalous dispersion while maintaining high optical Q. These results are the shortest wavelength soliton

microcombs demonstrated to date. Moreover, the hybridization method can be readily extended so as to produce solitons over the entire visible band. The generated solitons have pulse repetition rates of 20 GHz at both wavelengths. Such detectable and electronics-compatible repetition rate soliton microcombs at short wavelengths have direct applications in the development of miniature optical clocks [9, 22, 23] and potentially optical coherence tomography [24–26]. Also, any application requiring low-power near-visible mode-locked laser sources will benefit. The same dispersion control methods used here should be transferable to silica ridge resonator designs that contain silicon nitride waveguides for on-chip coupling to other photonic devices [47]. Dispersive wave generation at 758 nm was also demonstrated. It could be possible to design devices that use solitons formed at either 778 nm or 1064 nm for dispersive-wave generation into the visible and potentially into the ultra-violet as has been recently demonstrated using straight silica waveguides [42].

References

[1] Herr, T. *et al.* Temporal solitons in optical microresonators. *Nature Photonics* **8**, 145–152 (2014).

[2] Yi, X., Yang, Q.-F., Yang, K. Y., Suh, M.-G. & Vahala, K. Soliton frequency comb at microwave rates in a high-Q silica microresonator. *Optica* **2**, 1078–1085 (2015).

[3] Brasch, V. *et al.* Photonic chip–based optical frequency comb using soliton cherenkov radiation. *Science* **351**, 357–360 (2016).

[4] Wang, P.-H. *et al.* Intracavity characterization of micro-comb generation in the single-soliton regime. *Optics Express* **24**, 10890–10897 (2016).

[5] Joshi, C. *et al.* Thermally controlled comb generation and soliton modelocking in microresonators. *Optics Letters* **41**, 2565–2568 (2016).

[6] Kippenberg, T. J., Holzwarth, R. & Diddams, S. A. Microresonator-based optical frequency combs. *Science* **332**, 555–559 (2011).

[7] Yang, Q.-F., Yi, X., Yang, K. Y. & Vahala, K. Stokes solitons in optical microcavities. *Nature Physics* **13**, 53–57 (2017).

[8] Spencer, D. T. *et al.* Towards an integrated-photonics optical-frequency synthesizer with< 1 hz residual frequency noise. In *Optical Fiber Communication Conference*, M2J–2 (Optical Society of America, 2017).

[9] Frank, I. *et al.* A low-power, chip-scale optical atomic clock with enhanced stability. In *Joint Navigation Conference* (2017).

[10] Suh, M.-G., Yang, Q.-F., Yang, K. Y., Yi, X. & Vahala, K. J. Microresonator soliton dual-comb spectroscopy. *Science* **354**, 600–603 (2016).

[11] Dutt, A. *et al.* On-chip dual-comb source for spectroscopy. *Science Advances* **4**, e1701858 (2018).

[12] Pavlov, N. *et al.* Soliton dual frequency combs in crystalline microresonators. *Optics Letters* **42**, 514–517 (2017).

[13] Papp, S. B. & Diddams, S. A. Spectral and temporal characterization of a fused-quartz-microresonator optical frequency comb. *Physical Review A* **84**, 053833 (2011).

[14] Li, Q. *et al.* Stably accessing octave-spanning microresonator frequency combs in the soliton regime. *Optica* **4**, 193–203 (2017).

[15] Pfeiffer, M. H. *et al.* Octave-spanning dissipative Kerr soliton frequency combs in si_3n_4 microresonators. *Optica* **4**, 684–691 (2017).

[16] Luke, K., Okawachi, Y., Lamont, M. R., Gaeta, A. L. & Lipson, M. Broadband mid-infrared frequency comb generation in a si_3n_4 microresonator. *Optics Letters* **40**, 4823–4826 (2015).

[17] Savchenkov, A. A. *et al.* Generation of Kerr combs centered at 4.5 μm in crystalline microresonators pumped with quantum-cascade lasers. *Optics Letters* **40**, 3468–3471 (2015).

[18] Yu, M., Okawachi, Y., Griffith, A. G., Lipson, M. & Gaeta, A. L. Mode-locked mid-infrared frequency combs in a silicon microresonator. *Optica* **3**, 854–860 (2016).

[19] Hugi, A., Villares, G., Blaser, S., Liu, H. & Faist, J. Mid-infrared frequency comb based on a quantum cascade laser. *Nature* **492**, 229–233 (2012).

[20] Ludlow, A. D., Boyd, M. M., Ye, J., Peik, E. & Schmidt, P. O. Optical atomic clocks. *Reviews of Modern Physics* **87**, 637 (2015).

[21] Nez, F., Biraben, F., Felder, R. & Millerioux, Y. Optical frequency determination of the hyperfine components of the 5s12-5d32 two-photon transitions in rubidium. *Optics Communications* **102**, 432–438 (1993).

[22] Soltani, M., Matsko, A. & Maleki, L. Enabling arbitrary wavelength frequency combs on chip. *Laser & Photonics Reviews* **10**, 158–162 (2016).

[23] Papp, S. B. *et al.* Microresonator frequency comb optical clock. *Optica* **1**, 10–14 (2014).

[24] Lee, S.-J., Widiyatmoko, B., Kourogi, M. & Ohtsu, M. Ultrahigh scanning speed optical coherence tomography using optical frequency comb generators. *Japanese Journal of Applied Physics* **40**, L878 (2001).

[25] Kray, S., Spöler, F., Först, M. & Kurz, H. Dual femtosecond laser multiheterodyne optical coherence tomography. *Optics Letters* **33**, 2092–2094 (2008).

[26] Bajraszewski, T. *et al.* Improved spectral optical coherence tomography using optical frequency comb. *Optics Express* **16**, 4163–4176 (2008).

[27] Saha, K. *et al.* Broadband parametric frequency comb generation with a 1-μm pump source. *Optics Express* **20**, 26935–26941 (2012).

[28] Xue, X. *et al.* Second-harmonic-assisted four-wave mixing in chip-based microresonator frequency comb generation. *Light: Science & Applications* **6**, e16253 (2017).

[29] Jung, H., Stoll, R., Guo, X., Fischer, D. & Tang, H. X. Green, red, and IR frequency comb line generation from single IR pump in AlN microring resonator. *Optica* **1**, 396–399 (2014).

[30] Wang, L. *et al.* Frequency comb generation in the green using silicon nitride microresonators. *Laser & Photonics Reviews* **10**, 631–638 (2016).

[31] Savchenkov, A. *et al.* Kerr combs with selectable central frequency. *Nature Photonics* **5**, 293–296 (2011).

[32] Yang, Y. *et al.* Four-wave mixing parametric oscillation and frequency comb generation at visible wavelengths in a silica microbubble resonator. *Optics Letters* **41**, 5266–5269 (2016).

[33] Hausmann, B., Bulu, I., Venkataraman, V., Deotare, P. & Lončar, M. Diamond nonlinear photonics. *Nature Photonics* **8**, 369–374 (2014).

[34] Xue, X. *et al.* Mode-locked dark pulse Kerr combs in normal-dispersion microresonators. *Nature Photonics* **9**, 594–600 (2015).

[35] Del'Haye, P. *et al.* Octave spanning tunable frequency comb from a microresonator. *Physical Review Letters* **107**, 063901 (2011).

[36] Riemensberger, J. *et al.* Dispersion engineering of thick high-Q silicon nitride ring-resonators via atomic layer deposition. *Optics Express* **20**, 27661–27669 (2012).

[37] Okawachi, Y. *et al.* Bandwidth shaping of microresonator-based frequency combs via dispersion engineering. *Optics Letters* **39**, 3535–3538 (2014).

[38] Liu, Y. *et al.* Investigation of mode coupling in normal-dispersion silicon nitride microresonators for Kerr frequency comb generation. *Optica* **1**, 137–144 (2014).

[39] Ramelow, S. *et al.* Strong polarization mode coupling in microresonators. *Optics Letters* **39**, 5134–5137 (2014).

[40] Grudinin, I. S. & Yu, N. Dispersion engineering of crystalline resonators via microstructuring. *Optica* **2**, 221–224 (2015).

[41] Yang, K. Y. *et al.* Broadband dispersion-engineered microresonator on a chip. *Nature Photonics* **10**, 316–320 (2016).

[42] Oh, D. Y. *et al.* Coherent ultra-violet to near-infrared generation in silica ridge waveguides. *Nature Communications* **8**, 13922 (2017).

[43] Kippenberg, T., Spillane, S. & Vahala, K. Kerr-nonlinearity optical parametric oscillation in an ultrahigh-Q toroid microcavity. *Physical Review Letters* **93**, 083904 (2004).

[44] Moss, D. J., Morandotti, R., Gaeta, A. L. & Lipson, M. New CMOS-compatible platforms based on silicon nitride and Hydex for nonlinear optics. *Nature Photonics* **7**, 597–607 (2013).

[45] Xiong, C. *et al.* Aluminum nitride as a new material for chip-scale optomechanics and nonlinear optics. *New Journal of Physics* **14**, 095014 (2012).

[46] Lee, H. *et al.* Chemically etched ultrahigh-Q wedge-resonator on a silicon chip. *Nature Photonics* **6**, 369–373 (2012).

[47] Yang, K. Y. *et al.* Bridging ultrahigh-Q devices and photonic circuits. *Nature Photonics* **12**, 297–302 (2018).

[48] Milián, C., Gorbach, A. V., Taki, M., Yulin, A. V. & Skryabin, D. V. Solitons and frequency combs in silica microring resonators: Interplay of the Raman and higher-order dispersion effects. *Physical Review A* **92**, 033851 (2015).

[49] Karpov, M. *et al.* Raman self-frequency shift of dissipative Kerr solitons in an optical microresonator. *Physical Review Letters* **116**, 103902 (2016).

[50] Yi, X., Yang, Q.-F., Yang, K. Y. & Vahala, K. Theory and measurement of the soliton self-frequency shift and efficiency in optical microcavities. *Optics Letters* **41**, 3419–3422 (2016).

[51] Cai, M., Painter, O. & Vahala, K. J. Observation of critical coupling in a fiber taper to a silica-microsphere whispering-gallery mode system. *Physical Review Letters* **85**, 74–77 (2000).

[52] Spillane, S., Kippenberg, T., Painter, O. & Vahala, K. Ideality in a fiber-taper-coupled microresonator system for application to cavity quantum electrodynamics. *Physical Review Letters* **91**, 043902 (2003).

[53] Yi, X., Yang, Q.-F., Yang, K. Y. & Vahala, K. Active capture and stabilization of temporal solitons in microresonators. *Optics Letters* **41**, 2037–2040 (2016).

[54] Stone, J. R. *et al.* Initiating Kerr-soliton frequency combs apart from thermal bistability and mode perturbation effects. In *Conference on Lasers and Electro-Optics*, STu4J.4 (2017).

[55] Miller, S. A. *et al.* Tunable frequency combs based on dual microring resonators. *Optics Express* **23**, 21527–21540 (2015).

[56] Dai, D. & Bowers, J. E. Novel concept for ultracompact polarization splitter-rotator based on silicon nanowires. *Optics Express* **19**, 10940–10949 (2011).

[57] Chen, T., Lee, H. & Vahala, K. J. Thermal stress in silica-on-silicon disk resonators. *Applied Physics Letters* **102**, 031113 (2013).

[58] Coen, S. & Erkintalo, M. Universal scaling laws of Kerr frequency combs. *Optics Letters* **38**, 1790–1792 (2013).

[59] Herr, T. *et al.* Mode spectrum and temporal soliton formation in optical microresonators. *Physical Review Letters* **113**, 123901 (2014).

Chapter 6

DIRAC SOLITONS IN OPTICAL MICRORESONATORS

Wang, H. *et al.* Dirac solitons in optical microresonators. *Light: Science & Applications* **9**, 205 (2020).

Soliton mode locking in microresonators [1] provides a pathway for the miniaturization of frequency comb systems [2]. The dissipative solitons [3] formed in the resulting microcombs [4] are coherently pumped [5] and were first observed in optical fiber cavities [6]. In microresonators, such Kerr solitons (KSs) have been realized in a wide range of geometries and material systems [7–14]. Soliton microcomb devices have been tested in diverse system demonstrations, including spectroscopy [15–17], coherent communications [18], range detection [19–21], optical frequency synthesis [22], exoplanet studies [23, 24], and optical clocks [25]. Progress towards integration of the microcomb with pump and other control functions is also being made [26–28]. Modal coupling, wherein distinct mode families experience frequency degeneracy analogous to an energy level crossing [29], is an important feature of soliton formation in microresonators. Such crossings impart structure to the soliton spectral envelope [30] and are responsible for an intriguing range of microcomb phenomena of both scientific and technical importance, including dispersive wave emissions [9, 31], dark soliton formation [32], pump noise isolation [33], improved pumping efficiency [34, 35], and dispersion engineering for near-visible emissions [36, 37].

Here, a new type of soliton in microresonators, termed Dirac solitons (DSs), is shown to result from broadband modal coupling. The name originates from the nonlinear Dirac equations, which govern the dynamics of these solitons and are discussed below. A similar soliton has been theoretically studied in fiber Bragg gratings [38, 39] and later experimentally observed [40]. In these Bragg solitons, forward and backward propagating waves are coupled by a periodic structure, and a Dirac-like model has been applied to understand these systems [41, 42]. As shown recently for broadband coupling in a dimer resonator system [43], the co-existence of coupling and nonlinearity changes the solution behavior qualitatively, and a full understanding requires a non-perturbative approach. We show that broadband nonlinear coupling

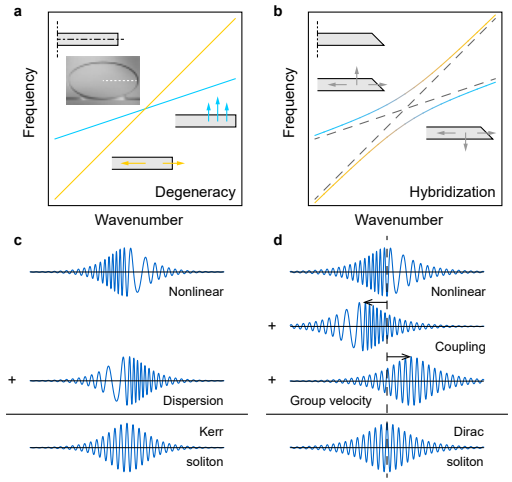

Figure 6.1: Principle of mode hybridization and Dirac solitons. (a) For a symmetric resonator cross section (top-left insets), TE and TM modes within the resonator can become accidentally degenerate at the same wavenumber. The bottom (right) inset depicts the TE (TM) mode electric field directions. (b) For an asymmetric resonator cross section (top-left inset), degeneracy is lifted, and an avoided crossing is created. The left and right insets depict the hybridized mode electric field directions. (c) Schematic of balancing nonlinear and dispersion effects for a KS. (d) Schematic of balancing nonlinear, coupling, and group velocity difference effects for one of the components in a DS.

results in a range of new phenomena in the Dirac soliton system, including polarization twisting along the soliton and asymmetrical soliton comb spectra. A closed-form expression for DSs is derived by solving the Lugiato-Lefever equation (LLE) [5, 44] augmented with mode coupling. Curiously, the requisite coupling conditions have been obtained experimentally in the literature for near-visible [36] and 1-μm-band [37] soliton generation. As shown here, these experiments were performed in a regime where Dirac solitons collapse into conventional Kerr solitons. New data from the 778-nm-band measurement featuring asymmetrical spectra will be presented, showing initial deviation away from conventional Kerr soliton behavior.

6.1 Polarization mode coupling and coupled LLEs

To illustrate the features of DSs, we consider the specific case of a circularly symmetric (whispering-gallery) resonator that has an initial reflection plane of symmetry in the plane of the resonator. The resulting geometry supports transverse-electric (TE) and transverse-magnetic (TM) mode families (Fig. 6.1a) that are symmetrical and anti-symmetrical, respectively, with respect to the reflection plane. A pair of

TE and TM modes can have accidental degeneracy for a particular wavenumber. By breaking the reflection geometry, it becomes possible to lift the degeneracy and create an avoided crossing [36]. In effect, the original modes are strongly coupled, and the eigenmodes of the non-symmetric system are hybrid modes, as shown in Fig. 6.1b. Loosely speaking, the hyperbolic shape of the eigenfrequency creates an anomalous dispersion window that is suitable for soliton generation. However, we note that this dispersion is not associated with a single mode family across the entire avoided crossing. Indeed, the mode composition changes when the wavenumber increases, evolving from TM to TE mode for the upper branch or vice versa for the lower branch.

The standard form of the LLE for one transverse mode family (denoted by mode 1) describes the temporal soliton dynamics in a microresonator [44]:

$$\frac{\partial E_1}{\partial t} = (-i\delta\omega - \frac{\kappa_1}{2})E_1 - i\hat{L}_1 E_1 + ig_{11}|E_1|^2 E_1 + f_1. \tag{6.1}$$

Here, E_1 is the slowly varying amplitude in a co-moving frame normalized to optical energy, defined via $\mathbf{E}_1 = E_1\mathbf{A}_1$, where $\mathbf{E}_1$ is the electric field and $\mathbf{A}_1$ is the normalized vector field distribution. The frequency detuning $\delta\omega = \omega_c - \omega_p$ is the frequency difference between the cavity resonant frequency ω_c and pump frequency ω_p. The Kerr nonlinear coefficient is $g_{11} = n_{(2)}\omega_c c/(n^2 V_{11})$, with speed of light in vacuum c, refractive index n, Kerr nonlinear index $n_{(2)}$, and mode volume $V_{11} = (\int |\mathbf{A}_1|^2 dV)^2/\int |\mathbf{A}_1|^4 dV$. κ_1 is the energy loss rate, and f_1 is the pumping term for mode 1. The linear dispersion operator $\tilde{L}_1$ describes mode dispersion and can be Taylor expanded as $\hat{L}_1 \approx -iD_{1,1}\partial_\theta - D_{2,1}\partial_\theta^2/2$, where θ is the angular coordinate and $D_{1,1}/(2\pi)$ and $D_{2,1}/(2\pi)$ are the free spectral range (FSR) and second-order dispersion (proportional to the group velocity dispersion (GVD)), respectively, for mode 1. In the case of a conservative system ($\kappa_1 = 0$ and $f_1 = 0$) and $D_{1,1} = 0$ (i.e. choosing a co-moving reference frame), the exact soliton solution to Eq. (6.1) is given by:

$$E_1 = \sqrt{\frac{2\delta\omega}{g_{11}}}\operatorname{sech}\left(\sqrt{\frac{2\delta\omega}{D_{2,1}}}\theta\right), \tag{6.2}$$

which is also commonly used as an ansatz to describe a KS [7].

To generalize the above LLE to the coupled pair of TE and TM modes (modes 1 and 2, respectively), we introduce mode coupling as well as cross-phase modulation

into the equations. The following two-mode coupled LLE results:

$$\begin{aligned}\frac{\partial E_1}{\partial t} &= (-i\delta\omega - \frac{\kappa_1}{2})E_1 + ig_c E_2 - \delta D_1 \frac{\partial E_1}{\partial \theta} \\ &\quad + i(g_{11}|E_1|^2 E_1 + g_{12}|E_2|^2 E_1) + f_1, \\ \frac{\partial E_2}{\partial t} &= (-i\delta\omega - \frac{\kappa_2}{2})E_2 + ig_c E_1 + \delta D_1 \frac{\partial E_2}{\partial \theta} \\ &\quad + i(g_{22}|E_2|^2 E_2 + g_{12}|E_1|^2 E_2) + f_2.\end{aligned} \tag{6.3}$$

Here, $g_c > 0$ gives the coupling rate between the two (originally uncoupled) modes, $g_{ij} = n_{(2)}\omega_c c/(n^2 V_{ij})$ $(i, j = 1, 2)$, and the mode volumes V_{11} and V_{22} and cross mode volume V_{12} are defined as $V_{ij} = (\int |\mathbf{A}_i|^2 dV \int |\mathbf{A}_j|^2 dV)/\int |\mathbf{A}_i|^2 |\mathbf{A}_j|^2 dV$. A reference frequency (relative to which all frequencies are measured) is chosen as the degeneracy frequency. In the symmetric co-moving frame (moving at a speed corresponding to $\bar{D}_1 = (D_{1,1} + D_{1,2})/2$), the group velocities of the two resulting hybrid modes become anti-symmetric with $\delta D_1 = |D_{1,1} - D_{1,2}|/2$. Here, second- and higher-order dispersions are ignored, as coupling-induced dispersion of the eigenfrequency is typically one order of magnitude larger than the intrinsic mode dispersion. The nonlinear terms include self-phase and cross-phase modulation. Other four-wave mixing terms that induce nonlinear coupling, such as $|E_1|^2 E_1 E_2^*$ and $E_1^2 (E_2^*)^2$, have been dropped because these are either forbidden by reflection symmetry or strongly suppressed by the phase mismatching of the underlying modes.

The LLE Eq. (6.1) (without loss and pump terms) is known as the nonlinear Schrödinger equation in theoretical physics. Similarly, the coupled LLE Eq. (6.3) presented here are a generalization of the nonlinear Dirac equations. When only cross-phase modulation is considered ($g_{11} = g_{22} = 0$), Eq. (6.3) reduces to the massive Thirring model in quantum field theory [45], which is known to support Dirac solitons [46, 47]. With equal but nonzero self-phase modulations ($g_{11} = g_{22}$), the Bragg soliton solution [38, 39] is recovered, which has been realized in fiber Bragg grating systems [40]. On the other hand, when second-order dispersion is present and is much stronger than the effect induced by linear inter-mode coupling within the band being considered, Eq. (6.3) becomes the vector soliton model in birefringent systems, where soliton solutions are also known [48–50]. We note that the vector soliton relies on both modes having anomalous dispersion, while anomalous dispersion is not required in the DS model.

Before proceeding to solve Eq. (6.3), it is helpful to understand why a DS solution exists in the absence of second-order dispersion. The conventional KS is a delicate

balance of the Kerr nonlinear effect, which creates chirping within a pulse, and the anomalous mode dispersion, which cancels the chirping effect (Fig. 6.1c). In the DS system, the hyperbolic-shaped upper-branch eigenfrequency spectrum (as in Fig. 6.1b) resembles a spectrum with anomalous dispersion. While this "dispersion" plays the same role as conventional dispersion and constitutes the foundation for the generation of the DS, this viewpoint only holds when the pumping (and soliton spectrum) is close to this branch. Indeed, in this case, it will be shown that it reduces to the conventional KS. In general, and as noted in the introduction, dispersion is only locally well defined in this spectrum, as the mode composition of the hybrid mode can change rapidly with respect to the wavenumber. Correspondingly, the dispersion interpretation fails for the general DS, and the coupling effect must be treated non-perturbatively. These rapid composition changes in the hybridized modes redistribute pulse energy in the frequency domain and produce a new contribution to chirping within the pulse, which manifests as phase differences between the two mode components of the pulse. Coupling then makes the two components interfere differently at different positions and leads to both chirping and pulse shifting. These effects are delicately canceled by nonlinear effects and group velocity differences, respectively (Fig. 6.1d), and maintain the DS pulse shape without anomalous dispersion. In the language of field theory, anomalous mode dispersion provides a positive "mass" for the KS field, which then becomes a well-defined non-relativistic field theory. The "mass" of the DS field is the inter-mode coupling, and the mode spectrum corresponds to a relativistic field theory.

6.2 Closed-form soliton solutions

To obtain an analytical solution for the coupled LLE, we consider a conservative system by setting $\kappa_1 = \kappa_2 = 0$ and $f_1 = f_2 = 0$. Eqs. (6.3) can then be solved by finding the invariants associated with the system (see Methods). The closed-form single bright soliton solution for Eqs. (6.3), without periodic boundary conditions, can be obtained as

$$E_{1,2} = \pm\sqrt{\frac{2g_c}{G}}\sqrt{1-\tilde{\xi}^2}\left(\frac{\delta D_1 \pm v}{\delta D_1 \mp v}\right)^{1/4} \times \frac{\left[\cosh\left(2\sqrt{1-\tilde{\xi}^2}\tilde{\theta}\right) - \tilde{\xi}\right]^{\pm\gamma/2}}{\left[\sqrt{1-\tilde{\xi}}\cosh\left(\sqrt{1-\tilde{\xi}^2}\tilde{\theta}\right) \mp i\sqrt{1+\tilde{\xi}}\sinh\left(\sqrt{1-\tilde{\xi}^2}\tilde{\theta}\right)\right]^{1\pm\gamma}} \exp\left(-i\frac{v}{\delta D_1}\tilde{\xi}\tilde{\theta}\right), \tag{6.4}$$

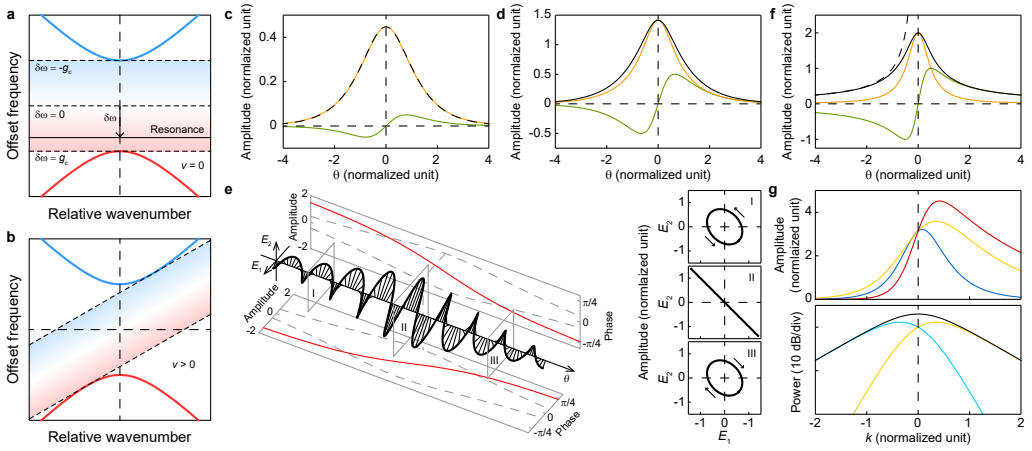

Figure 6.2: Closed-form solution of Dirac solitons in microresonators. (a) Resonance diagram showing two branches of hybrid modes, the allowed range for the soliton resonance line when $v = 0$ (shaded area), and the three special cases of detuning discussed in the text. (b) Same as panel (a) but shows only the range for the soliton resonance line with an arbitrary fixed positive repetition rate shift, v. (c) Real part (orange line) and imaginary part (green line) of the E_1 component of the DS at $\delta\omega = -0.9g_c$. The normalization scheme used for the plot is $g_c = 1$, $\delta D_1 = 1$ and $g_{11} + g_{12} = 1$. The black dashed curve shows the corresponding KS profile for comparison. (d) Real part (orange line), imaginary part (green line), and norm (black line) of the E_1 component of the DS at $\delta\omega = 0$. The normalization scheme used for the plot is the same as that in (c). (e) Polarization twist of DS at $\delta\omega = 0$. The two projections show the slowly varying amplitude envelope (grey dashed lines, left scale) and phase relative to the pulse center (red solid lines, right scale) of the field components. The right insets show the polarization states at the three different spatial slices marked on the plot. The arrow indicates the direction of state change over time. (f) Real part (orange line), imaginary part (green line), and norm (black solid line) of the E_1 component of the DS at $\delta\omega = g_c$. The normalization scheme used for the plot is the same as that in (c). The black dashed line shows the $1/\theta$ asymptote for the envelope. (g) Upper panel: frequency domain amplitudes for the E_1 component of the DS at $\delta\omega = -0.8g_c$ (blue line), $\delta\omega = 0$ (yellow line), and $\delta\omega = 0.8g_c$ (red line), plotted on a linear scale. Lower panel: frequency domain power distribution for the E_1 component (yellow line), E_2 component (cyan line), and combined (black line) DS at $\delta\omega = 0$, plotted on a log scale. The normalization scheme used for the plot is the same as that in (c).

$$G = \frac{\delta D_1 + v}{\delta D_1 - v}\frac{g_{11}}{2} + \frac{\delta D_1 - v}{\delta D_1 + v}\frac{g_{22}}{2} + g_{12}, \quad \gamma = \frac{1}{G}\left(\frac{\delta D_1 + v}{\delta D_1 - v}g_{11} - \frac{\delta D_1 - v}{\delta D_1 + v}g_{22}\right),$$

$$\tilde{\xi} = \frac{\delta D_1}{\sqrt{\delta D_1^2 - v^2}}\frac{\delta\omega}{g_c}, \quad \tilde{\theta} = \frac{g_c}{\sqrt{\delta D_1^2 - v^2}}\theta,$$

where E_1 (E_2) takes the upper (lower) sign in all instances of $\pm$ or $\mp$, v is the repetition rate shift in the symmetric co-moving frame, G is the combined nonlinear coefficient, γ is a phase exponent related to v, $\tilde{\xi}$ is the reduced detuning, and $\tilde{\theta}$ is the reduced coordinate. While dark soliton solutions and bright soliton on background solutions can also be found in the same conservative system (see Supplementary information), we will focus on this bright soliton solution and refer to it as the DS. In the following discussion of DS properties, we take the special case $g_{11} = g_{22}$ (i.e. additional exchange symmetry between the modes) and $v = 0$ (i.e. the pulse is stationary in the symmetric co-moving frame), and the general solution simplifies to

$$E_{1,2} = \sqrt{\frac{2(g_c^2 - \delta\omega^2)}{(g_{11} + g_{12})g_c}} \times \frac{1}{\pm\sqrt{g_c - \delta\omega}\cosh\left(\sqrt{g_c^2 - \delta\omega^2}\theta/\delta D_1\right) - i\sqrt{g_c + \delta\omega}\sinh\left(\sqrt{g_c^2 - \delta\omega^2}\theta/\delta D_1\right)}. \tag{6.5}$$

Figure 6.2a shows the offset frequency for the hybrid modes, defined as $\omega_{\text{off}} = \omega_k - \omega_c - k\bar{D}_1$, where k is the relative wavenumber (the difference between the absolute wavenumber and the wavenumber at the degeneracy point) and ω_k is the mode eigenfrequency at k. Due to the square roots in the special solution (Eq. (6.5)), the soliton detuning range can lie only in the band gap created by the avoided crossing. This phenomenon can be intuitively understood, as none of the comb lines can have the same frequency as the resonator modes, which would otherwise create infinite amplitudes on the modes due to perfect resonance with no loss. Geometrically, the resonance of the soliton can be described by the linear equation $\omega_{\text{DS}} = -\delta\omega + vk$, and the line cannot intersect the two hyperbolas of mode frequencies on the mode spectrum plot. The same also holds for the general solution (Eq. (6.4)) and is depicted in Fig. 6.2b (see Methods). As a result, the soliton cannot have a group velocity faster than the first mode or slower than the second mode. This argument does not apply to dark solitons and bright solitons on a background, where the resonance line always intersects the mode spectrum (see Supplementary information).

To understand the properties of the DS, we consider some special cases of detuning (marked in Fig. 6.2a). The first case is when $\delta\omega$ approaches $-g_c$, where the resonance line is close to the upper branch. By taking appropriate limits, Eq. (6.5)

reduces to:

$$E_{1,2} \approx \pm\sqrt{\frac{2(g_c + \delta\omega)}{g_{11} + g_{12}}}\operatorname{sech}\left(\sqrt{\frac{2g_c(g_c + \delta\omega)}{\delta D_1^2}}\theta\right), \tag{6.6}$$

which is exactly in the form of a conventional KS. A comparison of the exact DS near $\delta\omega = -g_c$ and the limiting KS is shown in Fig. 6.2c. The appearance of the sech-shaped KS here is not a coincidence. The effective nonlinear coefficient for a single component is $g_{11} + g_{12}$ (using $|E_1|^2 = |E_2|^2$), the effective detuning is $g_c + \delta\omega$, and the curvature of the eigenfrequency (the hybrid-mode equivalent of the second-order dispersion) is $\delta D_1^2/g_c$, as derived from coupled mode theory. The reduction of a DS to a KS is straightforward when these quantities are substituted into the KS solution. Thus, if the DS is close to the resonance (which is usually the case when the hybridization coupling g_c is large), the eigenfrequency spectrum is locally equivalent to a single mode in terms of dispersion, and mode composition differences for different wavenumbers can be ignored. Again, this phenomenon applies to the general solution (Eq. (6.4)) as well by explicitly reducing the coupled LLE to a single-mode LLE, and the truncation errors can also be estimated (see Methods).

The second case is when $\delta\omega = 0$, where the resonance line passes through the degeneracy point. In this case, Eq. (6.5) simplifies to:

$$E_{1,2} = \sqrt{\frac{2g_c}{g_{11} + g_{12}}}\frac{1}{\pm\cosh(g_c\theta/\delta D_1) - i\sinh(g_c\theta/\delta D_1)}, \tag{6.7}$$

and begins to deviate from a hyperbolic secant shape (Fig. 6.2d). With this simple analytical solution, it becomes apparent that each component of the wave packet has an overall phase shift when θ goes from $-\infty$ to ∞ ($\pi/2$ in this special case). This phase twist within the pulse contributes to the chirping and shifting of the soliton pulse when they are coupled together, as discussed in the previous section. If pulse polarization is considered, it also twists from the start of the pulse to the end of the pulse (Fig. 6.2e).

The last case we consider is when $\delta\omega$ approaches g_c, where the resonance line moves towards the lower branch and maximum red detuning is approached. As this phenomenon occurs, the exponential tails of the soliton decay at an increasingly slower rate until finally in the limit $\delta\omega \to g_c$ Eq. (6.5) becomes:

$$E_{1,2} \approx \sqrt{\frac{g_c}{g_{11} + g_{12}}}\frac{2}{\pm 1 - 2ig_c\theta/\delta D_1}, \tag{6.8}$$

showing that the solution decays polynomially rather than exponentially when $\theta \to \infty$ (Fig. 6.2f). The resulting polynomial tails can potentially enable long-range interactions of the DS.

We now turn to the frequency domain profile for Eq. (6.5) by the Fourier transform, which can also be expressed in closed form using contour integration:

$$\begin{aligned}&\int_{-\infty}^{\infty} E_{1,2} e^{-ik\theta} d\theta \\ &= \pm \pi \sqrt{\frac{\delta D_1^2}{(g_{11}+g_{12})g_c}} \operatorname{sech} \tilde{k} \exp\left[\pm \frac{\arccos(-\delta\omega/g_c)}{\pi} \tilde{k}\right],\end{aligned} \tag{6.9}$$

where k is the relative wavenumber and $\tilde{k} = \pi\delta D_1 k/(2\sqrt{g_c^2 - \delta\omega^2})$. Apart from the usual sech-shaped envelope, the extra exponential factor causes the spectrum of each component to become asymmetrical around $k = 0$ (Fig. 6.2g). This phenomenon can be explained by different mode compositions on the different sides of the spectrum. We note that the spectrum for the total power is still symmetric, which is consistent with the soliton carrying no total momentum in the symmetric co-moving frame. In the general $v \neq 0$ case, the spectrum for the total power is expected to become asymmetric around the center frequency of the soliton.

6.3 DS with dissipation and repetition rate shifts

In addition to being an exact solution to the conservative system, the solution (Eq. (6.4)) also serves as a DS ansatz for dissipative cases, similar to how a KS can be approximated by a sech-shaped soliton on a background [7]. As an example, here, we study the repetition rate shifts associated with the DS when externally pumped by continuous waves. Accordingly, we do not require $g_{11} = g_{22}$ or $v = 0$ and return to work with the general solution (Eq. (6.4)).

The repetition rates of ideal KSs remain constant when pumped in the same mode while the detuning changes, as formulated by the standard LLE. In contrast, real-world KSs may experience additional nonlinear effects, including dispersive wave backactions [33] or Raman effects [51], which lead to center frequency changes and repetition rate shifts. The mode hybridization process is similar to a mode crossing in dispersive wave generation where two modes are strongly coupled, and therefore, the DS is also expected to experience repetition rate shifts. As the repetition rate shift parameter v is free in the conservative case, we need to find the conditions that determine v when dissipation is present.

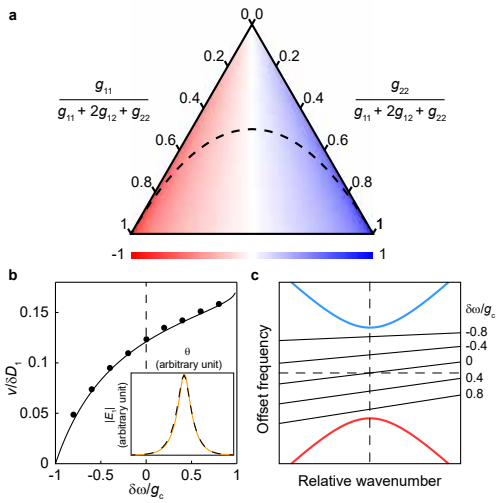

Figure 6.3: Repetition rate shifts in the DS. (a) Ternary plot of the normalized repetition rate shift $v/\delta D_1$ versus the proportions of nonlinear coefficients for $\delta\omega = 0$. $\kappa_1 = \kappa_2$ is assumed. The black dashed curve ($g_{11}g_{22} = g_{12}^2$) separates the parameter space into two regions; cross-phase modulation is dominant in the upper region, while self-phase modulation is dominant in the lower region. (b) Plot of the repetition rate shift versus the detuning. $\kappa_1 = \kappa_2$ is assumed. The parameters are $g_{11} = g_{12}$ and $g_{22} = 2g_{12}$. The black curve is the analytical result, and the dots are simulated data that use a modified split-step Fourier algorithm adapted to the hybrid system. The inset shows a comparison of the simulated (orange solid) and analytical (black dashed) pulse shape of $|E_1|$ at $\delta\omega = 0$. (c) Plot of repetition rate shifts on the mode spectrum. Each line indicates a soliton resonance line with different detunings (negative y-intercept). The parameters are the same as those in (b).

By calculating the momentum integral of the solution, the following criterion is obtained (see Methods):

$$\int \left(\kappa_1 |E_1|^2 \frac{\partial \arg E_1}{\partial \theta} + \kappa_2 |E_2|^2 \frac{\partial \arg E_2}{\partial \theta} \right) d\theta = 0, \tag{6.10}$$

where arg is the argument function and $E_{1,2}$ should be substituted by the DS solution. According to the above criterion, the phase twist of each component is essential in determining the repetition rate shift. Intuitively, this concept can be understood as the following: the pulse cannot carry any net momentum in the reference frame of the pumping, and any additional momentum will be damped out by the dissipation. All the above integrations can be carried out in closed form, leading to an equation in v, which can then be solved as the repetition rate shift.

For a fixed detuning $\delta\omega$, the repetition rate shift v depends on the ratios of the nonlinear coefficients g_{11}, g_{22} and g_{12}. Figure 6.3a plots the special case of $\delta\omega = 0$.

When the nonlinearity on the second mode increases, the optical field will shift to the first mode to compensate, leading to an increased overall speed of the pulse, and vice versa. As the repetition rate shift results from the imbalance of self-phase modulations, increasing the proportion of g_{12} leads to more stability in the repetition rate, while decreasing the proportion of g_{12} allows more tunability. We note that, depending on the nonlinear nature of the resonator material and the mode overlap, the cross-phase modulation may be larger or smaller than the self-phase modulation [52, 53]. Moreover, theoretical DS solutions exist for almost all combinations of nonlinear coefficients.

For the tunability of the DS repetition rate, Fig. 6.3b shows the repetition rate shift as the detuning changes. Near $\delta\omega = -g_c$, the repetition rate shift approaches zero, which is consistent with the local KS equivalence argument in the previous section. With a more red-detuned $\delta\omega$, the effect of imbalance in the nonlinear coefficients is more apparent, leading to repetition rate changes in the corresponding direction. Simulations of the coupled LLE have also been performed and show that both the simulated pulse shape and the repetition rate shifts agree with the analytical solutions (Fig. 6.3b). A graphical representation of the repetition rate shift is also shown in Fig. 6.3c. As an aside, breather-like states [54] have also been observed in the simulations, but the origin of breathing and whether it behaves in the same way as for KS breathers [55–58] is not yet fully understood.

Although the discussion so far has focused on pumping at the central mode, it can be readily generalized to off-center pumping by introducing additional detunings into each of the mode families and shifting the spectral centers of the solutions accordingly. The DS offers a novel and controllable way to tune the repetition rate of the frequency combs. Together with existing nonlinear processes for the resonator, the hybridization-induced shift can be tailored to enhance or suppress the overall repetition rate shift with respect to the pump detuning and may find application in optical frequency division or for pump noise isolation, such as what is performed using quiet point operation [33].

6.4 Implementation of Dirac solitons

The wedge resonator [59] is used to induce mode hybridization and Dirac soliton formation. This resonator offers very high-quality factors [60] and the independent control over key parameters during the fabrication process (Fig. 6.4a). A wedge is entirely characterized by three geometric parameters: the diameter D, which

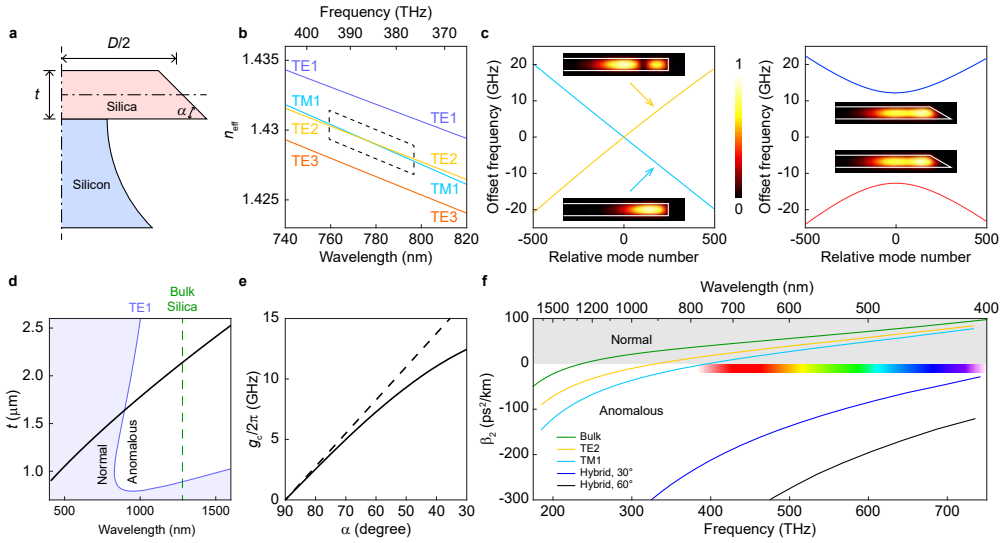

Figure 6.4: Implementation of mode hybridization. (a) Cross-sectional view of a silica wedge resonator on a silicon pillar (not to scale). The parameters that define the wedge geometry are also shown. (b) Plot of n_{eff} for the first four modes (TE1, TM1, TE2, and TE3) versus wavelength (740 to 820 nm) for a wedge resonator. The parameters are $t = 1.47$ μm and $\alpha = 90°$. (c) Left panel: mode spectrum plot for the boxed region in (b). The insets are simulated mode profiles (electric field norm). Right panel: same as left panel but with $\alpha = 30°$. (d) Relationship between t and λ_X (black curve). Additionally, the zero-dispersion wavelength of bulk silica (green dashed line) and the zero-dispersion boundary for the TE1 mode (purple curve) are shown. (e) Coupling g_c versus wedge angle α at $\lambda_X = 778$ nm. The dashed line is the result from perturbation theory (see Methods) and is tangent to the g_c curve at $\alpha = 90°$. (f) Effective GVD β_2 that can be achieved using mode hybridization across the infrared and visible spectra. The parameters are $\alpha = 30°$ and $\alpha = 60°$. The dispersion of bulk silica, TE2, and TM1 modes is also shown for comparison. The color bar shows the approximate color of light in the visible band.

depends on the lithographic pattern; the thickness t, which depends on the oxidation growth time of the silicon wafer; and the wedge angle α, which depends on the adhesion between silica and the photoresist used for patterning. In the following we will fix the resonator diameter as $D = 3.2$ mm (corresponding to a resonator FSR of approximately 20 GHz at approximately 1550 nm), but we note that this can be readily generalized to resonators of other sizes.

For a symmetrical wedge resonator ($\alpha = 90°$), the typical simulated effective refractive index n_{eff} versus wavelength is shown in Fig. 6.4b. At shorter wavelengths, TE1 and TM1 have the highest indices, followed by TE2, TE3, and other high-order modes. Since the electrical fields of the TM modes are along the thickness direction,

their indices are more sensitive to changes in the wavelength scale, and the index of TM1 decreases faster than TE2 as the wavelength increases. Eventually, TM1 and TE2 cross, and their relative positions are interchanged at longer wavelengths. However, for $\alpha = 90°$, no hybridization occurs, as the reflection symmetry prohibits interactions between modes of different parities. On the other hand, if we explicitly break the reflection symmetry of the resonator by decreasing the wedge angle ($\alpha < 90°$), the original modes will see an asymmetric change in the refractive index profile, which causes them to couple. Such couplings lift the degeneracy, leading to avoided crossing. The two cases are compared in Fig. 6.4c, where n_{eff} is first converted to the mode number m via $m = n_{\text{eff}} D\omega_m/(2c)$, where ω_m is the resonance (angular) frequency, and then plotted as offset (angular) frequencies $\omega_{\text{off}} = \omega_m - \omega_{\text{X}} - (m - m_{\text{X}})\bar{D}_1$ versus the relative mode number $m - m_{\text{X}}$, where the subscript X indicates the quantity at the degeneracy point. We note that the relative mode number has the same role as the relative wavenumber k in the theoretical analyses, except that it is restricted to integer values for periodic boundary conditions.

In view of perturbation theory [61], the wedge part of the resonator perturbs the underlying symmetrical structure and induces polarization coupling similar to the coupling obtained in directional couplers [62]. Therefore, we expect that the center wavelength of hybridization λ_{X} is determined by the thickness t, while the wedge angle controls the coupling strength g_{c}. A plot of λ_{X} versus t is shown as the black curve in Fig. 6.4d. As t is the only geometry scale close to optical wavelengths in the system, we expect that λ_{X} will scale linearly with t, which can be visually verified in the plot. This scaling allows for hybridization to occur at short wavelengths where the dispersion of the original modes (for example, the TE1 mode shown in the figure) is typically normal. A plot of g_{c} versus α is shown in Fig. 6.4e. While only a particular wavelength (778 nm) is shown, g_{c} depends on the wavelength very weakly, varying less than 5% from wavelengths of 400 to 1600 nm. The coupling strength scales linearly with α near $\alpha = 90°$, which can also be independently verified by first-order perturbation theory (see Methods), but the coupling effect eventually saturates at shallow wedge angles because mode profiles cannot "squeeze" into the wedge tip as α decreases. The calculated GVD β_2 is shown in Fig. 6.4f, which is related to D_2 via $\beta_2 = -nD_2/(cD_1^2)$. Using suitably designed thicknesses and wedge angles greater than 30°, an anomalous dispersion window can be created all the way down to the blue side of the visible spectrum, where simple geometrical dispersion fails to compensate for normal material dispersion.

6.5 Demonstration of Dirac solitons

Guided by these design principles, devices that target 1550 nm and 778 nm as their hybridization wavelengths were fabricated. The mode spectra are measured for each device using a tuneable laser and a calibrated Mach-Zehnder interferometer [8]. As expected, each of the devices shows a pair of modes with hyperbolic dispersion and large curvatures (Fig. 6.5a to 6.5c). The local D_2 of the anomalous branch can be fit to give $D_2 = 2\pi \times 401$ kHz (1550 nm) (Fig. 6.5b) and $D_2 = 2\pi \times 132$ kHz (778 nm), corresponding to $\beta_2 = -790$ ps^2 km^{-1} and $\beta_2 = -255$ ps^2 km^{-1}, respectively, which are orders of magnitude larger than the mode intrinsic GVD without hybridization.

Finally, to demonstrate the existence of DSs in wedge resonators with hybridized modes, we generated solitons at 778 nm. The detailed experimental setup and measurement procedures can be found elsewhere [36]. The optical spectrum of the soliton is shown in Fig. 6.5. A direct sech^2 fit to the spectrum reveals that the frequency components are highly asymmetric around the spectrum center, which results from the high-order dispersions of the mode and is a typical feature for DSs not being pumped in the crossing center. Indeed, the analytical DS solution derived here provides a good fit to the measured spectrum, further confirming the above theoretical results and their applicability for soliton modeling in microresonators. The detuning relative to the upper branch can be inferred from the fitting and is approximately 90 MHz, which is less than 5% of the band gap. We did not attempt to increase the detuning further due to pump power limitations. As an aside, we believe that a similar 780-nm soliton generated in [36], using the same resonator but under different pumping conditions, can also be classified as a DS.

To further validate the feasibility of DSs in the visible band, we also performed simulations of a DS near 532 nm. A resonator design is shown in Fig. 6.5e together with its simulated mode dispersions, and solitons can be found in the resonator with different pumping positions (Fig. 6.5f). The soliton at the crossing center has a more symmetric spectrum, while the soliton far away from the crossing center has a more skewed spectrum, as expected.

6.6 Discussion

Critical to the generation of solitons in microresonators is the control of mode dispersion. Bright soliton formation requires anomalous dispersion. The curvature of a circular resonator contributes to normal dispersion, shifting the zero-dispersion wavelength towards longer wavelengths as the resonator size decreases. Both this

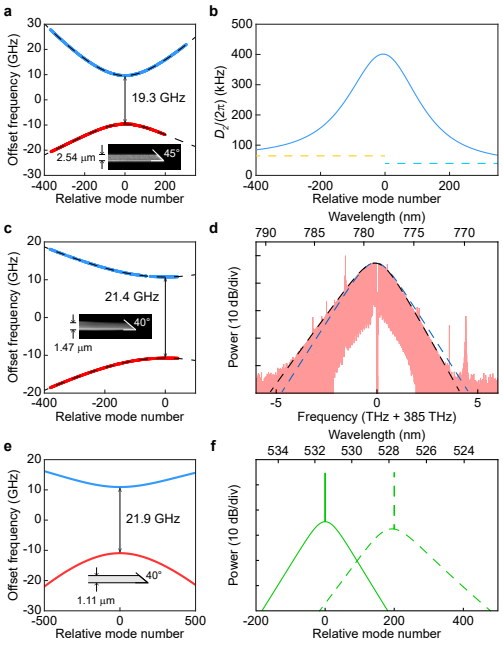

Figure 6.5: Demonstrations of mode hybridization and DS generation. (a) Measured mode spectrum for a wedge resonator with mode hybridization at approximately 1550 nm. The inset shows the geometry of the resonator. (b) Second-order dispersion of the upper branch derived from the fit in (a). The two dashed lines indicate the second-order dispersion of the underlying TE2 (left) and TM1 (right) modes without crossing. (c) Measured mode spectrum for a wedge resonator with mode hybridization at approximately 778 nm. The inset shows the geometry of the resonator. (d) Optical spectrum of a DS at 778 nm generated in a wedge resonator. The blue dashed line shows the sech^2 fit, and the black dashed line shows the DS fit. (e) Simulated mode spectrum for a wedge resonator with mode hybridization at approximately 532 nm. The inset shows the geometry of the resonator. (f) Simulated spectrum of a DS at 532 nm generated in the wedge resonator in (e). The solid line shows the spectrum when the system is pumped at the crossing center, while the dashed line shows the spectrum when the system is pumped 200 modes away from the crossing center. The detuning from the upper branch is fixed at 100 MHz. The mode quality factors are taken as 20×10^6 and are critically coupled. The pump powers are taken as 250 mW, and the polarization is matched to the mode in the upper branch being pumped.

and material dispersion have been managed over a range of wavelengths by using geometrical dispersion introduced through optical waveguide confinement [1]. However, normal dispersion of bulk dielectric materials towards shorter wavelengths makes generating visible solitons in dielectric microresonators extremely difficult, and its offset through waveguide confinement increases unwanted scattering loss,

which degrades the resonator Q factor and increases the pumping power (i.e. comb threshold power varies inversely quadratically with the Q factor [8, 63]). While the use of intra-cavity nonlinear optical processes such as second- or third-harmonic generation and sum-frequency generation can provide a way to bypass normal dispersion for comb generation in the visible band [13, 64–67], managing dispersion by mode coupling provides an alternative approach that can avoid waveguide confinement loss [36, 37, 68–72]. The practical management of dispersion for soliton formation at the edge of the visible band [36, 37] has been possible using Dirac solitons, and they can provide a way to further extend operation well into the visible region.

In summary, we demonstrated the peculiar characteristics of the Dirac soliton in microresonators by solving the corresponding conservative coupled LLE non-perturbatively and using the exact solution as a soliton ansatz for the hybrid system. The balance between nonlinearity and coupling provides a new viewpoint on the soliton and opens up further directions for the study of soliton dynamics. From an experimental viewpoint, generating DSs in resonator platforms is straightforward, but it might be challenging to observe some of their more unusual properties at large detunings. Decreasing the linear coupling (and thus the band gap) is beneficial for pushing the soliton deeper into the band gap, and tuning the pumping polarization to match the soliton decreases the pumping power requirements. We believe the formalism described here can be readily generalized to other systems, including Dirac solitons in waveguides, solitons on ordinary (non-polarization) mode crossings [33], and counter-propagating solitons with moderate coupling [73].

6.7 Methods

Solving the conservative coupled LLE

We copy the conservative coupled LLE here for convenience:

$$\frac{\partial E_1}{\partial t} = -i\delta\omega E_1 + ig_c E_2 - \delta D_1 \frac{\partial E_1}{\partial \theta} + i(g_{11}|E_1|^2 E_1 + g_{12}|E_2|^2 E_1), \tag{6.11}$$

$$\frac{\partial E_2}{\partial t} = -i\delta\omega E_2 + ig_c E_1 + \delta D_1 \frac{\partial E_2}{\partial \theta} + i(g_{22}|E_2|^2 E_2 + g_{12}|E_1|^2 E_2). \tag{6.12}$$

We seek soliton solutions in the form of $E_{1,2}(\theta - vt)$, where v is the repetition rate shift in the symmetric co-moving frame, which reduces the partial differential

equations to ordinary differential equations:

$$(\delta D_1 - v)\partial_\theta E_1 = -i\delta\omega E_1 + ig_c E_2 + i(g_{11}|E_1|^2 E_1 + g_{12}|E_2|^2 E_1), \tag{6.13}$$

$$-(\delta D_1 + v)\partial_\theta E_2 = -i\delta\omega E_2 + ig_c E_1 + i(g_{22}|E_2|^2 E_2 + g_{12}|E_1|^2 E_2). \tag{6.14}$$

Continuous symmetries of the system result in conservation laws [74], which can reduce the dimensions of the system. As the system is conservative, we expect the equations will have a Hamiltonian structure. Indeed, the following quantity is conserved when θ is viewed as an evolution coordinate [46]:

$$\begin{aligned}\bar{H} = &-\delta\omega(|E_1|^2 + |E_2|^2) + g_c(E_1^* E_2 + E_2^* E_1) \\ &+ \frac{1}{2}\left(g_{11}|E_1|^4 + g_{22}|E_2|^4 + 2g_{12}|E_1|^2|E_2|^2\right).\end{aligned} \tag{6.15}$$

The conservation of $\bar{H}$ can be verified by rewriting $(\delta D_1 - v)\partial_\theta E_1 = i\partial_{E_1^*}\bar{H}$ and $-(\delta D_1 + v)\partial_\theta E_2 = i\partial_{E_2^*}\bar{H}$.

Another quantity that is conserved is the photon number flow along the θ-axis:

$$\bar{N} = (\delta D_1 - v)|E_1|^2 - (\delta D_1 + v)|E_2|^2. \tag{6.16}$$

The conservation of $\bar{N}$ can be verified by observing that all the nonlinear terms do not change the individual numbers of particles, while the coupling terms do not change the total number of particles.

For soliton solutions, these two conserved quantities can be determined as $\bar{H} = \bar{N} = 0$ since the solution should vanish exponentially as $\theta \to \infty$ without periodic boundary conditions. This determination leads to the following amplitude-phase parametrization of the solutions:

$$E_1 = \frac{1}{\sqrt{\delta D_1 - v}}\psi \exp(i\chi_1), \quad E_2 = -\frac{1}{\sqrt{\delta D_1 + v}}\psi \exp(i\chi_2), \tag{6.17}$$

$$\psi = \sqrt{\delta D_1 - v}|E_1| = \sqrt{\delta D_1 + v}|E_2|, \quad \chi_{1,2} = \frac{1}{2i}\ln\frac{E_{1,2}}{E_{1,2}^*}, \tag{6.18}$$

which automatically satisfies the $\bar{N}$ conservation (the negative sign is added for later convenience). The $\bar{H}$ conservation reads as:

$$\begin{aligned}0 = &-\frac{2\delta D_1 \delta\omega}{\delta D_1^2 - v^2}\psi^2 - \frac{2g_c}{\sqrt{\delta D_1^2 - v^2}}\psi^2 \cos(\chi_2 - \chi_1) \\ &+ \left[\frac{g_{11}}{2(\delta D_1 - v)^2} + \frac{g_{22}}{2(\delta D_1 + v)^2} + \frac{g_{12}}{\delta D_1^2 - v^2}\right]\psi^4,\end{aligned} \tag{6.19}$$

from which the cosine of the phase difference $\chi_2 - \chi_1$ can be solved as:

$$\cos(\chi_2 - \chi_1) = \frac{G\psi^2 - 2\delta D_1 \delta\omega}{2g_c\sqrt{\delta D_1^2 - v^2}}, \tag{6.20}$$

where for convenience, we defined a combined nonlinear coefficient:

$$G = \frac{\delta D_1 + v}{\delta D_1 - v}\frac{g_{11}}{2} + \frac{\delta D_1 - v}{\delta D_1 + v}\frac{g_{22}}{2} + g_{12}. \tag{6.21}$$

Turning back to the original equations of evolution along θ, we substitute $E_{1,2}$ with the parametrization and split the real and imaginary parts:

$$\frac{\partial\psi^2}{\partial\theta} = \frac{2g_c}{\sqrt{\delta D_1^2 - v^2}}\psi^2 \sin(\chi_2 - \chi_1), \tag{6.22}$$

$$\frac{\partial\chi_1}{\partial\theta} = -\frac{\delta\omega}{\delta D_1 - v} - \frac{g_c}{\sqrt{\delta D_1^2 - v^2}}\cos(\chi_2 - \chi_1) + \left(\frac{g_{11}}{(\delta D_1 - v)^2} + \frac{g_{12}}{\delta D_1^2 - v^2}\right)\psi^2, \tag{6.23}$$

$$-\frac{\partial\chi_2}{\partial\theta} = -\frac{\delta\omega}{\delta D_1 + v} - \frac{g_c}{\sqrt{\delta D_1^2 - v^2}}\cos(\chi_2 - \chi_1) + \left(\frac{g_{22}}{(\delta D_1 + v)^2} + \frac{g_{12}}{\delta D_1^2 - v^2}\right)\psi^2. \tag{6.24}$$

For the differential equation for ψ^2, expressing $\sin(\chi_2 - \chi_1)$ in terms of ψ^2 gives:

$$\frac{\partial\psi^2}{\partial\theta} = \pm\frac{2g_c}{\sqrt{\delta D_1^2 - v^2}}\psi^2\sqrt{1 - \left(\frac{G\psi^2 - 2\delta D_1\delta\omega}{2g_c\sqrt{\delta D_1^2 - v^2}}\right)^2}, \tag{6.25}$$

which can be integrated (with the boundary condition $\psi^2 \to 0$ as $\theta \to \infty$) in terms of elementary functions:

$$\psi^2 = \frac{g_c\sqrt{\delta D_1^2 - v^2}}{G}\frac{2(1 - \tilde{\xi}^2)}{\cosh\left(2\sqrt{1 - \tilde{\xi}^2}\tilde{\theta}\right) - \tilde{\xi}}, \tag{6.26}$$

where the pulse center is chosen as $\theta = 0$ without loss of generality and the reduced detuning and coordinate are defined as:

$$\tilde{\xi} = \frac{\delta D_1}{\sqrt{\delta D_1^2 - v^2}}\frac{\delta\omega}{g_c}, \tag{6.27}$$

$$\tilde{\theta} = \frac{g_c}{\sqrt{\delta D_1^2 - v^2}}\theta, \tag{6.28}$$

As an aside, we also obtain that:

$$\cos(\chi_2 - \chi_1) = \frac{1 - \tilde{\xi}\cosh\left(2\sqrt{1-\tilde{\xi}^2}\tilde{\theta}\right)}{\cosh\left(2\sqrt{1-\tilde{\xi}^2}\tilde{\theta}\right) - \tilde{\xi}}. \tag{6.29}$$

The differential equation for $\chi_{1,2}$ can be integrated after substitution of the above solution for ψ^2 and $\cos(\chi_2 - \chi_1)$. Because the equation has global phase symmetry ($E_{1,2} \to e^{i\phi}E_{1,2}$, where ϕ is an arbitrary constant phase), we can fix $\chi_1(\theta = 0) = 0$, which also forces $\chi_2 = 0$ through $\cos(\chi_1 - \chi_2)|_{\theta=0} = 1$. We obtain:

$$\begin{aligned}\chi_1 = &-\frac{v}{\delta D_1}\tilde{\xi}\tilde{\theta} \\ &+ \left[\frac{1}{G}\left(\frac{\delta D_1 + v}{\delta D_1 - v}g_{11} - \frac{\delta D_1 - v}{\delta D_1 + v}g_{22}\right) + 1\right]\arctan\left[\sqrt{\frac{1+\tilde{\xi}}{1-\tilde{\xi}}}\tanh\left(\sqrt{1-\tilde{\xi}^2}\tilde{\theta}\right)\right],\end{aligned} \tag{6.30}$$

$$\begin{aligned}\chi_2 = &-\frac{v}{\delta D_1}\tilde{\xi}\tilde{\theta} \\ &- \left[\frac{1}{G}\left(\frac{\delta D_1 - v}{\delta D_1 + v}g_{22} - \frac{\delta D_1 + v}{\delta D_1 - v}g_{11}\right) + 1\right]\arctan\left[\sqrt{\frac{1+\tilde{\xi}}{1-\tilde{\xi}}}\tanh\left(\sqrt{1-\tilde{\xi}^2}\tilde{\theta}\right)\right].\end{aligned} \tag{6.31}$$

With these results, the soliton solutions can be expressed as:

$$\begin{aligned}E_1 = &+\sqrt{\frac{2g_c}{G}}\sqrt{1-\tilde{\xi}^2}\left(\frac{\delta D_1 + v}{\delta D_1 - v}\right)^{1/4} \\ &\times \frac{\left[\cosh\left(2\sqrt{1-\tilde{\xi}^2}\tilde{\theta}\right) - \tilde{\xi}\right]^{\gamma/2}}{\left[\sqrt{1-\tilde{\xi}}\cosh\left(\sqrt{1-\tilde{\xi}^2}\tilde{\theta}\right) - i\sqrt{1+\tilde{\xi}}\sinh\left(\sqrt{1-\tilde{\xi}^2}\tilde{\theta}\right)\right]^{1+\gamma}}\exp\left(-i\frac{v}{\delta D_1}\tilde{\xi}\tilde{\theta}\right),\end{aligned} \tag{6.32}$$

$$\begin{aligned}E_2 = &-\sqrt{\frac{2g_c}{G}}\sqrt{1-\tilde{\xi}^2}\left(\frac{\delta D_1 - v}{\delta D_1 + v}\right)^{1/4} \\ &\times \frac{\left[\cosh\left(2\sqrt{1-\tilde{\xi}^2}\tilde{\theta}\right) - \tilde{\xi}\right]^{-\gamma/2}}{\left[\sqrt{1-\tilde{\xi}}\cosh\left(\sqrt{1-\tilde{\xi}^2}\tilde{\theta}\right) + i\sqrt{1+\tilde{\xi}}\sinh\left(\sqrt{1-\tilde{\xi}^2}\tilde{\theta}\right)\right]^{1-\gamma}}\exp\left(-i\frac{v}{\delta D_1}\tilde{\xi}\tilde{\theta}\right),\end{aligned} \tag{6.33}$$

where we introduce the phase exponent:

$$\gamma = \frac{1}{G}\left(\frac{\delta D_1 + v}{\delta D_1 - v} g_{11} - \frac{\delta D_1 - v}{\delta D_1 + v} g_{22}\right). \tag{6.34}$$

Although we have not been very rigorous for multivalued functions encountered in the calculations, direct substitution shows that the $E_{1,2}$ obtained above is indeed a solution to the original conservative LLE when principal branches are used.

Resonance line and the band gap

The general bright soliton solution includes the square root of $1 - \tilde{\xi}^2$, which requires that $|\tilde{\xi}| < 1$. Expanded with resonator parameters, this gives:

$$|\delta\omega| \leq \frac{\sqrt{\delta D_1^2 - v^2}}{\delta D_1} g_c. \tag{6.35}$$

For a fixed v, the inequality gives the detuning range where the solution is well defined. A quick plot of the range (Fig. 6.2b) shows that the boundaries are tangent to the mode spectrum curves. Indeed, using coupled mode theory, the frequencies can be described as:

$$\omega_\pm = \mp\sqrt{\delta D_1^2 k^2 + g_c^2}, \tag{6.36}$$

where ω_+ (ω_-) is the eigenfrequency for the lower symmetric branch (upper anti-symmetric branch) and k is the wavenumber. The tangent lines for the upper branch with slope v satisfy:

$$v = \frac{\partial \omega_-}{\partial k} = \frac{\delta D_1^2 k}{\sqrt{\delta D_1^2 k^2 + g_c^2}}. \tag{6.37}$$

Eliminating k recovers the previous boundaries. Thus, the soliton resonance lines can stay only in the band gap and cannot cut through the band curves.

We note that in dissipative cases, v is not fixed but depends on the pumping details (as discussed in the main text), so this point should not be understood as a limitation on detuning when pumping the soliton. Instead, the detuning range should be determined from the momentum constraints imposed on the soliton at fixed k (the longitudinal mode being pumped).

Reduction of a DS to a KS

Following the above discussions on resonance lines, we focus on the case in which $\tilde{\xi} \to -1^+$, where the resonance line is almost tangent to the upper branch of the

mode spectrum. Taking the limits and expanding the reduced quantities results in

$$E_{1,2} = \pm\sqrt{\frac{2g_c}{G}}\sqrt{1+\tilde{\xi}}\left(\frac{\delta D_1 \pm v}{\delta D_1 \mp v}\right)^{1/4}\mathrm{sech}\left(\sqrt{2(1+\tilde{\xi})}\tilde{\theta}\right)\exp\left(i\frac{v}{\delta D_1}\tilde{\theta}\right), \tag{6.38}$$

$$E_{1,2} = \pm\sqrt{\frac{2\delta D_1(\delta\omega - \delta\omega_{\min})}{G(\delta D_1 \mp v)}}\mathrm{sech}\left(\sqrt{2(\delta\omega - \delta\omega_{\min})}\sqrt{\frac{g_c\delta D_1}{(\delta D_1^2 - v^2)^{3/2}}}\theta\right)$$
$$\times\exp\left(i\frac{g_c v}{\delta D_1\sqrt{\delta D_1^2 - v^2}}\theta\right), \tag{6.39}$$

where $\delta\omega_{\min} = -g_c\sqrt{\delta D_1^2 - v^2}/\delta D_1$. The hyperbolic secant form is now apparent, and to complete the reduction, we explicitly calculate the local quantities of the mode spectrum.

When the resonance line is tangent to the mode spectrum, the wavenumber k can be solved from the previous section:

$$k = \frac{g_c v}{\delta D_1\sqrt{\delta D_1^2 - v^2}}, \tag{6.40}$$

which matches the exponential term. The minimum detuning that can be achieved at this particular m also matches $\delta\omega_{\min}$. The local second-order dispersion is given by:

$$\frac{\partial^2\omega_-}{\partial k^2} = \frac{g_c^2\delta D_1^2}{(\delta D_1^2 k^2 + g_c^2)^{3/2}} = \frac{(\delta D_1^2 - v^2)^{3/2}}{g_c\delta D_1}, \tag{6.41}$$

where we have eliminated k using v and it matches the dispersion term. The mode composition can be found using coupled mode theory and can be found as:

$$\frac{E_1}{E_2} = -\frac{\omega_- + \delta D_1 k}{g_c} = \frac{\sqrt{\delta D_1 + v}}{\sqrt{\delta D_1 - v}}, \tag{6.42}$$

which agrees with the prefactors in $E_{1,2}$ and is also consistent with the conservation of $\bar{N}$. Finally, the effective nonlinear coefficient $G(\delta D_1^2 - v^2)/(2\delta D_1^2)$ can be calculated as a weighted average of the nonlinear coefficients, the weight being the power proportions on each mode derived above. It matches the nonlinear coefficient except for the extra factor $(\delta D_1 \pm v)/(2\delta D_1)$, which is the power ratio of each mode component to the total power and is a result of expressing the solution using components rather than the hybridized field.

To complete the discussion of reducing a DS to a KS, we also present a perturbative approach that is explicitly based on the hybridized field. We begin by defining the following auxiliary fields:

$$\psi_- = \left(\sqrt{\frac{\delta D_1 - v}{2\delta D_1}}E_1 - \sqrt{\frac{\delta D_1 + v}{2\delta D_1}}E_2\right)\exp\left(i\frac{v}{\delta D_1}\tilde{\xi}\tilde{\theta}\right), \tag{6.43}$$

$$\psi_+ = \left(\sqrt{\frac{\delta D_1 - v}{2\delta D_1}}E_1 + \sqrt{\frac{\delta D_1 + v}{2\delta D_1}}E_2\right)\exp\left(i\frac{v}{\delta D_1}\tilde{\xi}\tilde{\theta}\right). \tag{6.44}$$

We note that while the ψ_+ component is the normalized linear eigenstate of the lower branch at the wavenumber corresponding to v, the ψ_- term defined here is, in general, not the eigenstate of the upper branch, and ψ_- and ψ_+ are not orthogonal (although in the special case $\psi_+ = 0$, ψ_- becomes proportional to the true field amplitude). Rewriting the conservative coupled LLE in terms of $\psi_\pm$ results in:

$$\begin{aligned}\frac{\partial\psi_+}{\partial\tilde{\theta}} = -i(1+\tilde{\xi})\psi_- + \frac{i\delta D_1}{2g_c\sqrt{\delta D_1^2 - v^2}}\Bigg[&\frac{\delta D_1 + v}{\delta D_1 - v}\frac{g_{11}}{2}|\psi_+ + \psi_-|^2(\psi_+ + \psi_-) \\ &- g_{12}(\psi_+^2 - \psi_-^2)\psi_-^* \\ &- \frac{\delta D_1 - v}{\delta D_1 + v}\frac{g_{22}}{2}|\psi_+ - \psi_-|^2(\psi_+ - \psi_-)\Bigg],\end{aligned} \tag{6.45}$$

$$\begin{aligned}\frac{\partial\psi_-}{\partial\tilde{\theta}} = i(1-\tilde{\xi})\psi_+ + \frac{i\delta D_1}{2g_c\sqrt{\delta D_1^2 - v^2}}\Bigg[&\frac{\delta D_1 + v}{\delta D_1 - v}\frac{g_{11}}{2}|\psi_+ + \psi_-|^2(\psi_+ + \psi_-) \\ &+ g_{12}(\psi_+^2 - \psi_-^2)\psi_+^* \\ &+ \frac{\delta D_1 - v}{\delta D_1 + v}\frac{g_{22}}{2}|\psi_+ - \psi_-|^2(\psi_+ - \psi_-)\Bigg],\end{aligned} \tag{6.46}$$

where we have substituted $\delta\omega$ and θ with $\tilde{\xi}$ and $\tilde{\theta}$, respectively, for later convenience. Based on the structure of the above equation, we seek the following solution near $\tilde{\xi} \to -1^+$:

$$\psi_- \sim O(1+\tilde{\xi})^{1/2}, \quad \psi_+ \sim O(1+\tilde{\xi}), \tag{6.47}$$

Keeping the lowest-order terms gives:

$$\frac{\partial\psi_+}{\partial\tilde{\theta}} = -i(1+\tilde{\xi})\psi_- + \frac{i\delta D_1}{2g_c\sqrt{\delta D_1^2 - v^2}}G|\psi_-|^2\psi_-, \tag{6.48}$$

$$\frac{\partial\psi_-}{\partial\tilde{\theta}} = 2i\psi_+. \tag{6.49}$$

Combining gives:

$$\frac{1}{2}\frac{\partial^2\psi_-}{\partial\tilde{\theta}^2} - (1+\tilde{\xi})\psi_- + \frac{\delta D_1}{2g_c\sqrt{\delta D_1^2 - v^2}}G|\psi_-|^2\psi_- = 0, \tag{6.50}$$

which is the steady-state single-mode LLE and its solution is the same as the limit of $E_{1,2}$ as derived above.

Repetition rate shifts in the DS

We copy the dissipative coupled LLE here for convenience:

$$\frac{\partial E_1}{\partial t} = -i\delta\omega E_1 + ig_c E_2 - \delta D_1\frac{\partial E_1}{\partial\theta} + i(g_{11}|E_1|^2E_1 + g_{12}|E_2|^2E_1) - \frac{\kappa_1}{2}E_1 + f_1, \tag{6.51}$$

$$\frac{\partial E_2}{\partial t} = -i\delta\omega E_2 + ig_c E_1 + \delta D_1\frac{\partial E_2}{\partial\theta} + i(g_{22}|E_2|^2E_2 + g_{12}|E_1|^2E_2) - \frac{\kappa_2}{2}E_2 + f_2. \tag{6.52}$$

We define the following momentum integral in the hybrid system:

$$P = \int\left[E_1^*\left(-i\frac{\partial E_1}{\partial\theta}\right) + E_2^*\left(-i\frac{\partial E_2}{\partial\theta}\right)\right]d\theta. \tag{6.53}$$

For a steady-state solution, P should be a constant in time. We thus calculate the first derivative of P with respect to t:

$$0 = \frac{\partial P}{\partial t} = \int\left(-i\frac{\partial E_1^*}{\partial t}\frac{\partial E_1}{\partial\theta} + i\frac{\partial E_1}{\partial t}\frac{\partial E_1^*}{\partial\theta} - i\frac{\partial E_2^*}{\partial t}\frac{\partial E_2}{\partial\theta} + i\frac{\partial E_2}{\partial t}\frac{\partial E_2^*}{\partial\theta}\right)d\theta, \tag{6.54}$$

where we have used integration by parts to move the spatial derivatives to the conjugated field. After plugging the equations of motion into the integral, all the conservative terms cancel each other out and the pumping terms vanish by integration by parts. We are left with:

$$\frac{\kappa_1}{2}\int\left(iE_1^*\frac{\partial E_1}{\partial\theta} - iE_1\frac{\partial E_1^*}{\partial\theta}\right)d\theta + \frac{\kappa_2}{2}\int\left(iE_2^*\frac{\partial E_2}{\partial\theta} - iE_2\frac{\partial E_2^*}{\partial\theta}\right)d\theta = 0. \tag{6.55}$$

Rewriting the above equation using arguments gives:

$$\kappa_1\int|E_1|^2\frac{\partial\arg E_1}{\partial\theta}d\theta + \kappa_2\int|E_2|^2\frac{\partial\arg E_2}{\partial\theta}d\theta = 0. \tag{6.56}$$

To proceed further, we take the soliton ansatz as the exact solution of the DS derived earlier. In this case, the integration can be carried out analytically:

$$\begin{aligned}&\int|E_{1,2}|^2\frac{\partial\arg E_{1,2}}{\partial\theta}d\theta\\ =&\frac{2g_c}{G}\sqrt{\frac{\delta D_1\pm v}{\delta D_1\mp v}}\left[\left(-\frac{v}{\delta D_1}+\gamma\pm1\right)(\pi-\arccos\tilde{\xi})\tilde{\xi} + (\gamma\pm1)\sqrt{1-\tilde{\xi}^2}\right].\end{aligned} \tag{6.57}$$

All the quantities can be explicitly expressed in v, and the resulting equation can be solved numerically.

In the special case of $\kappa_1 = \kappa_2$ and $\delta\omega = 0$, we have $\tilde{\xi} = 0$ independent of v, and the criterion is greatly simplified:

$$\frac{v}{\delta D_1} = -\gamma. \tag{6.58}$$

Expanding γ gives a cubic equation in v and is used in the plot of Fig. 6.3a.

First-order perturbation calculation of mode coupling in wedge resonators

Here, using first-order degeneracy perturbation theory and the integral form of the propagation constant, we derive the mode coupling in wedge resonators as an overlap integral of the unperturbed modes.

For a circular waveguide, the angular momentum number (angular propagation constant) of a mode can be expressed as [61]:

$$m = \frac{\omega_0}{2c} \frac{\int \left[n^2 (E_r^* E_r + E_z^* E_z - E_\theta^* E_\theta) + c^2 (B_r^* B_r + B_z^* B_z - B_\theta^* B_\theta) \right] r dr dz}{\int c (E_r B_z^* - E_z B_r^*) dr dz}, \tag{6.59}$$

where ω_0 is the angular frequency of the light and E_r, E_z, E_θ (B_r, B_z, B_θ) are the mode electric field (magnetic flux density) components (the coordinate system in use is shown in Fig. 6.6). The linear propagation of a field (with fixed ω_0) is described by $dE_1/d\theta = imE_1$, where E_1 is the field amplitude at different angular positions. If the mode profile in another waveguide with a slightly different shape is nearly identical to the current waveguide, which is usually true up to the first order of the geometry differences, then the same integral can be used to calculate the propagation constant using the known field profile and the perturbed refractive index profile.

For a pair of nearly degenerate modes, the propagation constant generalizes into a matrix:

$$\frac{d}{d\theta} \begin{pmatrix} E_1 \\ E_2 \end{pmatrix} = i \begin{pmatrix} m_{11} & m_{12} \\ m_{21} & m_{22} \end{pmatrix} \begin{pmatrix} E_1 \\ E_2 \end{pmatrix}, \tag{6.60}$$

$$m_{ij} = \frac{\omega_0}{2c} \times \frac{\int \left[n^2 (E_{r,i}^* E_{r,j} + E_{z,i}^* E_{z,j} - E_{\theta,i}^* E_{\theta,j}) + c^2 (B_{r,i}^* B_{r,j} + B_{z,i}^* B_{z,j} - B_{\theta,i}^* B_{\theta,j}) \right] r dr dz}{\sqrt{\int c (E_{r,i} B_{z,i}^* - E_{z,i} B_{r,i}^*) dr dz} \sqrt{\int c (E_{r,j} B_{z,j}^* - E_{z,j} B_{r,j}^*) dr dz}}. \tag{6.61}$$

The off-diagonal elements m_{12} and m_{21} have an overlap integral structure and are proportional to g_c. Since the modes are orthogonal in the original waveguide, only the changes in refractive index induce coupling:

$$m_{ij} = \frac{\omega_0}{2c} \frac{\int \Delta(n^2)(E^*_{r,i}E_{r,j} + E^*_{z,i}E_{z,j} - E^*_{\theta,i}E_{\theta,j})rdrdz}{\sqrt{\int c(E_{r,i}B^*_{z,i} - E_{z,i}B^*_{r,i})drdz}\sqrt{\int c(E_{r,j}B^*_{z,j} - E_{z,j}B^*_{r,j})drdz}}, \quad (6.62)$$

where $\Delta(n^2)$ is the change in n^2 of the perturbed waveguide compared to the original waveguide.

The introduction of the wedge angle adds a dielectric triangle to the lower-right part and subtracts a dielectric triangle to the upper-right part (Fig. 6.6). As these are the only areas in which the refractive index changes, the overlap integral is effectively restricted to the triangles. If $\pi/2 - \alpha$ is small, we can further replace all the fields by their values on the vertical boundary of the wedge. This replacement results in:

$$m_{12} \approx \frac{\omega_0}{2c}(n^2_M - 1) \frac{-\int_{-t/2}^{t/2}(E^*_{r,1}E_{r,2} + E^*_{z,1}E_{z,2} - E^*_{\theta,1}E_{\theta,2})(D/2)(\pi/2 - \alpha)zdz}{\sqrt{\int c(E_{r,1}B^*_{z,1} - E_{z,1}B^*_{r,1})drdz}\sqrt{\int c(E_{r,2}B^*_{z,2} - E_{z,2}B^*_{r,2})drdz}}, \quad (6.63)$$

where n_M is the dielectric index. The integral can be further reduced by symmetry, using $E_{r,1}(z) = E_{r,1}(-z)$, $E_{z,1}(z) = -E_{z,1}(-z)$ and $E_{\theta,1}(z) = E_{\theta,1}(-z)$ for the TE mode and $E_{r,2}(z) = -E_{r,2}(-z)$, $E_{z,2}(z) = E_{z,2}(-z)$ and $E_{\theta,2}(z) = -E_{\theta,2}(-z)$ for the TM mode. This process reduces the integration limits by half:

$$\begin{aligned} m_{12} \approx{}& \frac{\omega_0}{c}\frac{D}{2}(n^2_M - 1) \\ &\times \frac{-\int_0^{t/2}[(n^2_M + 1)D^*_{r,1}D_{r,2}/(2n^2_M\varepsilon_0^2) + E^*_{z,1}E_{z,2} - E^*_{\theta,1}E_{\theta,2}]_{r=D/2}zdz}{\sqrt{\int c(E_{r,1}B^*_{z,1} - E_{z,1}B^*_{r,1})drdz}\sqrt{\int c(E_{r,2}B^*_{z,2} - E_{z,2}B^*_{r,2})drdz}}(\frac{\pi}{2} - \alpha), \end{aligned} \quad (6.64)$$

where the radial electric field is replaced by the electric displacement field D_r to prevent ambiguities across the dielectric boundary; ε_0 is the vacuum permittivity.

Finally, m_{12} can be converted to g_c in the same way that the effective index is

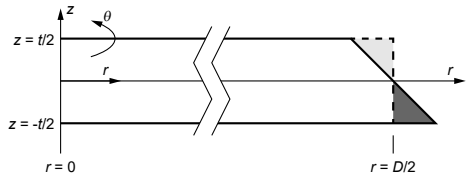

Figure 6.6: Illustration of the perturbation induced by the wedge angle in the wedge resonator. The light grey area indicates the dielectric removed compared to a symmetric resonator, while the dark grey area indicates the dielectric added. The cylindrical coordinates used to describe the resonator are also shown.

converted to the mode spectrum:

$$\begin{aligned} g_{\mathrm{c}} &= \frac{2c}{n_{\mathrm{eff}} D}|m_{12}| \\ &\approx \frac{\omega_0}{n_{\mathrm{eff}}}(n_{\mathrm{M}}^2 - 1) \\ &\times \frac{\left|\int_0^{t/2}[(n_{\mathrm{M}}^2+1)D_{r,1}^* D_{r,2}/(2n_{\mathrm{M}}^2\varepsilon_0^2) + E_{z,1}^* E_{z,2} - E_{\theta,1}^* E_{\theta,2}]_{r=D/2} z dz\right|}{\sqrt{\int c(E_{r,1}B_{z,1}^* - E_{z,1}B_{r,1}^*)drdz}\sqrt{\int c(E_{r,2}B_{z,2}^* - E_{z,2}B_{r,2}^*)drdz}}(\frac{\pi}{2} - \alpha). \end{aligned} \tag{6.65}$$

Given a target hybridization wavelength, modes in symmetric resonators with different thicknesses can be simulated to find the degeneracy point, and the mode coupling in the asymmetric case can be estimated from the above overlap integral without actually simulating the asymmetric resonators. For 780-nm-wavelength silica resonators (using $n_{\mathrm{M}} = 1.454$), the prefactor in g_{c} is 15.78 GHz, or 0.275 GHz per degree angle. This estimate agrees with the full simulation results for wedge resonators for α close to 90° (Fig. 6.4e).

6.8 Supplementary information

The conservative coupled Lugiato-Lefever equations may admit solutions with nonzero backgrounds, where the fields do not vanish when $\theta \to \pm\infty$. In the following we will show the existence of these solutions with the help of a phase space and then derive some special cases of such solutions. We note that, while these solutions are valid for the conservative hybrid-mode system, the addition of loss or other broadband effects may change the solutions in a qualitative way. The background fields also make the solutions difficult to satisfy the periodic conditions

for a resonator. It is not known if soliton solutions with backgrounds can exist in a lossy resonator in the form given below.

The equations for the Dirac soliton reads

$$(\delta D_1 - v)\partial_\theta E_1 = -i\delta\omega E_1 + ig_c E_2 + i(g_{11}|E_1|^2 E_1 + g_{12}|E_2|^2 E_1), \tag{6.66}$$

$$-(\delta D_1 + v)\partial_\theta E_2 = -i\delta\omega E_2 + ig_c E_1 + i(g_{22}|E_2|^2 E_2 + g_{12}|E_1|^2 E_2). \tag{6.67}$$

As in the main text, we introduce the following quantities:

$$\begin{aligned}\bar{H} = &-\delta\omega(|E_1|^2 + |E_2|^2) + g_c(E_1^* E_2 + E_2^* E_1) \\ &+ \frac{1}{2}\left(g_{11}|E_1|^4 + g_{22}|E_2|^4 + 2g_{12}|E_1|^2|E_2|^2\right),\end{aligned} \tag{6.68}$$

$$\bar{N} = (\delta D_1 - v)|E_1|^2 - (\delta D_1 + v)|E_2|^2, \tag{6.69}$$

$$G = \frac{\delta D_1 + v}{\delta D_1 - v}\frac{g_{11}}{2} + \frac{\delta D_1 - v}{\delta D_1 + v}\frac{g_{22}}{2} + g_{12}. \tag{6.70}$$

We begin by obtaining the background (continuous-wave) solutions in the system. To eliminate the global phase dependence, we rewrite the equations of motion using two amplitude variables, $|E_1|$ and $|E_2|$, and a phase difference variable, $\chi \equiv \arg(E_1 E_2^*)$:

$$(\delta D_1 - v)\partial_\theta |E_1| = g_c |E_2| \sin\chi, \tag{6.71}$$

$$(\delta D_1 + v)\partial_\theta |E_2| = g_c |E_1| \sin\chi, \tag{6.72}$$

$$\begin{aligned}\partial_\theta\chi = &-\frac{2\delta D_1 \delta\omega}{\delta D_1^2 - v^2} + \left(\frac{g_c}{\delta D_1 - v}\frac{|E_2|}{|E_1|} + \frac{g_c}{\delta D_1 + v}\frac{|E_1|}{|E_2|}\right)\cos\chi \\ &+ \left(\frac{g_{11}|E_1|^2 + g_{12}|E_2|^2}{\delta D_1 - v} + \frac{g_{22}|E_2|^2 + g_{12}|E_1|^2}{\delta D_1 + v}\right).\end{aligned} \tag{6.73}$$

We denote the background solutions as $|E_1|_0$, $|E_2|_0$, and χ_0, and at these points all three derivatives should vanish. This happens when $|E_1|_0$ and $|E_2|_0$ are both zero, or are both nonzero. As we have solved the first case in the previous section, we will focus on the case where $|E_1|_0 > 0$ and $|E_2|_0 > 0$. In this case $\sin\chi_0 = 0$, and $\chi_0 = 0$ or π, i.e. the two components in the background are completely in-phase or out-of-phase relative to the mode coupling.

A two-dimensional phase space can be constructed from the real and imaginary parts of $E_1 E_2^*$ (Fig. 6.7a). The fields at each θ correspond to a point in the diagram, and follow a contour defined by constant $\bar{H}$ and $\bar{N}$ as θ varies. Background solutions appear in the diagram as fixed points on the real axis. Soliton solutions converge

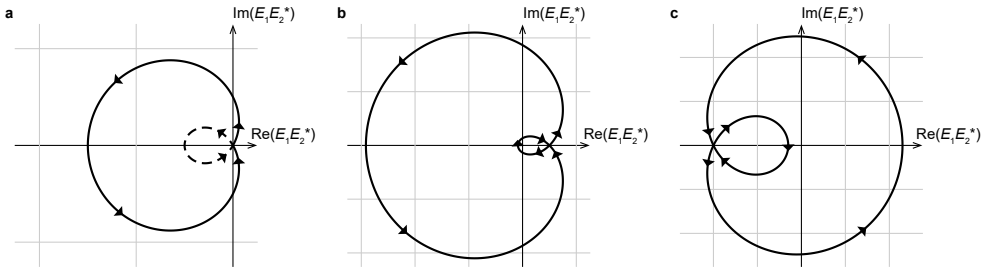

Figure 6.7: Phase space portraits of solitons in the hybrid-mode system. For simplicity we choose $g_{11} = g_{22} = 0$ ($G = g_{12}$) in these plots. The length of one grid unit in the plot represents $2g_c/G$. Arrows indicate the direction of state change when θ increases. (a) The phase space portrait for bright solitons with $v = 0$, $\delta\omega = -g_c/2$ (dashed line) and $v = 0$, $\delta\omega = g_c/2$ (solid line). (b) The phase space portrait for dark soliton and soliton-on-background solutions, with a component-in-phase background. Parameters are $v = 0$, $\delta\omega = 2g_c$ and $|E_1|_0^2 = |E_2|_0^2 = g_c/G$. (c) The phase space portrait for dark soliton and soliton-on-background solutions, with a component-out-of-phase background. Parameters are $v = -5/3\delta D_1$, $\delta\omega = 3g_c$ and $|E_1|_0^2 = |E_2|_0^2 = 4g_c/G$. In both (b) and (c), the saddle point topology is present near the background state.

to the background for $\theta \to \pm\infty$, and therefore are homoclinic orbits connecting the background state to itself (Fig. 6.7b). The shape of the orbit is a limaçon and is described by the following equation:

$$\left[zz^* + \frac{a}{2}(z + z^*)\right]^2 = b^2 zz^*, \quad z = E_1E_2^* - |E_1|_0|E_2|_0\cos\chi_0, \tag{6.74}$$

$$a = \frac{2g_c}{G}(1 + G|E_1|_0|E_2|_0\cos\chi_0/g_c), \tag{6.75}$$

$$b = \frac{g_c}{|G|}\frac{\left|(\delta D_1 - v)|E_1|_0^2 + (\delta D_1 + v)|E_2|_0^2\right|}{|E_1|_0|E_2|_0}\sqrt{\frac{1 + G|E_1|_0|E_2|_0\cos\chi_0/g_c}{\delta D_1^2 - v^2}}. \tag{6.76}$$

According to the properties of a limaçon, when $b < |a|$ the curve has a inner loop, and the background solution becomes a saddle point (Fig. 6.7b). The inner loop and the outer loop each correspond to a soliton solution, where the inner loop resembles the conventional dark soliton and the outer loop is a soliton-on-background solution. If $b > |a|$, the limaçon is a simple closed curve that does not pass through the background state, and the solution becomes a Turing roll. For the critical case $b = |a|$, the limaçon reduces to a cardioid, and only the soliton-on-background solution remains.

The sign of $\cos\chi_0$ determines if the background components are in-phase or out-of-phase, and how the limaçon is oriented. For $|v| < \delta D_1$, the $b \leq |a|$ condition results in $\chi_0 = 0$. In this case the reduced detuning is restricted to $\tilde{\xi} \geq 1$, and the resonance line of the soliton intersects the bottom branch twice. For $|v| > \delta D_1$, $\cos\chi_0$ has the opposite sign to G, which may become negative. No particular restrictions have been found for the detuning $\delta\omega$, and the resonance line of the soliton intersects both branches once. Typical phase spaces of these two cases are illustrated in Figs. 6.7b and 6.7c. The case $|v| = \delta D_1$ does not correspond to solitons, as one of the $|E_{1,2}|$ loses its dynamics, and all solutions are continuous waves.

In the following, we derive the analytical solutions for these solitons. We restrict ourselves to the case $|v| < \delta D_1$ to avoid the discussions on parameters that may change sign, but the technique can be readily generalized. We introduce additional reduced variables to simplify the expressions:

$$\tilde{E}_1 \equiv \sqrt{\delta D_1 - v}E_1, \qquad \tilde{E}_2 \equiv \sqrt{\delta D_1 + v}E_2, \qquad \tilde{G} \equiv \frac{G}{g_c}|E_1|_0|E_2|_0. \tag{6.77}$$

Similarly, $|\tilde{E}_1|_0$ and $|\tilde{E}_2|_0$ are the values of the corresponding variable at the background.

We extend the definition of ψ^2 as

$$\psi^2 \equiv \frac{1}{2}(|\tilde{E}_1|^2 + |\tilde{E}_2|^2) = \frac{1}{2}\left[(\delta D_1 - v)|E_1|^2 + (\delta D_1 + v)|E_2|^2\right], \tag{6.78}$$

which has the same meaning as the ψ^2 in the main text when $\bar{N} = 0$. The value of ψ^2 at the background reads $\psi_0^2 \equiv \left[(\delta D_1 - v)|E_1|_0^2 + (\delta D_1 + v)|E_2|_0^2\right]/2$. The differential equation for ψ^2 reads

$$\partial_\theta\psi^2 = 2|E_1||E_2|\sin\chi \tag{6.79}$$

$$= \frac{\delta D_1}{\sqrt{\delta D_1^2 - v^2}}(\psi^2 - \psi_0^2)\sqrt{4(1+\tilde{G}) - \frac{[\tilde{G}(\psi^2 - \psi_0^2) - 2\psi_0^2]^2}{|\tilde{E}_1|_0^2|\tilde{E}_2|_0^2}}, \tag{6.80}$$

where we have used the conservation of $\bar{H}$ and $\bar{N}$ and substituted their values at the background. Integration gives

$$\psi^2 = \psi_0^2 + \frac{2\left[\psi_0^4 - (1+\tilde{G})|\tilde{E}_1|_0^2|\tilde{E}_2|_0^2\right]}{\tilde{G}\left[\psi_0^2 + \sigma\sqrt{1+\tilde{G}}|\tilde{E}_1|_0|\tilde{E}_2|_0\cosh(\beta\tilde{\theta})\right]}, \tag{6.81}$$

$$\beta \equiv \sqrt{4\tilde{G} - \frac{\bar{N}^2}{|\tilde{E}_1|_0^2|\tilde{E}_2|_0^2}}, \quad \tilde{\theta} = \frac{g_c}{\sqrt{\delta D_1^2 - v^2}}\theta. \tag{6.82}$$

The saddle point criterion from the limaçon ensures that β is a real number. The σ before the cosh function is determined by how the square root is taken. For dark-soliton-like solutions (inner loop of the limaçon) we take $\sigma = 1$, and for soliton-on-background solutions (outer loop of the limaçon) we take $\sigma = -1$.

The rest of the solution process is identical to the bright soliton case, which proceeds by finding the equation for $\arg E_{1,2}$ followed by integration. Combining all results above, the field solution can be written as

$$E_1 = \left[|E_1|_0^2 - \frac{|\tilde{E}_1|_0|\tilde{E}_2|_0\beta^2\cosh(\beta\tilde{\theta}) + i(\bar{N} + 2\tilde{G}|\tilde{E}_1|_0^2)\beta\sinh(\beta\tilde{\theta})}{(\delta D_1 - v)\tilde{G}\left[2\sigma\sqrt{1+\tilde{G}} + 2\psi_0^2/(|\tilde{E}_1|_0|\tilde{E}_2|_0)\cosh(\beta\tilde{\theta}) + i\beta\sinh(\beta\tilde{\theta})\right]}\right]^{1/2}$$
$$\times\left[\frac{2\sigma\sqrt{1+\tilde{G}} + 2\psi_0^2/(|\tilde{E}_1|_0|\tilde{E}_2|_0)\cosh(\beta\tilde{\theta}) - i\beta\sinh(\beta\tilde{\theta})}{2\sigma\sqrt{1+\tilde{G}}\cosh(\beta\tilde{\theta}) + 2\psi_0^2/(|\tilde{E}_1|_0|\tilde{E}_2|_0)}\right]^{\gamma/2}\exp(ik_0\theta), \tag{6.83}$$

$$E_2 = \pm\left[|E_2|_0^2 - \frac{|\tilde{E}_1|_0|\tilde{E}_2|_0\beta^2\cosh(\beta\tilde{\theta}) + i(\bar{N} + 2\tilde{G}|\tilde{E}_2|_0^2)\beta\sinh(\beta\tilde{\theta})}{(\delta D_1 + v)\tilde{G}\left[2\sigma\sqrt{1+\tilde{G}} + 2\psi_0^2/(|\tilde{E}_1|_0|\tilde{E}_2|_0)\cosh(\beta\tilde{\theta}) + i\beta\sinh(\beta\tilde{\theta})\right]}\right]^{1/2}$$
$$\times\left[\frac{2\sigma\sqrt{1+\tilde{G}} + 2\psi_0^2/(|\tilde{E}_1|_0|\tilde{E}_2|_0)\cosh(\beta\tilde{\theta}) - i\beta\sinh(\beta\tilde{\theta})}{2\sigma\sqrt{1+\tilde{G}}\cosh(\beta\tilde{\theta}) + 2\psi_0^2/(|\tilde{E}_1|_0|\tilde{E}_2|_0)}\right]^{\gamma/2}\exp(ik_0\theta), \tag{6.84}$$

$$k_0 \equiv \frac{1}{2\delta D_1}\left(g_c\frac{|E_2|_0^2 - |E_1|_0^2}{|E_1|_0|E_2|_0} + (g_{11} - g_{12})|E_1|_0^2 - (g_{22} - g_{12})|E_2|_0^2\right), \tag{6.85}$$

where the sign of E_2 is negative if the limaçon loop encloses the origin, or positive if the origin is not enclosed. $|E_1|_0$ and $|E_2|_0$ are the background field amplitudes, i.e. the positive solutions to the following equation:

$$\begin{aligned}2\delta D_1\delta\omega =& g_c(\delta D_1 + v)\frac{|E_2|_0}{|E_1|_0} + g_c(\delta D_1 - v)\frac{|E_1|_0}{|E_2|_0}\\ &+ (g_{11}|E_1|_0^2 + g_{12}|E_2|_0^2)(\delta D_1 + v) + (g_{22}|E_2|_0^2 + g_{12}|E_1|_0^2)(\delta D_1 - v).\end{aligned} \tag{6.86}$$

A special case can be obtained by setting $g_{11} = g_{22}$, $v = 0$, and $|E_1|_0 = |E_2|_0 = \sqrt{(\delta\omega - g_c)/(g_{11} + g_{12})}$. In this case

$$E_1 = -E_2^* = \sqrt{\frac{\delta\omega - g_c}{g_{11} + g_{12}}}\frac{\sqrt{\delta\omega - g_c} - i\sigma\sqrt{\delta\omega}\sinh(2\sqrt{(\delta\omega - g_c)g_c}\theta/\delta D_1)}{\sqrt{\delta\omega}\cosh(2\sqrt{(\delta\omega - g_c)g_c}\theta/\delta D_1) + \sigma}. \tag{6.87}$$

References

[1] Kippenberg, T. J., Gaeta, A. L., Lipson, M. & Gorodetsky, M. L. Dissipative Kerr solitons in optical microresonators. *Science* **361**, eaan8083 (2018).

[2] Diddams, S. A., Vahala, K. J. & Udem, T. Optical frequency combs: Coherently uniting the electromagnetic spectrum. *Science* **369**, eaay3676 (2020).

[3] Akhmediev, N. & Ankiewicz, A. *Dissipative solitons: from optics to biology and medicine* (Berlin: Springer, 2008).

[4] Kippenberg, T. J., Holzwarth, R. & Diddams, S. Microresonator-based optical frequency combs. *Science* **332**, 555–559 (2011).

[5] Wabnitz, S. Suppression of interactions in a phase-locked soliton optical memory. *Optics Letters* **18**, 601–603 (1993).

[6] Leo, F. *et al.* Temporal cavity solitons in one-dimensional Kerr media as bits in an all-optical buffer. *Nature Photonics* **4**, 471–476 (2010).

[7] Herr, T. *et al.* Temporal solitons in optical microresonators. *Nature Photonics* **8**, 145–152 (2014).

[8] Yi, X., Yang, Q.-F., Yang, K. Y., Suh, M.-G. & Vahala, K. Soliton frequency comb at microwave rates in a high-Q silica microresonator. *Optica* **2**, 1078–1085 (2015).

[9] Brasch, V. *et al.* Photonic chip–based optical frequency comb using soliton Cherenkov radiation. *Science* **351**, 357–360 (2016).

[10] Joshi, C. *et al.* Thermally controlled comb generation and soliton modelocking in microresonators. *Optics Letters* **41**, 2565–2568 (2016).

[11] Wang, P.-H. *et al.* Intracavity characterization of micro-comb generation in the single-soliton regime. *Optics Express* **24**, 10890–10897 (2016).

[12] Gong, Z. *et al.* High-fidelity cavity soliton generation in crystalline AlN micro-ring resonators. *Optics Letters* **43**, 4366–4369 (2018).

[13] He, Y. *et al.* Self-starting bi-chromatic $LiNbO_3$ soliton microcomb. *Optica* **6**, 1138–1144 (2019).

[14] Moille, G. *et al.* Dissipative Kerr solitons in a III-V microresonator. *Laser & Photonics Reviews* **14**, 2000022 (2020).

[15] Suh, M.-G., Yang, Q.-F., Yang, K. Y., Yi, X. & Vahala, K. J. Microresonator soliton dual-comb spectroscopy. *Science* **354**, 600–603 (2016).

[16] Yang, Q.-F. *et al.* Vernier spectrometer using counterpropagating soliton microcombs. *Science* **363**, 965–968 (2019).

[17] Bao, C. *et al.* Interleaved difference-frequency generation for microcomb spectral densification in the mid-infrared. *Optica* **7**, 309–315 (2020).

[18] Marin-Palomo, P. *et al.* Microresonator-based solitons for massively parallel coherent optical communications. *Nature* **546**, 274–279 (2017).

[19] Suh, M.-G. & Vahala, K. J. Soliton microcomb range measurement. *Science* **359**, 884–887 (2018).

[20] Trocha, P. *et al.* Ultrafast optical ranging using microresonator soliton frequency combs. *Science* **359**, 887–891 (2018).

[21] Riemensberger, J. *et al.* Massively parallel coherent laser ranging using a soliton microcomb. *Nature* **581**, 164–170 (2020).

[22] Spencer, D. T. *et al.* An optical-frequency synthesizer using integrated photonics. *Nature* **557**, 81–85 (2018).

[23] Suh, M.-G. *et al.* Searching for exoplanets using a microresonator astrocomb. *Nature Photonics* **13**, 25–30 (2019).

[24] Obrzud, E. *et al.* A microphotonic astrocomb. *Nature Photonics* **13**, 31–35 (2019).

[25] Newman, Z. L. *et al.* Architecture for the photonic integration of an optical atomic clock. *Optica* **6**, 680–685 (2019).

[26] Stern, B., Ji, X., Okawachi, Y., Gaeta, A. L. & Lipson, M. Battery-operated integrated frequency comb generator. *Nature* **562**, 401–405 (2018).

[27] Shen, B. *et al.* Integrated turnkey soliton microcombs. *Nature* **582**, 365–369 (2020).

[28] Liu, J. *et al.* Monolithic piezoelectric control of soliton microcombs. *Nature* **583**, 385–390 (2020).

[29] Carmon, T. *et al.* Static envelope patterns in composite resonances generated by level crossing in optical toroidal microcavities. *Physical Review Letters* **100**, 103905 (2008).

[30] Herr, T. *et al.* Mode spectrum and temporal soliton formation in optical microresonators. *Physical Review Letters* **113**, 123901 (2014).

[31] Yang, Q.-F., Yi, X., Yang, K. Y. & Vahala, K. Spatial-mode-interaction-induced dispersive-waves and their active tuning in microresonators. *Optica* **3**, 1132–1135 (2016).

[32] Xue, X. *et al.* Mode-locked dark pulse Kerr combs in normal-dispersion microresonators. *Nature Photonics* **9**, 594–600 (2015).

[33] Yi, X. *et al.* Single-mode dispersive waves and soliton microcomb dynamics. *Nature Communications* **8**, 14869 (2017).

[34] Xue, X., Zheng, X. & Zhou, B. Super-efficient temporal solitons in mutually coupled optical cavities. *Nature Photonics* **13**, 616–622 (2019).

[35] Kim, B. Y. *et al.* Turn-key, high-efficiency Kerr comb source. *Optics Letters* **44**, 4475–4478 (2019).

[36] Lee, S. H. *et al.* Towards visible soliton microcomb generation. *Nature Communications* **8**, 1295 (2017).

[37] Karpov, M., Pfeiffer, M. H., Liu, J., Lukashchuk, A. & Kippenberg, T. J. Photonic chip-based soliton frequency combs covering the biological imaging window. *Nature Communications* **9**, 1146 (2018).

[38] Christodoulides, D. N. & Joseph, R. I. Slow Bragg solitons in nonlinear periodic structures. *Physical Review Letters* **62**, 1746–1749 (1989).

[39] Aceves, A. B. & Wabnitz, S. Self-induced transparency solitons in nonlinear refractive periodic media. *Physics Letters A* **141**, 37–42 (1989).

[40] Eggleton, B. J., De Sterke, C. M. & Slusher, R. E. Bragg solitons in the nonlinear Schrödinger limit: experiment and theory. *Journal of the Optical Society of America B* **16**, 587–599 (1999).

[41] Wabnitz, S. Forward mode coupling in periodic nonlinear-optical fibers: modal dispersion cancellation and resonance solitons. *Optics Letters* **14**, 1071–1073 (1989).

[42] Christodoulides, D. N. & Joseph, R. I. Nonlinear wave propagation in optically active and birefringent media. *Optics Letters* **16**, 446–448 (1991).

[43] Tikan, A. *et al.* Emergent nonlinear phenomena in a driven dissipative photonic dimer. *Nature Physics* (2021).

[44] Lugiato, L. A. & Lefever, R. Spatial dissipative structures in passive optical systems. *Physical Review Letters* **58**, 2209–2211 (1987).

[45] Thirring, W. E. A soluble relativistic field theory. *Annals of Physics* **3**, 91–112 (1958).

[46] Kuznetsov, E. A. & Mikhailov, A. V. On the complete integrability of the two-dimensional classical thirring model. *Theoretical and Mathematical Physics* **30**, 193–200 (1977).

[47] Pelinovsky, D. E. & Shimabukuro, Y. Orbital stability of Dirac solitons. *Letters in Mathematical Physics* **104**, 21–41 (2014).

[48] Christodoulides, D. N. & Joseph, R. Vector solitons in birefringent nonlinear dispersive media. *Optics Letters* **13**, 53–55 (1988).

[49] Cundiff, S. *et al.* Observation of polarization-locked vector solitons in an optical fiber. *Physical Review Letters* **82**, 3988–3991 (1999).

[50] Tang, D., Zhang, H., Zhao, L. & Wu, X. Observation of high-order polarization-locked vector solitons in a fiber laser. *Physical Review Letters* **101**, 153904 (2008).

[51] Yi, X., Yang, Q.-F., Yang, K. Y. & Vahala, K. Theory and measurement of the soliton self-frequency shift and efficiency in optical microcavities. *Optics Letters* **41**, 3419–3422 (2016).

[52] Boyd, R. W. *Nonlinear optics* (San Diego: Academic Press, 2008).

[53] Hill, L., Oppo, G.-L., Woodley, M. T. & Del'Haye, P. Effects of self-and cross-phase modulation on the spontaneous symmetry breaking of light in ring resonators. *Physical Review A* **101**, 013823 (2020).

[54] Akhmediev, N. N. & Ankiewicz, A. *Solitons: nonlinear pulses and beams* (London: Chapman & Hall, 1997).

[55] Bao, C. *et al.* Observation of Fermi-Pasta-Ulam recurrence induced by breather solitons in an optical microresonator. *Physical Review Letters* **117**, 163901 (2016).

[56] Yu, M. *et al.* Breather soliton dynamics in microresonators. *Nature Communications* **8**, 14569 (2017).

[57] Lucas, E., Karpov, M., Guo, H., Gorodetsky, M. & Kippenberg, T. Breathing dissipative solitons in optical microresonators. *Nature Communications* **8**, 736 (2017).

[58] Guo, H. *et al.* Intermode breather solitons in optical microresonators. *Physical Review X* **7**, 041055 (2017).

[59] Lee, H. *et al.* Chemically etched ultrahigh-Q wedge-resonator on a silicon chip. *Nature Photonics* **6**, 369–373 (2012).

[60] Wu, L. *et al.* Greater than one billion Q factor for on-chip microresonators. *Optics Letters* **45**, 5129–5131 (2020).

[61] Snyder, A. W. & Love, J. D. *Optical waveguide theory* (New York: Springer, 1983).

[62] Dai, D. & Bowers, J. E. Novel concept for ultracompact polarization splitter-rotator based on silicon nanowires. *Optics Express* **19**, 10940–10949 (2011).

[63] Li, J., Lee, H., Chen, T. & Vahala, K. J. Low-pump-power, low-phase-noise, and microwave to millimeter-wave repetition rate operation in microcombs. *Physical Review Letters* **109**, 233901 (2012).

[64] Miller, S. *et al.* On-chip frequency comb generation at visible wavelengths via simultaneous second-and third-order optical nonlinearities. *Optics Express* **22**, 26517–26525 (2014).

[65] Wang, L. *et al.* Frequency comb generation in the green using silicon nitride microresonators. *Laser & Photonics Reviews* **10**, 631–638 (2016).

[66] Xue, X. *et al.* Second-harmonic-assisted four-wave mixing in chip-based microresonator frequency comb generation. *Light: Science & Applications* **6**, e16253 (2017).

[67] Chen, H.-J. *et al.* Chaos-assisted two-octave-spanning microcombs. *Nature Communications* **11**, 2336 (2020).

[68] Ramelow, S. *et al.* Strong polarization mode coupling in microresonators. *Optics Letters* **39**, 5134–5137 (2014).

[69] Liu, Y. *et al.* Investigation of mode coupling in normal-dispersion silicon nitride microresonators for Kerr frequency comb generation. *Optica* **1**, 137–144 (2014).

[70] Miller, S. A. *et al.* Tunable frequency combs based on dual microring resonators. *Optics Express* **23**, 21527–21540 (2015).

[71] Soltani, M., Matsko, A. & Maleki, L. Enabling arbitrary wavelength frequency combs on chip. *Laser & Photonics Reviews* **10**, 158–162 (2016).

[72] D'Aguanno, G. & Menyuk, C. R. Coupled Lugiato-Lefever equation for nonlinear frequency comb generation at an avoided crossing of a microresonator. *The European Physical Journal D* **71**, 74 (2017).

[73] Yang, Q.-F., Yi, X., Yang, K. & Vahala, K. Counter-propagating solitons in microresonators. *Nature Photonics* **11**, 560–564 (2017).

[74] Landau, L. D. & Lifshitz, E. M. *Mechanics*, vol. 1 (Oxford: Butterworth-Heinemann, 1976).

Chapter 7

VERNIER SPECTROMETER USING COUNTERPROPAGATING SOLITON MICROCOMBS

Yang, Q.-F. *et al.* Vernier spectrometer using counterpropagating soliton microcombs. *Science* **363**, 965–968 (2019).

Frequency-agile lasers are ubiquitous in sensing, spectroscopy, and optical communications [1–3], and measurement of their optical frequency for tuning and control is traditionally performed by grating and interferometer-based spectrometers, but more recently these measurements can make use of optical frequency combs [4]. Frequency combs provide a remarkably stable measurement grid against which optical signal frequencies can be determined subject to the ambiguity introduced by the equally spaced comb lines. The ambiguity is resolved for continuously frequency swept signals by counting comb teeth [5] relative to a known comb tooth; and this method has enabled measurement of remarkably high chirp rates [6]. However, many signal sources will experience intentional or unintentional frequency jumps. Here, the ambiguity can be resolved using a second frequency comb that has a different comb line spacing so as to provide a frequency Vernier scale for comparison with the first comb [7–9]. This Vernier concept is also used in dual comb spectroscopy [10, 11], but in measuring active signals, the method can be enhanced to more directly (and hence quickly) identify signal frequencies through a signal correlation technique [9]. Moreover, continuous as opposed to discretely sampled frequencies are measured in the active approach. The power of the Vernier-based method relies upon mapping of optical comb frequencies into a radio-frequency grid of frequencies, the precision of which is set by the relative line-by-line frequency stability of the two frequency combs. This stability can be guaranteed by self-referencing each comb using a common high-stability radio-frequency source or through optical locking of each comb to reference lasers whose relative stability is ensured by mutual locking to a common optical cavity.

We demonstrate a broad-band, high-resolution Vernier microresonator soliton spectrometer (MSS) using a single miniature comb device that generates two mutually-phase-locked combs. The principle of operation relies upon an optical phase lock-

ing effect observed in the generation of counter-propagating solitons within high-Q whispering gallery resonators [12]. Soliton generation in microcavities is being studied for miniaturization to the chip-scale of complete comb systems, and these soliton microcombs have now been demonstrated in a wide range of microcavity systems [13]. It has been shown that counter-propagating solitons can have distinct, controllable repetition rates and that their underlying comb spectra can be readily phase locked at two spectral points [12]. This mutual double-locking creates line-by-line relative frequency stability for the underlying microcomb spectra that is more characteristic of fully self-referenced dual comb systems. The resulting Vernier of comb frequencies in the optical domain maps to an exceptionally stable radio frequency grid for implementation of the spectrometer.

7.1 Main results

The spectral relationship of the doubled-locked cw and ccw solitons reveals the inherent optical frequency Vernier (Fig. 7.1A). A single laser source is modulated (Fig. 7.1B) to produce the two mutually-coherent pump lines at order $\mu = N$ with frequency separation $\Delta\nu$ (MHz range). The distinct pump frequencies cause the soliton repetition rates to differ by Δf_r as a result of the Raman self-frequency-shift [12, 14–17]. As detailed elsewhere, the cw and ccw combs will experience frequency locking (induced by optical backscattering) at order $\mu = 0$ for certain pumping frequencies [12]. This locking requires that $\Delta\nu = N\Delta f_r$. Also, because the two pump frequencies are derived from radio-frequency modulation of a single laser source, they have a high relative frequency stability ($\Delta\nu$ is very stable) and are effectively locked at order $\mu = N$. This double locking sets up a stable Vernier in the respective soliton comb frequencies. The counter-propagating solitons are generated in a high-Q silica microresonator with 3 mm diameter (22 GHz soliton repetition rate) [18]. Details on the soliton generation process can be found elsewhere [12, 19, 20]. Typical optical spectra of cw and ccw solitons span the telecommunication C-band (Fig. 7.1C).

The spectrometer operates as follows. A test laser frequency f_L is measured using either of the following expressions: $f_L = nf_{r1,2} + \Delta f_{n1,2} + f_0$ where n is the comb order nearest to the laser frequency, $f_{r1,2}$ are the comb repetition rates, $\Delta f_{n1,2}$ are the heterodyne beat frequencies of the test laser with the two frequency comb teeth at order $\mu = n$, and f_0 is the frequency at $\mu = 0$. $f_{r1,2}$ and $\Delta f_{n1,2}$ are measured by co-detection of the combs and the test laser to produce the electrical signals $V_{1,2}$ in Fig. 7.1B. Fast Fourier transform (FFT) of V_1V_2 gives the spectral line at $n\Delta f_r$ (Fig.

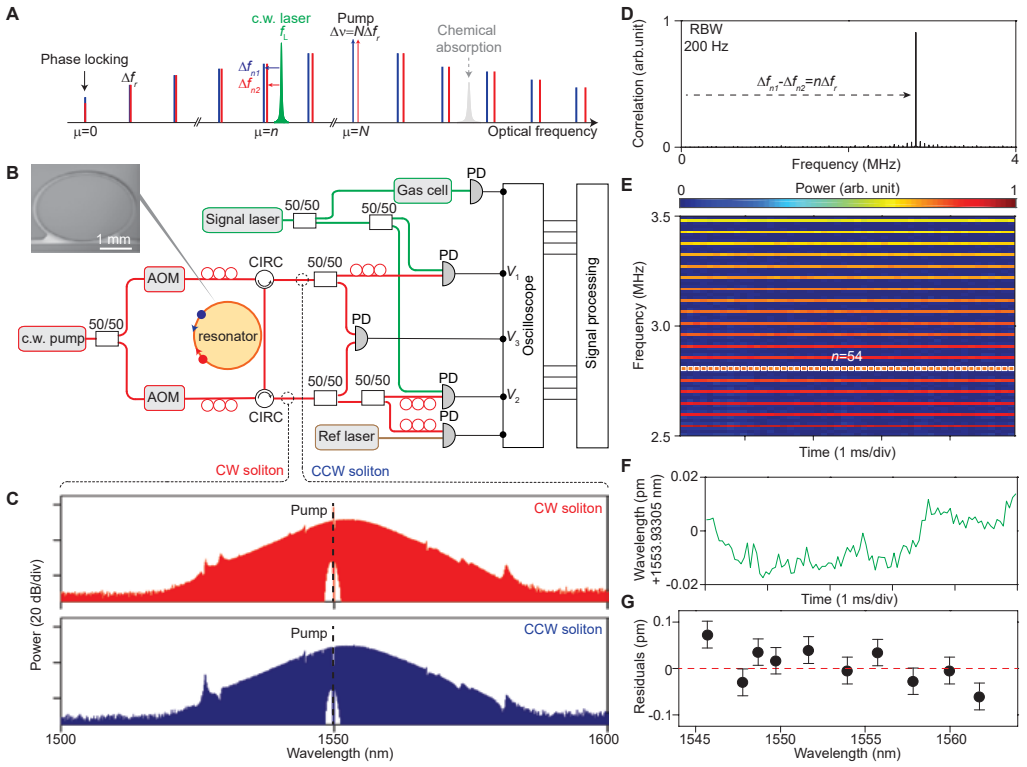

Figure 7.1: Spectrometer concept, experimental setup, and static measurement. (a) Counter propagating soliton frequency combs (red and blue) feature repetition rates that differ by Δf_r, phase-locking at the comb line with index $\mu = 0$ and effective locking at $\mu = N$ thereby setting up the Vernier spectrometer. Tunable laser and chemical absorption lines (grey) can be measured with high precision. (b) Experimental setup. AOM: acousto-optic modulator; CIRC: circulator; PD: photodetector. Small red circles are polarization controllers. Supplementary information includes more detail. Inset: scanning electron microscope image of a silica resonator. (c) Optical spectra of counter-propagating solitons. Pumps are filtered and denoted by dashed lines. (d) Typical measured spectrum of V_1V_2 used to determine order n. For this spectrum: $\Delta f_{n1} - \Delta f_{n2} = 2.8052$ MHz and $\Delta f_r = 52$ kHz giving $n = 54$. (e) The spectrograph of the dual soliton interferogram (pseudo color). Line spacing gives $\Delta f_r = 52$ kHz. White squares correspond to the index $n = 54$ in panel (c). (f) Measured wavelength of an external cavity diode laser operated in steady state. (g) Residual deviations between ECDL laser frequency measurement as given by the MSS and a wavemeter. Error bars give the systematic uncertainty as limited by the reference laser in panel (b).

7.1D) using the correlation method [9] and in turn the order n (procedure described in Supplementary information). f_0 is determined by applying this procedure to the reference laser frequency f_{ref} (stabilized using an internal molecular reference). All of these data inputs are automatically processed in real time to measure f_L.

As a preliminary test, the frequency of an external-cavity-diode-laser is measured and compared against a wavemeter. Fig. 7.1D and 1E ($n = 54$) are from this measurement. The real-time measured wavelength of the laser (Fig. 7.1F) fluctuates within ±0.02 pm over a 5 ms time interval. The measurement was repeated from 1545 to 1560 nm with residual deviations less than 0.1 pm versus the wavemeter measurement (Fig. 7.1G). These deviations are believed to be limited by the wavemeter resolution (±0.1 pm). The systematic uncertainty of absolute wavelength in the current setup is set by the reference laser to around ±4 MHz (±0.03 pm).

The large, microwave-rate free-spectral range of the MSS enables tracking of lasers undergoing fast-chirping or discontinuous broadband tuning. Although correlation is performed with a time interval $T_W = 1/\Delta f_r$, the instantaneous frequency of the laser relative to the combs can be acquired at a much faster rate set by the desired time-bandwidth-limited resolution. To avoid aliasing of the correlation measurement (i.e. to determine n uniquely), the amount of frequency-chirping should not exceed the repetition rate f_r within the measurement window T_W, which imposes a maximum resolvable chirping-rate of $f_r \times \Delta f_r$. This theoretical limit is 1 PHz/s for the MSS and represents a boost of 100× compared with previous Vernier spectrometers [9].

Measurement of rapid continuous-tuning of an external cavity diode laser is shown in Fig. 7.2A. The correlation measurement evolves as the laser is tuned over multiple FSRs of the comb and thereby determines the index n as a function of time (Fig. 7.2A upper panel). Measurement of the linear frequency chirp (-12.4 THz/s) as well as the frequency versus time at high resolution (by subtracting the average linear frequency ramp) are shown in the Fig. 7.2A middle and lower panels, respectively. The discontinuities in the measurement are caused by electrical frequency dividers used to reduce the detected signal frequency for processing by a low-bandwidth oscilloscope (see Supplementary information). The dividers can be eliminated by using a faster oscilloscope. In Fig. 7.2B measurement of broadband step tuning (mode hopping) of an integrated-ring-resonator tunable III-V/Silicon laser diode [21] is presented. Fast step tuning between 1551.427 nm and 1557.613 nm every 1 ms with the corresponding index n stepping between $n = 64$ and $n = 29$ is observed. The lower panel in Fig. 7.2B gives a higher resolution zoom-in of one of the step regions. The data points in these measurements are acquired over 1 μs so the resolution is approximately 1 MHz.

This combination of speed and precision is also useful for spectroscopic measure-

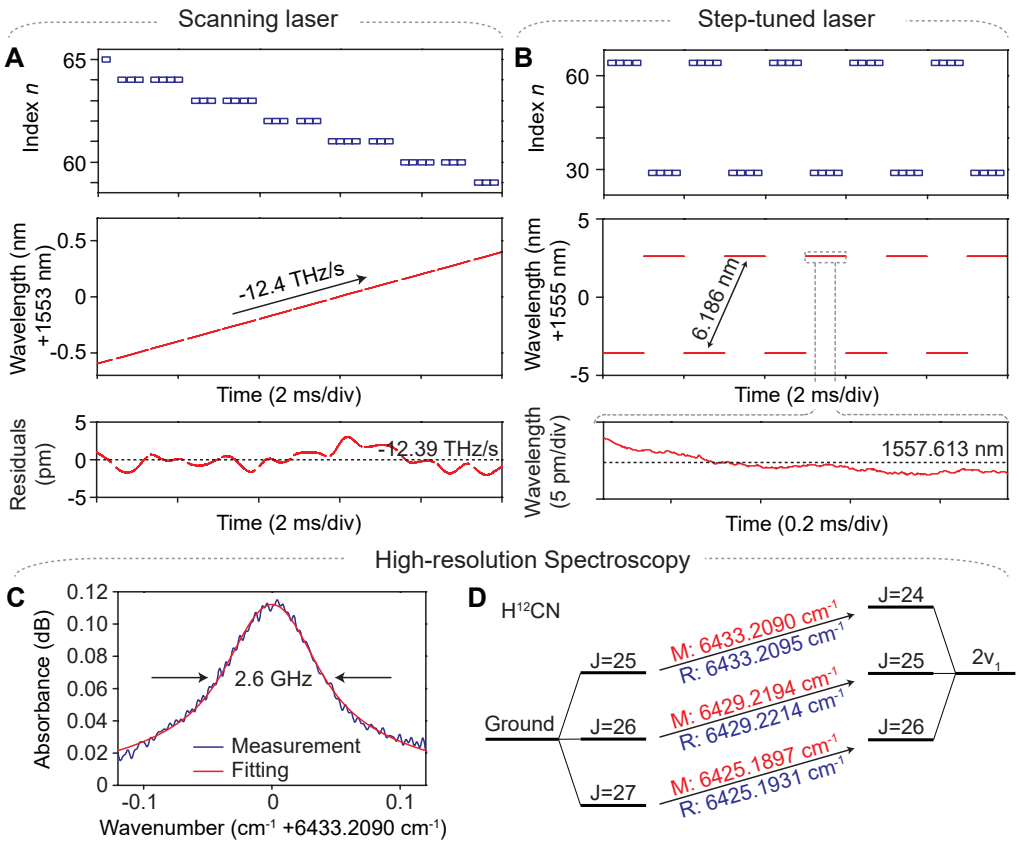

Figure 7.2: Laser tuning and spectroscopy measurements. (a) Measurement of a rapidly tuning laser showing index n (upper), instantaneous frequency (middle), and higher resolution plot of wavelength relative to average linear rate (lower), all plotted versus time. (b) Measurement of a broadband step-tuned laser as for laser in panel (a). Lower panel is a zoom-in to illustrate resolution of the measurement. (c) Spectroscopy of $H^{12}C^{14}N$ gas. A vibronic level of $H^{12}C^{14}N$ gas at 5 Torr is resolved using the laser in panel a. (d) Energy level diagram showing transitions between ground state and $2\nu_1$ levels. The measured (reference) transition wavenumbers are noted in red (blue).

ments of gas-phase chemicals using tunable, single-frequency lasers. To demonstrate, an absorption line of $H^{12}C^{14}N$ at 5 Torr is obtained by a scanning laser calibrated using the MSS (Fig. 7.2C). The linewidth is around 2.6 GHz and the absorbance is as weak as 0.12 dB. Separate measurements on vibronic transitions between the ground state and $2\nu_1$ states were performed. The corresponding transition wavenumbers obtained by pseudo-Voigt fitting are in excellent agreement with the HITRAN database (Fig. 7.2D) [22].

To illustrate a measurement of more complex multi-line spectra, a fiber mode-locked laser (FMLL) is characterized (Fig. 7.3A). The FMLL full spectrum (Fig. 7.3B) was

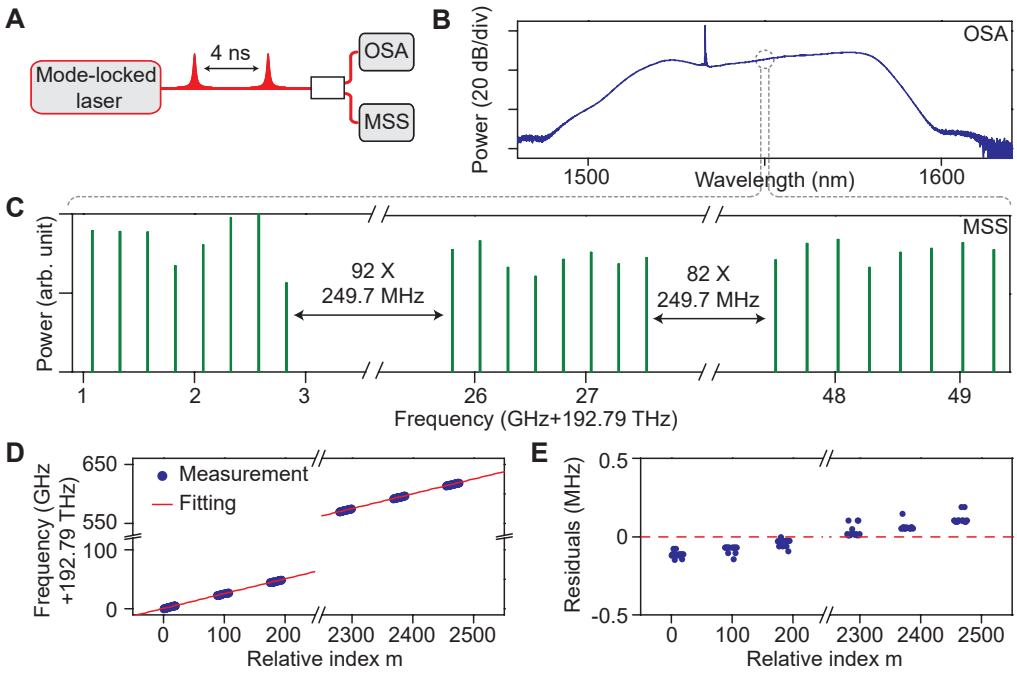

Figure 7.3: Measurement of a fiber mode-locked laser. (a) Pulse trains generated from a fiber mode-locked laser (FMLL) are sent into an optical spectral analyzer (OSA) and the MSS. (b) Optical spectrum of the FMLL measured by the OSA. (c) Optical spectrum of the FMLL measured using the MSS over a 60-GHz frequency range (indicated by dashed line). (d) Measured (blue) and fitted (red) FMLL mode frequencies versus index. The slope of the fitted line is set to 249.7 MHz, the measured FMLL repetition rate. (e) Residual MSS deviation between measurement and fitted value.

first bandpass filtered to prevent detector saturation. Also, the frequency extraction procedure is modified to enable unique identification of many frequencies (see Supplementary information). The reconstructed FMLL spectrum measured using the MSS is plotted in Fig. 7.3C. In an additional study of the FMLL, the MSS is used to measure 6 closely-spaced-in-frequency groups of lines located at various spectral locations spanning 2500 free-spectral-range's of the mode locked laser (Fig. 7.3D). A linear fitting defined as $f_m = f_o + m f_{\text{rep}}$ is plotted for comparison by using the photodetector-measured FMLL repetition rate $f_{\text{rep}} = 249.7$ MHz where m and f_o represent the relative mode index and fitted offset frequency at $m = 0$, respectively. The residual deviation between the measurement and linear fitting is shown in Fig. 7.3E and gives good agreement. The slight tilt observed in Fig. 7.3E is believed to result from drifting of soliton repetition rates which were not monitored real-time. Also, variance of residuals within each group comes from the 300 kHz linewidth of

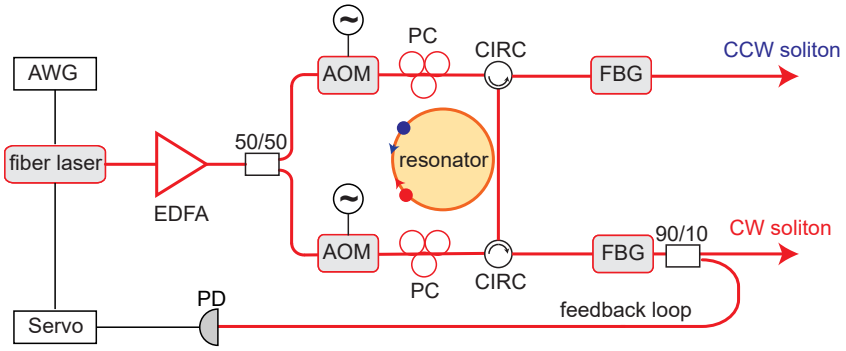

Figure 7.4: Detailed experimental setup for soliton generation. AWG: arbitrary waveform generator; EDFA: erbium-doped fiber amplifier; AOM: acousto-optic modulator; PC: polarization controller; CIRC: circulator; FBG: fiber Bragg grating; PD: photodetector.

each FMLL line. Drifting of the reference laser and FMLL carrier-envelope offset also contribute to the observed residuals across different measurements.

Our soliton spectrometer uses dual-locked counter-propagating soliton microcombs to provide high-resolution frequency measurement of rapid continuously and step tuned lasers as well as complex multi-line spectra. In combination with a tunable laser, the spectrometer also enables precise measurement of absorption spectra including random spectral access (as opposed to only continuous spectral scanning). Further optimization of this system could include generation of solitons from distinct mode families thereby allowing tens-of-MHz repetition rate offset to be possible [23]. If such solitons can be dual-locked, the increased acquisition speed would enable measurement of chirping-rates much higher than PHz/s. Operation beyond the telecommunications band would also clearly be useful and could use internal [24] or on-chip spectral broadeners [25], and methods for generation of soliton microcombs into the visible band are possible [26]. Besides the performance enhancement realized with the soliton microcombs, the use of dual-locked counter-propagating solitons provides a considerable technical simplification by eliminating the need for a second mutually phase locked comb. Finally, chip integrable versions of the current device employing silicon nitride waveguides are possible [27]. These and other recently demonstrated compact and low-power soliton systems [28, 29] point towards the possibility of compact microresonator soliton spectrometers.

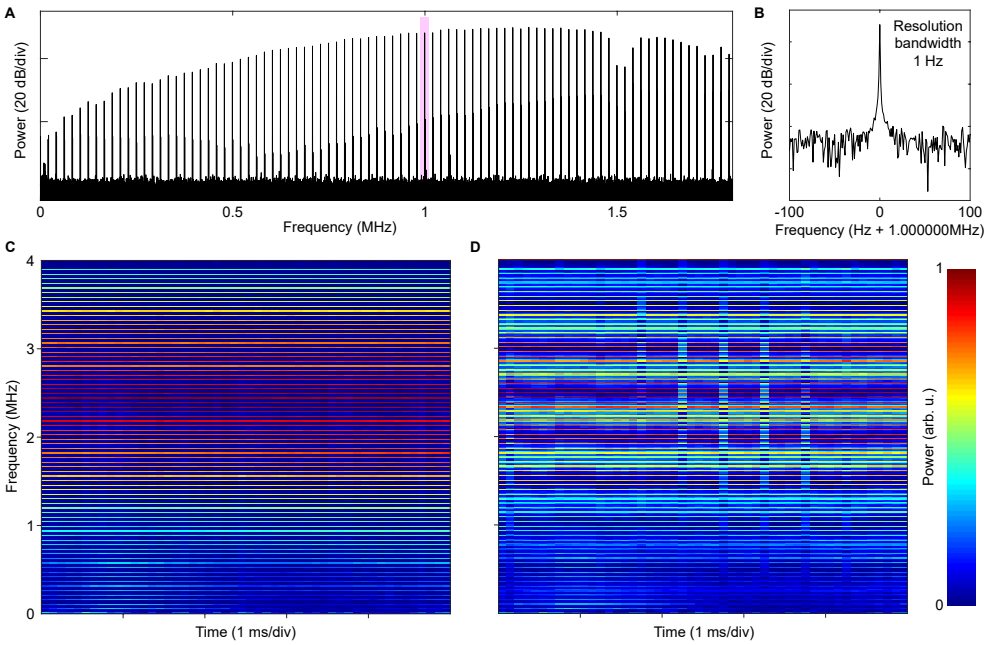

Figure 7.5: Interferograms of cw and ccw solitons. (a) A typical interferogram in frequency domain. (b) A zoom-in of line 48 centered at 1.000000 MHz (shaded region in panel A). (c) Spectrogram of Fig. 7.1D in the main text showing more lines. (d) Same as in (c) but the frequency spacing has been deliberately chosen so that artifacts appear in the scan.

7.2 Supplementary information

Acquisition of correlation signal

The correlation method can be understood as a calculation of the frequency difference $\Delta f_{n2} - \Delta f_{n1} = n\Delta f_r$ by formation of V_1V_2 followed by fast Fourier transform (FFT). The FFT spectrum of V_1V_2 gives the spectral line at $n\Delta f_r$ (Fig. 7.1D). To determine n requires $\Delta f_r = f_{r2} - f_{r1}$, which is measured by heterodyne of the solitons to produce electrical signal V_3. Figure 1E is a narrow frequency span of the FFT of V_3 and shows how the optical frequency Vernier is mapped into a stable radio-frequency grid with line spacing Δf_r. The order corresponding to the FFT of the V_1V_2 signal (Fig. 7.1D spectrum) is also indicated. These steps are performed automatically to provide a real time measurement of f_L relative to f_0.

Electrical divider discussion

The bandwidth limit of the oscilloscope used in this experiment is 2.5 GHz and in order to measure frequencies $\Delta f_{n1,2}$ up to 11 GHz, microwave frequency dividers were used that function between 0.5 GHz to 10 GHz and provide an 8× division

ratio. The use of these dividers created 3 GHz frequency unresolvable bands within one FSR of the optical combs, which caused the discontinuities in the lower panel in Fig. 7.2A. Meanwhile, the repetition rate difference corresponding to the divided signals will also decrease proportionally by a factor of 8, which in turn reduces the maximum resolvable chirping rate to 125 THz/s. The dividers can be omitted by using a higher-bandwidth oscilloscope, which eliminates the above unresolvable bands and allows chirp-rate measurements approaching the theoretical limit.

Sample preparation and soliton generation

The silica microresonators are fabricated on a 4-inch silicon wafer with a 8-μm-thick thermally-grown silica layer. The detailed fabrication process can be found elsewhere [18]. The intrinsic quality factor of the resonators used in this work ranges between 200 to 300 million. Light is coupled to the resonator via a tapered fiber; however, it is also possible to use silica resonators having an integrated silicon nitride waveguide [27].

The detailed experimental setup for soliton generation is illustrated in Fig. 7.4. A continuous-wave fiber laser is amplified by an erbium-doped fiber amplifier (EDFA), and split by a 50/50 directional coupler for clockwise (cw) and counter-clockwise (ccw) soliton generation. The fiber laser has a free-running linewidth less than 2 kHz over 100 ms. Two acousto-optic modulators (AOMs) are used to independently control the pump frequency and power in both directions. The pump power in each direction is around 200 mW and is attenuated after the resonator by a fiber Bragg grating (FBG). The filtered transmitted power for the cw direction is split by a 90/10 directional coupler and the 10 percent output port is used in a servo control loop to stabilize the solitons. By scanning the laser from the blue side to the red side of the resonance, solitons form simultaneously in both directions with characteristic “step-like” features in the transmitted power scan [12, 13, 19]. A fast power modulation is first applied to extend the existence range of the solitons. Then the long term stability of the solitons is maintained by introducing a feed back loop control described in detail elsewhere [19, 20]. This method maintains a constant soliton power on one of the soliton streams through servo control of the pumping frequency. It has the desirable effect of forcing the pump laser frequency to track the microresonator pumping mode as its frequency slowly drifts. As a result, it was not necessary to provide any temperature stabilization to the resonator in the measurement.

Characterization of soliton phase locking

The underlying mechanism leading to phase locking of counter-propagating (CP) solitons has been described in detail elsewhere [12]. Once the solitons are phase-locked, their relative frequency becomes very stable and their baseband inteferogram features sharp spectral lines (linewidths well below 1 Hz) in the frequency domain (Fig. 7.5A and 7.5B). To ensure that the solitons are locked during the measurement, the spectrogram of the CP soliton beatnotes is monitored as shown in Fig. 7.1D in the main text. In the locked case, sharp, horizontal spectral lines persist over the measurement time (Fig. 7.5C). The acquisition time window T_W should be chosen to be integer multiples of $1/\Delta f_r$, where Δf_r is the repetition rate difference, so that the frequency of the beatnotes can be accurately resolved. If this is not the case, artifacts will appear in the spectrogram due to misalignment of the frequency grids (Fig. 7.5D).

Signal processing: general processing algorithm

Through heterodyne of the test laser with the nearest comb teeth, the phase ψ of the test laser is related to the electrical signals $V_{1,2}$ by

$$V_{1,2} \propto \cos(\psi - 2\pi\nu_{n1,2}t), \tag{7.1}$$

where $\nu_{n1,2}$ represent the frequencies of nearest comb teeth and have order n. We also have $\nu_{n2} - \nu_{n1} = n\Delta f_r$ as a result of the CP soliton locking. A Hilbert transform is used to extract the time-dependent phase $\psi - 2\pi\nu_{n1,2}t$ from $V_{1,2}$ which thereby gives the heterodyne frequencies via

$$\Delta f_{n1,2} = \dot{\psi}/2\pi - \nu_{n1,2}. \tag{7.2}$$

Each data point of $\Delta f_{n1,2}$ is obtained by linear fitting of the phase over a specified time interval that sets the frequency resolution. Similarly, the heterodyne frequency between the reference laser and the soliton comb can be retrieved to determine the frequency f_0 (see discussion in main text).

The Fourier transform of the product V_1V_2 is given by

$$\begin{aligned}\widetilde{V_1V_2}(f) &\propto \int_0^{T_W} \frac{e^{i(\psi-2\pi\nu_{n1}t)} + e^{-i(\psi-2\pi\nu_{n1}t)}}{2} \frac{e^{i(\psi-2\pi\nu_{n2}t)} + e^{-i(\psi-2\pi\nu_{n2}t)}}{2} e^{-2\pi i f t}\mathrm{d}t \\ &\propto \delta(|f| - n\Delta f_r),\end{aligned} \tag{7.3}$$

where sum frequency terms in the integrand are assumed to be filtered out and are therefore discarded. To accurately extract the above spectral signal, the acquisition

time window T_W should be an integer multiple of $1/\Delta f_r$, which is also related to the pump frequency offset $\Delta\nu$ by $T_W = N_W N/\Delta\nu$ where N is the pump order and N_W is an integer. Moreover, the number of sampled points, which equals the product of oscilloscope sampling rate f_{samp} and T_W, should also be an integer (i.e. $f_{\text{samp}} N_W N/\Delta\nu$ is an integer). In this work, f_{samp} is usually set to 2.5 or 5 GHz/s and it is found that simple adjustment of $\Delta\nu$ is sufficient to satisfy this condition. As a result it is not necessary to synchronize the oscilloscope to external sources. It is noted that this method is simpler than the asynchronous detection used in previous work [9].

On account of the limited bandwidth of the oscilloscope used in work, it was necessary to apply electrical frequency division to the detected signals for proceesing by the oscilloscope. When frequency dividers are used (division ratio $r = 8$), the divided electrical signals (indicated by superscript d) yield

$$V_{1,2}^{\text{d}} \propto \cos((\psi - 2\pi\nu_{n1,2}t)/r). \tag{7.4}$$

As a result, the divided frequencies also satisfy $\Delta f_{n1,2}^{\text{d}} = \Delta f_{n1,2}/r$, and the correlation between the divided signals scales proportionally by

$$\Delta f_{n1}^{\text{d}} - \Delta f_{n2}^{\text{d}} = n\Delta f_r/r. \tag{7.5}$$

Therefore the required resolution bandwidth to resolve the ambiguity n from the measured correlation is $\Delta f_r/r$, which increases the minimal acquisition time to $T_W^{\text{d}} = rT_W$.

Signal processing: absorption spectroscopy

To perform the absorption spectroscopy, the laser transmission through the $H^{12}C^{14}N$ gas cell is recorded while the laser is continuously scanning. A portion of the laser signal is also meaured in the MSS to determine its frequency during the scan. A pseudo-Voigt lineshape (linear combination of Gaussian and Lorentz profile) is fitted to the spectrum and the central frequency is then extracted.

Signal processing: mode-locked laser measurement

The algorithm used here to extract a large number of frequencies simultaneously using the MSS is different from the previous single-frequency measurements. Rather than multiplying the signals V_1 and V_2 followed by Fast Fourier Transform (FFT) in order to determine the microcomb order, we directly FFT the signals V_1 and V_2 followed by filtering and then frequency correlation. This avoids the generation

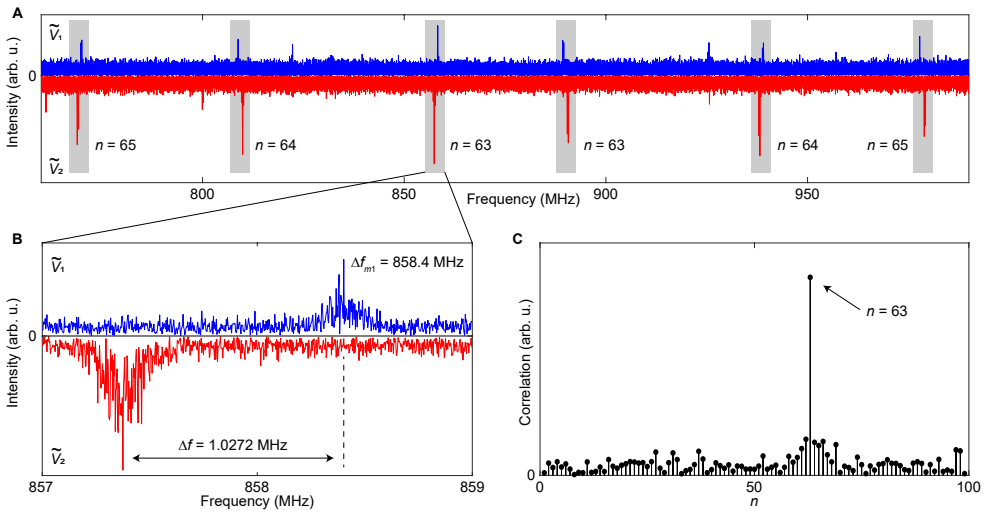

Figure 7.6: Multi-frequency measurements. (a) A section of $\tilde{V}_{1,2}$. Pairs of beatnotes coming from the same laser are highlighted and the derived n value is marked next to each pair of beatnotes. (b) Zoom-in on the highlighted region near 858 MHz in (a). Two beatnotes are separated by 1.0272 MHz. (c) Cross-correlation of $\tilde{V}_1$ and $\tilde{V}_2$ is calculated for each n and the maximum can be found at $n = 63$.

of ambiguities. To explain the approach, first consider an implementation similar to that reported in the main text. There, a fiber mode locked laser (FMLL) comb with free-spectral-range (FSR) of about 250 MHz was optically filtered to create a narrower frequency range of FMLL laser lines extending over only a few microcomb lines. The signals V_1 and V_2 upon FFT therefore produce a large set of frequencies representing the individual beats of each FMLL laser line (index m) with microcomb modes (index n). Fig. 7.6A gives a narrow frequency span of a typical FFT generated this way for both the V_1 and V_2 signals. A zoom-in of one pair of V_1 and V_2 signals is provided in Figure 7.6B and a remarkably precise frequency separation between the beats (in view of the spectral breadth of each beat) can be determined by correlating the upper (blue) and lower (red) spectrum (see Fig. 7.6C). This precision results from the underlying high relative frequency stability of the cw and ccw microcomb frequencies. As described in the main text, this frequency separation is a multiple of Δf_r, and a plot of the correlation versus the frequency separation (in units of Δf_r) is provided in Fig. 7.6C, where the peak of the correlation gives the index $n = 63$ for this pair of beat frequencies. Proceeding this way for each pair of peaks in Fig. 7.6A allows determination of n from which the frequency of the corresponding FMLL line can be determined. It is interesting to note that in Fig. 7.3A, there are two sets of peaks that give n=63, 64, and 65. These correspond to FMLL lines that are

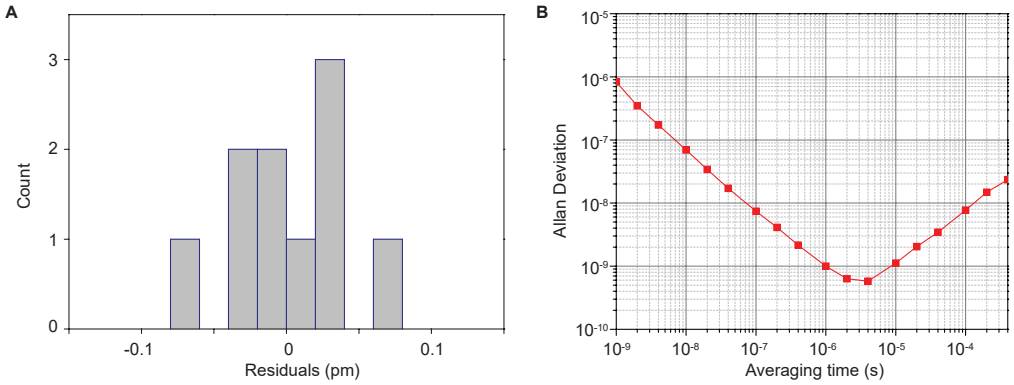

Figure 7.7: Statistics and Allan deviation. (a) Histogram of the residual deviations shown in Fig. 7.1G of the main text. The variance is 0.0016 pm. (b) Allan deviation of measured frequency of a static laser as a function of averaging time. The relative frequency stability reaches 6×10^{-10} at 4 μs integration time.

higher and lower in frequency relative to the microcomb modes with indices n=63, 64, and 65. The relative alignment of the blue and red peaks which switches sign for these sets of beat frequencies allows determination of which FMLL line is lower and higher in frequency relative to the microcomb lines.

To provide more rigor to this explanation, the electrical signals consist of multiple beat components given by,

$$V_{1,2} = \sum_m V_{m1,2}, \quad V_{m1,2} \propto \cos(\psi_m - 2\pi\nu_{\mu(m)1,2}t), \tag{7.6}$$

where ψ_m and $\nu_{\mu(m)1,2}$ represent the phase of the m-th FMLL mode and the frequencies of the microcomb order nearest to this FMLL mode, respectively, and where $\mu(m)$ denotes the comb order nearest the m-th FMLL mode. As described in the main text, the frequencies $\nu_{\mu(m)1,2}$ are related to the repetition rate difference by $\nu_{\mu(m)2} - \nu_{\mu(m)1} = \mu(m)\Delta f_r$. The FFT of $V_{1,2}$ is denoted by $\tilde{V}_{1,2}$ and the correlation given in Fig. 7.6C (and used to determine the comb order n of each spectral component) is given by,

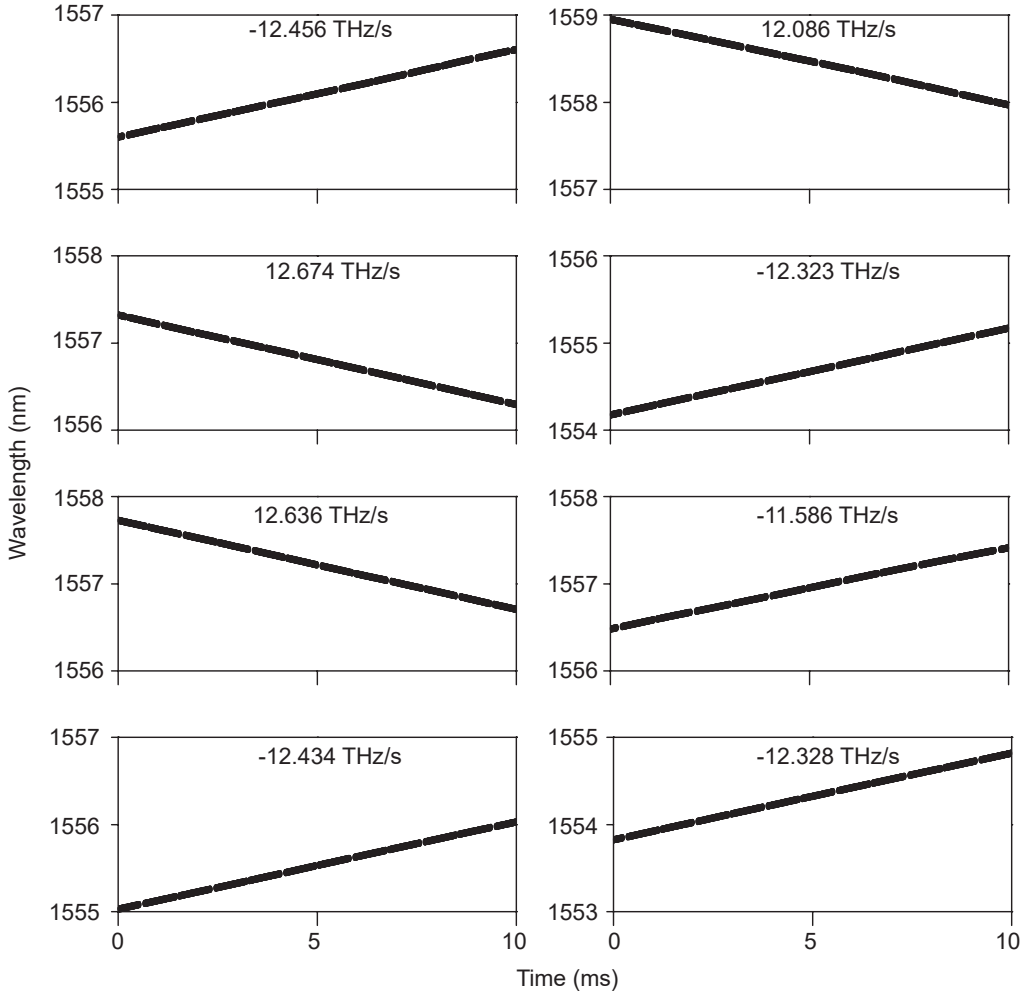

Figure 7.8: Additional measurement of fast-chirped lasers. Measurements of the wavelengths of an external-cavity diode laser tuned at its maximum speed using the MSS. The extracted average chirp-rates are shown at the top of each panel.

$$
\begin{aligned}
&\int_{\Delta f_{m1}-\kappa/2}^{\Delta f_{m1}+\kappa/2} \tilde{V}_1(f)\tilde{V}_2^*(f+n\Delta f_r)\mathrm{d}f \\
&\approx \int_{-\infty}^{\infty} \mathrm{d}f \int V_{m1}(t)e^{2\pi i f t}\mathrm{d}t \int V_{m2}(t')e^{-2\pi i(f+n\Delta f_r)t'}\mathrm{d}t' \\
&= \int V_{m1}(t)V_{m2}(t)e^{-2\pi i n\Delta f_r t}\mathrm{d}t \\
&\propto \int \frac{e^{i(\psi_m-2\pi\nu_{\mu1}t)}+e^{-i(\psi_m-2\pi\nu_{\mu1}t)}}{2}\frac{e^{i(\psi_m-2\pi\nu_{\mu2}t)}+e^{-i(\psi_m-2\pi\nu_{\mu2}t)}}{2}e^{-2\pi i n\Delta f_r t}\mathrm{d}t \\
&\propto \delta(\mu(m)-n),
\end{aligned}
$$

where Δf_{m1} denotes the peak frequency of the beatnote, κ is a predetermined range of

integration to cover the linewidth of the beatnote (here $\kappa = 2$ MHz), and where sum frequency terms in the integrand have been discarded. Therefore for each spectral component m, its associated microcomb order number $\mu(m)$ can be determined by varying n in the above correlation until it reaches maximum (see Fig. 7.6C). The n value with the maximum correlation will be assigned to the peak as the tooth number $\mu(m)$, and then the absolute frequency can be recovered.

The limit of this process to accommodate more FMLL frequencies is much higher than that given by the filter bandwidth studied in this work. It is instead set by the spectral density of FMLL-microcomb beat lines that can be reasonably resolved within the microcomb FSR spectral span.

Additional measurements

To validate the repeatability of results, we conducted multiple measurements with static, dynamic, and mode-locked lasers beyond those results presented in the main text. For example, shown in Fig. 7.7A is the histogram of residual deviations between an ECDL laser frequency measured by the MSS and a wavemeter. This specific data set is compiled from Fig. 7.1G of the main text. The variance is calculated to be 0.0016 pm.

To further benchmark the performance of the MSS, we also evaluated the Allan deviation for MSS measurement of a static laser. The extracted Allan deviation is plotted in Fig. 7.7B and decreases to 6×10^{-10} (120 kHz in absolute frequency) at 4 μs. It is noted that this Allan deviation includes noise contributions from the reference laser, the ECDL, as well as the soliton microcomb repetition rate.

Also, additional measurements of fast chirped lasers using the MSS are plotted in Fig. 7.8. The laser is an ECDL tuned at its maximum speed, similar to the case presented in Fig. 7.2A of the main text. Both positive and negative chirping rates at different wavelengths are resolved.

References

[1] Willner, A., Yu, C. & Pan, Z. *Optical Fiber Telecommunications VB (Fifth Edition): Chapter 7* (Academic Press, 2008).

[2] Allen, M. G. Diode laser absorption sensors for gas-dynamic and combustion flows. *Measurement Science and technology* **9**, 545–562 (1998).

[3] Choma, M. A., Sarunic, M. V., Yang, C. & Izatt, J. A. Sensitivity advantage

of swept source and fourier domain optical coherence tomography. *Optics Express* **11**, 2183–2189 (2003).

[4] Diddams, S. A. The evolving optical frequency comb. *Journal of the Optical Society of America B* **27**, B51–B62 (2010).

[5] Del'Haye, P., Arcizet, O., Gorodetsky, M. L., Holzwarth, R. & Kippenberg, T. J. Frequency comb assisted diode laser spectroscopy for measurement of microcavity dispersion. *Nature Photonics* **3**, 529–533 (2009).

[6] Coddington, I., Giorgetta, F. R., Baumann, E., Swann, W. C. & Newbury, N. R. Characterizing fast arbitrary cw waveforms with 1500 THz/s instantaneous chirps. *IEEE Journal of Selected Topics in Quantum Electronics* **18**, 228–238 (2012).

[7] Ma, L.-S., Zucco, M., Picard, S., Robertsson, L. & Windeler, R. S. A new method to determine the absolute mode number of a mode-locked femtosecond-laser comb used for absolute optical frequency measurements. *IEEE Journal of Selected Topics in Quantum Electronics* **9**, 1066–1071 (2003).

[8] Peng, J.-L., Liu, T.-A. & Shu, R.-H. Optical frequency counter based on two mode-locked fiber laser combs. *Applied Physics B* **92**, 513–518 (2008).

[9] Giorgetta, F., Coddington, I., Baumann, E., Swann, W. & Newbury, N. Fast high-resolution spectroscopy of dynamic continuous-wave laser sources. *Nature Photonics* **4**, 853–857 (2010).

[10] Coddington, I., Newbury, N. & Swann, W. Dual-comb spectroscopy. *Optica* **3**, 414–426 (2016).

[11] Suh, M.-G., Yang, Q.-F., Yang, K. Y., Yi, X. & Vahala, K. J. Microresonator soliton dual-comb spectroscopy. *Science* **354**, 600–603 (2016).

[12] Yang, Q.-F., Yi, X., Yang, K. Y. & Vahala, K. Counter-propagating solitons in microresonators. *Nature Photonics* **11**, 560–564 (2017).

[13] Kippenberg, T. J., Gaeta, A. L., Lipson, M. & Gorodetsky, M. L. Dissipative Kerr solitons in optical microresonators. *Science* **361**, eaan8083 (2018).

[14] Milián, C., Gorbach, A. V., Taki, M., Yulin, A. V. & Skryabin, D. V. Solitons and frequency combs in silica microring resonators: Interplay of the Raman and higher-order dispersion effects. *Physical Review A* **92**, 033851 (2015).

[15] Karpov, M. *et al.* Raman self-frequency shift of dissipative Kerr solitons in an optical microresonator. *Physical Review Letters* **116**, 103902 (2016).

[16] Yi, X., Yang, Q.-F., Yang, K. Y. & Vahala, K. Theory and measurement of the soliton self-frequency shift and efficiency in optical microcavities. *Optics Letters* **41**, 3419–3422 (2016).

[17] Yang, Q.-F., Yi, X., Yang, K. Y. & Vahala, K. Spatial-mode-interaction-induced dispersive-waves and their active tuning in microresonators. *Optica* **3**, 1132–1135 (2016).

[18] Lee, H. *et al.* Chemically etched ultrahigh-Q wedge-resonator on a silicon chip. *Nature Photonics* **6**, 369–373 (2012).

[19] Yi, X., Yang, Q.-F., Yang, K. Y., Suh, M.-G. & Vahala, K. Soliton frequency comb at microwave rates in a high-Q silica microresonator. *Optica* **2**, 1078–1085 (2015).

[20] Yi, X., Yang, Q.-F., Youl, K. & Vahala, K. Active capture and stabilization of temporal solitons in microresonators. *Optics Letters* **41**, 2037–2040 (2016).

[21] Tran, M. A., Huang, D., Komljenovic, T., Peters, J. & Bowers, J. E. A 2.5 khz linewidth widely tunable laser with booster SOA integrated on silicon. *Proceedings of the 2018 IEEE International Semiconductor Laser Conference, Santa Fe* (2018).

[22] Gordon, I. E. *et al.* The HITRAN2016 molecular spectroscopic database. *Journal of Quantitative Spectroscopy and Radiative Transfer* **203**, 3–69 (2017).

[23] Lucas, E. *et al.* Spatial multiplexing of soliton microcombs. *Nature Photonics* **12**, 699–705 (2018).

[24] Brasch, V. *et al.* Photonic chip-based optical frequency comb using soliton Cherenkov radiation. *Science* **351**, 357–360 (2016).

[25] Lamb, E. S. *et al.* Optical-frequency measurements with a Kerr microcomb and photonic-chip supercontinuum. *Physical Review Applied* **9**, 024030 (2018).

[26] Lee, S. H. *et al.* Towards visible soliton microcomb generation. *Nature Communications* **8**, 1295 (2017).

[27] Yang, K. Y. *et al.* Bridging ultrahigh-Q devices and photonic circuits. *Nature Photonics* **12**, 297 (2018).

[28] Stern, B., Ji, X., Okawachi, Y., Gaeta, A. L. & Lipson, M. Battery-operated integrated frequency comb generator. *Nature* **562**, 401–405 (2018).

[29] Liu, J. *et al.* Ultralow-power chip-based soliton microcombs for photonic integration. *Optica* **5**, 1347–1353 (2018).

Chapter 8

TOWARDS MILLI-HERTZ LASER FREQUENCY NOISE ON A CHIP

Wang, H., Wu, L., Yuan, Z. & Vahala, K. Towards milli-hertz laser frequency noise on a chip. Preprint at https://arxiv.org/abs/2010.09248 (2020).

Brillouin microlasers were first studied about a decade ago [1–4], and have emerged as a powerful platform for narrow linewidth operation. Unlike conventional lasers, Brillouin devices derive optical gain through a process that is parametric in nature, but that resembles stimulated emission on account of damping of the phonons involved in the amplification process [5]. The phonon participation drastically impacts the fundamental linewidth of the Brillouin laser, increasing it by about 600 fold (equal to the number of thermal Brillouin quanta at the operating temperature) relative to the quantum limit [6], and leading to a temperature-dependent linewidth [7]. Otherwise, the linewidth formula is Schawlow-Townes like in the way that it scales inversely with optical power and roughly inverse-quadratically with cavity Q factor [8]. These features provide a way to reduce fundamental linewidth even in the presence of the large thermal noise contribution. The parametric nature of the Brillouin process also allows pump frequency noise to leak into the laser frequency noise [9]. However, this leakage is strongly suppressed when the optical cavity damping is low relative to the phonon damping.

Nonetheless, as chip-based devices Brillouin lasers present considerable challenges for narrow linewidth operation. For example, specialized processing methods are required to attain the highest possible optical Q factors. Also, thermo-refractive noise [10, 11], which scales about inversely with mode volume, is a significant source of noise, especially at low offset frequencies. Even with these challenges, early work attained Brillouin fundamental linewidths below 1 Hz [6]. Frequency stability improvement was also demonstrated by locking these devices to compact reference cavities [12]. Also significant, the application of chip-based Brillouin devices to microwave synthesis [13, 14] and Sagnac gyroscopes [15–17] showed that thermorefractive noise and pump noise do not significantly impact the relative coherence of co-lasing Stokes waves (i.e. their beatnote linewidth). Thus, such

specific operational modalities can leverage the narrow fundamental linewidths of chip-based Brillouin lasers. Towards full integration, narrow-linewidth Brillouin laser designs have also emerged that feature integrated waveguides [16, 18, 19]. If combined with pump sources, they could potentially provide robust sources of high coherence light.

Here, we report measurement of an ultra-low frequency noise level of 9 mHz·Hz/Hz in an on-chip stimulated Brillouin laser (SBL) at an output power of 0.9 mW. Both the noise level and its power dependence when compared to theory [6] suggest that it is fundamental in origin and would correspond to a linewidth of 60 mHz. This linewidth is 5× lower than in previous reports, and to measure it, an enhancement of the self-heterodyne optical frequency discriminator method [20–22] is applied. Indeed, the current frequency noise measurement provides a way to test and analyze this noise measurement method. The ultra-low noise level is made possible by the high optical Q of the resonator in combination with higher single-mode optical power through suppression of Brillouin cascade [23].

8.1 Background on Brillouin cascade

Phase matching for efficient Brillouin laser oscillation requires that the frequency separation between the pumped resonator mode and Stokes laser mode equals the Brillouin shift frequency (to within the Brillouin gain bandwidth). For counter-propagating pump and Stokes waves in the silica resonators studied here, the shift is about 10.8 GHz for pumping near 1550 nm. Matching this shift to within the Brillouin gain bandwidth is readily accomplished by microfabrication control of the resonator diameter, which aligns the free-spectral-range (FSR) of the resonator to the Brillouin shift frequency [4]. However, because FSR dispersion is small compared with the gain bandwidth, the neighboring longitudinal mode readily phase matches to the initial Stokes laser wave, and it will lase (i.e. lasing cascade [6]) when the initial Stokes power reaches a certain threshold (Fig. 8.1a, upper panel). Cascading effectively clamps the laser power of the first Stokes wave (now the pumping wave) and increases its noise due to the second-order Stokes wave [23], both of which are undesirable for ultra-low-noise applications. The introduction of dispersion within the same mode family during microfabrication [24] or the use different transverse mode families for pumping and Stokes oscillation [1, 2], as employed here, will block the cascading action (see Fig. 8.1a, lower panel) so that Brillouin laser power can increase well beyond the normal cascade threshold point.

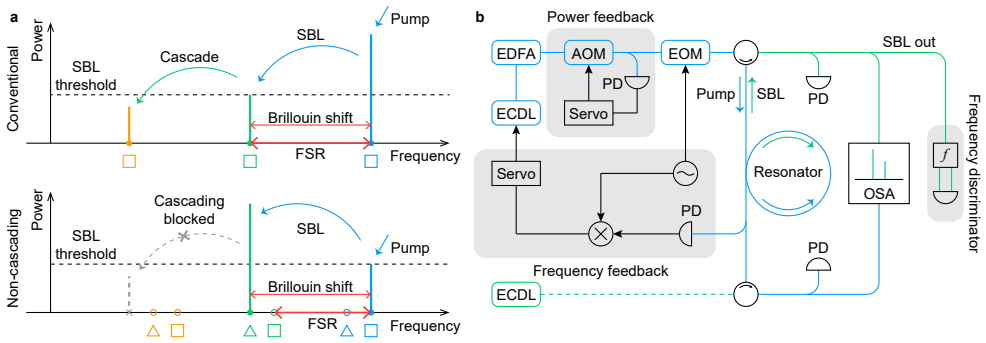

Figure 8.1: Operation of Brillouin lasers and experimental setup. (a) Upper panel: spectral diagram for conventional Brillouin laser operation, where the FSR is matched to the Brillouin frequency shift. Lower panel: spectral diagram for non-cascading laser operation, where FSR is mismatched from the Brillouin shift. Markers below the modes indicate two transverse mode families. Modes with the same marker shape belong to the same mode family. (b) Experimental setup. An external-cavity diode laser (ECDL) is amplified by an erbium-doped fiber amplifier (EDFA) and sent to a tapered fiber for coupling to the resonator. The laser power is actively stabilized by an acousto-optic modulator (AOM) with power feedback from a photodetector (PD). The laser frequency is Pound-Drever-Hall (PDH) locked to the resonance using an electro-optic modulator (EOM) and the error signal feeds back directly into ECDL. The Brillouin laser wave, propagating in the opposite direction of the pumping, is collected with a circulator. An optical spectrum analyzer (OSA) is used to monitor pump and SBL spectra and to ensure that no cascading occurs. The laser output is also sent to an optical frequency discriminator to measure the frequency noise. An auxiliary ECDL launched in the opposite direction to the pump is used for Q and dispersion measurements. The detailed description of the optical frequency discriminator is provided in Fig. 8.3a.

To inhibit cascade in this work, a silica wedge resonator [4] is fabricated with an FSR of 8.9 GHz (smaller than the Brillouin shift of around 10.7 GHz), which thereby prevents cascade within any of the longitudinal mode families. Phase matching is then provided by pumping and laser oscillation on modes belonging to different transverse mode families. Because the resonator features a moderate density of very-high-Q modes within one FSR [25], the mode selection to enable phase matching is relatively straightforward and is described below. The high optical Q factor of both modes is important because the laser threshold power is inversely proportional to both the pump mode Q and the SBL mode Q. The experimental setup is described in Fig. 8.1b.

8.2 Pump and SBL mode selection

To locate phase-matched high-Q mode-pairs in the resonator, the dispersion of several mode families is measured using a tunable external-cavity diode laser (ECDL) together with a calibrated Mach-Zehnder interferometer [26]. Measurements of several transverse mode families (index m) plotted versus longitudinal mode number μ are presented in Fig. 8.2. Before plotting, a constant offset frequency ν_0 (here taken as the SBL frequency) is subtracted as well as a linear dispersion term equal to $\mu \times \mathrm{FSR}$ where FSR is the free spectral range of the Brillouin laser mode (see below). The plotted lines are therefore given by: $\Delta\nu_\mu^m \equiv \nu_\mu^m - \nu_0 - \mu \times \mathrm{FSR}$, where ν_μ^m is the frequency of longitudinal mode μ belonging to transverse mode family m.

Two mode families are highlighted using blue and green data points. Simulated mode field distributions of these two modes are shown in the Fig. 8.2 inset, and the modes are determined to be the TM2 (green) and TM4 (blue). The TM2 mode is selected as the lasing mode and the plot uses its FSR in the calculation of $\Delta\nu_\mu^m$. As a result, the green data points appear horizontal in the plot. Both of these mode families feature high intrinsic Q-factors around 400 million and also experience only a few mode crossings over a wide wavelength band. The pump mode must be located one Brillouin shift higher in frequency relative to the laser mode frequency. This condition, represented by the red phase-matching line in Fig. 8.2, is wrapped (modulo the Brillouin shift) in making the plot, and the pumping wavelength is determined to be around 1563 nm. The lasing threshold is 0.9 mW and the generated laser output power exceeds 0.9 mW at pumping power of 35.7 mW. The beatnote of pump and SBL signals is also shown as an inset in Fig. 8.2.

8.3 Cross-correlation method

The self-heterodyne optical frequency discriminator approach [20–22] was first applied to measure the frequency noise spectral density of the generated laser signal (Fig. 8.3a). However, at high offset frequencies (above 1 MHz), the frequency noise floor and measurement sensitivity were found to be limited by technical noise from the photodetector (PD), which is quantified by the noise equivalent power (NEP). This technical noise prevented measurement of fundamental frequency noise below $0.1\mathrm{Hz}^2/\mathrm{Hz}$. To overcome this limitation, we applied cross correlation (XCOR) of the electrical signals produced at the interferometer output. Electrical oscillators employ XCOR with a reference oscillator to measure phase noise [27], and it has also been applied recently to measure frequency-comb generated microwave signals by heterodyne with two reference comb signals [28]. The present measurement is

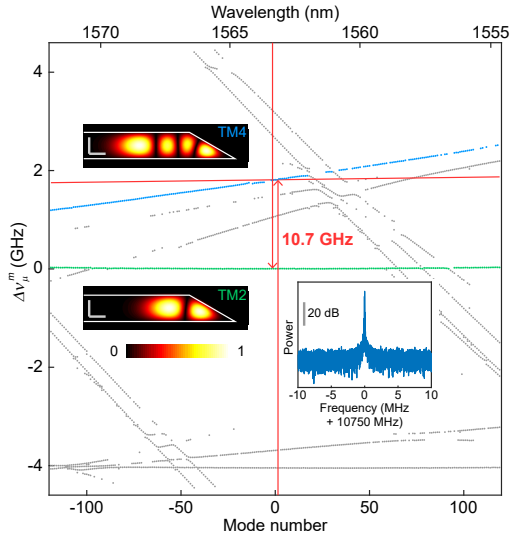

Figure 8.2: Mode selection for non-cascading Brillouin laser operation. Mode dispersion of the resonator is measured over a spectral region spanning several hundred longitudinal mode numbers. The intended SBL mode family (TM2) is highlighted in green and its corresponding pump phase-matching line is shown in red. The intended pump mode family (TM4) is highlighted in blue. First-order dispersion is introduced into the plot so that the laser mode family data points appear horizontal. Left insets: Simulated electric field distributions (norm) of the TM4 and TM2 modes. Scale bars are 5 μm. Lower right inset: Measured electrical spectrum of the pump and Brillouin laser beatnote signal.

distinct in applying XCOR to optical phase noise measurement, and also does not require reference optical or radio frequency oscillators. Moreover, the very low frequency noise of the device studied here illustrates the power of XCOR to boost sensitivity in this context.

As shown in Fig. 8.3a, the measurement setup employs an AOM to split the input light into frequency-shifted (1^{st} order output) and un-shifted parts (0^{th} order output), the latter being delayed by a 1-km-long fiber. However, instead of a single photodetector, two photodetectors receive the optical signals. Their outputs are recorded using an oscilloscope for subsequent XCOR to remove detector technical noise. The AOM is driven with a 55 MHz radio-frequency signal, which also determines the carrier frequency of the electrical signals from the two PDs. These signals are acquired with an oscilloscope having a 500 MHz sampling rate to prevent aliasing of the signal. AC coupling is used to block the low-frequency components at the oscilloscope. Delays between the channels are estimated to be less than 0.5 ns and are not considered in subsequent analyses. 0.2 seconds of waveform (100×10^6

points in each channel, 200×10^6 points total) are collected and transferred to a computer for processing. Phase signals are extracted with a Hilbert transform. The Hilbert transform creates distortions at the endpoints of the signal, thus the first and last 10 ms (5×10^6 points) for each channel are discarded after the transform. The remaining points are separated into segments (rectangular windowing), each with a 0.1 ms length (corresponding to a resolution bandwidth of 10 kHz), and Fourier transformed to extract the phase noise amplitude at a given offset frequency. For offset frequencies less than 200 kHz, resolution bandwidths are made smaller, and the segment lengths are adjusted accordingly. The correlation can then be found as the product between the Fourier coefficients of the two phase signals, averaged over different segments.

The correlation of the frequency noise measured by the cross-correlator contains contributions from both frequency noise and intensity noise:

$$C_\nu(f) = f^2 C_\phi(f) - f^2[C_a(f_c + f) + C_a(f_c - f)], \tag{8.1}$$

where $C_\phi(f)$ and $C_a(f)$ are the transferred phase and amplitude noise at offset frequency f:

$$C_\phi(f) = [2 - 2\,(1 - \tau_0 \mathrm{BW})^+ \cos(2\pi f \tau)] \frac{1}{f^2} S_\nu(f), \tag{8.2}$$

$$C_a(f) = [2 + 2\,(1 - \tau_0 \mathrm{BW})^+ \cos(2\pi f \tau)] \frac{1}{4} S_I(f). \tag{8.3}$$

Here $S_\nu(f)$ and $S_I(f)$ are the two-sided spectral densities of frequency noise and relative intensity noise (RIN) of the laser, BW is the resolution bandwidth of the cross-correlator (taken as 10 kHz), τ_0 is the delay time of the frequency discriminator measurement setup, and $x^+ = \max(0, x)$ is the ramp function. We assumed that noise at different offset frequencies is independent. The ramp filter term before the $\cos(2\pi f \tau)$ term is an artifact of the rectangular window chosen. Using a window with higher dynamic range decreases the filtering effect at the expense of offset frequency resolution. To separate the frequency noise and RIN, we tune the carrier frequency f_c to an integer multiple of $1/\tau_0$. In this case the correlation reads

$$\begin{aligned} C_\nu(f) = {} & 2\left[1 - (1 - \tau_0 \mathrm{BW})^+ \cos(2\pi f \tau_0)\right] S_\nu(f) \\ & - \frac{1}{2}\left[1 + (1 - \tau_0 \mathrm{BW})^+ \cos(2\pi f \tau_0)\right] \\ & \times f^2 (S_I(f_\mathrm{c} + f) + S_I(f_\mathrm{c} - f)), \end{aligned} \tag{8.4}$$

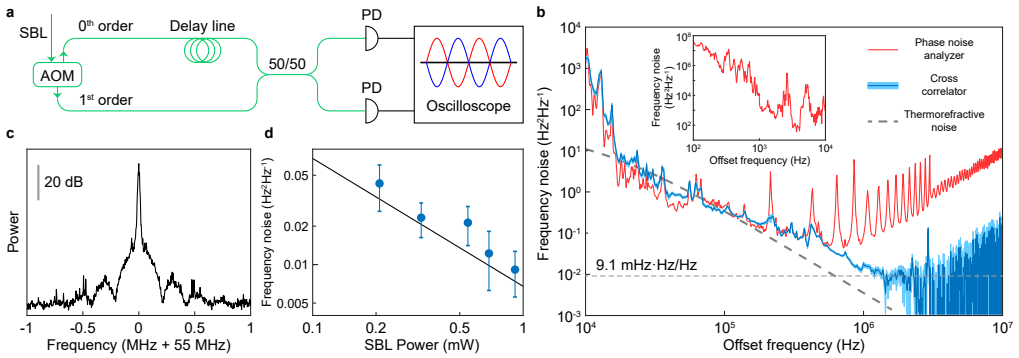

Figure 8.3: Brillouin laser frequency noise measurement. (a) Experimental setup of the optical frequency discriminator in Fig. 8.1b. (b) SBL frequency noise measured by conventional optical discriminator method in combination with an electrical phase noise analyzer (red) and by the cross-correlation technique (blue). The light blue shading shows the error range (standard error of the mean). The average frequency noise between 1.5 MHz and 2 MHz offset frequency is 9 mHz $\cdot$ Hz/Hz and is shown as a horizontal dashed line. The dashed curve (dark gray) shows the simulated thermorefractive noise for the laser mode. Inset: low-offset-frequency portion of the frequency noise as measured by the phase noise analyzer. (c) Electrical spectrum of the frequency discriminator output from a single PD. (d) Theoretical fundamental frequency noise plotted versus laser output power (black line) [6] assuming a zero alpha parameter [29]. Dots are inferred from measurement data and error bars are standard deviations.

where the modulations on frequency noise and RIN are now completely out of phase. The DC and $1/\tau_0$ frequency components of the correlations are extracted by filtering and then recombined to remove the intensity noise and estimate the frequency noise. Error bars of each correlation are determined by the variance of the correlation over different signal segments, and then propagated to the estimated frequency noise.

8.4 Frequency noise measurement

A comparison of the measurements both with and without application of the XCOR method is presented in Fig. 8.3b. Here, the red trace is a phase noise analyzer measurement of the electrical signal produced by detection of a single output from the interferometer, while the blue trace results by applying the XCOR meausurement. Both traces overlap well at low offset frequencies (below 500 kHz), and a single PD is sufficient to measure the frequency noise accurately. At these frequencies, noise is believed to be thermo-refractive in origin based on simulations [30] shown in the figure (dashed line). However, at higher offset frequencies, the noise measurement sensitivity is enhanced by 10 to 15 dB using the XCOR method. Here, the detector

noise is suppressed by cross correlation. As an aside, the Pound Drever Hall locking loop (see experimental setup in Fig. 8.1b) has a bandwidth of 10 kHz, and we believe it does not influence the measured noise at high offset frequencies.

The rising noise levels at the highest offset frequencies in the XCOR data are not believed to be fundamental and, instead, are attributed to the short averaging time resulting from the limited memory of the oscilloscope. Also, the noise spectra measured using the conventional (non XCOR) approach contain spurs that originate from destructive interference produced by the delay in the interferometer (first order corresponds to $1/\tau_0 = 214$ kHz, where $\tau_0 = 4.67$ μs is the delay time). The spectral modulations resulting from the interference are shown in Fig. 8.3c, which gives the electrical spectrum of a detected output from the interferometer. These modulations, once digitally removed in the phase noise spectra, leave the spurs as an artifact.

A narrow portion of the measured XCOR spectrum Fig. 8.3b is approximately white noise like. By averaging the measured frequency noise between 1.5 MHz to 2 MHz, this frequency noise level is estimated to be 9 mHz $\cdot$ Hz/Hz (equivalent to a Lorentzian linewidth of 60 mHz). To investigate the possible origin of this noise, we measured the frequency noise at several laser power levels. The results are summarized in Fig. 8.3d and vary inversely with laser power, which is consistent with fundamental laser frequency noise. As an additional check, the theoretical fundamental frequency noise level can be calculated and compared to the measured noise. The lasing TM2 mode has a loaded (external) quality factor of $Q_{\mathrm{T}} = 269\times10^6$ ($Q_{\mathrm{ex}} = 729\times10^6$). Using the fundamental linewidth formula for the Brillouin laser [6], the two-sided frequency noise of the laser is given by,

$$S_{\nu,\mathrm{F}} = \frac{h\nu_0^3 n_{\mathrm{th}}}{2Q_{\mathrm{T}}Q_{\mathrm{ex}}P_{\mathrm{SBL}}}, \tag{8.5}$$

where h is the Planck constant, P_{SBL} is the SBL output power, $\nu_0 = 191.8$ THz is the optical frequency of the SBL, and n_{th} is the thermal occupation of the phonon mode. At room temperature, $n_{\mathrm{th}} \approx 568$, which gives $S_{\nu,\mathrm{F}}\times P_{\mathrm{SBL}} = 6.77$ mW $\cdot$ mHz $\cdot$ Hz/Hz. The fundamental frequency noise is plotted in Fig. 8.3d assuming a zero alpha parameter [29] and is in good agreement with measured data.

It is important to also consider the level of pump frequency noise that couples into the SBL frequency noise, given by

$$S_{\nu,\mathrm{P}} = \left(\frac{\kappa}{\kappa+\Gamma}\right)^2 S_{\mathrm{P}}, \tag{8.6}$$

where S_P is the two-sided frequency noise of the pump laser, and the factor involving $\kappa = 2\pi\nu_0/Q_T$ and Γ (the Brillouin gain linewidth) gives the suppression of pump frequency noise by the Brillouin process [9]. The frequency noise of the pump laser (Newport, TLB-6728) was measured to be 90 Hz^2/Hz at 1 MHz offset frequency. This requires a Brillouin suppression factor of about 45 dB in order for coupled pump frequency noise to be less than the measured frequency noise level. Using the measured Q_T in the suppression formula gives a Brillouin gain linewidth of about $\Gamma/(2\pi) = 130$ MHz which is around 3× larger than in our previous measurements of SBL in silica [6]. This discrepancy might originate from higher-order acoustic mode participation in the two transverse mode SBL generation. Such a mode could have a larger phonon decay rate. Phonon decay rates as large as 150 MHz have been reported for silica-based structures in the literature [16]. Importantly, the SBL pumping power was varied by attenuation using the AOM (Fig. 8.1b) so that pump frequency noise S_P did not change during the collection of the data in Fig. 8.3d. It cannot therefore explain the inverse power dependence observed in Fig. 8.3d. Nonetheless, the limited spectral span of the white noise data, makes it difficult to completely confirm the origin of the noise. We are currently working towards increasing the spectral span over which ultra-low white noise level is observable.

8.5 Discussion

We have demonstrated sub-10 mHz · Hz/Hz fundamental frequency noise levels using a chip-based Brillouin laser. The low noise level results from a combination of the high-Q resonator with increased operational power through non-cascading operation. The frequency noise level was too low to measure using conventional optical discrimination methods, and cross-correlation was applied to this technique to obtain a sensitivity boost as large as 15 dB.

Several other strategies might be employed to achieve further noise level improvements. For example, increasing laser power ultimately leads to under-coupling of the pump mode to the resonator caused by back action from the lasing mode. This, in turn, decreases differential efficiency and laser power. To isolate this loading back action, a single-cascading scheme can be used (Fig. 8.4a), which would block the cascade at the second order (instead of first order). In this configuration, pump loading would remain constant. A calculation showing the potential improvement is provided in Fig. 8.4b, and a demonstration of this scheme using the same resonator as in the text is shown in Fig. 8.4c. At yet higher laser powers, parametric oscillation due to the Kerr effect within the transverse mode families could limit operation.

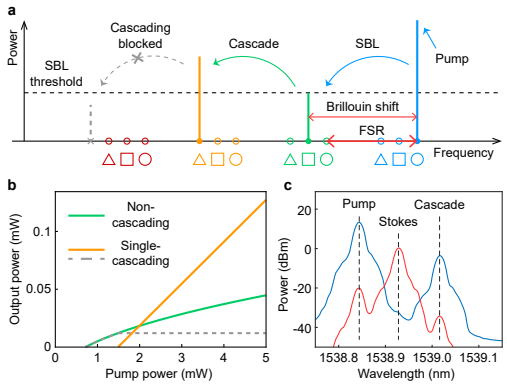

Figure 8.4: Proposed single-cascading Brillouin laser pumping scheme. (a) Spectral diagram for single-cascading Brillouin laser operation. Markers below the modes indicate their transverse mode families. (b) Calculated output laser power versus pump power for non-cascading (green) and single-cascading (orange) pumping schemes, assuming constant external coupling to resonator modes from the tapered fiber. Dashed gray line shows the output power of the first Stokes mode in the single-cascading pumping scheme, which is clamped at the lasing threshold when the first-order cascaded mode start to lase. (c) Measured optical spectrum traces showing single-cascading SBL action. Blue and red traces are the forward and backward output power from the resonator, showing the pump, Stokes, and cascade modes, and second-order cascade lasing is not observed.

However, it should be possible to inhibit this oscillation through dispersion engineering [31] or possible operation in the normal dispersion regime. Finally, operation with reduced amplitude-phase coupling is also important for minimization of the Brillouin laser linewidth [29].

Overall, the results presented here demonstrate the potential for silica-based high-Q laser platforms to achieve extremely narrow fundamental laser linewidths. Even while the noise at low offset frequencies remains high, these noise sources can be suppressed in applications such as the Sagnac gyroscope that rely upon relative noise of co-lasing waves. Likewise, applications that are sensitive to only short-term frequency noise can benefit from these improvements.

References

[1] Grudinin, I. S., Matsko, A. B. & Maleki, L. Brillouin lasing with a CaF_2 whispering gallery mode resonator. *Physical Review Letters* **102**, 043902 (2009).

[2] Tomes, M. & Carmon, T. Photonic micro-electromechanical systems vibrating

at X-band (11-GHz) rates. *Physical Review Letters* **102**, 113601 (2009).

[3] Pant, R. *et al.* On-chip stimulated Brillouin scattering. *Optics Express* **19**, 8285–8290 (2011).

[4] Lee, H. *et al.* Chemically etched ultrahigh-Q wedge-resonator on a silicon chip. *Nature Photonics* **6**, 369–373 (2012).

[5] Shen, Y. R. & Bloembergen, N. Theory of stimulated Brillouin and Raman scattering. *Physical Review* **137**, A1787–A1805 (1965).

[6] Li, J., Lee, H., Chen, T. & Vahala, K. J. Characterization of a high coherence, Brillouin microcavity laser on silicon. *Optics Express* **20**, 20170–20180 (2012).

[7] Suh, M.-G., Yang, Q.-F. & Vahala, K. J. Phonon-limited-linewidth of Brillouin lasers at cryogenic temperatures. *Physical Review Letters* **119**, 143901 (2017).

[8] Schawlow, A. L. & Townes, C. H. Infrared and optical masers. *Physical Review* **112**, 1940 (1958).

[9] Debut, A., Randoux, S. & Zemmouri, J. Linewidth narrowing in Brillouin lasers: Theoretical analysis. *Physical Review A* **62**, 023803 (2000).

[10] Gorodetsky, M. L. & Grudinin, I. S. Fundamental thermal fluctuations in microspheres. *Journal of the Optical Society of America B* **21**, 697–705 (2004).

[11] Matsko, A. B., Savchenkov, A. A., Yu, N. & Maleki, L. Whispering-gallery-mode resonators as frequency references. I. fundamental limitations. *Journal of the Optical Society of America B* **24**, 1324–1335 (2007).

[12] Loh, W. *et al.* Dual-microcavity narrow-linewidth Brillouin laser. *Optica* **2**, 225–232 (2015).

[13] Li, J., Lee, H. & Vahala, K. J. Microwave synthesizer using an on-chip Brillouin oscillator. *Nature Commun.* **4**, 2097 (2013).

[14] Li, J., Yi, X., Lee, H., Diddams, S. A. & Vahala, K. J. Electro-optical frequency division and stable microwave synthesis. *Science* **345**, 309–313 (2014).

[15] Li, J., Suh, M.-G. & Vahala, K. Microresonator Brillouin gyroscope. *Optica* **4**, 346–348 (2017).

[16] Gundavarapu, S. *et al.* Sub-hertz fundamental linewidth photonic integrated Brillouin laser. *Nature Photonics* **13**, 60–67 (2019).

[17] Lai, Y.-H. *et al.* Earth rotation measured by a chip-scale ring laser gyroscope. *Nature Photonics* **14**, 345–349 (2020).

[18] Otterstrom, N. T., Behunin, R. O., Kittlaus, E. A., Wang, Z. & Rakich, P. T. A silicon Brillouin laser. *Science* **360**, 1113–1116 (2018).

[19] Yang, K. Y. *et al.* Bridging ultrahigh-Q devices and photonic circuits. *Nature Photonics* **12**, 297–302 (2018).

[20] Van Exter, M., Kuppens, S. & Woerdman, J. Excess phase noise in self-heterodyne detection. *IEEE Journal of Quantum Electronics* **28**, 580–584 (1992).

[21] Ludvigsen, H., Tossavainen, M. & Kaivola, M. Laser linewidth measurements using self-homodyne detection with short delay. *Optics Communications* **155**, 180–186 (1998).

[22] Jin, W. *et al.* Hertz-linewidth semiconductor lasers using CMOS-ready ultra-high-Q microresonators. *Nature Photonics* (2021).

[23] Behunin, R. O., Otterstrom, N. T., Rakich, P. T., Gundavarapu, S. & Blumenthal, D. J. Fundamental noise dynamics in cascaded-order Brillouin lasers. *Physical Review A* **98**, 023832 (2018).

[24] Puckett, M., Bose, D., Nelson, K. & Blumenthal, D. J. Higher order cascaded SBS suppression using gratings in a photonic integrated ring resonator laser. In *CLEO: Science and Innovations*, SM4O–1 (Optical Society of America, 2019).

[25] Wu, L. *et al.* Greater than one billion Q-factor for on-chip microresonators. *Optics Letters* **45**, 5129–5131 (2020).

[26] Yi, X., Yang, Q.-F., Yang, K. Y., Suh, M.-G. & Vahala, K. Soliton frequency comb at microwave rates in a high-Q silica microresonator. *Optica* **2**, 1078–1085 (2015).

[27] Walls, W. F. Cross-correlation phase noise measurements. In *Proceedings of the 1992 IEEE Frequency Control Symposium*, 257–261 (IEEE, 1992).

[28] Xie, X. *et al.* Photonic microwave signals with zeptosecond-level absolute timing noise. *Nature Photonics* **11**, 44–47 (2017).

[29] Yuan, Z., Wang, H., Wu, L., Gao, M. & Vahala, K. Linewidth enhancement factor in a microcavity Brillouin laser. *Optica* **7**, 1150–1153 (2020).

[30] Kondratiev, N. & Gorodetsky, M. Thermorefractive noise in whispering gallery mode microresonators: Analytical results and numerical simulation. *Physical Letters A* **382**, 2265–2268 (2018).

[31] Yang, K. Y. *et al.* Broadband dispersion-engineered microresonator on a chip. *Nature Photonics* **10**, 316–320 (2016).

Chapter 9

LINEWIDTH ENHANCEMENT FACTOR IN A MICROCAVITY BRILLOUIN LASER

Yuan, Z., Wang, H., Wu, L., Gao, M. & Vahala, K. Linewidth enhancement factor in a microcavity Brillouin laser. *Optica* **7**, 1150–1153 (2020).

The linewidth of stimulated Brillouin lasers (SBLs) has received considerable attention for some time. SBLs based on optical fiber [1], for example, feature narrow linewidths that are useful for generation of highly stable microwave sources [2, 3]. More recently, broad interest in micro and nanoscale Brillouin devices [4] has focused attention on tiny, often chip-scale, SBLs in several systems [5–12]. These devices have high power efficiency [13], provide flexible operating wavelengths [14], and their fundamental linewidth can be reduced to less than 1 Hz [12, 13]. For these reasons they are being applied in a range of applications including radio-frequency synthesizers [15, 16], ring-laser gyroscopes [12, 17, 18], and high-coherence reference sources [9].

SBLs derive gain through a process that is parametric in nature and for which scattering of an optical pump into a Stokes wave from an acoustic phonon must be phase-matched [19, 20]. When the phonon field is strongly damped, the process mimics stimulated emission. Nonetheless, phonon participation introduces dramatic differences into SBL linewidth behavior compared with conventional lasers. For example, while the conventional Schawlow-Townes laser linewidth [21] is insensitive to temperature, the fundamental SBL linewidth is proportional to the number of thermo-mechanical quanta in the phonon mode and therefore to the Boltzmann energy $k_{\mathrm{B}}T$ [13]. This dependence has been verified from cryogenic to room temperature [22]. Brillouin lasers can also oscillate on multiple lines through the process of cascade [13], in which an initial Stokes wave can serve to pump a second Stokes wave and so forth. Cascading introduces additional contributions to the SBL linewidth [23]. Finally, the parametric nature of the process means that pump phase noise couples through to the laser linewidth, although it is strongly suppressed by the phonon damping [24].

The fundamental linewidth of lasers is increased by the well-known linewidth en-

hancement factor α that characterizes amplitude-phase coupling of the field [25]. This quantity is best known for its impact on the linewidth of semiconductor lasers [26], and its understanding, control, and measurement have long been subjects of interest [27–29]. Here, the linewidth enhancement factor is studied in SBLs. The parametric nature of Brillouin gain is shown to strongly influence this parameter. Phase mismatch causes a non-zero α factor. Measurements of SBL frequency noise are used to determine α versus controlled amounts of phase mismatch, and the results are in good agreement with theory. Significant enhancements to the linewidth are predicted and measured even when the SBL is operated only modestly away from perfect phase matching.

9.1 Main results

Amplitude-phase coupling occurs at a specified optical frequency when the real and imaginary parts of the optical susceptibility (equivalently refractive index and gain) experience correlated variations subject to a third parameter. The ratio of the real to imaginary variation is the α parameter [26]. With a non-zero α-parameter, noise that normally couples only into the laser field amplitude can also couple into the phase. And because phase fluctuations are responsible for the finite laser linewidth [25], the non-zero α-factor thereby causes linewidth enhancement. For a physical understanding of how a non zero α parameter arises within the SBL system, consider Fig. 9.1a (a detailed analysis is provided in Supplementary information). Optical pumping at frequency ω_P on a cavity mode causes a Lorentzian-shaped gain spectrum through the Brillouin process. The Brillouin gain spectrum is frequency down-shifted by the phonon frequency Ω (Brillouin shift frequency) relative to the pumping frequency. Laser action at frequency ω_L is possible when a second cavity mode lies within the gain spectrum, which requires that $\Delta\omega \equiv \omega_P - \omega_L$ is close in value to Ω. Perfect phase matching corresponds to laser oscillation at the peak of the gain (i.e. $\Delta\omega = \Omega$). Also shown in Fig. 9.1a is the refractive index spectrum associated with the gain spectrum according to the Kramers-Kronig relations. It is apparent that α (the ratio of variation of real to imaginary susceptibility) will be zero for phase-matched operation, while it increases with increased frequency detuning relative to perfect phase matching.

Analysis (Supplementary information) shows that the α-factor enhancement of the fundamental SBL linewidth $\Delta\nu_{SBL}$ is

$$\Delta\nu_{SBL} = \Delta\nu_0(1 + \alpha^2), \tag{9.1}$$

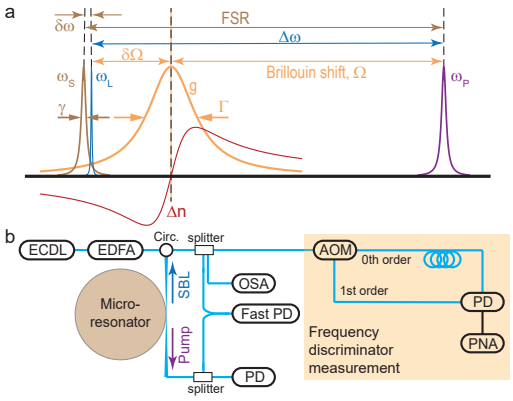

Figure 9.1: SBL phase mismatch illustration and experimental setup. (a) Brillouin gain process in the frequency domain. Purple (brown) curve refers to pump (Stokes) cavity mode at frequency ω_P (ω_S). Blue curve refers to the SBL laser signal at frequency ω_L. Orange and red curves correspond to gain (g) spectrum and refractive index (Δn), respectively. Brillouin shift frequency (Ω), gain spectrum linewidth (Γ), and cavity linewidth (γ) are also indicated. Frequency detunings $\delta\omega$ and $\delta\Omega$ are defined in the text. (b) Experimental setup for α and linewidth measurement. An external cavity diode laser (ECDL) (Newport, TLB-6728) near 1550 nm passes through an erbium-doped fiber amplifier (EDFA) and is coupled to the microcavity (a silica wedge resonator [8]) using a tapered fiber [30, 31]. Its frequency is Pound-Drever-Hall locked (not shown) to the center of cavity resonance. Pump power is controlled using an acousto-optic modulator (AOM) as an attenuator in combination with a feedback loop (not shown). The resonator diameter is around 7.1 mm, corresponding to an FSR of 10.8 GHz, which is selected to closely match the Brillouin shift frequency in silica at 1550 nm. The resonator chip temperature is actively stabilized to 26.5000 ± 0.0005°C using a temperature controller. The SBL emission propagates opposite to the direction of pumping on account of the phase-matching condition. The emission is coupled to a series of measurement instruments through a circulator. An optical spectrum analyzer (OSA) is used to record the laser and pump spectra as well as to measure SBL power. Pump and SBL signals are mixed on a fast photodetector (PD) (Thorlabs, DXM30AF) to measure their frequency difference. Another PD monitors the pumping power. An interferometer is used to measure the laser frequency noise. Therein, the laser signal is sent into an AOM which is split into frequency-shifted (1st order) and unshifted (0th order) signals. The latter is delayed in a 1-km long fiber and then the two signals are mixed on a PD (Newport, 1811-FC). The delay sets up a frequency to amplitude discriminator with discrimination gain proportional to the amount of the interferometer delay. To measure the frequency noise spectral density, the detected current is measured using an electrical phase noise analyzer (PNA) and the spectrum is fit to obtain the two-sided spectral density of the SBL laser (Supplementary information).

where $\Delta\nu_0$ is the non-enhanced ($\alpha = 0$) SBL linewidth given below as Eq. 9.3,

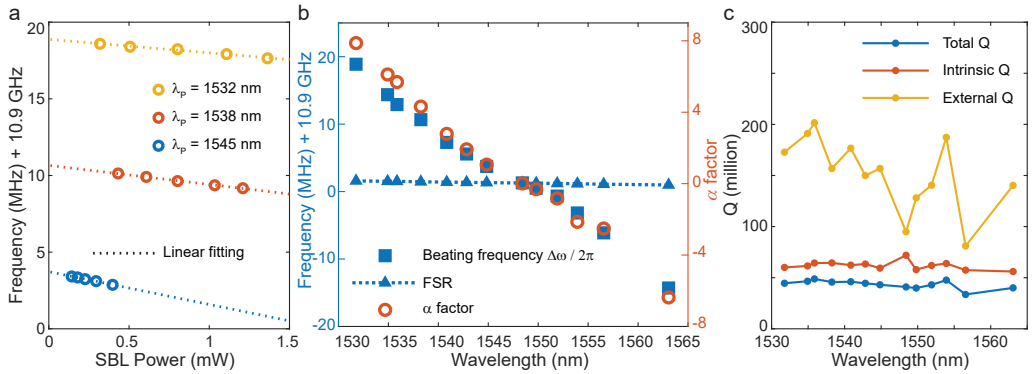

Figure 9.2: Brillouin gain phase mismatch and α factor. (a) Beating frequency between the pump laser and the SBL is plotted as a function of SBL power. Linear fitting is applied to eliminate the influence of the Kerr effect and α factor backaction, and the y-axis intercept is plotted as $\Delta\omega$ in panel (b). Blue, red, and yellow traces correspond to measurements at 1545 nm, 1538 nm, and 1532 nm, respectively. (b) The extrapolated beating frequency (squares) and FSR (triangles) are plotted versus wavelength. The calculated α factor (red circles) is plotted versus wavelength using Eq. (9.2). The Brillouin gain center occurs at around 1548 nm where FSR = $\Delta\omega$. (c) Total (Q_T), intrinsic (Q_0), and external (Q_{ex}) quality factors are plotted versus wavelength. The values are measured in the same transverse mode family.

and where the linewidth enhancement factor can be expressed using two equivalent frequency-detuning quantities relative to perfect phase matching,

$$\alpha = \frac{2\delta\Omega}{\Gamma} = \frac{2\delta\omega}{\gamma}. \tag{9.2}$$

In the first equality, phonon mode detuning $\delta\Omega \equiv \Omega - \Delta\omega$ is normalized by Γ, the Brillouin gain bandwidth (i.e. phonon decay rate constant). In the second equality, optical mode detuning $\delta\omega \equiv \Delta\omega - \mathrm{FSR}$ (FSR is the unpumped cavity free-spectral-range) is normalized by γ, the photon decay rate constant. Note that the sign of α changes to either side of perfect phase matching. Also, as an aside, $\delta\omega$ is the mode pulling induced by the Brillouin gain spectrum [13]. $\Delta\nu_0$ is given by

$$\Delta\nu_0 = \left(\frac{\Gamma}{\gamma+\Gamma}\right)^2 \frac{\hbar\omega_L^3 n_{th}}{4\pi Q_T Q_{ex} P_{SBL}}, \tag{9.3}$$

where $\hbar$ is the reduced Planck's constant, P_{SBL} is the SBL output power, and n_{th} is the number of thermal quanta in the phonon mode. This expression is the same as that derived in ref. [13], except for omission of the zero-point energy terms and also inclusion of the near-unity correction factor $[\Gamma/(\gamma+\Gamma)]^2$ relating to the finite damping rate of the phonons (derivation in Supplementary information).

As a first step towards verification of Eqs. (9.1) and (9.2), it is necessary to measure the phase mismatch detuning at each point where linewidth will be measured. The experimental setup and information on the high-Q silica whispering-gallery microcavity used to generate Brillouin laser action are provided in Fig. 9.1b and its caption. To vary the phase mismatch detuning, the pump laser wavelength λ_P is tuned, which is achieved by selecting different longitudinal modes within the same transverse mode family as pump and Stokes modes. This has the effect of varying Ω through the relationship $\Omega = 4\pi n c_s/\lambda_P$ (n: refractive index, c_s: speed of sound in the microcavity). Since Ω is not directly measurable in the experiment, we instead obtained information on the phase mismatch using $\delta\omega$, which requires measurement of $\Delta\omega$ and FSR.

The frequency $\Delta\omega$ is determined by first measuring the beating frequency of the pump and the SBL using a fast photodetector, followed by measurement of the detected current on an electrical spectrum analyzer. Beyond being influenced by mode pulling as noted above, this beating frequency is also slightly shifted via backaction of the amplitude-phase coupling (Supplementary information) and the optical Kerr effect [32], both of which are proportional to the SBL powers. Therefore, to account for these effects, the beatnote frequencies were measured at 5 different SBL power levels. Representative measurements performed at three pump wavelengths are shown in Fig. 9.2a. The y-intercept of these plots provides the required beating frequency in the absence of the above effects and a summary plot of a series of such measurements is provided as the blue-square data points in Fig. 9.2b. As an aside, the data point near 1559 nm is missing because of strong mode crossings at this wavelength in the SBL microcavity (i.e. higher-order mode families become degenerate with the SBL mode family).

To determine the FSR at each pumping wavelength, the mode spectrum of the resonator is measured by scanning a tunable laser whose frequency is measured using a radio-frequency calibrated interferometer [33]. The measured FSR is plotted versus wavelength as the dotted line in Fig. 9.2b. Measurement of the FSR this way also ensured that pumping was performed on the same transverse mode family as the pumping wavelength was tuned. This is important since mode volume would change strongly were mode family to change. In Fig. 9.2b, the phase-matching condition (gain center) occurs when FSR equals $\Delta\omega$ ($\delta\omega = 0$) at around 1548 nm pump wavelength. We can also use the Brillouin shift at gain center to infer that $c_s = 5845$ m/s, which is consistent with the material properties of silica [34].

Finally, γ is determined by measurement of the cavity linewidth at each wavelength (equivalently, the total Q-factor Q_T of the resonator). By measurement of both linewidth and transmission on cavity resonance, it is possible to extract both the intrinsic Q-factor Q_0 and external coupling Q-factor Q_{ex} at each wavelength ($1/Q_T = 1/Q_0 + 1/Q_{ex}$). A plot of the results is provided in Fig. 9.2c. The Q_0 values inferred this way are relatively constant across the measured modes, while the Q_{ex} exhibits variation that reflects wavelength dependency of the coupling condition. The Q factors are significantly lower than state-of-the-art resonators of the same kind [8], which is intentional and increases the sensitivity of noise measurement that follows. Using Eq. 9.2, the theoretical α factor as a function of wavelength from 1532 nm to 1563 nm is plotted in Fig. 9.2b (red circles). Deviations of beating frequency and the α factor from a linear trend are a result of variations of total Q factor across the measured wavelengths. The largest α factor is greater than 7 so that a fundamental linewidth enhancement of more than $1 + 7^2 = 50$ is expected at the largest detuning values.

A frequency discriminator method [35, 36] is used to measure the noise spectrum of the two-sided white frequency noise spectral density S_w of the SBL as described in the Fig. 9.1b caption. The fundamental noise component in S_w, defined as S_F, is related to the fundamental SBL linewidth through $2\pi S_F = \Delta\nu_{SBL}$ [32] where $\Delta\nu_{SBL}$ is given in Eq. 9.3. And the inverse power dependence contained in $\Delta\nu_{SBL}$ is used to extract S_F from the measurement of S_w. Data plots of S_w versus inverse power at three pumping wavelengths are shown in the inset of Fig. 9.3 and reveal this power dependence. Of importance to this measurement is that optical pumping power was controlled by attenuation of the pump so that its phase noise was constant throughout the measurement. Therefore, only the intrinsic contribution to linewidth could cause the observed power dependence. The slope is equal to S_F normalized to an output power of 1 mW. Linear fitting provides the slopes which are plotted versus wavelength in the main panel of Fig. 9.3. The corresponding minimum measured fundamental noise is about S_F =0.2 Hz^2/Hz ($\Delta\nu_{SBL}$ = 1.25 Hz) near the phase matching condition (gain center), and the maximum fundamental noise is more than S_F =10 Hz^2/Hz ($\Delta\nu_{SBL}$ = 63 Hz), corresponding to 50× noise enhancement, at the largest mismatch detunings. Comparison to Eq. (9.3) is provided as the green plot in Fig. 9.3. In this plot Q_T, Q_{ex} and α (Fig. 9.2b and c) measurements at each wavelength are used with no free parameters. γ can be obtained from Q_T, and we can infer $\Gamma/2\pi$ to be 34.7 MHz, assuming it is constant over wavelength. Also, n_{th}= 572 is used (corresponding to the operating temperature of 26.5 °C). There

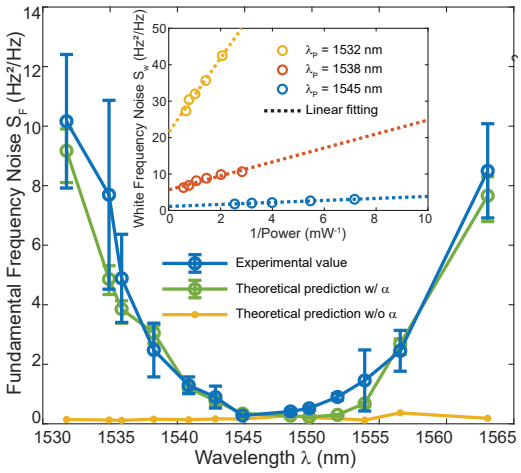

Figure 9.3: SBL frequency noise enhancement. Measured SBL frequency noise S_F (blue); theoretical S_F (Eqn. 9.3) prediction (green) with α obtained from Fig. 9.2b; and non-enhanced S_0 formula (α=0) [13] prediction (yellow); all plotted versus pump wavelength normalized to 1 mW output power. Error bars on the S_F noise correspond to the error in determining slope (see inset). Error bars on the Eqn. 9.3 prediction mainly arise from errors in $\Delta\omega$ and Q measurement errors. Variations of the α=0 prediction mainly arise from Q_{ex} differences. Inset: SBL frequency noise S_w is plotted versus the reciprocal of SBL output power. A linear fitting is applied to determine S_F from the slope, and then plotted in the main panel. Blue, red, and yellow data correspond to measurements at 1545 nm, 1538 nm, and 1532 nm, respectively.

is overall good agreement with the measured linewidth values. The conventional $S_0 = \Delta\nu_0/(2\pi)$ (with α=0) is also plotted for comparison.

The nonzero intercept on the y axis of the inset to Fig. 9.3 is believed to be associated with transferred pump phase noise associated with imperfect PDH locking. This contribution will increase with increasing α. Both it and the linewidth contribution of the pump phase noise are discussed in Supplementary information. We have also verified the α measurement results in another SBL resonator. Details can be found in Supplementary information.

As an aside, relative intensity noise of the SBLs is another important characteristic of laser operation, and a typical measured spectrum is shown in Supplementary information. Also, as noted in the introduction, Brillouin lasers can oscillate multi-line by cascade [13], and under these conditions additional terms appear in the linewidth expression [23]. In the context of the present discussion, it is therefore of interest to consider the impact of the α factor on linewidth under conditions of cascaded operation. This is done in Supplementary information.

We have studied the linewidth enhancement factor α in a Brillouin laser. A modification to the fundamental linewidth formula that incorporates the α factor was theoretically derived and then tested experimentally in a high-Q silica whispering gallery resonator. Phase matching of the Brillouin process determines the sign and magnitude of α. Under perfect phase-matching conditions, corresponding to laser oscillation at the Brillouin gain maximum, α=0. However, measurement and theory show that the mismatch (induced here by tuning of the pumping wavelength) leads to α factors greater than 7 yielding frequency noise and fundamental linewidth enhancement as large as 50×. The sign of α can also be controlled through the sign of the frequency mismatch detuning. Although the phase-matching condition was controlled here by tuning of pumping wavelength, it should also be possible to vary phase matching and therefore α through control of the temperature. This would vary the Brillouin shift frequency by way of the temperature dependence of the sound velocity. The results presented here stress the importance of proper pumping wavelength selection and observance of temperature control for narrow linewidth operation of SBLs. These considerations will be important in all applications of these devices that are sensitive to frequency noise and linewidth.

9.2 Supplementary information

Derivation of the Alpha factor in Brillouin lasers

We derive the α factor in stimulated Brillouin laser (SBL) systems by starting from the Hamiltonian of the system:

$$H = \hbar(\omega_{\mathrm{P}}\tilde{A}^{\dagger}\tilde{A} + \omega_{\mathrm{s}}\tilde{a}^{\dagger}\tilde{a} + \Omega\tilde{b}^{\dagger}\tilde{b}) + \hbar g_{\mathrm{B}}(\tilde{A}^{\dagger}\tilde{a}\tilde{b} + \tilde{A}\tilde{a}^{\dagger}\tilde{b}^{\dagger}), \tag{9.4}$$

where $\tilde{A}$, $\tilde{a}$, and $\tilde{b}$ are the lowering operators of the pump, Stokes, and phonon modes, respectively; ω_{P}, ω_{s}, and Ω are the resonance frequencies of the pump, Stokes, and phonon modes, respectively; and g_{B} is the single-particle Brillouin coupling [13]. We have ignored terms that are strongly out of phase match (i.e. energy non-conserving) in the Hamiltonian to simplify the discussion. The fast time dependencies are removed from the operators as follows:

$$A \equiv \tilde{A}\exp(i\omega_{\mathrm{P,in}}t), \tag{9.5}$$

$$a \equiv \tilde{a}\exp(i\omega_{\mathrm{L}}t), \tag{9.6}$$

$$b \equiv \tilde{b}\exp(i\Omega_{\mathrm{L}}t), \tag{9.7}$$

where A, a, and b are the slow-varying lowering operators; $\omega_{\mathrm{P,in}}$ is the pumping frequency; ω_{L} is the SBL frequency and Ω_{L} is the mechanical vibration frequency.

Replacing the operators with the slow-varying ones results in an effective Hamiltonian:

$$H = \hbar(\delta\omega_{\mathrm{P}} A^{\dagger}A + \delta\omega a^{\dagger}a + \delta\Omega b^{\dagger}b) + \hbar g_{\mathrm{B}}(A^{\dagger}ab + Aa^{\dagger}b^{\dagger}), \tag{9.8}$$

where $\delta\omega_{\mathrm{P}} \equiv \omega_{\mathrm{P}} - \omega_{\mathrm{P,in}}$ is the pump mode frequency detuning compared to the external pump, and $\delta\omega \equiv \omega_{\mathrm{s}} - \omega_{\mathrm{L}}$ ($\delta\Omega \equiv \Omega - \Omega_{\mathrm{L}}$) is the detuning of Stokes (phonon) cavity mode compared to the laser (mechanical vibration) frequency. We note that the slow-varying amplitudes are directly referenced to the true oscillating frequencies of each mode instead of the resonance frequencies, which removes the fast time dependence in the interaction terms.

The Heisenberg equations of motion for the Stokes mode and the phonon mode are derived. Then, the quantum operators are replaced with classical fields as the dominant source of noise in this system is the phonon thermal noise [13]. Finally, phenomenological damping terms are inserted as follows,

$$\frac{da}{dt} = -\left(\frac{\gamma}{2} + i\delta\omega\right) a - ig_{\mathrm{B}} A b^{*}, \tag{9.9}$$

$$\frac{db}{dt} = -\left(\frac{\Gamma}{2} + i\delta\Omega\right) b - ig_{\mathrm{B}} A a^{*}, \tag{9.10}$$

where γ (Γ) is the energy decay rates for the Stokes (phonon) mode.

We first seek nonzero steady-state solutions to the above equations that represent SBLs. By writing the equation for b^{*} using Eq. (9.10),

$$\frac{db^{*}}{dt} = -\left(\frac{\Gamma}{2} - i\delta\Omega\right) b^{*} + ig_{\mathrm{B}} A^{*} a, \tag{9.11}$$

the equations (9.9) and (9.11) form a linear system in a and b^{*}. The requirement for nonzero solutions (i.e. zero determinant of the coefficient matrix) gives the equation:

$$\left(\frac{\gamma}{2} + i\delta\omega\right)\left(\frac{\Gamma}{2} - i\delta\Omega\right) - g_{\mathrm{B}}^{2}|A|_{0}^{2} = 0, \tag{9.12}$$

where the subscript 0 indicates steady state. This complex equation can be solved as

$$\frac{2\delta\omega}{\gamma} = \frac{2\delta\Omega}{\Gamma}, \tag{9.13}$$

$$g_{\mathrm{B}}^{2}|A|_{0}^{2} = \frac{\gamma\Gamma}{4}\left(1 + \frac{4\delta\Omega^{2}}{\Gamma^{2}}\right). \tag{9.14}$$

For convenience, we define $\alpha \equiv 2\delta\omega/\gamma = 2\delta\Omega/\Gamma$ and later demonstrate that α is indeed the linewidth enhancement factor. With α defined, the steady-state pump

photon number is

$$|A|_0^2 = \frac{\gamma\Gamma}{4}\frac{1+\alpha^2}{g_B^2} = \frac{\gamma}{2g}(1+\alpha^2), \tag{9.15}$$

where the Brillouin gain coefficient $g = 2g_B^2/\Gamma$ has been defined. Since $\Gamma \gg \gamma$ in our microcavity system, we can adiabatically eliminate b^* from Eq. (9.9) by setting $db^*/dt = 0$ in Eq. (9.11),

$$\frac{da}{dt} = \left(-\frac{\gamma}{2} + \frac{g|A|^2}{1+\alpha^2}\right)(1+i\alpha)\,a, \tag{9.16}$$

where the definition of α has been used. Here, $|A|^2$ implicitly depends on a through the pump mode dynamics and controls the gain saturation. Alternatively, Eqn. 9.16 can be represented using the amplitude $|a|$ and phase $\phi_a = \ln(a/a^*)/(2i)$ variables,

$$\frac{d|a|}{dt} = \left(-\frac{\gamma}{2} + \frac{g|A|^2}{1+\alpha^2}\right)|a|, \tag{9.17}$$

$$\frac{d\phi_a}{dt} = \left(-\frac{\gamma}{2} + \frac{g|A|^2}{1+\alpha^2}\right)\alpha, \tag{9.18}$$

which illustrates that $\alpha = |a|\dot{\phi}_a/|\dot{a}|$ represents amplitude-phase coupling.

Henry [26] defined the α factor as the ratio of the change in real part of the refractive index and the change in the imaginary part. Below we show that this interpretation is consistent with that derived from the coupled-mode equations. For a system with Lorentzian gain, the imaginary part of the gain-induced susceptibility can be written as

$$\chi_I(\omega_B) = -\frac{\chi_B}{1+4\omega_B^2/\Gamma^2}, \tag{9.19}$$

where Γ is the gain bandwidth, χ_B is a positive constant describing the strength of the gain at the line center, and the angular frequency ω_B is referenced to the gain center (i.e. detuning relative to gain center). By the Kramers-Kronig relations, χ_I necessarily leads to the real part of the susceptibility χ_R through the relation,

$$\chi_R(\omega_B) = \frac{1}{\pi}\int_{-\infty}^{\infty}\frac{\chi_I(\omega_B')}{\omega_B' - \omega_B}d\omega_B' = \chi_B\frac{2\omega_B/\Gamma}{1+4\omega_B^2/\Gamma^2}. \tag{9.20}$$

The refractive index can be written as $n(\omega_B)^2 = n^2 + \chi_R + i\chi_I$, where n is the material refractive index (dispersion in n has been ignored). Assuming $\chi_B \ll n^2$, we can find the real part n' and imaginary part n'' of the refractive index:

$$n' = n + \frac{\chi_R}{2n} = n + \frac{\chi_B}{2n}\frac{2\omega_B/\Gamma}{1+4\omega_B^2/\Gamma^2}, \tag{9.21}$$

$$n'' = \frac{\chi_{\mathrm{I}}}{2n} = -\frac{\chi_{\mathrm{B}}}{2n}\frac{1}{1+4\omega_{\mathrm{B}}^2/\Gamma^2}. \tag{9.22}$$

The α factor can then be obtained as

$$\alpha = -\frac{\partial n'/\partial\chi_{\mathrm{B}}}{\partial n''/\partial\chi_{\mathrm{B}}} = \frac{2\omega_{\mathrm{B}}}{\Gamma}. \tag{9.23}$$

Setting $\omega_{\mathrm{B}} = \delta\Omega$ recovers the desired result, $\alpha = 2\delta\Omega/\Gamma$. There are different conventions regarding the sign of α, and here we choose the negative sign which would be consistent with the $\exp(-i\omega t)$ phasor used throughout.

To further establish the connection of α to linewidth broadening, the SBL linewidth is derived. We will again assume $\Gamma \gg \gamma$ and defer the more general case to Section 3. For this analysis we add classical noise terms to Eqs. (9.9) and (9.10),

$$\frac{da}{dt} = -\frac{\gamma}{2}(1+i\alpha)\,a - ig_{\mathrm{B}}Ab^* + f_a(t), \tag{9.24}$$

$$\frac{db}{dt} = -\frac{\Gamma}{2}(1+i\alpha)\,b - ig_{\mathrm{B}}Aa^* + f_b(t), \tag{9.25}$$

where f_a and f_b are classical noise operators for the Stokes and phonon mode, respectively, satisfying the following correlations:

$$\langle f_a^*(t+\tau)f_a(t)\rangle = 0, \tag{9.26}$$

$$\langle f_b^*(t+\tau)f_b(t)\rangle = n_{\mathrm{th}}\Gamma\delta(\tau), \tag{9.27}$$

and n_{th} is the number of thermal quanta in the phonon mode (thermal quanta in the optical modes are negligible at room temperature).

Adiabatically eliminating b gives

$$\frac{da}{dt} = \left(-\frac{\gamma}{2} + \frac{g|A|^2}{1+\alpha^2}\right)(1+i\alpha)\,a + \tilde{f}_a(t), \tag{9.28}$$

$$\tilde{f}_a \equiv f_a - \frac{ig_{\mathrm{B}}A}{1-i\alpha}\frac{2}{\Gamma}f_b^*, \tag{9.29}$$

where we defined a composite fluctuation term $\tilde{f}_a$ for the SBL. Its correlation reads

$$\begin{aligned}\langle \tilde{f}_a^*(t)\tilde{f}_a(0)\rangle &= \langle f_a^*(t)f_a(0)\rangle + \frac{g_{\mathrm{B}}^2|A|_0^2}{1+\alpha^2}\frac{4}{\Gamma^2}\langle f_b^*(t)f_b(0)\rangle \\ &= n_{\mathrm{th}}\gamma\delta(t),\end{aligned} \tag{9.30}$$

which is independent of α. Applying a standard linewidth analysis, the SBL linewidth is found as

$$\Delta\omega_{\mathrm{SBL}} = \frac{\gamma}{2N_a}n_{\mathrm{th}}\left(1+\alpha^2\right), \tag{9.31}$$

where $N_a = |a|^2$ is the steady-state photon number in the Stokes mode. This is readily shown to agree with Eq. (3) in the main text in the limit of $\Gamma \to \infty$ when expressed in terms of output SBL power.

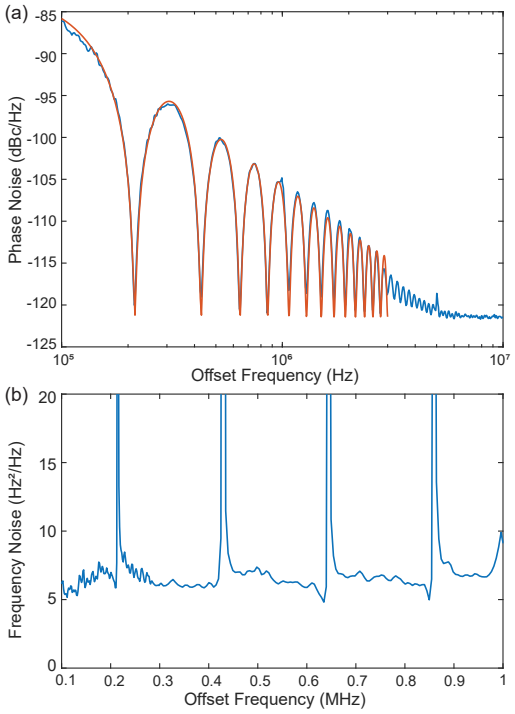

Figure 9.4: SBL noise measurement and fitting. (a) Blue curve is the measured phase noise spectrum from the self-heterodyne output when pump wavelength is 1538 nm and SBL power is 1.29 mW. Red curve is the fitting according to Eq. (9.36) to obtain the frequency noise S. (b) The converted frequency noise spectrum from panel (a).

Frequency discriminator measurements

In this section, the frequency noise measurement is studied to arrive at the transfer function that relates the measured phase noise spectrum (see Fig. 9.4 (a)) to the frequency noise spectral density S plotted in Fig. 3 of the main text. As shown in the Supplementary information of our previous work [8], pump noise conversion is believed to be the dominant noise source at low offset frequency, while white Schawlow-Townes-like noise dominates at high offset frequency (usually over 100 kHz).

For white frequency noise, the correlation of the time derivative of the phase satisfies

$$\langle \dot{\phi}(t+\tau)\dot{\phi}(t)\rangle = \Delta\omega_{\mathrm{N}}\delta(\tau), \tag{9.32}$$

where $\Delta\omega_{\mathrm{N}}$ is the Lorentzian full-width-at-half-maximum linewidth in rad/s, including both fundamental ($\Delta\omega_{\mathrm{SBL}}$) and technical contributions. The two-sided spectral density function for the instantaneous frequency $\nu \equiv \dot{\phi}/(2\pi)$ is given by the Fourier

transform of the correlation function:

$$S_{\mathrm{w}} = \frac{1}{4\pi^2}\int_{-\infty}^{\infty}\langle\dot{\phi}(t+\tau)\dot{\phi}(t)\rangle e^{-2\pi i f\tau}d\tau = \frac{\Delta\omega_{\mathrm{N}}}{4\pi^2}, \tag{9.33}$$

where S_{w} is the white frequency noise spectral density as in the main text.

On account of the time delayed path in the frequency discrimination system, the detected output returns a signal with a noisy phase $\phi(t+\tau) - \phi(t)$, where τ is the interferometer delay. We are thus interested in the frequency noise of $\nu(\tau) \equiv (\dot{\phi}(t+\tau) - \dot{\phi}(t))/(2\pi)$. By the time-shifting property of the Fourier transform,

$$S_{\nu(\tau)}(f) = S_{\mathrm{w}}(2 - e^{2\pi i f\tau} - e^{-2\pi i f\tau}) = 4\sin^2(\pi f\tau)S_{\mathrm{w}}. \tag{9.34}$$

The detected output from the self-heterodyne interferometer is analyzed by a phase noise analyzer. Therefore, converting to phase noise gives

$$S_{\phi(\tau)}(f) = \frac{1}{f^2}S_{\nu(\tau)}(f) = 4\frac{\sin^2(\pi f\tau)}{f^2}S_{\mathrm{w}}. \tag{9.35}$$

A typical measured phase-noise spectrum is shown in Fig. 9.4. In fitting the spectrum, there is both the sinc^2-shaped noise spectrum contributed by the SBL laser, and a noise floor contributed by the photodetector noise equivalent power (NEP). Thus, the following equation is used to describe the total phase noise,

$$S_{\mathrm{Total},\phi}(f) = S_{\mathrm{NEP}} + 4\pi^2\tau^2\mathrm{sinc}^2(\pi f\tau)S_{\mathrm{w}}, \tag{9.36}$$

where $\mathrm{sinc}(z) \equiv \sin z/z$, $S_{\mathrm{Total},\phi}(f)$ is the total measured phase noise, and S_{NEP} is the NEP contributed phase noise (determined by averaging the measured phase noise between 8 MHz to 10 MHz). S_{w} and the time delay τ are fitting parameters in the measurement (the fiber delay has around 1 km length and therefore provides an approximate delay of $\tau \approx 4.67$ μs). The fitting is performed within the frequency range between 0.1 MHz and 3 MHz, since technical noise becomes significant below 0.1 MHz, while the fringe contrast is reduced for frequencies higher than 3 MHz on account of reduced resolution.

To explicitly illustrate that the measured noise is approximately white over this frequency range, we convert the phase noise from discriminator measurement to frequency noise by dividing out the response function, $4\pi^2\tau^2\mathrm{sinc}^2(\pi f\tau)$. As shown in Fig. 9.4 (b), the overall frequency noise is nearly white except for some spikes resulting from zeros in the response function in combination with the NEP noise contributions.

Full analysis of the Brillouin laser noise

In this section, a more complete analysis of the SBL frequency noise is presented that includes both the effect of the pumping noise and also does not make the adiabatic approximation (i.e. $\Gamma \gg \gamma$). The equations of motion for the Stokes, phonon, and pump mode amplitudes, with damping and pumping terms, are:

$$\frac{da}{dt} = -\frac{\gamma}{2}(1+i\alpha)\,a - ig_{\mathrm{B}}Ab^*, \tag{9.37}$$

$$\frac{db}{dt} = -\frac{\Gamma}{2}(1+i\alpha)\,b - ig_{\mathrm{B}}Aa^*, \tag{9.38}$$

$$\frac{dA}{dt} = -\left(\frac{\gamma}{2} + i\delta\omega_{\mathrm{P}}\right)A - ig_{\mathrm{B}}ab + \sqrt{\kappa}A_{\mathrm{in}}, \tag{9.39}$$

where the pump and Stokes mode have the same decay rate γ, κ is the external coupling rate, $A_{\mathrm{in}} > 0$ is the external pumping amplitude (normalized to photon rate), and the other symbols have the same meaning as in Section 1.

It is convenient to work with amplitude ($|a|, |b|, |A|$) and phase ($\phi_a = \ln(a/a^*)/(2i)$, similar definitions for ϕ_b and ϕ_A) variables. Their equations can be rewritten as

$$\frac{d|a|}{|a|dt} = -\frac{\gamma}{2} + g_{\mathrm{B}}\frac{|A||b|}{|a|}\sin\theta, \tag{9.40}$$

$$\frac{d|b|}{|b|dt} = -\frac{\Gamma}{2} + g_{\mathrm{B}}\frac{|A||a|}{|b|}\sin\theta, \tag{9.41}$$

$$\frac{d|A|}{|A|dt} = -\frac{\gamma}{2} - g_{\mathrm{B}}\frac{|a||b|}{|A|}\sin\theta + \sqrt{\kappa}\frac{A_{\mathrm{in}}}{|A|}\cos\phi_A, \tag{9.42}$$

$$\frac{d\phi_a}{dt} = -\frac{\gamma}{2}\alpha - g_{\mathrm{B}}\frac{|A||b|}{|a|}\cos\theta, \tag{9.43}$$

$$\frac{d\phi_b}{dt} = -\frac{\Gamma}{2}\alpha - g_{\mathrm{B}}\frac{|A||a|}{|b|}\cos\theta, \tag{9.44}$$

$$\frac{d\phi_A}{dt} = -\delta\omega_{\mathrm{P}} - g_{\mathrm{B}}\frac{|a||b|}{|A|}\cos\theta - \sqrt{\kappa}\frac{A_{\mathrm{in}}}{|A|}\sin\phi_A, \tag{9.45}$$

where we defined the phase difference $\theta = \phi_A - \phi_a - \phi_b$. The steady-state solutions (indicated by a subscript 0) are given by,

$$\cos\theta_0 = -\frac{\alpha}{\sqrt{1+\alpha^2}}, \tag{9.46}$$

$$\sin\theta_0 = \frac{1}{\sqrt{1+\alpha^2}}, \tag{9.47}$$

$$|A|_0^2 = \frac{\gamma}{2g}\left(1+\alpha^2\right), \tag{9.48}$$

$$|b|_0^2 = \frac{\gamma}{\Gamma} N_a, \tag{9.49}$$

$$\sqrt{\kappa} A_{\text{in}} \cos\phi_{A,0} = |A|_0 \left(\frac{\gamma}{2} + \frac{g N_a}{1+\alpha^2} \right), \tag{9.50}$$

$$\delta\omega_{\text{P}} = \frac{\alpha}{1+\alpha^2} g N_a - \sqrt{\kappa} \frac{A_{\text{in}}}{|A|_0} \sin\phi_{A,0}, \tag{9.51}$$

where we used the definition $g = 2g_{\text{B}}^2/\Gamma$. Also, although we expressed everything in terms of SBL photon numbers $N_a \equiv |a|_0^2$, it is the input amplitude A_{in} that determines N_a.

Because the pump mode is Pound-Drever-Hall (PDH) locked to the cavity resonance $\phi_{A,0} = 0$. Thus, the input amplitude and detuning can be further simplified as

$$\sqrt{\kappa} A_{\text{in},0} = \left(\frac{\gamma}{2} + \frac{g N_a}{1+\alpha^2} \right) \sqrt{\frac{\gamma}{2g}} \sqrt{1+\alpha^2}, \tag{9.52}$$

$$\delta\omega_{\text{P},0} = \frac{\alpha}{1+\alpha^2} g N_a, \tag{9.53}$$

We note that the $\delta\omega_{\text{P},0}$ obtained here is, up to zeroth order of γ/Γ, equal to the negative of beatnote change between the pump and SBL signals induced by amplitude-phase coupling, as measured in Fig. 2a in the main text.

After the steady-state solutions are obtained, the dynamical equations are linearized by defining relative amplitude change variables (e.g., $\delta a = |a|/|a|_0 - 1$) and phase change variables (e.g., $\delta\phi_a = \phi_a - \phi_{a,0}$). Also, Langevin terms are added to the right side of the equations. These are, as before, classical and include only the thermal noise contributions. The linearized equations with noise terms are:

$$\frac{d\delta a}{dt} = \frac{\gamma}{2}(\delta A + \delta b - \delta a - \alpha\delta\theta) + f_{\delta a}, \tag{9.54}$$

$$\frac{d\delta b}{dt} = \frac{\Gamma}{2}(\delta A + \delta a - \delta b - \alpha\delta\theta) + f_{\delta b}, \tag{9.55}$$

$$\frac{d\delta A}{dt} = -\frac{\gamma}{2}\delta A - \frac{g N_a}{1+\alpha^2}(\delta a + \delta b - \alpha\delta\theta), \tag{9.56}$$

$$\frac{d\delta\phi_a}{dt} = \frac{\gamma}{2}(\alpha\delta A + \alpha\delta b - \alpha\delta a + \delta\theta) + f_{\delta\phi,a}, \tag{9.57}$$

$$\frac{d\delta\phi_b}{dt} = \frac{\Gamma}{2}(\alpha\delta A + \alpha\delta a - \alpha\delta b + \delta\theta) + f_{\delta\phi,b}, \tag{9.58}$$

$$\begin{aligned}\frac{d\delta\phi_A}{dt} = {} & \frac{g N_a}{1+\alpha^2}(\alpha\delta a + \alpha\delta b - \alpha\delta A + \delta\theta) \\ & - \left(\frac{\gamma}{2} + \frac{g N_a}{1+\alpha^2} \right)(\delta\phi_A + f_{\delta\phi,A}),\end{aligned} \tag{9.59}$$

where f_z represents noise input to the variable z. It is convenient to switch to the frequency domain using $d/dt \to i\omega$. The power spectral density of each noise term can be written as

$$S_{f,\delta a} = S_{f,\delta\phi,a} = 0, \tag{9.60}$$

$$S_{f,\delta b} = S_{f,\delta\phi,b} = \frac{n_{\text{th}}}{2}\frac{\Gamma}{|b|_0^2}, \tag{9.61}$$

$$S_{f,\delta\phi,A} = S_{\phi,\text{Pump}}, \tag{9.62}$$

where $S_{\phi,\text{Pump}}$ is the input phase noise contributed by the pump, and each noise term is independent of others. We have ignored the relative intensity noise of the pump, but it can also be analyzed similarly.

The above linear equations can be directly inverted, and the solution for $\delta\phi_a$ is, to the lowest order in ω,

$$\begin{aligned}\delta\phi_a = &\frac{i}{(\gamma+\Gamma)\omega}\left(\alpha\Gamma f_{\delta a} - \alpha\gamma f_{\delta b} - \Gamma f_{\delta\phi,a} + \gamma f_{\delta\phi,b}\right)\\ &- \frac{\gamma}{\gamma+\Gamma} f_{\delta\phi,A},\end{aligned} \tag{9.63}$$

where the lowest order of ω approximation remains valid when $\omega \ll \gamma$. From here we obtain the phase noise of the SBL,

$$\begin{aligned}S_{\phi,\text{SBL}} = &\frac{\alpha^2\Gamma^2 S_{f,\delta a} + \alpha^2\gamma^2 S_{f,\delta b} - \Gamma^2 S_{f,\delta\phi,a} + \gamma^2 S_{f,\delta\phi,b}}{(\gamma+\Gamma)^2\omega^2}\\ &+ \left(\frac{\gamma}{\gamma+\Gamma}\right)^2 S_{f,\delta\phi,A},\end{aligned} \tag{9.64}$$

$$S_{\phi,\text{SBL}} = \frac{\Gamma^2\left(1+\alpha^2\right)}{(\gamma+\Gamma)^2\omega^2}\frac{\gamma}{2N_a}n_{\text{th}} + \left(\frac{\gamma}{\gamma+\Gamma}\right)^2 S_{\phi,\text{Pump}}. \tag{9.65}$$

Converting to frequency noise gives

$$S_{\nu,\text{SBL}} = \frac{\Gamma^2\left(1+\alpha^2\right)}{4\pi^2(\gamma+\Gamma)^2}\frac{\gamma}{2N_a}n_{\text{th}} + \left(\frac{\gamma}{\gamma+\Gamma}\right)^2 S_{\nu,\text{Pump}}. \tag{9.66}$$

Thus, the fundamental linewidth of the SBL is given by

$$\Delta\omega_{\text{SBL}} = \left(\frac{\Gamma}{\gamma+\Gamma}\right)^2\left(1+\alpha^2\right)\frac{\gamma}{2N_a}n_{\text{th}}. \tag{9.67}$$

Note that the above derivation automatically incorporates non-adiabaticity and the linewidth enhancement factor. Also, the transduction of the pump phase noise is, when the pump mode is PDH locked,

$$S_{\nu,\text{SBL}} = \left(\frac{\gamma}{\gamma+\Gamma}\right)^2 S_{\nu,\text{P}}, \tag{9.68}$$

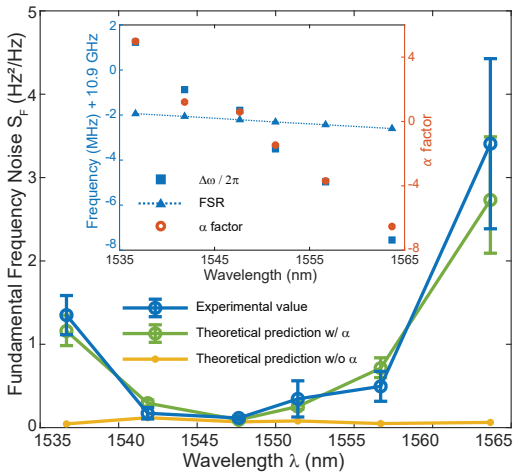

Figure 9.5: SBL frequency noise enhancement measured using a second device. Measured SBL fundamental frequency noise S_{F} (blue); theoretical S_{F} prediction (green) with α obtained from the plot provided in the inset. The non-enhanced S_0 formula (α=0) prediction (yellow) is also shown. All data are plotted versus pump wavelength and normalized to 1 mW output power. Inset: The extrapolated beating frequency (squares) and FSR (triangles) are plotted versus wavelength. The calculated α factor (red circles) is plotted versus wavelength.

and is independent of the α factor.

We briefly comment on the noise behavior when $\delta\omega_{\mathrm{P}}$ is tuned away from its PDH-locked value, which happens because the PDH locking can reduce, but not totally eliminate, the drifting in $\delta\omega_{\mathrm{P}}$. Repeating the previous analyses, we arrive at the following expression for $S_{\nu,\mathrm{SBL}}$ and expand it as a series in the relative variation of detuning:

$$\frac{S_{\nu,\mathrm{SBL}}}{S_{\nu,\mathrm{P}}} \approx \left(\frac{\gamma}{\gamma+\Gamma}\right)^2 + \alpha^2\left(\frac{\gamma}{\gamma+\Gamma}\right)\left(\frac{\delta\omega_{\mathrm{P}}}{\delta\omega_{\mathrm{P},0}}-1\right) + \frac{\alpha^4}{4}\left(\frac{\delta\omega_{\mathrm{P}}}{\delta\omega_{\mathrm{P},0}}-1\right)^2, \tag{9.69}$$

where we have kept only the lowest-order term in γ/Γ for each coefficient. As the last term no longer contains the γ/Γ reduction, the phase noise transduction is strongly dependent upon α. Thus an imperfect PDH locking increases the transferred pump phase noise in proportion to α^2.

Noise enhancement measured in a second device

To verify the generality of our findings, we have performed the experiment on another device and summarized the main data in Fig. 9.5. Data definition and

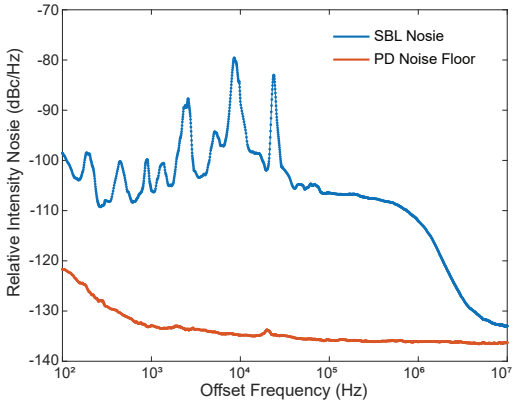

Figure 9.6: Typical measured relative intensity noise of SBLs. The output SBL power is 0.31mW at 1550 nm. The intrinsic (coupling) Q factor is 162.7×10^6 (434.5×10^6).

calculation methods are the same as the main text. In the measurement, we have chosen six longitudinal modes in one transverse mode family. This device has a lowest frequency noise S_F of 0.10 Hz^2/Hz and the measured α factor is as large as 6. The measured noise enhancement is overall in good agreement with the α factor predictions.

Relative intensity noise

Relative intensity noise (RIN) of the SBL is measured by coupling the laser to a photodetector, filtering out the DC part, and analyzing the high-frequency part with an electric spectrum analyzer. A typical RIN measurement is shown in Fig. 9.6.

Alpha factor in cascaded Brillouin lasers

Here we study the effect of the anti-Stokes process on the α factor in a cascaded Brillouin laser system. For this analysis, we introduce another pair of modes, a_c and b_c, which are the amplitude of the second-order Stokes mode and the associated phonon mode (normalized to particle numbers), respectively. The cascading Hamiltomian becomes

$$\begin{aligned} H = &\hbar(\delta\omega_P A^\dagger A + \delta\omega a^\dagger a + \delta\Omega b^\dagger b + \delta\omega_c a_c^\dagger a_c + \delta\Omega_c b_c^\dagger b_c) \\ &+ \hbar g_B(A^\dagger ab + Aa^\dagger b^\dagger) + \hbar g_B(a^\dagger a_c b_c + a a_c^\dagger b_c^\dagger), \end{aligned} \tag{9.70}$$

where $\delta\omega_c$ ($\delta\Omega_c$) is the detuning of the cascading Stokes (phonon) mode compared to the laser (mechanical vibration) frequency. Although we focus on a single order of cascade, the method can be readily generalized to high-order cascading SBLs.

The classical equations of motion for the cascading Stokes mode and the phonon mode read

$$\frac{da_\mathrm{c}}{dt} = -\left(\frac{\gamma}{2} + i\delta\omega_\mathrm{c}\right) a_\mathrm{c} - ig_\mathrm{B} a b_\mathrm{c}^*, \tag{9.71}$$

$$\frac{db_\mathrm{c}}{dt} = -\left(\frac{\Gamma}{2} + i\delta\Omega_\mathrm{c}\right) b_\mathrm{c} - ig_\mathrm{B} a a_\mathrm{c}^*. \tag{9.72}$$

By the same argument from Section 1, we define an alpha factor for the two detunings:

$$\alpha_\mathrm{c} \equiv \frac{2\delta\omega_\mathrm{c}}{\gamma} = \frac{2\delta\Omega_\mathrm{c}}{\Gamma}. \tag{9.73}$$

By obtaining the steady-state solutions and upon substitution into the equations for the first Stokes mode, we find

$$\frac{da}{dt} = -\left(\frac{\gamma}{2} + i\delta\omega\right) a - ig_\mathrm{B} A b^* - \frac{gN_{a,\mathrm{c}}}{1+\alpha_\mathrm{c}^2}(1 - i\alpha_\mathrm{c}) a, \tag{9.74}$$

$$\frac{db}{dt} = -\left(\frac{\Gamma}{2} + i\delta\Omega\right) b - ig_\mathrm{B} A a^*, \tag{9.75}$$

where $N_{a,\mathrm{c}} \equiv |a_\mathrm{c}|^2$. This extra term introduces extra loss and frequency shift induced by the cascading Stokes wave. This can be made more explicit by rearranging the loss and detuning terms as follows,

$$\frac{da}{dt} = -\left(\frac{\gamma}{2} + \frac{gN_{a,\mathrm{c}}}{1+\alpha_\mathrm{c}^2}\right) a - i\left(\delta\omega - \frac{gN_{a,\mathrm{c}}}{1+\alpha_\mathrm{c}^2}\alpha_\mathrm{c}\right) a - ig_\mathrm{B} A b^*, \tag{9.76}$$

Thus the α factor for the first Stokes SBL can be defined as,

$$\alpha \equiv \frac{2\delta\Omega}{\Gamma} = \left(\delta\omega - \frac{gN_{a,\mathrm{c}}}{1+\alpha_\mathrm{c}^2}\alpha_\mathrm{c}\right)\left(\frac{\gamma}{2} + \frac{gN_{a,\mathrm{c}}}{1+\alpha_\mathrm{c}^2}\right)^{-1}. \tag{9.77}$$

Since the α factors are defined using laser detunings, these are not directly observable in the experiment. Additional phase-matching equations are required to determine the detunings,

$$\delta\Omega + \delta\omega = \frac{\Gamma+\gamma}{2}\alpha', \tag{9.78}$$

$$\delta\Omega_\mathrm{c} + \delta\omega_\mathrm{c} = \frac{\Gamma+\gamma}{2}\alpha_\mathrm{c}' + \delta\omega, \tag{9.79}$$

where $\alpha' \equiv 2(\mathrm{FSR} - \Omega)/(\Gamma+\gamma)$ and $\alpha_\mathrm{c}' \equiv 2(\mathrm{FSR}_\mathrm{c} - \Omega_\mathrm{c})/(\Gamma+\gamma)$ are the non-cascading α factors, FSR (FSR_c) is the mode spacing between pump and Stokes (Stokes and cascading Stokes), and Ω (Ω_c) is the phonon frequency for the Stokes (cascading Stokes) process. In principle, the above equations, together with Eq.

(9.77) and Eq. (9.73), form a closed set of nonlinear equations that can be solved iteratively. In the limit of $\Gamma \gg \gamma$, the mode-pulling effects are weak enough, and we can expand α and α_c to first order of γ/Γ. The results are

$$\alpha = \alpha' + \frac{2}{\Gamma}\frac{gN_{a,c}}{1+(\alpha_c')^2}(\alpha_c' - \alpha'), \tag{9.80}$$

$$\alpha_c = \alpha_c' + \frac{\gamma}{\Gamma}\alpha' - \frac{2}{\Gamma}\frac{gN_{a,c}}{1+(\alpha_c')^2}(\alpha_c' - \alpha'). \tag{9.81}$$

While the amplitude-phase coupling is given by the α factors above, these factors are no longer related to the SBL noise when cascading. The noise on b_c will be coupled to a due to the anti-Stokes process $a^\dagger a_c b_c + a a_c^\dagger b_c^\dagger$. Using the techniques in Section 3, the linewidth of the SBL can be found, up to zeroth order of γ/Γ, as

$$\Delta\omega_{SBL} = \Delta\omega_{SBL,1} + \Delta\omega_{SBL,2}, \tag{9.82}$$

where the contribution from the first phonon mode reads

$$\begin{aligned}\Delta\omega_{SBL,1} = \frac{gn_{th}}{\gamma}&\frac{2gN_{a,c} + \gamma(1+\alpha_c^2)}{(1+\alpha_c^2)(2+\alpha^2+\alpha_c^2)^2} \\ &\times (\alpha^4 - 4\alpha^3\alpha_c + 2\alpha^2(\alpha_c^2+4) + 4\alpha\alpha_c^3 + \alpha_c^4 + 4),\end{aligned} \tag{9.83}$$

and the contribution from the second phonon mode via the anti-Stokes process reads

$$\begin{aligned}\Delta\omega_{SBL,2} = \frac{n_{th,c}}{\gamma}&\frac{2}{N_{a,c}(1+\alpha_c^2)(2+\alpha^2+\alpha_c^2)^2} \\ &\times \left[g^2N_{a,c}^2(\alpha^4 - 4\alpha^3\alpha_c + 2\alpha^2(\alpha_c^2+4) + 4\alpha\alpha_c^3 + \alpha_c^4 + 4)\right. \\ &+ 2gN_{a,c}\gamma(\alpha_c^2+1) \\ &\times (-\alpha^3\alpha_c + \alpha^2(\alpha_c^2+2) + \alpha(3\alpha_c^2+2)\alpha_c + \alpha_c^4) \\ &\left.+ \gamma^2(\alpha+\alpha_c)^2(1+\alpha_c^2)^3\right],\end{aligned} \tag{9.84}$$

where $n_{th,c}$ is the number of thermal quanta in the cascading phonon mode. We note that the second contribution has a nonphysical divergence with $N_{a,c} \to 0$ when $\alpha + \alpha_c \neq 0$. This is because the noise of amplitude-phase coupling from the anti-Stokes process is not white near the threshold of lasing. A special case is $\alpha = \alpha_c = 0$, which leads to

$$\Delta\omega_{SBL} = (2gN_{a,c} + \gamma)\frac{gn_{th}}{\gamma} + 2gN_{a,c}\frac{gn_{th,c}}{\gamma}. \tag{9.85}$$

This result is consistent with previous analyses on cascading SBLs [23].

References

[1] Stokes, L., Chodorow, M. & Shaw, H. All-fiber stimulated Brillouin ring laser with submilliwatt pump threshold. *Optics Letters* **7**, 509–511 (1982).

[2] Yao, X. S. High-quality microwave signal generation by use of Brillouin scattering in optical fibers. *Optics Letters* **22**, 1329–1331 (1997).

[3] Callahan, P. T., Gross, M. C. & Dennis, M. L. Frequency-independent phase noise in a dual-wavelength Brillouin fiber laser. *IEEE Journal of Quantum Electronics* **47**, 1142–1150 (2011).

[4] Eggleton, B. J., Poulton, C. G. & Pant, R. Inducing and harnessing stimulated Brillouin scattering in photonic integrated circuits. *Advances in Optics and Photonics* **5**, 536–587 (2013).

[5] Tomes, M. & Carmon, T. Photonic micro-electromechanical systems vibrating at X-band (11-GHz) rates. *Physical Review Letters* **102**, 113601 (2009).

[6] Grudinin, I. S., Matsko, A. B. & Maleki, L. Brillouin lasing with a CaF_2 whispering gallery mode resonator. *Physical Review Letters* **102**, 043902 (2009).

[7] Pant, R. *et al.* On-chip stimulated Brillouin scattering. *Optics Express* **19**, 8285–8290 (2011).

[8] Lee, H. *et al.* Chemically etched ultrahigh-Q wedge-resonator on a silicon chip. *Nature Photonics* **6**, 369–373 (2012).

[9] Loh, W. *et al.* Dual-microcavity narrow-linewidth Brillouin laser. *Optica* **2**, 225–232 (2015).

[10] Otterstrom, N. T., Behunin, R. O., Kittlaus, E. A., Wang, Z. & Rakich, P. T. A silicon Brillouin laser. *Science* **360**, 1113–1116 (2018).

[11] Yang, K. Y. *et al.* Bridging ultrahigh-Q devices and photonic circuits. *Nature Photonics* **12**, 297–302 (2018).

[12] Gundavarapu, S. *et al.* Sub-hertz fundamental linewidth photonic integrated Brillouin laser. *Nature Photonics* **13**, 60–67 (2019).

[13] Li, J., Lee, H., Chen, T. & Vahala, K. J. Characterization of a high coherence, Brillouin microcavity laser on silicon. *Optics Express* **20**, 20170–20180 (2012).

[14] Li, J., Lee, H. & Vahala, K. J. Low-noise Brillouin laser on a chip at 1064 nm. *Optics Letters* **39**, 287–290 (2014).

[15] Li, J., Lee, H. & Vahala, K. J. Microwave synthesizer using an on-chip Brillouin oscillator. *Nature Communications* **4**, 2097 (2013).

[16] Li, J., Yi, X., Lee, H., Diddams, S. A. & Vahala, K. J. Electro-optical frequency division and stable microwave synthesis. *Science* **345**, 309–313 (2014).

[17] Li, J., Suh, M.-G. & Vahala, K. Microresonator Brillouin gyroscope. *Optica* **4**, 346–348 (2017).

[18] Lai, Y.-H. *et al.* Earth rotation measured by a chip-scale ring laser gyroscope. *Nature Photonics* **14**, 345–349 (2020).

[19] Shen, Y. R. & Bloembergen, N. Theory of stimulated Brillouin and Raman scattering. *Physical Review* **137**, A1787–A1805 (1965).

[20] Boyd, R. W. *Nonlinear Optics* (Academic press, 2003).

[21] Schawlow, A. L. & Townes, C. H. Infrared and optical masers. *Physical Review* **112**, 1940 (1958).

[22] Suh, M.-G., Yang, Q.-F. & Vahala, K. J. Phonon-limited-linewidth of Brillouin lasers at cryogenic temperatures. *Physical Review Letters* **119**, 143901 (2017).

[23] Behunin, R. O., Otterstrom, N. T., Rakich, P. T., Gundavarapu, S. & Blumenthal, D. J. Fundamental noise dynamics in cascaded-order Brillouin lasers. *Physical Review A* **98**, 023832 (2018).

[24] Debut, A., Randoux, S. & Zemmouri, J. Linewidth narrowing in Brillouin lasers: Theoretical analysis. *Physical Review A* **62**, 023803 (2000).

[25] Lax, M. Quantum noise. X. density-matrix treatment of field and population-difference fluctuations. *Physical Review* **157**, 213–231 (1967).

[26] Henry, C. Theory of the linewidth of semiconductor lasers. *IEEE Journal of Quantum Electronics* **18**, 259–264 (1982).

[27] Vahala, K., Chiu, L. C., Margalit, S. & Yariv, A. On the linewidth enhancement factor α in semiconductor injection lasers. *Applied Physics Letters* **42**, 631–633 (1983).

[28] Harder, C., Vahala, K. & Yariv, A. Measurement of the linewidth enhancement factor α of semiconductor lasers. *Applied Physics Letters* **42**, 328–330 (1983).

[29] Henning, I. & Collins, J. Measurements of the semiconductor laser linewidth broadening factor. *Electronics Letters* **19**, 927–929 (1983).

[30] Cai, M., Painter, O. & Vahala, K. J. Observation of critical coupling in a fiber taper to a silica-microsphere whispering-gallery mode system. *Physical Review Letters* **85**, 74–77 (2000).

[31] Spillane, S. M., Kippenberg, T. J., Painter, O. J. & Vahala, K. J. Ideality in a fiber-taper-coupled microresonator system for application to cavity quantum electrodynamics. *Physical Review Letters* **91**, 043902 (2003).

[32] Wang, H., Lai, Y.-H., Yuan, Z., Suh, M.-G. & Vahala, K. Petermann-factor limited sensing near an exceptional point. *Nature Communications* **11**, 1610 (2020).

[33] Yi, X., Yang, Q.-F., Yang, K. Y., Suh, M.-G. & Vahala, K. Soliton frequency comb at microwave rates in a high-Q silica microresonator. *Optica* **2**, 1078–1085 (2015).

[34] Rumble, J. R. (ed.) *CRC handbook of chemistry and physics* (CRC press, Internet Version 2019), 100 edn.

[35] Van Exter, M., Kuppens, S. & Woerdman, J. Excess phase noise in self-heterodyne detection. *IEEE Journal of Quantum Electronics* **28**, 580–584 (1992).

[36] Ludvigsen, H., Tossavainen, M. & Kaivola, M. Laser linewidth measurements using self-homodyne detection with short delay. *Optics Communications* **155**, 180–186 (1998).

Chapter 10

PETERMANN-FACTOR SENSITIVITY LIMIT NEAR AN EXCEPTIONAL POINT IN A BRILLOUIN RING LASER GYROSCOPE

Wang, H., Lai, Y.-H., Yuan, Z., Suh, M.-G. & Vahala, K. Petermann-factor sensitivity limit near an exceptional point in a Brillouin ring laser gyroscope. *Nature Communications* **11**, 1610 (2020).

Non-Hermitian Hamiltonians [1, 2] describing open systems can feature singularities called exceptional points (EPs) [3–5]. EPs have been experimentally realized in several systems [6–8] and applied to demonstrate non-reciprocal transmission [9–11] and lasing dynamics control [12–15]. Moreover, resonant frequencies become strongly dependent on externally applied perturbations near an EP which has given rise to the concept of EP-enhanced sensing in photonics [16–19] and electronics [20, 21]. While increased sensor responsivity has been demonstrated in several systems [22–25], signal-to-noise performance (sensitivity) has been considered only theoretically [26–30].

Recently, strong responsivity improvement near an EP was reported in a Brillouin ring laser gyroscope by monitoring an increase in the gyroscope scale factor (i.e. transduction factor of rotation-rate into a signal) [24]. At the same time, however, measurement of the gyroscope Allan deviation versus averaging time showed that short-term laser frequency noise also increased near the EP. This noise was random-walk in nature, suggesting a fundamental origin. Moreover, it depended upon system bias relative to the EP in such a way so as to precisely compensate the observed EP-enhanced transduction. As a result, the gyroscope's angular random walk, the metric used to quantify short-term rotation sensitivity, was observed to maintain a constant value (i.e. independent of gyroscope bias relative to the EP). In effect, the measurements showed that gyroscope sensitivity (i.e. weakest rotation signal measurable at a given detection bandwidth) is not improved by operation near the EP even while the gyroscope responsiveness through improved transduction (scale factor) increases.

As with all laser gyroscopes, the Brillouin ring laser gyroscope measures rotations

through the Sagnac effect [31]. Clockwise (cw) and counter-clockwise (ccw) lasing waves experience opposing frequency shifts when the plane of the gyroscope rotates. By mixing the two laser fields on a detector, their difference frequency therefore reveals the rotation-induced frequency shift added onto a constant bias frequency (which is at audio rates in this case [24]). Frequency noise in the beat frequency therefore determines the measurement sensitivity. This noise has both a technical component (observable on longer time scales in the Allan deviation [24]) as well as a random walk component that, absent the EP, is known to result from fundamental linewidth broadening of the Brillouin laser waves [32, 33]. Significantly, subsequent measurement of the random walk component showed that none of the parameters which normally impact its magnitude (e.g., laser power, cavity Q factor) varied near the EP, therefore suggesting that frequency noise (and linewidth) is increased by way of another mechanism.

Laser linewidth can also be broadened by the Petermann factor [34–39]. This mechanism is associated with non-orthogonality of a mode spectrum, and its connection to EPs has been considered in theoretical studies of microresonators [40, 41]. However, despite continued theoretical interest [42, 43], including the development of new techniques for determination of linewidth in general laser systems [44], the observation of Petermann linewidth broadening near exceptional points was reported only recently by the Yang group in a phonon laser system [45]. And the link between Petermann-factor-induced noise and EP sensor performance is unexplored. Here, it is shown that mode non-orthogonality induced by the EP limits the gyroscope sensitivity via Petermann-factor linewidth broadening. Indeed, analysis and measurement confirm near perfect cancellation of the signal transduction improvement by increasing Petermann-factor noise so that the gyroscope's fundamental signal-to-noise ratio (SNR) and hence sensitivity is not improved by operation near the EP. These results are further confirmed using an Adler phase locking equation approach [46, 47] which is also applied to analyze the combined effect of dissipative and conservative coupling on the system.

10.1 Main results

Biorthogonal noise enhancement theory

The gyroscope uses a high-Q silica whispering gallery resonator [48] in a ring-laser configuration [32]. As illustrated in Fig. 10.1a, optical pumping of cw and ccw directions on the same whispering-gallery mode index induces laser action through the Brillouin process. On account of the Brillouin phase matching condition, these

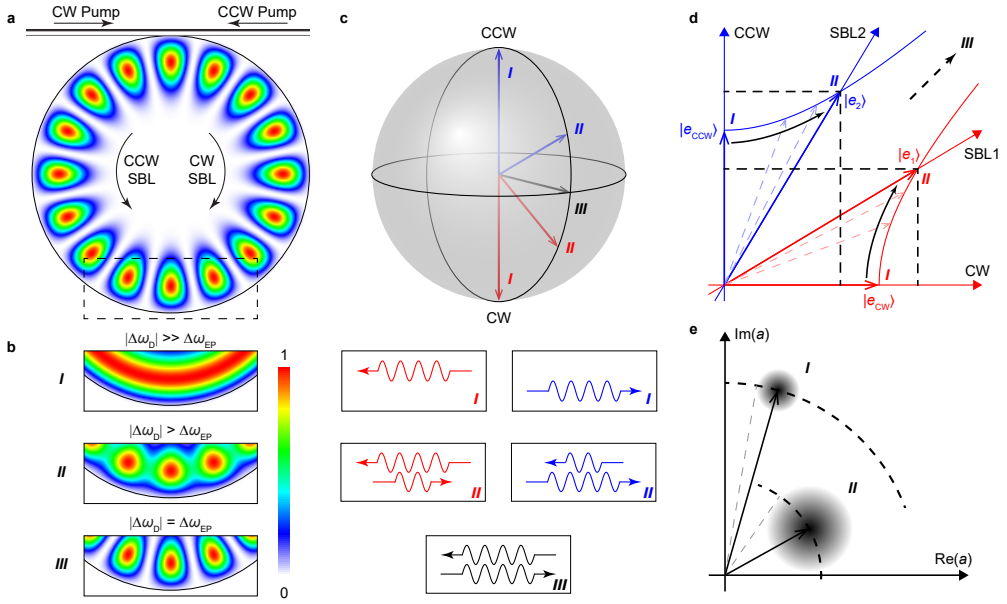

Figure 10.1: Brillouin laser linewidth enhancement near an exceptional point. (a) Diagram of whispering-gallery mode resonator with the energy distribution of an eigenmode superimposed. The eigenmode energy distribution corresponds to state *III* in panel (b). Optical pumps on the coupling waveguide and whispering-gallery SBL modes are indicated by arrows. (b) Mode energy distributions for three different states: far from EP (state *I*) the eigenmodes are traveling cw or ccw waves; near EP (state *II*) the eigenmodes are hybrids of cw and ccw waves; at EP (state *III*) eigenmodes coalesce to a standing wave. (c) Bloch sphere showing the eigenstates for cases *I*, *II*, and *III* with corresponding cw and ccw composition. (d), Illustration of the cw-ccw and SBL1-SBL2 coordinate systems. Unit vectors for states *I* and *II* are shown on each axis. As the system is steered towards the EP, the SBL axes move toward each other so that unit vectors along the SBL axes lengthen as described by the two hyperbolas. This is illustrated by decomposing a unit vector of the non-orthogonal SBL coordinate system using the orthogonal cw-ccw coordinates [e.g., $(5/4, 3/4)^T$ and $(3/4, 5/4)^T$ for state *II*]. Consequently, the field amplitude is effectively shortened in the SBL basis. (e) Phasor representation of the complex amplitude of a lasing mode for states *I* and *II* provides an interpretation of linewidth enhancement. Phasor length is shortened and noise is enhanced as the system is steered to the EP, leading to an increased phasor angle diffusion and laser linewidth enhancement (see Supplementary information 3).

stimulated Brillouin laser (SBL) waves propagate in a direction opposite to their corresponding pump waves [33]. Dissipative backscattering [49] couples the SBLs, and the following Hamiltonian governs the above-laser-threshold motion [24]:

$$H = \begin{pmatrix} \omega_{\mathrm{cw}} & i\Delta\omega_{\mathrm{EP}}/2 \\ i\Delta\omega_{\mathrm{EP}}/2 & \omega_{\mathrm{ccw}} \end{pmatrix}, \tag{10.1}$$

where H describes the dynamics via $id\Psi/dt = H\Psi$ and $\Psi = (a_{cw}, a_{ccw})^T$ is the column vector of SBL mode amplitudes (square of norm is photon number). Also, $\Delta\omega_{EP}$ is a non-Hermitian term related to the coupling rate between the two SBL modes, and ω_{cw} (ω_{ccw}) is the active-cavity resonance angular frequency of the cw (ccw) SBL mode above laser threshold. The dependence of ω_{cw}, ω_{ccw}, and $\Delta\omega_{EP}$ on other system parameters, most notably the angular rotation rate and the optical pumping frequencies, has been suppressed for clarity.

A class of EP sensors operate by measuring the frequency difference of the two system eigenmodes. This difference is readily calculated from Eq. (10.1) as $\Delta\omega_S = \sqrt{\Delta\omega_D^2 - \Delta\omega_{EP}^2}$ where $\Delta\omega_D \equiv \omega_{ccw} - \omega_{cw}$ is the resonance frequency difference and $\Delta\omega_{EP}$ is the critical value of $\Delta\omega_D$ at which the system is biased at the EP. As illustrated in Fig. 10.1b,c the vector composition of the SBL modes strongly depends upon the system proximity to the EP. For $|\Delta\omega_D| \gg \Delta\omega_{EP}$ the SBL modes (unit vectors) are orthogonal cw and ccw waves. However, closer to the EP the waves become admixtures of these states that are no longer orthogonal. At the EP, the two waves coalesce to a single state vector (a standing wave in the whispering gallery). Rotation of the gyroscope in state *II* in Fig. 10.1 ($|\Delta\omega_D| > \Delta\omega_{EP}$) introduces a perturbation to $\Delta\omega_D$ whose transduction into $\Delta\omega_S$ is enhanced relative to the conventional Sagnac factor [31]. This EP-induced signal-enhancement-factor (SEF) is given by [24],

$$\mathrm{SEF} = \left|\frac{\partial\Delta\omega_S}{\partial\Delta\omega_D}\right|^2 = \frac{\Delta\omega_D^2}{\Delta\omega_D^2 - \Delta\omega_{EP}^2}, \tag{10.2}$$

where SEF refers to the signal power (not amplitude) enhancement. This factor has recently been verified in the Brillouin ring laser gyroscope [24]. The control of $\Delta\omega_D$ (and in turn $\Delta\omega_S$) in that work and here is possible by tuning of the optical pumping frequencies and is introduced later.

$\Delta\omega_S$ is measured as the beat frequency of the SBL laser signals upon photodetection and the SNR is set by the laser linewidth. To understand the linewidth behavior, a bi-orthogonal basis is used as described in Supplementary information 1 and 3. As shown there and illustrated in Fig. 10.1d, the peculiar properties of non-orthogonal systems near the EP cause the unit vectors (optical modes) to be lengthened. This lengthening results in an effectively shorter laser field amplitude. Also, noise into the mode is increased as illustrated in Fig. 10.1e. Because the laser linewidth can be understood to result from diffusion of the phasor in Fig. 10.1e, linewidth increases upon operation close to the EP. And the linewidth enhancement is given by the

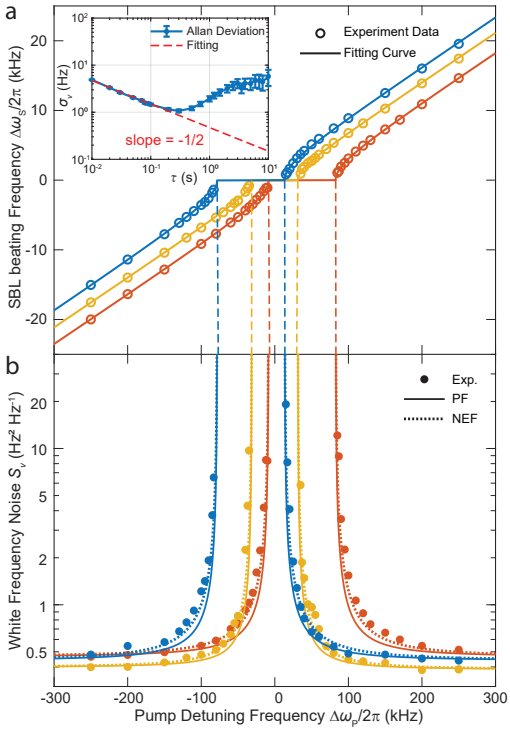

Figure 10.2: Measured linewidth enhancement of SBLs near the exceptional point. (a) Measured SBL beating frequency is plotted versus pump detuning for three distinct locking zones, corresponding SBL amplitude ratios q: 1.15 (blue), 1 (orange), 0.85 (red). Solid curves are theoretical fittings. Inset is a typical Allan deviation measurement of frequency ($\sigma_\nu(\tau)$) versus gate time τ. Error bars give the standard error of the mean. The short-term part is fitted with $\sqrt{S_\nu/(2\tau)}$ where S_ν is the one-sided power spectral density of the white frequency noise plotted in panel (b). (b) Measured white frequency noise of the beating signal determined using the Allan deviation measurement. Data point color corresponds to the amplitude ratios used in panel (a). The Petermann factor PF (solid lines) and NEF (dashed lines) theoretical predictions use parameters obtained by fitting from panel (a).

Petermann factor (see Supplementary information 2),

$$\mathrm{PF} = \frac{1}{2}\left(1 + \frac{\mathrm{Tr}(H_0^\dagger H_0)}{|\mathrm{Tr}(H_0^2)|}\right) = \frac{\Delta\omega_\mathrm{D}^2}{\Delta\omega_\mathrm{D}^2 - \Delta\omega_\mathrm{EP}^2}, \tag{10.3}$$

where Tr is the matrix trace operation and $H_0 = H - \mathrm{Tr}(H)/2$ is the traceless part of H. As derived in Supplementary information 2, the first part of this equation is a basis independent form and is valid for a general two-dimensional system. The second part is specific to the current SBL system. Inspection of Eq. (10.2) and Eq. (10.3) shows that SEF = PF. As a result, the SNR is not expected to improve through operation near the EP when the system is fundamental-noise limited.

Petermann noise measurement

To verify the above predictions, the output of a single pump laser (~1553.3 nm) is divided into two branches that are coupled into cw and ccw directions of the resonator using a tapered fiber [50, 51]. Both pump powers are actively stabilized. The resonator is mounted in a sealed box and a thermo-electric cooler (TEC) controls the chip temperature which is monitored using a thermistor (fluctuations are held within 5 mK). Each pumping branch has its frequency controlled using acousto-optic modulators (AOMs). SBL power is also monitored and controlled so that fluctuations are within 0.6%. Even with the control of temperature and power, the Allan deviation at longer gate times reflects technical-noise drifting that is observed to be more pronounced for operation near the EP. As described in Ref. [24], the ccw pump laser frequency is Pound-Drever-Hall (PDH) locked to one resonator mode and the cw pump laser can then be independently tuned by the AOM. This pump detuning frequency ($\Delta\omega_P$) is therefore controlled to radio-frequency precision. It is used to precisely adjust $\Delta\omega_D$ and in turn $\Delta\omega_S$ as shown in three sets of measurements in Fig. 10.2a. Here, the photodetected SBL beat frequency $\Delta\omega_S$ is measured using a frequency counter. The data sets are taken for three distinct SBL output amplitude ratios as discussed further below. A solid curve fitting is also presented using $\Delta\omega_S = \pm\sqrt{\Delta\omega_D^2 - \Delta\omega_{EP}^2}$, where $\Delta\omega_D = \frac{\gamma/\Gamma}{1+\gamma/\Gamma}\Delta\omega_P + \frac{1}{1+\gamma/\Gamma}\Delta\omega_{Kerr}$ (see Supplementary information 4). Also, γ is the photon decay rate, Γ is the Brillouin gain bandwidth [33], and $\Delta\omega_{Kerr}$ is a Kerr effect correction that is explained below. As an aside, the data plot and theory show a frequency locking zone, the boundaries of which occur at the EP.

The frequency counter data are also analyzed as an Allan deviation (Adev) measurement (Fig. 10.2a inset). The initial roll-off of the Adev features a slope of $-1/2$ corresponding to white frequency noise [52]. This was also verified in separate measurements of the beat frequency using both an electrical spectrum analyzer and a fast Fourier transform. The slope of this region is fit to $\sqrt{S_\nu/(2\tau)}$ where S_ν is the one-sided spectral density of the white frequency noise. Adev measurement at each of the detuning points in Fig. 10.2a is used to infer the S_ν values that are plotted in Fig. 10.2b. There, a frequency noise enhancement is observed as the system is biased towards an EP. Also plotted is the Petermann factor noise enhancement (Eq. (10.3)). Aside from a slight discrepancy at intermediate detuning frequencies (analyzed further below), there is overall excellent agreement between theory and measurement. The frequency noise levels measured in Fig. 10.2b are consistent with fundamental SBL frequency noise (see Methods). Significantly, the fundamental

nature of the noise, the good agreement between the PF prediction (Eq. (10.3)) and measurement in Fig. 10.2b, and separate experimental work [24] that has verified the theoretical form of the SEF (Eq. (10.3)) confirm that SEF = PF so that the fundamental sensitivity limit of the gyroscope is not improved by operation near the EP.

Adler noise analysis

While the Petermann factor analysis provides very good agreement with the measured results, we also derived an Adler-like coupled mode equation analysis for the Brillouin laser system. This approach is distinct from the bi-orthogonal framework and, while more complicated, provides additional insights into the system behavior. Adapting analysis applied in the noise analysis of ring laser gyroscopes [47], a noise enhancement factor NEF results (see Supplementary information 4),

$$\mathrm{NEF} = \frac{\Delta\omega_{\mathrm{D}}^2 + \Delta\omega_{\mathrm{EP}}^2/2}{\Delta\omega_{\mathrm{D}}^2 - \Delta\omega_{\mathrm{EP}}^2}. \tag{10.4}$$

It is interesting that this result, despite the different physical context of the Brillouin laser system, has a similar form to one derived for polarization-mode-coupled laser systems [53]. The PF and NEF predictions are shown on Fig. 10.2b, and the Adler-derived NEF correction provides slightly better agreement with the data at the intermediate detuning values.

Adler locking bandwidth analysis

The Adler approach is also useful to explain a locking zone dependence upon SBL amplitudes observed in Fig. 10.2a. As shown in Supplementary information 4, this variation can be explained through the combined action of the Kerr effect and intermodal coupling coefficients of both dissipative and conservative nature. Specifically, the locking bandwidth is found to exhibit the following dependence upon the amplitude ratio $q = |a_{\mathrm{ccw}}/a_{\mathrm{cw}}|$ of the SBL lasers,

$$\Delta\omega_{\mathrm{EP}}^2 = \left(\frac{\Gamma}{\Gamma+\gamma}\right)^2 \left[\left(q + \frac{1}{q}\right)^2 |\kappa|^2 + \left(q - \frac{1}{q}\right)^2 |\chi|^2\right], \tag{10.5}$$

where κ is the dissipative coupling and χ is the conservative coupling between cw and ccw SBL modes. The locking zone boundaries in terms of pump detuning frequency have been measured (Fig. 10.3 inset) for a series of different SBL powers. Using this data, the locking bandwidth is expressed in pump frequency detuning ($\Delta\omega_{\mathrm{P}}$) units using $\Delta\omega_C \equiv (1 + \Gamma/\gamma)\Delta\omega_{\mathrm{EP}}$ and plotted versus q in the main panel of

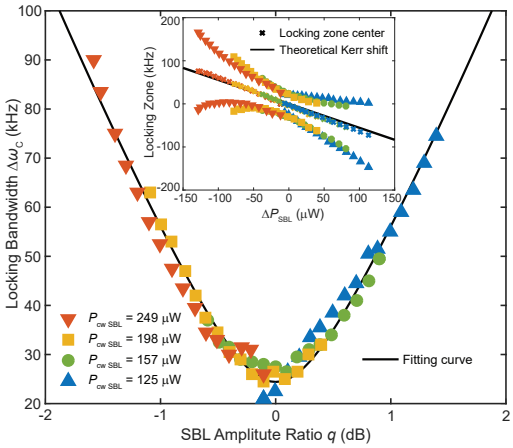

Figure 10.3: Locking zone bandwidth versus SBL amplitude ratio. Measured locking zone bandwidth is plotted versus amplitude ratio q of the SBL lasers. The cw power is held constant at four values (see legend) to create the data composite. The solid black curve is Eq. (10.5). Inset: the measured locking zone boundaries are plotted versus the SBL power differences ($\Delta P_{\mathrm{SBL}} = P_{\mathrm{ccw}} - P_{\mathrm{cw}}$). Colors and symbols correspond to the main panel. The center of the locking zone is also indicated and is shifted by the Kerr nonlinearity which varies as the SBL power difference. Black line gives the theoretical prediction (no free parameters).

Fig. 10.3. The plot agrees well with Eq. (10.5) (fitting shown in black) and gives $|\kappa| = 0.93$ kHz, $|\chi| = 8.21$ kHz.

Finally, the center of the locking band is shifted by the Kerr effect and (in pump frequency detuning $\Delta\omega_{\mathrm{P}}$ units) can be expressed as $-(\Gamma/\gamma)\Delta\omega_{\mathrm{Kerr}}$, where $\Delta\omega_{\mathrm{Kerr}} = \eta\left(|a_{\mathrm{ccw}}|^2 - |a_{\mathrm{cw}}|^2\right) = (\eta\Delta P_{\mathrm{SBL}})/(\gamma_{\mathrm{ex}}\hbar\omega)$ is the Kerr induced SBL resonance frequency difference, $\Delta P_{\mathrm{SBL}} = P_{\mathrm{ccw}} - P_{\mathrm{cw}}$ is the output power difference of the SBLs, and γ_{ex} is the photon decay rate due to the output coupling. Also, $\eta = n_2\hbar\omega^2 c/(Vn_0^2)$ is the single-photon Kerr-effect angular frequency shift with ω the SBL angular frequency, n_2 the Kerr-nonlinear refractive index of silica, V the mode volume, n_0 the linear refractive index, and c the speed of light in vacuum. If the white frequency noise floors in Fig. 10.2 are used to infer the resonator quality factor, then a Kerr nonlinearity value of 558 Hz $\mu\mathrm{W}^{-1}$ is predicted (see Methods). This value gives the line plot in the Fig. 10.3 inset (with no free parameters) which agrees with experiment.

Discussion

Prior work has shown that Brillouin laser gyroscopes when operated near an EP have an improved responsivity (equivalently, an increase in the gyroscope's scale factor for

transduction of rotation rate into the Sagnac frequency shift) [24]. At the same time, these measurements have shown that the gyroscope's sensitivity did not improve near the EP. We have verified through measurement and theory that mode non-orthogonality induced by the EP explains this latter result. Specifically, increasing mode non-orthogonality occurs when the two system eigenvectors (optical modes) begin to coalesce near the EP. This, in turn, increases laser frequency noise from an increasing Petermann factor and thereby reduces sensitivity. Curiously, these two mechanisms, the enhanced transduction and enhanced noise, feature an almost identical dependence upon the system's proximity to the EP. In effect, the increased signal response in the gyroscope arising from the EP does not lead to an improvement in the minimum detectable signal (sensitivity).

It is interesting to note that a recent theoretical study of noise limitations in a class of non-lasing EP sensors showed no fundamental sensitivity advantage for operation near the EP [28]. Nonetheless it is still possible that other sensing modalities could benefit from operation near an EP. Moreover, open systems offer other potentially useful ways for transduction of rotation [54]. Also, the proposal of conservative nonlinear mode coupling provides a potential way to enhance the Sagnac effect [55–57]. The apparent divergence of the linewidth near the EP is an interesting feature of the current model and also one that agrees well with the data (at least in the range of the measurement). Nonetheless, constraints to this divergence set by the linewidth of the passive cavity loss are a subject of further study. More generally, the excellent control of the state space that is possible in the Brillouin system can provide a new platform for study of the remarkable physics associated with exceptional points.

10.2 Methods

Linewidth and Allan deviation measurement

In experiments, frequency is measured in the time domain using a frequency counter, and its Allan deviation is calculated for different averaging times (Fig. 10.2a). The Allan deviation $\sigma_\nu(\tau)$ for a signal frequency is defined by

$$\sigma_\nu(\tau) \equiv \sqrt{\frac{1}{2(M-1)} \sum_{k=1}^{M-1} (\overline{\nu}_{k+1} - \overline{\nu}_k)^2}, \tag{10.6}$$

where τ is the averaging time, M is the number of frequency measurements, and $\overline{\nu}_k$ is the average frequency of the signal (measured in Hz) in the time interval between $k\tau$ and $(k+1)\tau$. The Allan deviation follows a $\tau^{-1/2}$ dependence when the underlying frequency noise spectral density is white [52], as occurs for laser

frequency noise limited by spontaneous emission. White noise causes the lineshape of the laser to be a Lorentzian. White noise is also typically dominant in the Allan deviation plot at shorter averaging times where flicker noise and frequency drift are not yet important. This portion of the Allan deviation plot can be fit using $\sigma_\nu(\tau) = \sqrt{S_\nu/(2\tau)}$ where S_ν is the white frequency noise one-sided spectral density function. This result can be further converted to the Lorentzian full-width at half maximum (FWHM) linewidth $\Delta\nu_{\mathrm{FWHM}}$ (measured in Hz) using the conversion

$$S_\nu = 2\sigma_\nu^2(\tau)\tau = \frac{1}{\pi}\Delta\nu_{\mathrm{FWHM}}. \tag{10.7}$$

Experimental parameters and data fitting

The resonator is pumped at the optical wavelength $\lambda = 1553.3$ nm, which, subject to the Brillouin phase matching condition, corresponds to a phonon frequency (Stokes frequency shift) of approximately $\Omega_{\mathrm{phonon}}/(2\pi) = 10.8$ GHz. Quality factors of the SBL modes are measured using a Mach-Zehnder interferometer, and a loaded Q factor $Q_{\mathrm{T}} = 88 \times 10^6$ and coupling Q factor $Q_{\mathrm{ex}} = 507 \times 10^6$ are obtained.

The theoretical formula for the white frequency noise of the beat frequency far away from the EP reads

$$S_\nu = \left(\frac{\Gamma}{\gamma+\Gamma}\right)^2 \frac{\hbar\omega^3}{4\pi^2 Q_{\mathrm{T}} Q_{\mathrm{ex}}}\left(\frac{1}{P_{\mathrm{cw}}} + \frac{1}{P_{\mathrm{ccw}}}\right)(n_{\mathrm{th}} + N_{\mathrm{th}} + 1), \tag{10.8}$$

which results from summing the Schawlow-Townes-like linewidths of the SBL laser waves [33]. In the expression, N_{th} and n_{th} are the thermal occupation numbers of the SBL state and phonon state, respectively. At room temperature, $n_{\mathrm{th}} \approx 577$ and $N_{\mathrm{th}} \approx 0$. For the power balanced case (orange data set in Fig. 10.2), $P_{\mathrm{cw}} = P_{\mathrm{ccw}} = 215$ μW, and the predicted white frequency noise (Eq. (8)) is $S_\nu = 0.50$ Hz^2 Hz^{-1}. For the blue (red) data set, P_{cw} (P_{ccw}) is decreased by 1.22 dB (1.46 dB) so that $S_\nu = 0.58$ (0.60) Hz^2 Hz^{-1} is calculated. On the other hand, the measured values for the blue, orange, and red data sets in Fig. 10.2b (i.e. white frequency noise floors far from EP) give $S_\nu = 0.44, 0.39, 0.46$ Hz^2 Hz^{-1}, respectively. The difference here is attributed to errors in Q measurement. For example, the experimental values of noise can be used to infer a corrected coupling Q factor $Q_{\mathrm{ex}} \approx 658 \times 10^6$. Using this value below yields an excellent prediction of the Kerr nonlinear coefficient which supports this belief.

The beating frequency in Fig. 10.2a is fit using the following relations:

$$\begin{aligned}\Delta\omega_{\mathrm{S}} &= \mathrm{sgn}(\Delta\omega_{\mathrm{D}})\sqrt{\Delta\omega_{\mathrm{D}}^2 - \Delta\omega_{\mathrm{EP}}^2},\\ \Delta\omega_{\mathrm{D}} &= \frac{\gamma/\Gamma}{1+\gamma/\Gamma}\Delta\omega_{\mathrm{P}} + \frac{1}{1+\gamma/\Gamma}\Delta\omega_{\mathrm{Kerr}},\end{aligned} \tag{10.9}$$

where sgn is the sign function and γ/Γ, $\Delta\omega_{\mathrm{Kerr}}$ and $\Delta\omega_{\mathrm{EP}}$ are fitting parameters. The fitting gives $\gamma/\Gamma = 0.076$ consistently, while $\Delta\omega_{\mathrm{Kerr}}$ and $\Delta\omega_{\mathrm{EP}}$ are separately adjusted in each data set. These parameters feature a power dependence that is fully explored in Fig. 10.3 and the related main text discussion.

The theoretical Kerr coefficient used in Fig. 10.3 can be calculated as follows. Assuming $n_2 \approx 2.7 \times 10^{-20}$ m^2/W, $n_0 = 1.45$ for the silica material, and $V = 10^7$ μm^3 (obtained through finite-element simulations for the 36mm-diameter disk used here), gives $\eta/2\pi \approx 10^{-5}$ Hz. Using the Q_{ex} corrected by the white frequency noise data (see discussion above), $\gamma_{\mathrm{ex}}/2\pi = 299$ kHz so that $\Delta\omega_{\mathrm{Kerr}}/(2\pi\Delta P_{\mathrm{SBL}}) \approx 42$ Hz μW^{-1}. When $\gamma/\Gamma = 0.076$, the center shift of pump locking band is $-(\Gamma/\gamma)\Delta\omega_{\mathrm{Kerr}}$ = 558 Hz μW^{-1}. This value agrees very well with experiment (Fig. 10.3 inset).

10.3 Supplementary information

Non-Hermitian Hamiltonian and bi-orthogonal relations

Here we briefly review the framework for working with general non-Hermitian matrices. An n-dimensional matrix M has n eigenvalues μ_1, μ_2, ... μ_n. For simplicity we will assume that all of the eigenvalues are distinct, i.e. $\mu_j \neq \mu_k$ if $j \neq k$. In this case, M will have n right eigenvectors and n left eigenvectors associated with each μ_j:

$$M|v_j^{\mathrm{R}}\rangle = \mu_j|v_j^{\mathrm{R}}\rangle, \;\; \langle v_j^{\mathrm{L}}|M = \langle v_j^{\mathrm{L}}|\mu_j, \tag{10.10}$$

To make sense of the left eigenvectors, note that $M^\dagger|v_j^{\mathrm{L}}\rangle = \mu_j^*|v_j^{\mathrm{L}}\rangle$, thus the left eigenvector is the eigenstate as if loss is changed to gain and vice versa. Since M is in general non-Hermitian, there is no guarantee that $|v_j^{\mathrm{L}}\rangle = |v_j^{\mathrm{R}}\rangle$, and many of the decomposition results that hold in the Hermitian case will fail. However we note that

$$\mu_j\langle v_j^{\mathrm{L}}|v_k^{\mathrm{R}}\rangle = \langle v_j^{\mathrm{L}}|M|v_k^{\mathrm{R}}\rangle = \mu_k\langle v_j^{\mathrm{L}}|v_k^{\mathrm{R}}\rangle \;\Rightarrow\; \langle v_j^{\mathrm{L}}|v_k^{\mathrm{R}}\rangle = 0, \;\forall j \neq k. \tag{10.11}$$

Thus the left and right eigenvectors associated with different eigenvalues are bi-orthogonal. We also note that the right eigenvectors are complete and form a set of

basis (as M is non-degenerate and finite-dimensional), and we can decompose the identity matrix and M as follows:

$$1 = \sum_j \frac{|v_j^{\mathrm{R}}\rangle\langle v_j^{\mathrm{L}}|}{\langle v_j^{\mathrm{L}}|v_j^{\mathrm{R}}\rangle}, \tag{10.12}$$

$$M = \sum_j \frac{|v_j^{\mathrm{R}}\rangle\langle v_j^{\mathrm{L}}|}{\langle v_j^{\mathrm{L}}|v_j^{\mathrm{R}}\rangle}\mu_j, \tag{10.13}$$

where each term is a "projector" onto the eigenvectors. Again we note that $\langle v_j^{\mathrm{L}}|v_j^{\mathrm{R}}\rangle$ may be negative and even complex, which results in special normalizations of the vectors. For simplicity we will choose $\langle v_j^{\mathrm{L}}|v_j^{\mathrm{R}}\rangle = 1$ by rescaling the vectors and adjusting the relative phase (such vectors are sometimes said to be bi-orthonormal). With this normalization in place, the above decompositions simplify further as follows:

$$1 = \sum_j |v_j^{\mathrm{R}}\rangle\langle v_j^{\mathrm{L}}|, \tag{10.14}$$

$$M = \sum_j |v_j^{\mathrm{R}}\rangle\langle v_j^{\mathrm{L}}|\mu_j. \tag{10.15}$$

We note that, as a result of using bi-orthonormal left and right vectors, the vectors themselves are not normalized, i.e. $\langle v_j^{\mathrm{L}}|v_j^{\mathrm{L}}\rangle$ and $\langle v_j^{\mathrm{R}}|v_j^{\mathrm{R}}\rangle$ need not be 1 for each j. There is one extra degree of freedom per mode for fixing the lengths, but the length normalization factors do not affect the physical observables if such factors are kept consistently through the calculations. In Supplementary information 3, a "natural" normalization will be chosen when we give a physical meaning to these factors.

Petermann factor of a two-dimensional Hamiltonian

Here we derive the Petermann factor of a two-dimensional Hamiltonian H. Denote the two normalized right (left) eigenvectors of H as $|\psi_1^{\mathrm{R}}\rangle$ and $|\psi_2^{\mathrm{R}}\rangle$ ($|\psi_1^{\mathrm{L}}\rangle$ and $|\psi_2^{\mathrm{L}}\rangle$). The Petermann factors of these two eigenmodes can then be expressed as [35]

$$\mathrm{PF}_1 = \langle\psi_1^{\mathrm{L}}|\psi_1^{\mathrm{L}}\rangle\langle\psi_1^{\mathrm{R}}|\psi_1^{\mathrm{R}}\rangle, \tag{10.16}$$

$$\mathrm{PF}_2 = \langle\psi_2^{\mathrm{L}}|\psi_2^{\mathrm{L}}\rangle\langle\psi_2^{\mathrm{R}}|\psi_2^{\mathrm{R}}\rangle. \tag{10.17}$$

We will first prove that $\mathrm{PF}_1 = \mathrm{PF}_2$, which can then be identified as the Petermann factor for the entire system. Note that $|\psi_1^{\mathrm{L}}\rangle$ and $|\psi_2^{\mathrm{R}}\rangle$ are orthogonal and span the two-dimensional space. As a result, the identity can be expressed using this set of basis vectors as follows:

$$1 = \frac{|\psi_1^{\mathrm{L}}\rangle\langle\psi_1^{\mathrm{L}}|}{\langle\psi_1^{\mathrm{L}}|\psi_1^{\mathrm{L}}\rangle} + \frac{|\psi_2^{\mathrm{R}}\rangle\langle\psi_2^{\mathrm{R}}|}{\langle\psi_2^{\mathrm{R}}|\psi_2^{\mathrm{R}}\rangle}. \tag{10.18}$$

Now apply this expansion to $|\psi_1^{\mathrm{R}}\rangle$ and obtain

$$|\psi_1^{\mathrm{R}}\rangle = \frac{1}{\langle\psi_1^{\mathrm{L}}|\psi_1^{\mathrm{L}}\rangle}|\psi_1^{\mathrm{L}}\rangle + \frac{\langle\psi_2^{\mathrm{R}}|\psi_1^{\mathrm{R}}\rangle}{\langle\psi_2^{\mathrm{R}}|\psi_2^{\mathrm{R}}\rangle}|\psi_2^{\mathrm{R}}\rangle, \tag{10.19}$$

where $\langle\psi_1^{\mathrm{L}}|\psi_1^{\mathrm{R}}\rangle = 1$ has been used. Left multiplication by $\langle\psi_1^{\mathrm{R}}|$ results in

$$\langle\psi_1^{\mathrm{R}}|\psi_1^{\mathrm{R}}\rangle = \frac{1}{\langle\psi_1^{\mathrm{L}}|\psi_1^{\mathrm{L}}\rangle} + \frac{\langle\psi_1^{\mathrm{R}}|\psi_2^{\mathrm{R}}\rangle\langle\psi_2^{\mathrm{R}}|\psi_1^{\mathrm{R}}\rangle}{\langle\psi_2^{\mathrm{R}}|\psi_2^{\mathrm{R}}\rangle}. \tag{10.20}$$

Thus we obtain,

$$\frac{1}{\mathrm{PF}_1} = 1 - \frac{\langle\psi_1^{\mathrm{R}}|\psi_2^{\mathrm{R}}\rangle\langle\psi_2^{\mathrm{R}}|\psi_1^{\mathrm{R}}\rangle}{\langle\psi_1^{\mathrm{R}}|\psi_1^{\mathrm{R}}\rangle\langle\psi_2^{\mathrm{R}}|\psi_2^{\mathrm{R}}\rangle}, \tag{10.21}$$

which is symmetric with respect to the indexes 1 and 2 and thereby completes the proof that $\mathrm{PF}_1 = \mathrm{PF}_2 \equiv \mathrm{PF}$.

Next, PF is expressed using the Hamiltonian instead of its eigenvectors. We begin by noting that the identity operator added to the Hamiltonian will not modify the eigenvectors. As a result, the trace can be removed from H without changing the value of PF:

$$H_0 \equiv H - \frac{1}{2}\mathrm{Tr}(H), \tag{10.22}$$

where Tr is the matrix trace and H_0 is the traceless part of H. Using the bi-orthogonal expansion, H_0 has the form

$$H_0 = \mu(|\psi_1^{\mathrm{R}}\rangle\langle\psi_1^{\mathrm{L}}| - |\psi_2^{\mathrm{R}}\rangle\langle\psi_2^{\mathrm{L}}|), \tag{10.23}$$

where μ is the first eigenvalue. Consider next the quantity $\mathrm{Tr}(H_0^\dagger H_0)$:

$$\begin{aligned}\mathrm{Tr}(H_0^\dagger H_0) = |\mu|^2(&\langle\psi_1^{\mathrm{L}}|\psi_1^{\mathrm{L}}\rangle\langle\psi_1^{\mathrm{R}}|\psi_1^{\mathrm{R}}\rangle + \langle\psi_2^{\mathrm{L}}|\psi_2^{\mathrm{L}}\rangle\langle\psi_2^{\mathrm{R}}|\psi_2^{\mathrm{R}}\rangle \\ &-\langle\psi_2^{\mathrm{L}}|\psi_1^{\mathrm{L}}\rangle\langle\psi_1^{\mathrm{R}}|\psi_2^{\mathrm{R}}\rangle - \langle\psi_1^{\mathrm{L}}|\psi_2^{\mathrm{L}}\rangle\langle\psi_2^{\mathrm{R}}|\psi_1^{\mathrm{R}}\rangle),\end{aligned} \tag{10.24}$$

where we used the fact that $\mathrm{Tr}(|\alpha\rangle\langle\beta|) = \langle\beta|\alpha\rangle$. To simplify the expression, note that each of the first two terms equals PF. Moreover, the third term can be evaluated by expressing $|\psi_1^{\mathrm{L}}\rangle$ as a combination of right eigenvectors using Eq. (10.19):

$$-\langle\psi_2^{\mathrm{L}}|\psi_1^{\mathrm{L}}\rangle\langle\psi_1^{\mathrm{R}}|\psi_2^{\mathrm{R}}\rangle = \frac{\langle\psi_1^{\mathrm{R}}|\psi_2^{\mathrm{R}}\rangle\langle\psi_2^{\mathrm{R}}|\psi_1^{\mathrm{R}}\rangle}{\langle\psi_2^{\mathrm{R}}|\psi_2^{\mathrm{R}}\rangle}\langle\psi_1^{\mathrm{L}}|\psi_1^{\mathrm{L}}\rangle = \mathrm{PF} - 1. \tag{10.25}$$

Similarly, the fourth term also equals PF − 1. Thus

$$\mathrm{Tr}(H_0^\dagger H_0) = |\mu|^2(4\mathrm{PF} - 2). \tag{10.26}$$

Finally, to eliminate the eigenvalue μ, we calculate

$$\mathrm{Tr}(H_0^2) = \mu^2(\langle\psi_1^{\mathrm{L}}|\psi_1^{\mathrm{R}}\rangle^2 + \langle\psi_2^{\mathrm{L}}|\psi_2^{\mathrm{R}}\rangle^2) = 2\mu^2, \tag{10.27}$$

and the PF can be solved as

$$\mathrm{PF} = \frac{1}{2}\left(1 + \frac{\mathrm{Tr}(H_0^\dagger H_0)}{|\mathrm{Tr}(H_0^2)|}\right), \tag{10.28}$$

which completes the proof.

We note that while a Hermitian Hamiltonian with $H_0^\dagger = H_0$ results in PF = 1, the converse is not always true. Consider the example of $H_0 = i\sigma_z$ where σ_z is the Pauli matrix. This would effectively describe two orthogonal modes with different gain, and direct calculation shows that PF = 1.

Field amplitude and noise in a non-orthogonal system

Here we consider the physical interpretation of increased linewidth whereby the effective field amplitude decreases while the effective noise input increases as a result of non-orthogonality. This analysis considers a hypothetical laser mode that is part of the bi-orthogonal system. It skips key steps normally taken in a more rigorous laser noise analysis in order to make clearer the essential EP physics. A more complete study of the Brillouin laser system is provided in Supplementary information 4.

The two-dimensional system is described by the column vector $|\Psi\rangle \leftrightarrow (a_{\mathrm{cw}}, a_{\mathrm{ccw}})^T$ whose components are the orthogonal field amplitudes a_{cw} and a_{ccw}. The equation of motion reads $id|\Psi\rangle/dt = H|\Psi\rangle$, where H is the two-dimensional Hamiltonian. Now assume that $|\Psi\rangle = c_1|\psi_1^{\mathrm{R}}\rangle$, i.e. only the first eigenmode of the system is excited. We interpret c_1 as the phasor for the eigenmode. We see that $|c_1|^2 = \langle\Psi|\Psi\rangle/\langle\psi_1^{\mathrm{R}}|\psi_1^{\mathrm{R}}\rangle$ is reduced from the true square amplitude $\langle\Psi|\Psi\rangle$ by a factor of the length squared of the right eigenvector $\langle\psi_1^{\mathrm{R}}|\psi_1^{\mathrm{R}}\rangle$. The equation of motion for c_1 reads

$$i\frac{dc_1}{dt} = i\frac{d\langle\psi_1^{\mathrm{L}}|\Psi\rangle}{dt} = \langle\psi_1^{\mathrm{L}}|H_0|\psi_1^{\mathrm{R}}\rangle c_1 = \mu_1 c_1. \tag{10.29}$$

Here, we are assuming that the mode experiences both loss and saturable gain that are absorbed into the definition of the eigenvalue μ_1. To simplify the following calculations, we set the real part of μ_1 to 0, since any frequency shift can be removed with an appropriate transformation to slowly varying amplitudes.

To introduce noise into the system resulting from the amplification process the equation of motion is modified as follows: $id|\Psi\rangle/dt = H_0|\Psi\rangle + |F\rangle$. Here, $|F\rangle \leftrightarrow$

$(\overline{F}_{\mathrm{cw}}(t), \overline{F}_{\mathrm{ccw}}(t))^T$ is a column vector with fluctuating components. The noise correlation of these components is assumed to be given by

$$\langle \overline{F}^*_{\mathrm{cw}}(t)\overline{F}_{\mathrm{cw}}(t')\rangle = \langle \overline{F}^*_{\mathrm{ccw}}(t)\overline{F}_{\mathrm{ccw}}(t')\rangle = \theta\delta(t-t'), \tag{10.30}$$

$$\langle \overline{F}^*_{\mathrm{cw}}(t)\overline{F}_{\mathrm{ccw}}(t')\rangle = \langle \overline{F}^*_{\mathrm{ccw}}(t)\overline{F}_{\mathrm{cw}}(t')\rangle = 0, \tag{10.31}$$

where θ is a quantity with frequency dimensions. We note that the assumption of vanishing correlations between the fluctuations on different modes is not trivial. Even if the basis is orthogonal, the non-Hermitian nature of the Hamiltonian means that dissipative mode coupling will generally be present in the system. This will be associated with fluctuations that can induce off-diagonal elements in the correlation matrix. In the system studied here, we will show in Supplementary information 4 that the main source of noise comes from the phonons, and fluctuations due to the non-Hermitian Hamiltonian are negligible, thereby justifying the assumption made here. Taking account of the fluctuations, the equation of motion for c_1 can be modified as follows,

$$\frac{dc_1}{dt} = -|\mu_1|c_1 + \langle \psi_1^{\mathrm{L}}|F\rangle = -|\mu_1|c_1 + \overline{F}_1, \tag{10.32}$$

where the fluctuation term for the first eigenmode is defined as $\overline{F}_1 = \langle \psi_1^{\mathrm{L}}|F\rangle$. Its correlation reads

$$\langle \overline{F}^*_1(t)\overline{F}_1(t')\rangle = \theta\langle \psi_1^{\mathrm{L}}|\psi_1^{\mathrm{L}}\rangle\delta(t-t'), \tag{10.33}$$

which, upon comparison to Eq. (10.30), shows that the noise input to the right eigenvector field amplitude (c_1) is enhanced (relative to the noise input to either the cw or ccw fields alone) by a factor of the length squared of the left eigenvector $\langle \psi_1^{\mathrm{L}}|\psi_1^{\mathrm{L}}\rangle$.

We are interested in the phase fluctuations of c_1. Here, it is assumed that the mode is pumped to above threshold and is lasing. Under these conditions, it is possible to separate amplitude and phase fluctuations of the field. We rewrite $c_1 = |c_1|\exp(-i\phi_c)$ and obtain the rate of change of the phase variable as follows:

$$\frac{d\phi_c}{dt} = \frac{i}{2|c_1|}\left(\overline{F}_1 e^{i\phi_c} - \overline{F}^*_1 e^{-i\phi_c}\right), \tag{10.34}$$

which describes white frequency noise of the laser field (equivalently phase noise diffusion). The correlation can be calculated as

$$\begin{aligned}\langle \dot{\phi}_c(t)\dot{\phi}_c(t')\rangle &= \frac{\theta}{2|c_1|^2}\langle \psi_1^{\mathrm{L}}|\psi_1^{\mathrm{L}}\rangle\delta(t-t') = \frac{\theta}{2\langle\Psi|\Psi\rangle}\langle \psi_1^{\mathrm{R}}|\psi_1^{\mathrm{R}}\rangle\langle \psi_1^{\mathrm{L}}|\psi_1^{\mathrm{L}}\rangle\delta(t-t') \\ &= \mathrm{PF}\times\frac{\theta}{2\langle\Psi|\Psi\rangle}\delta(t-t'),\end{aligned} \tag{10.35}$$

where the non-enhanced linewidth is $\Delta\omega_0 = \theta/(2\langle\Psi|\Psi\rangle)$ [58] and the enhanced linewidth is given by $\Delta\omega = \mathrm{PF} \times \Delta\omega_0$. From the above derivation, the PF enhancement is the result of two effects, the reduction of effective square amplitude ($|c_1|^2 = \langle\Psi|\Psi\rangle/\langle\psi_1^{\mathrm{R}}|\psi_1^{\mathrm{R}}\rangle$) and the enhancement of noise by $\langle\psi_1^{\mathrm{L}}|\psi_1^{\mathrm{L}}\rangle$.

Up to now we have not chosen individual normalizations for $\langle\psi_1^{\mathrm{L}}|\psi_1^{\mathrm{L}}\rangle$ and $\langle\psi_1^{\mathrm{R}}|\psi_1^{\mathrm{R}}\rangle$ as they appear together in the Petermann factor. Motivated by the fact that left and right eigenvectors can be mapped onto the same Hilbert space, we select the symmetric normalization:

$$\langle\psi_1^{\mathrm{L}}|\psi_1^{\mathrm{L}}\rangle = \langle\psi_1^{\mathrm{R}}|\psi_1^{\mathrm{R}}\rangle = \sqrt{\mathrm{PF}}, \tag{10.36}$$

With this normalization, the squared field amplitude is reduced and the noise input is increased both by a factor of $\sqrt{\mathrm{PF}}$, resulting in the linewidth enhancement by a factor of PF. We note that other interpretations are possible through different normalizations. For example, in Siegman's analysis $\langle\psi_1^{\mathrm{L}}|\psi_1^{\mathrm{L}}\rangle = \mathrm{PF}$ and $\langle\psi_1^{\mathrm{R}}|\psi_1^{\mathrm{R}}\rangle = 1$ is chosen, and the enhancement is fully attributed to noise increase by a factor of PF [35] .

Langevin formalism

Here we analyze the system with a Langevin formalism, which includes Brillioun gain, the Sagnac effect, and the Kerr effect. An Adler-like equation will be derived that provides an improved laser linewidth formula and an expression for the locking bandwidth dependence on the field amplitude ratio.

First we summarize symbols and give their definitions. For readability, all cw subscript will be replaced by $\overline{1}$ and all ccw subscript will be replaced by $\overline{2}$. The modes are pumped at angular frequencies $\omega_{\mathrm{P},\overline{1}}$ and $\omega_{\mathrm{P},\overline{2}}$. These frequencies will generally be different from the unpumped resonator mode frequency. The cw and ccw stimulated Brillouin lasers (SBLs) oscillate on the same longitudinal mode with frequency ω. This frequency is shifted for both cw and ccw waves by the same amount as a result of the pump-induced Kerr shift. On the other hand, the Kerr effect causes cross-phase and self-phase modulation of the cw and ccw waves that induces different frequency shifts in these waves. This shift and the rotation-induced Sagnac shift are accounted for using offset frequencies $\delta\omega_{\overline{1}} = -\eta\left(a_{\overline{1}}^{\dagger}a_{\overline{1}} + 2a_{\overline{2}}^{\dagger}a_{\overline{2}}\right) - \Omega\omega D/(2n_{\mathrm{g}}c)$ and $\delta\omega_{\overline{2}} = -\eta\left(a_{\overline{2}}^{\dagger}a_{\overline{2}} + 2a_{\overline{1}}^{\dagger}a_{\overline{1}}\right) + \Omega\omega D/(2n_{\mathrm{g}}c)$ relative to ω, where $\eta = n_2\hbar\omega^2 c/(Vn_0^2)$ is the single-photon nonlinear angular frequency shift, n_2 is the nonlinear refractive index, V is the mode volume, n_0 is the linear refractive index, c is the speed of light

in vacuum, Ω is the rotation rate, D is the resonator diameter, and n_g is the group index. Phonon modes have angular frequencies $\Omega_{\text{phonon}} = 2\omega n_0 v_s/c$, where v_s is the velocity of the phonons. The loss rate of phonon modes is denoted as Γ (also known as the gain bandwidth) and the loss rate of the SBL modes are assumed equal and denoted as γ. In addition, coupling between the two SBL modes is separated as a dissipative part and conservative part, denoted as κ and χ, respectively. These rates will be assumed to satisfy $\Gamma \gg \gamma \gg |\kappa|, |\chi|$ to simplify the calculations, which is *a posteriori* verified in our system. In the following analysis, we will treat the SBL modes and phonon modes quantum mechanically and define $a_{\bar{1}}$ ($a_{\bar{2}}$) and $b_{\bar{1}}$ ($b_{\bar{2}}$) as the lowering operators of the cw (ccw) components of the SBL and phonon modes, respectively. Meanwhile, pump modes are treated as a noise-free classical fields $A_{\bar{1}}$ and $A_{\bar{2}}$ (photon-number-normalized amplitudes).

Using these definitions, the full equations of motion for the SBL and phonon modes read

$$\dot{a}_{\bar{1}} = -\left(\frac{\gamma}{2} + i\omega + i\delta\omega_{\bar{1}}\right) a_{\bar{1}} + (\kappa + i\chi) a_{\bar{2}} - i g_{ab} A_{\bar{2}} b_{\bar{2}}^{\dagger} \exp(-i\omega_{\text{P},\bar{2}} t) + F_{\bar{1}}(t), \tag{10.37}$$

$$\dot{a}_{\bar{2}} = -\left(\frac{\gamma}{2} + i\omega + i\delta\omega_{\bar{2}}\right) a_{\bar{2}} + (\kappa^* + i\chi^*) a_{\bar{1}} - i g_{ab} A_{\bar{1}} b_{\bar{1}}^{\dagger} \exp(-i\omega_{\text{P},\bar{1}} t) + F_{\bar{2}}(t), \tag{10.38}$$

$$\dot{b}_{\bar{1}}^{\dagger} = -\left(\frac{\Gamma}{2} - i\Omega_{\text{phonon}}\right) b_{\bar{1}}^{\dagger} + i g_{ab} A_{\bar{1}}^{*} a_{\bar{2}} \exp(i\omega_{\text{P},\bar{1}} t) + f_{\bar{1}}^{\dagger}(t), \tag{10.39}$$

$$\dot{b}_{\bar{2}}^{\dagger} = -\left(\frac{\Gamma}{2} - i\Omega_{\text{phonon}}\right) b_{\bar{2}}^{\dagger} + i g_{ab} A_{\bar{2}}^{*} a_{\bar{1}} \exp(i\omega_{\text{P},\bar{2}} t) + f_{\bar{2}}^{\dagger}(t), \tag{10.40}$$

where g_{ab} is the single-particle Brillioun coupling coefficient. The fluctuation operators $F(t)$ and $f(t)$ associated with the field operators have the following correlations:

$$\langle F_{\bar{1}}^{\dagger}(t) F_{\bar{1}}(t') \rangle = \langle F_{\bar{2}}^{\dagger}(t) F_{\bar{2}}(t') \rangle = \gamma N_{\text{th}} \delta(t - t'), \tag{10.41}$$

$$\langle F_{\bar{1}}(t) F_{\bar{1}}^{\dagger}(t') \rangle = \langle F_{\bar{2}}(t) F_{\bar{2}}^{\dagger}(t') \rangle = \gamma (N_{\text{th}} + 1) \delta(t - t'), \tag{10.42}$$

$$\langle f_{\bar{1}}^{\dagger}(t) f_{\bar{1}}(t') \rangle = \langle f_{\bar{2}}^{\dagger}(t) f_{\bar{2}}(t') \rangle = \Gamma n_{\text{th}} \delta(t - t'), \tag{10.43}$$

$$\langle f_{\bar{1}}(t) f_{\bar{1}}^{\dagger}(t') \rangle = \langle f_{\bar{2}}(t) f_{\bar{2}}^{\dagger}(t') \rangle = \Gamma (n_{\text{th}} + 1) \delta(t - t'), \tag{10.44}$$

where N_{th} and n_{th} are the thermal occupation numbers of the SBL state and phonon state. In addition, there are non-zero cross-correlations of the photon fluctuation

operators due to the dissipative coupling:

$$\langle F_{\bar{2}}^{\dagger}(t)F_{\bar{1}}(t')\rangle = -2\kappa N_{\mathrm{th}}\delta(t-t'), \tag{10.45}$$

$$\langle F_{\bar{1}}^{\dagger}(t)F_{\bar{2}}(t')\rangle = -2\kappa^{*} N_{\mathrm{th}}\delta(t-t'), \tag{10.46}$$

$$\langle F_{\bar{2}}(t)F_{\bar{1}}^{\dagger}(t')\rangle = -2\kappa^{*}(N_{\mathrm{th}}+1)\delta(t-t'), \tag{10.47}$$

$$\langle F_{\bar{1}}(t)F_{\bar{2}}^{\dagger}(t')\rangle = -2\kappa(N_{\mathrm{th}}+1)\delta(t-t'). \tag{10.48}$$

All other cross correlations not explicitly written are 0.

Single SBL

We first study a single laser mode and its corresponding phonon field ($a_{\bar{1}}$ and $b_{\bar{2}}$) by neglecting κ and χ. By introducing the slow varying envelope with $a_{\bar{1}} = \alpha_{\bar{1}}\mathrm{e}^{-i\omega t}$ and $b_{\bar{2}} = \beta_{\bar{2}}\mathrm{e}^{-i(\omega_{\mathrm{P},\bar{2}}-\omega)t}$, the following equations result:

$$\dot{\alpha}_{\bar{1}} = -\left(\frac{\gamma}{2} + i\delta\omega_{\bar{1}}\right)\alpha_{\bar{1}} - ig_{ab}A_{\bar{2}}\beta_{\bar{2}}^{\dagger} + F_{\bar{1}}(t)\mathrm{e}^{i\omega t}, \tag{10.49}$$

$$\dot{\beta}_{\bar{2}}^{\dagger} = -\left(\frac{\Gamma}{2} + i\Delta\Omega_{\bar{2}}\right)\beta_{\bar{2}}^{\dagger} + ig_{ab}A_{\bar{2}}^{*}\alpha_{\bar{1}} + f_{\bar{2}}^{\dagger}(t)\mathrm{e}^{-i(\omega_{\mathrm{P},\bar{2}}-\omega)t}, \tag{10.50}$$

where we have defined the frequency mismatch $\Delta\Omega_{\bar{2}} = \omega_{\mathrm{P},\bar{2}} - \omega - \Omega_{\mathrm{phonon}}$. Neglecting the weak Kerr effect term in $\delta\omega_{\bar{1}}$, this is a set of linear equations in $a_{\bar{1}}$ and $b_{\bar{2}}$. The eigenvalues of the coefficient matrix,

$$\begin{pmatrix} -\gamma/2 - i\delta\omega_{\bar{1}} & -ig_{ab}A_{\bar{2}} \\ ig_{ab}A_{\bar{2}}^{*} & -\Gamma/2 - i\Delta\Omega_{\bar{2}} \end{pmatrix}, \tag{10.51}$$

can be solved as

$$\mu_{1,2} = \frac{1}{4}\left(-\Gamma - \gamma - 2i\delta\omega_{\bar{1}} - 2i\Delta\Omega_{\bar{2}} \pm \sqrt{16g_{ab}^{2}|A_{\bar{2}}|^{2} + (\Gamma - \gamma - 2i\delta\omega_{\bar{1}} + 2i\Delta\Omega_{\bar{2}})^{2}}\right). \tag{10.52}$$

At the lasing threshold, the first eigenvalue μ_1 has a real part of 0. This can be rewritten as

$$16g_{ab}^{2}|A_{\bar{2}}|^{2} + (\Gamma - \gamma - 2i\delta\omega_{\bar{1}} + 2i\Delta\Omega_{\bar{2}})^{2} = (\Gamma + \gamma + 2i\delta\omega_{\bar{1}} + 2i\Delta\Omega_{\bar{2}} + 4i\mathrm{Im}(\mu_1))^{2}. \tag{10.53}$$

Solving this complex equation gives the SBL eigenfrequency as well as the lasing threshold,

$$\mu_1 = -i\frac{\gamma\Delta\Omega_{\bar{2}} + \Gamma\delta\omega_{\bar{1}}}{\Gamma + \gamma}, \tag{10.54}$$

$$g_{ab}^{2}|A_{\bar{2}}|^{2} = \frac{\Gamma\gamma}{4}\left(1 + \frac{4(\Delta\Omega_{\bar{2}} - \delta\omega_{\bar{1}})^{2}}{(\Gamma + \gamma)^{2}}\right). \tag{10.55}$$

The threshold at perfect phase matching ($\Delta\Omega_{\bar{2}} = \delta\omega_{\bar{1}}$) is usually written in a more familiar form $g_0|A_{\bar{2}}|^2 = \gamma/2$, where g_0 is the Brillouin gain factor [33]. Comparison gives

$$g_{ab} = \sqrt{\frac{g_0\Gamma}{2}}. \tag{10.56}$$

We also introduce the modal Brillioun gain function for a single direction:

$$g_{\bar{1}} \equiv \frac{g_0}{1 + 4(\delta\omega_{\bar{1}} - \Delta\Omega_{\bar{2}})^2/(\Gamma+\gamma)^2}, \tag{10.57}$$

so that the threshold can be written as

$$g_{\bar{1}}|A_{\bar{2}}|^2 = \frac{\gamma}{2}. \tag{10.58}$$

With the threshold condition solved, the matrix can be decomposed using the bi-orthogonal approach outlined in Supplementary information 1. The linear combination that describes the composite SBL mode can be found as

$$\overline{\alpha}_{\bar{1}} = \frac{\Gamma}{\gamma+\Gamma}\left[\alpha_{\bar{1}} - i\frac{g_{ab}}{\Gamma}\frac{2}{1 + 2i(\Delta\Omega_{\bar{2}} - \delta\omega_{\bar{1}})/(\Gamma+\gamma)}A_{\bar{2}}\beta^{\dagger}_{\bar{2}}\right], \tag{10.59}$$

where the factor $\Gamma/(\gamma+\Gamma)$ properly normalizes $\overline{\alpha}_{\bar{1}}$ so that $\overline{\alpha}_{\bar{1}} = \alpha_{\bar{1}}$ when only the SBL mode is present in the system, and we have dropped its dependence on the phase mismatch $\Delta\Omega_{\bar{2}} - \delta\omega_{\bar{1}}$ for simplicity. The associated equation of motion is

$$\frac{d}{dt}\overline{\alpha}_{\bar{1}} = -i\frac{\gamma\Delta\Omega_{\bar{2}} + \Gamma\delta\omega_{\bar{1}}}{\Gamma+\gamma}\overline{\alpha}_{\bar{1}} + \overline{F}_{\bar{1}}(t), \tag{10.60}$$

where the frequency term now includes a mode-pulling contribution so that the SBL laser frequency is given by

$$\omega_{\mathrm{S},\bar{1}} = \omega + \frac{\gamma\Delta\Omega_{\bar{2}} + \Gamma\delta\omega_{\bar{1}}}{\Gamma+\gamma}. \tag{10.61}$$

Also, we have defined a combined fluctuation operator for $\overline{\alpha}_{\bar{1}}$,

$$\overline{F}_{\bar{1}}(t) = \frac{\Gamma}{\gamma+\Gamma}\left[F_{\bar{1}}(t)\mathrm{e}^{i\omega t} - i\sqrt{\frac{1 - 2i(\Delta\Omega_{\bar{2}} - \delta\omega_{\bar{1}})/(\Gamma+\gamma)}{1 + 2i(\Delta\Omega_{\bar{2}} - \delta\omega_{\bar{1}})/(\Gamma+\gamma)}}\sqrt{\frac{\gamma}{\Gamma}}f^{\dagger}_{\bar{2}}(t)\mathrm{e}^{-i(\omega_{\mathrm{P},\bar{2}}-\omega)t}\right], \tag{10.62}$$

with the following correlations,

$$\langle \overline{F}_{\bar{1}}^{\dagger}(t)\overline{F}_{\bar{1}}(t')\rangle = \left(\frac{\Gamma}{\gamma+\Gamma}\right)^2 \left(\langle F_{\bar{1}}^{\dagger}(t)F_{\bar{1}}(t')\rangle + \frac{\gamma}{\Gamma}\langle f_{\bar{1}}^{\dagger}(t)f_{\bar{1}}(t')\rangle\right)$$
$$= \left(\frac{\Gamma}{\gamma+\Gamma}\right)^2 \gamma(n_{\mathrm{th}}+N_{\mathrm{th}})\delta(t-t'), \tag{10.63}$$
$$\langle \overline{F}_{\bar{1}}(t)\overline{F}_{\bar{1}}^{\dagger}(t')\rangle = \left(\frac{\Gamma}{\gamma+\Gamma}\right)^2 \left(\langle F_{\bar{1}}(t)F_{\bar{1}}^{\dagger}(t')\rangle + \frac{\gamma}{\Gamma}\langle f_{\bar{1}}(t)f_{\bar{1}}^{\dagger}(t')\rangle\right)$$
$$= \left(\frac{\Gamma}{\gamma+\Gamma}\right)^2 \gamma(n_{\mathrm{th}}+N_{\mathrm{th}}+2)\delta(t-t'), \tag{10.64}$$

We can now write $\overline{\alpha}_{\bar{1}}(t) = \sqrt{N_{\bar{1}}}\exp(-i\phi_{\bar{1}})$, where $N_{\bar{1}}$ is the photon number, $\phi_{\bar{1}}$ is the phase for the SBL, and where amplitude fluctuations have been ignored on account of quenching of these fluctuations above laser threshold. We note that amplitude fluctuations may result in linewidth corrections similar to the Henry α factor, but we will ignore these effects here. The full equation of motion for $\phi_{\bar{1}}$ is

$$\dot{\phi}_{\bar{1}} = \omega_{\mathrm{S},\bar{1}} - \omega + \Phi_{\bar{1}}(t), \quad \Phi_{\bar{1}}(t) = \frac{i}{2\sqrt{N_{\bar{1}}}}(\overline{F}_{\bar{1}}(t)\mathrm{e}^{i\phi_{\bar{1}}} - \overline{F}_{\bar{1}}^{\dagger}(t)\mathrm{e}^{-i\phi_{\bar{1}}}). \tag{10.65}$$

The correlation of the noise operator is given by,

$$\langle \Phi_{\bar{1}}(t)\Phi_{\bar{1}}(t')\rangle = \frac{1}{4N_{\bar{1}}}(\langle \overline{F}_{\bar{1}}^{\dagger}(t)\overline{F}_{\bar{1}}(t')\rangle + \langle \overline{F}_{\bar{1}}(t)\overline{F}_{\bar{1}}^{\dagger}(t')\rangle$$
$$= \left(\frac{\Gamma}{\gamma+\Gamma}\right)^2 \frac{\gamma}{2N_{\bar{1}}}(n_{\mathrm{th}}+N_{\mathrm{th}}+1)\delta(t-t'), \tag{10.66}$$

and we identify the coefficient before the delta function,

$$\Delta\omega_{\mathrm{FWHM},\bar{1}} = \left(\frac{\Gamma}{\gamma+\Gamma}\right)^2 \frac{\gamma}{2N_{\bar{1}}}(n_{\mathrm{th}}+N_{\mathrm{th}}+1), \tag{10.67}$$

as the full-width half-maximum (FWHM) linewidth of the SBL.

In the experiment, the frequency noise of the SBL beating signal is measured. To compare against the experiment, we calculate the FWHM linewidth for the beating signal by adding together the linewidths in two directions:

$$\Delta\omega_{\mathrm{FWHM}} = \Delta\omega_{\mathrm{FWHM},\bar{1}} + \Delta\omega_{\mathrm{FWHM},\bar{2}} = \left(\frac{\Gamma}{\gamma+\Gamma}\right)^2 \left(\frac{1}{2N_{\bar{1}}} + \frac{1}{2N_{\bar{2}}}\right)\gamma(n_{\mathrm{th}}+N_{\mathrm{th}}+1), \tag{10.68}$$

and then convert to the one-sided power spectral density S_ν:

$$S_\nu = \frac{1}{\pi}\frac{\Delta\omega_{\mathrm{FWHM}}}{2\pi} = \left(\frac{\Gamma}{\gamma+\Gamma}\right)^2 \frac{\hbar\omega^3}{4\pi^2 Q_{\mathrm{T}}Q_{\mathrm{ex}}}\left(\frac{1}{P_{\mathrm{cw}}} + \frac{1}{P_{\mathrm{ccw}}}\right)(n_{\mathrm{th}}+N_{\mathrm{th}}+1), \tag{10.69}$$

where Q_{T} and Q_{ex} are the loaded and coupling Q factors, and P_{cw} and P_{ccw} are the SBL powers in each direction.

Two SBLs

Now we can apply a similar procedure to the two pairs of photon and phonon modes with coupling on the optical modes. We write the equations of motion for the SBL modes:

$$\frac{d}{dt}\overline{\alpha}_{\overline{1}} = -i(\omega_{\mathrm{S},\overline{1}} - \omega)\overline{\alpha}_{\overline{1}} + \frac{\Gamma}{\gamma+\Gamma}(\kappa + i\chi)\alpha_{\overline{2}} + \overline{F}_{\overline{1}}(t), \tag{10.70}$$

$$\frac{d}{dt}\overline{\alpha}_{\overline{2}} = -i(\omega_{\mathrm{S},\overline{2}} - \omega)\overline{\alpha}_{\overline{2}} + \frac{\Gamma}{\gamma+\Gamma}(\kappa^* + i\chi^*)\alpha_{\overline{1}} + \overline{F}_{\overline{2}}(t), \tag{10.71}$$

where quantities with the opposite subscript are defined similarly. We note that the coupling term involves the optical modes $\alpha_{\overline{1}}$ and $\alpha_{\overline{2}}$ only. However, no additional coupling occurs between the other components of the SBL eigenstates $\overline{\alpha}_{\overline{1}}$ and $\overline{\alpha}_{\overline{2}}$, and these states do not change up to first order of κ/γ and χ/γ. Thus we can approximate the optical mode $\alpha_{\overline{1}}$ with the composite SBL mode $\overline{\alpha}_{\overline{1}}$. Within these approximations the lasing thresholds are also the same as the independent case [24]. The equations now become

$$\frac{d}{dt}\overline{\alpha}_{\overline{1}} = -i(\omega_{\mathrm{S},\overline{1}} - \omega)\overline{\alpha}_{\overline{1}} + (\overline{\kappa} + i\overline{\chi})\overline{\alpha}_{\overline{2}} + \overline{F}_{\overline{1}}(t), \tag{10.72}$$

$$\frac{d}{dt}\overline{\alpha}_{\overline{2}} = -i(\omega_{\mathrm{S},\overline{2}} - \omega)\overline{\alpha}_{\overline{2}} + (\overline{\kappa}^* + i\overline{\chi}^*)\overline{\alpha}_{\overline{1}} + \overline{F}_{\overline{2}}(t), \tag{10.73}$$

where we have defined mode-pulled coupling rates $\overline{\kappa} = \kappa\Gamma/(\gamma+\Gamma)$ and $\overline{\chi} = \chi\Gamma/(\gamma+\Gamma)$.

We can write $\overline{\alpha}_j(t) = \sqrt{N_j}\exp(-i\phi_j)$ with $j = \overline{1}, \overline{2}$, and once again ignore amplitude fluctuations. The equations of motion for the phases are

$$\frac{d}{dt}\phi_{\overline{1}} = (\omega_{\mathrm{S},\overline{1}} - \omega) - q\mathrm{Im}[(\overline{\kappa} + i\overline{\chi})\mathrm{e}^{(i\phi_{\overline{1}} - i\phi_{\overline{2}})}] + \frac{i}{2\sqrt{N_{\overline{1}}}}(\overline{F}_{\overline{1}}(t)\mathrm{e}^{i\phi_{\overline{1}}} - \overline{F}^{\dagger}_{\overline{1}}(t)\mathrm{e}^{-i\phi_{\overline{1}}}), \tag{10.74}$$

$$\frac{d}{dt}\phi_{\overline{2}} = (\omega_{\mathrm{S},\overline{2}} - \omega) - q^{-1}\mathrm{Im}[(\overline{\kappa}^* + i\overline{\chi}^*)\mathrm{e}^{(i\phi_{\overline{2}} - i\phi_{\overline{1}})}] + \frac{i}{2\sqrt{N_{\overline{2}}}}(\overline{F}_{\overline{2}}(t)\mathrm{e}^{i\phi_{\overline{2}}} - \overline{F}^{\dagger}_{\overline{2}}(t)\mathrm{e}^{-i\phi_{\overline{2}}}), \tag{10.75}$$

where we have defined the amplitude ratio $q = \sqrt{N_{\overline{2}}/N_{\overline{1}}}$ for simplicity. As we measure the beatnote frequency, it is convenient to define $\phi \equiv \phi_{\overline{2}} - \phi_{\overline{1}}$ from which we obtain

$$\frac{d\phi}{dt} = (\omega_{\mathrm{S},\overline{2}} - \omega_{\mathrm{S},\overline{1}}) + \mathrm{Im}\left\{\left[q(\overline{\kappa} + i\overline{\chi}) + q^{-1}(\overline{\kappa} - i\overline{\chi})\right]\mathrm{e}^{-i\phi}\right\} + \Phi(t), \tag{10.76}$$

where the combined noise term and its correlation are given by

$$\Phi = -\frac{i}{2\sqrt{N_{\bar{1}}}}(\overline{F}_{\bar{1}}(t)\mathrm{e}^{i\phi_{\bar{1}}} - \overline{F}^{\dagger}_{\bar{1}}(t)\mathrm{e}^{-i\phi_{\bar{1}}}) + \frac{i}{2\sqrt{N_{\bar{2}}}}(\overline{F}_{\bar{2}}(t)\mathrm{e}^{i\phi_{\bar{2}}} - \overline{F}^{\dagger}_{\bar{2}}(t)\mathrm{e}^{-i\phi_{\bar{2}}}), \quad (10.77)$$

$$\begin{aligned}\langle\Phi(t)\Phi(t')\rangle = &\left(\frac{\Gamma}{\gamma+\Gamma}\right)^2\delta(t-t') \\ &\times\left[\left(\frac{1}{2N_{\bar{1}}}+\frac{1}{2N_{\bar{2}}}\right)\gamma(N_{\mathrm{th}}+n_{\mathrm{th}}+1)+\frac{2}{\sqrt{N_{\bar{1}}N_{\bar{2}}}}\left(N_{\mathrm{th}}+\frac{1}{2}\right)\mathrm{Re}(\kappa\mathrm{e}^{-i\phi(t)})\right],\end{aligned} \quad (10.78)$$

Since both N_{th} and κ/γ is small, we will discard the last time-varying term and write

$$\langle\Phi(t)\Phi(t')\rangle \approx \Delta\omega_{\mathrm{FWHM}}\delta(t-t'), \quad (10.79)$$

where $\Delta\omega_{\mathrm{FWHM}} = \Gamma^2/(\gamma+\Gamma)^2[(2N_{\bar{1}})^{-1}+(2N_{\bar{2}})^{-1}]\gamma(N_{\mathrm{th}}+n_{\mathrm{th}}+1)$ is the linewidth of the beating signal far from the EP (see also the single SBL discussion).

This equation can be further simplified by introducing an overall phase shift with $\overline{\phi} = \phi - \phi_0$, where $\phi_0 = \mathrm{Arg}\left[q(\overline{\kappa}+i\overline{\chi})+q^{-1}(\overline{\kappa}-i\overline{\chi})\right]$ and $\mathrm{Arg}(z)$ is the phase of z:

$$\frac{d\overline{\phi}}{dt} = \Delta\omega_{\mathrm{D}} - \Delta\omega_{\mathrm{EP}}\sin\overline{\phi} + \Phi(t), \quad (10.80)$$

with

$$\Delta\omega_{\mathrm{D}} = \omega_{\mathrm{S},\bar{2}} - \omega_{\mathrm{S},\bar{1}} = \frac{\gamma}{\Gamma+\gamma}(\omega_{\mathrm{P},\bar{1}} - \omega_{\mathrm{P},\bar{2}}) + \frac{\Gamma}{\Gamma+\gamma}\left[\eta(N_{\bar{2}} - N_{\bar{1}}) + \frac{\omega D}{n_{\mathrm{g}}c}\Omega\right], \quad (10.81)$$

$$\begin{aligned}\Delta\omega_{\mathrm{EP}}^2 &= \left|q(\overline{\kappa}+i\overline{\chi})+q^{-1}(\overline{\kappa}-i\overline{\chi})\right|^2 \\ &= \left(\frac{\Gamma}{\gamma+\Gamma}\right)^2\left[\left(q+\frac{1}{q}\right)^2|\kappa|^2+\left(q-\frac{1}{q}\right)^2|\chi|^2+2\left(q^2-\frac{1}{q^2}\right)\mathrm{Im}(\kappa\chi^*)\right],\end{aligned} \quad (10.82)$$

This is an Adler equation with a noisy input. It shows the dependence of locking bandwidth on the amplitude ratio and coupling coefficients. Moreover, it is clear that in the absence of $\Delta\omega_{\mathrm{EP}}$, the beating linewidth would be given by $\Delta\omega_{\mathrm{FWHM}}$. The locking term $\Delta\omega_{\mathrm{EP}}\sin\overline{\phi}$ makes the rate of phase change nonuniform and increases the linewidth.

The following part of analysis is dedicated to obtaining the linewidth from this stochastic Adler equation. We define $z_\phi = \exp(-i\overline{\phi})$ and rewrite

$$\frac{d}{dt}z_\phi = -iz_\phi(\Delta\omega_{\mathrm{D}} + \Delta\omega_{\mathrm{EP}}\frac{z_\phi - z_\phi^{-1}}{2i} + \Phi). \quad (10.83)$$

The solution to the Adler equation is periodic when no noise is present. To see this explicitly, we use a linear fractional transform:

$$z_t = \frac{(\Delta\omega_D - \Delta\omega_S)z_\phi + i\Delta\omega_{EP}}{\Delta\omega_{EP}z_\phi + i(\Delta\omega_D - \Delta\omega_S)}, \quad z_\phi = -i\frac{(\Delta\omega_D - \Delta\omega_S)z_t - \Delta\omega_{EP}}{\Delta\omega_{EP}z_t - (\Delta\omega_D - \Delta\omega_S)}, \quad |z_\phi| = |z_t| = 1, \tag{10.84}$$

$$\frac{1}{z_t}\frac{d}{dt}z_t = i\Delta\omega_S - i\frac{\Delta\omega_{EP}(z_t + z_t^{-1})/2 - \Delta\omega_D}{\Delta\omega_S}\Phi, \tag{10.85}$$

where we introduced $\Delta\omega_S = \sqrt{\Delta\omega_D^2 - \Delta\omega_{EP}^2}$ (which has the same meaning in the main text). The noiseless solution of z_t would be $z_t = \exp(i\Delta\omega_S t)$, and z_ϕ can be expanded in z_t as

$$z_\phi = -i\frac{\Delta\omega_D - \Delta\omega_S}{\Delta\omega_{EP}} + 2i\frac{\Delta\omega_S}{\Delta\omega_{EP}}\sum_{p=1}^{\infty}\left(\frac{\Delta\omega_D - \Delta\omega_S}{\Delta\omega_{EP}z_t}\right)^p, \tag{10.86}$$

where we have assumed $\Delta\omega_D > \Delta\omega_{EP}$ for convenience so that convergence can be guaranteed (for the case $\Delta\omega_D < -\Delta\omega_{EP}$ we can expand near $z_t = 0$ instead of $z_t = \infty$). Thus the signal consists of harmonics oscillating at frequency $p\Delta\omega_S$ with exponentially decreasing amplitudes. The noise added only changes the phase of z_t (as the coefficient is purely imaginary) and to the lowest order the only effect of noise is to broaden each harmonic.

The linewidth can be found from the spectral density, which is given by the Fourier transform of the correlation function:

$$W_E(\omega) \propto \mathcal{F}_\tau\{\langle z_\phi^*(t)z_\phi(t+\tau)\rangle\}(\omega), \tag{10.87}$$

and the correlation is given by

$$\langle z_\phi^*(t)z_\phi(t+\tau)\rangle = \left(\frac{\Delta\omega_D - \Delta\omega_S}{\Delta\omega_{EP}}\right)^2 + 4\frac{\Delta\omega_S^2}{\Delta\omega_{EP}^2}\sum_{p=1}^{\infty}\left(\frac{\Delta\omega_D - \Delta\omega_S}{\Delta\omega_{EP}}\right)^{2p}\langle z_t(t)^p z_t(t+\tau)^{-p}\rangle, \tag{10.88}$$

where we have discarded the $\langle z_t(t)^p z_t(t+\tau)^{-q}\rangle$ $(p \neq q)$ terms since they vanish at the lowest order of $\Delta\omega_{FWHM}$.

To further calculate each $\langle z_t(t)^p z_t(t+\tau)^{-p}\rangle \equiv C_p(\tau)$, we require the integral form of the Fokker-Planck equation: if $dX(t) = \mu(X,t)dt + \sigma(X,t)dW$ is a stochastic differential equation (in the Stratonovich interpretation), where W is a Wiener process, then for $f(X)$ as a function of X, the differential equation for its average reads

$$\frac{d}{dt}\langle f(X)\rangle = \langle(\mu + \frac{\sigma}{2}\frac{\partial\sigma}{\partial X})f'(X)\rangle + \langle\frac{1}{2}\sigma^2 f''(X)\rangle. \tag{10.89}$$

Applying the Fokker-Planck equation to $C_p(\tau)$, with the stochastic equation for z_t, gives

$$\begin{aligned}
&\frac{dC_p(\tau)}{d\tau} \\
&= -p\langle i\Delta\omega_{\mathrm{S}} z_t(t)^p z_t(t+\tau)^{-p}\rangle \\
&+p\langle\left[\frac{\Delta\omega_{\mathrm{FWHM}}}{2\Delta\omega_{\mathrm{S}}^2}\left(\Delta\omega_{\mathrm{EP}}\frac{z_t(t+\tau)+z_t^{-1}(t+\tau)}{2}-\Delta\omega_{\mathrm{D}}\right)\left(\Delta\omega_{\mathrm{EP}} z_t(t+\tau)-\Delta\omega_{\mathrm{D}}\right)\right] \\
&\quad\times z_t(t)^p z_t(t+\tau)^{-p}\rangle \\
&-p(p+1)\langle\frac{\Delta\omega_{\mathrm{FWHM}}}{2\Delta\omega_{\mathrm{S}}^2}\left(\Delta\omega_{\mathrm{EP}}\frac{z_t(t+\tau)+z_t^{-1}(t+\tau)}{2}-\Delta\omega_{\mathrm{D}}\right)^2 z_t(t)^p z_t(t+\tau)^{-p}\rangle
\end{aligned} \tag{10.90}$$

$$\approx\left(-ip\Delta\omega_{\mathrm{S}}-p^2\frac{\Delta\omega_{\mathrm{D}}^2+\Delta\omega_{\mathrm{EP}}^2/2}{2\Delta\omega_{\mathrm{S}}^2}\Delta\omega_{\mathrm{FWHM}}\right)C_p(\tau), \tag{10.91}$$

and $C_p(0)=1$, where again $\langle z_t(t)^p z_t(t+\tau)^{-q}\rangle$ $(p\neq q)$ terms are discarded. Thus completing the Fourier transform for each term gives the linewidth of the respective harmonics. In particular, the linewidth of the fundamental frequency can be found through

$$W_{E,1}(\omega)\propto\frac{\Delta\overline{\omega}_{\mathrm{FWHM}}}{(\omega-\Delta\omega_{\mathrm{S}})^2+\Delta\overline{\omega}_{\mathrm{FWHM}}^2/4}, \tag{10.92}$$

with

$$\Delta\overline{\omega}_{\mathrm{FWHM}}=\frac{\Delta\omega_{\mathrm{D}}^2+\Delta\omega_{\mathrm{EP}}^2/2}{\Delta\omega_{\mathrm{S}}^2}\Delta\omega_{\mathrm{FWHM}}=\frac{\Delta\omega_{\mathrm{D}}^2+\Delta\omega_{\mathrm{EP}}^2/2}{\Delta\omega_{\mathrm{D}}^2-\Delta\omega_{\mathrm{EP}}^2}\Delta\omega_{\mathrm{FWHM}}. \tag{10.93}$$

We see that this result is different from the Petermann factor result, which is a theory linear in photon numbers and does not correctly take account of the saturation of the lasers and the Adler mode-locking effect.

From the expressions of $\Delta\omega_{\mathrm{D}}$ [Eq. (10.81)] and $\Delta\omega_{\mathrm{EP}}$ [Eq. (10.82)], the beating frequency can be expressed using the following hierarchy of equations:

$$\Delta\omega_{\mathrm{S}}=\mathrm{sgn}(\Delta\omega_{\mathrm{D}})\sqrt{\Delta\omega_{\mathrm{D}}^2-\Delta\omega_{\mathrm{EP}}^2}, \tag{10.94}$$

$$\Delta\omega_{\mathrm{D}}=\frac{\gamma}{\Gamma+\gamma}\Delta\omega_{\mathrm{P}}+\frac{\Gamma}{\Gamma+\gamma}\Delta\omega_{\mathrm{Kerr}}, \tag{10.95}$$

$$\Delta\omega_{\mathrm{P}}=\omega_{\mathrm{P},\bar{1}}-\omega_{\mathrm{P},\bar{2}}, \tag{10.96}$$

$$\Delta\omega_{\mathrm{Kerr}}=\eta(N_{\bar{2}}-N_{\bar{1}})=\frac{\eta\Delta P_{\mathrm{SBL}}}{\gamma_{\mathrm{ex}}\hbar\omega}, \tag{10.97}$$

where sgn is the sign function and we take $\Omega = 0$ (no rotation). For the Kerr shift, $\Delta P_{\mathrm{SBL}} = P_{\mathrm{ccw}} - P_{\mathrm{cw}}$ is the output power difference of the SBLs, and γ_{ex} is the photon decay rate due to the output coupling. The center of the locking band can be found by setting $\Delta\omega_{\mathrm{D}} = 0$, which leads to $\Delta\omega_{\mathrm{P}} = -(\Gamma/\gamma)\Delta\omega_{\mathrm{Kerr}}$.

We would like to remark that the equation for locking bandwidth $\Delta\omega_{\mathrm{EP}}$ in the main text does not contain the phase-sensitive term $\mathrm{Im}(\kappa\chi^*)$. This terms leads to asymmetry of the locking band with respect to q and $1/q$ and has not been observed in the experimental data. We believe its contribution can be neglected. In other special cases, $\mathrm{Im}(\kappa\chi^*)$ disappears if there is a dominant, symmetric scatterer that determines both κ and χ (e.g. the taper coupling point), or becomes negligible if there are many small scatterers that add up incoherently (e.g. surface roughness). This term can also be absorbed into the first two terms so the locking bandwidth is rewritten using effective κ, χ and a net amplitude imbalance q_0. Thus power calibration errors in the experiment may be confused with the phase-sensitive term in the locking bandwidth.

Technical noise considerations

Here we briefly consider the impact of technical noise to the readout signal. Two important noise sources are temperature drifts and imprecisely-defined pump frequencies, both of which change the phase mismatch $\Delta\Omega$. For a single SBL, the phase mismatch is transduced into the laser frequency through the mode-pulling effect [Eq. (10.61) and (10.81)], which gives a noise transduction factor of $\gamma^2/(\Gamma+\gamma)^2$. With $\gamma/\Gamma = 0.076$ fitted from experimental data, the mode-pulling effect reduces pump noise by -23 dB. The Pound-Drever-Hall locking loop in the system also suppresses noise at low offset frequencies. For counter-pumping of SBLs, the pumping sources are derived from the same laser, and their frequency difference is determined by radio-frequency signals, thus the system has a strong common-mode noise rejection. Within the model described by Eq. (10.81), the SBL frequency is dependent on the pump frequency difference only, and features a very high common-mode noise rejection. Other effects that are not considered in the model (i.e. drift of frequency difference between pump and SBL modes) are believed to be minor for offset frequencies above 10Hz, where the Allan deviation shows a slope of $-1/2$ corresponding to white frequency noise.

References

[1] Bender, C. M. & Boettcher, S. Real spectra in non-Hermitian Hamiltonians having PT symmetry. *Physical Review Letters* **80**, 5243 (1998).

[2] Bender, C. M. Making sense of non-Hermitian Hamiltonians. *Reports on Progress in Physics* **70**, 947 (2007).

[3] Feng, L., El-Ganainy, R. & Ge, L. Non-Hermitian photonics based on parity–time symmetry. *Nature Photonics* **11**, 752–762 (2017).

[4] El-Ganainy, R., Khajavikhan, M., Christodoulides, D. N. & Ozdemir, S. K. The dawn of non-Hermitian optics. *Communications Physics* **2**, 37 (2019).

[5] Miri, M.-A. & Alù, A. Exceptional points in optics and photonics. *Science* **363**, eaar7709 (2019).

[6] Lee, S.-B. *et al.* Observation of an exceptional point in a chaotic optical microcavity. *Physical Review Letters* **103**, 134101 (2009).

[7] Guo, A. *et al.* Observation of PT-symmetry breaking in complex optical potentials. *Physical Review Letters* **103**, 093902 (2009).

[8] Rüter, C. E. *et al.* Observation of parity–time symmetry in optics. *Nature Physics* **6**, 192–195 (2010).

[9] Regensburger, A. *et al.* Parity–time synthetic photonic lattices. *Nature* **488**, 167–171 (2012).

[10] Peng, B. *et al.* Parity–time-symmetric whispering-gallery microcavities. *Nature Physics* **10**, 394–398 (2014).

[11] Doppler, J. *et al.* Dynamically encircling an exceptional point for asymmetric mode switching. *Nature* **537**, 76–79 (2016).

[12] Peng, B. *et al.* Loss-induced suppression and revival of lasing. *Science* **346**, 328–332 (2014).

[13] Feng, L., Wong, Z. J., Ma, R.-M., Wang, Y. & Zhang, X. Single-mode laser by parity-time symmetry breaking. *Science* **346**, 972–975 (2014).

[14] Hodaei, H., Miri, M.-A., Heinrich, M., Christodoulides, D. N. & Khajavikhan, M. Parity-time–symmetric microring lasers. *Science* **346**, 975–978 (2014).

[15] Brandstetter, M. *et al.* Reversing the pump dependence of a laser at an exceptional point. *Nature Communications* **5**, 4034 (2014).

[16] Wiersig, J. Enhancing the sensitivity of frequency and energy splitting detection by using exceptional points: application to microcavity sensors for single-particle detection. *Physical Review Letters* **112**, 203901 (2014).

[17] Liu, Z.-P. *et al.* Metrology with PT-symmetric cavities: enhanced sensitivity near the PT-phase transition. *Physical Review Letters* **117**, 110802 (2016).

[18] Ren, J. *et al.* Ultrasensitive micro-scale parity-time-symmetric ring laser gyroscope. *Optics Letters* **42**, 1556–1559 (2017).

[19] Sunada, S. Large Sagnac frequency splitting in a ring resonator operating at an exceptional point. *Physical Review A* **96**, 033842 (2017).

[20] Chen, P.-Y. *et al.* Generalized parity–time symmetry condition for enhanced sensor telemetry. *Nature Electronics* **1**, 297–304 (2018).

[21] Dong, Z., Li, Z., Yang, F., Qiu, C.-W. & Ho, J. S. Sensitive readout of implantable microsensors using a wireless system locked to an exceptional point. *Nature Electronics* **2**, 335–342 (2019).

[22] Chen, W., Özdemir, Ş. K., Zhao, G., Wiersig, J. & Yang, L. Exceptional points enhance sensing in an optical microcavity. *Nature* **548**, 192–196 (2017).

[23] Hodaei, H. *et al.* Enhanced sensitivity at higher-order exceptional points. *Nature* **548**, 187–191 (2017).

[24] Lai, Y.-H., Lu, Y.-K., Suh, M.-G., Yuan, Z. & Vahala, K. Observation of the exceptional-point-enhanced Sagnac effect. *Nature* **576**, 65–69 (2019).

[25] Hokmabadi, M. P., Schumer, A., Christodoulides, D. N. & Khajavikhan, M. Non-Hermitian ring laser gyroscopes with enhanced Sagnac sensitivity. *Nature* **576**, 70–74 (2019).

[26] Zhang, M. *et al.* Quantum noise theory of exceptional point sensors. *Physical Review Letters* **123**, 180501 (2019).

[27] Langbein, W. No exceptional precision of exceptional-point sensors. *Physical Review A* **98**, 023805 (2018).

[28] Lau, H.-K. & Clerk, A. A. Fundamental limits and non-reciprocal approaches in non-Hermitian quantum sensing. *Nature Communications* **9**, 4320 (2018).

[29] Chen, C., Jin, L. & Liu, R.-B. Sensitivity of parameter estimation near the exceptional point of a non-Hermitian system. *New Journal of Physics* **21**, 083002 (2019).

[30] Mortensen, N. A. *et al.* Fluctuations and noise-limited sensing near the exceptional point of parity-time-symmetric resonator systems. *Optica* **5**, 1342–1346 (2018).

[31] Post, E. J. Sagnac effect. *Reviews of Modern Physics* **39**, 475–493 (1967).

[32] Li, J., Suh, M.-G. & Vahala, K. Microresonator Brillouin gyroscope. *Optica* **4**, 346–348 (2017).

[33] Li, J., Lee, H., Chen, T. & Vahala, K. J. Characterization of a high coherence, Brillouin microcavity laser on silicon. *Optics Express* **20**, 20170–20180 (2012).

[34] Petermann, K. Calculated spontaneous emission factor for double-heterostructure injection lasers with gain-induced waveguiding. *IEEE Journal of Quantum Electronics* **15**, 566–570 (1979).

[35] Siegman, A. Excess spontaneous emission in non-hermitian optical systems. I. Laser amplifiers. *Physical Review A* **39**, 1253 (1989).

[36] Hamel, W. & Woerdman, J. Observation of enhanced fundamental linewidth of a laser due to nonorthogonality of its longitudinal eigenmodes. *Physical Review Letters* **64**, 1506 (1990).

[37] Cheng, Y.-J., Fanning, C. & Siegman, A. Experimental observation of a large excess quantum noise factor in the linewidth of a laser oscillator having nonorthogonal modes. *Physical Review Letters* **77**, 627 (1996).

[38] Wenzel, H., Bandelow, U., Wunsche, H.-J. & Rehberg, J. Mechanisms of fast self pulsations in two-section DFB lasers. *IEEE Journal of Quantum Electronics* **32**, 69–78 (1996).

[39] Berry, M. V. Mode degeneracies and the Petermann excess-noise factor for unstable lasers. *Journal of Modern Optics* **50**, 63–81 (2003).

[40] Lee, S.-Y. *et al.* Divergent Petermann factor of interacting resonances in a stadium-shaped microcavity. *Physical Review A* **78**, 015805 (2008).

[41] Wiersig, J., Kim, S. W. & Hentschel, M. Asymmetric scattering and nonorthogonal mode patterns in optical microspirals. *Physical Review A* **78**, 053809 (2008).

[42] Schomerus, H. Excess quantum noise due to mode nonorthogonality in dielectric microresonators. *Physical Review A* **79**, 061801 (2009).

[43] Yoo, G., Sim, H.-S. & Schomerus, H. Quantum noise and mode nonorthogonality in non-hermitian PT-symmetric optical resonators. *Physical Review A* **84**, 063833 (2011).

[44] Chong, Y. & Stone, A. D. General linewidth formula for steady-state multimode lasing in arbitrary cavities. *Physical Review Letters* **109**, 063902 (2012).

[45] Zhang, J. *et al.* A phonon laser operating at an exceptional point. *Nature Photonics* **12**, 479–484 (2018).

[46] Adler, R. A study of locking phenomena in oscillators. *Proceedings of the IRE* **34**, 351–357 (1946).

[47] Cresser, J. Quantum noise in ring-laser gyros. III. Approximate analytic results in unlocked region. *Physical Review A* **26**, 398 (1982).

[48] Lee, H. *et al.* Chemically etched ultrahigh-Q wedge-resonator on a silicon chip. *Nature Photonics* **6**, 369–373 (2012).

[49] Spreeuw, R., Neelen, R. C., Van Druten, N., Eliel, E. & Woerdman, J. Mode coupling in a He-Ne ring laser with backscattering. *Physical Review A* **42**, 4315 (1990).

[50] Cai, M., Painter, O. & Vahala, K. J. Observation of critical coupling in a fiber taper to a silica-microsphere whispering-gallery mode system. *Physical Review Letters* **85**, 74 (2000).

[51] Spillane, S., Kippenberg, T., Painter, O. & Vahala, K. Ideality in a fiber-taper-coupled microresonator system for application to cavity quantum electrodynamics. *Physical Review Letters* **91**, 043902 (2003).

[52] Ferre-Pikal, E. S. *et al.* IEEE standard definitions of physical quantities for fundamental frequency and time metrology—random instabilities. *IEEE Std Std 1139-2008* c1–35 (2009).

[53] Van der Lee, A. *et al.* Excess quantum noise due to nonorthogonal polarization modes. *Physical Review Letters* **79**, 4357 (1997).

[54] Sarma, R., Ge, L., Wiersig, J. & Cao, H. Rotating optical microcavities with broken chiral symmetry. *Physical Review Letters* **114**, 053903 (2015).

[55] Kaplan, A. & Meystre, P. Enhancement of the Sagnac effect due to nonlinearly induced nonreciprocity. *Optics Letters* **6**, 590–592 (1981).

[56] Wright, E. M., Meystre, P., Firth, W. & Kaplan, A. Theory of the nonlinear Sagnac effect in a fiber-optic gyroscope. *Physical Review A* **32**, 2857 (1985).

[57] Del Bino, L., Silver, J. M., Stebbings, S. L. & Del'Haye, P. Symmetry breaking of counter-propagating light in a nonlinear resonator. *Scientific Reports* **7**, 43142 (2017).

[58] Sargent III, M., Scully, M. O. & Lamb Jr, W. E. *Laser Physics* (Addison-Wesley Pub. Co., 1974).